
A microwave chip-based beamsplitter for guided low-energy electrons

Jakob Hammer



München 2014

A microwave chip-based beamsplitter for guided low-energy electrons

Jakob Hammer

Dissertation
an der Fakultät für Physik
der Ludwig-Maximilians-Universität
München

vorgelegt von
Jakob Hammer
aus Dachau

München, den 17. November 2014

Erstgutachter: Prof. Dr. Peter Hommelhoff

Zweitgutachter: Prof. Dr. Jörg Schreiber

Tag der mündlichen Prüfung: 19. Dezember 2014

Für Bine und meine Eltern

Zusammenfassung

Gegenstand der vorliegenden Arbeit sind Experimente, in denen freie Elektronen in den Mikrowellenfeldern eines Quadrupolleiters manipuliert werden. Die Erzeugung der elektrischen Felder mit Hilfe eines planaren Mikrowellensubstrats ermöglicht es, die Bewegung langsamer Elektronen mit Energien unterhalb von 10 eV auf vielfältige Art und Weise zu beeinflussen. In diesem Zusammenhang bieten planare Substrate den zentralen Vorteil, dass fein strukturierte Potentiallandschaften im Nahfeld der Mikrowellenanregung erzeugt werden können. Zudem kann ein tiefer Einschluss der Elektronen in diesem Potential gewährleistet werden. Dies schafft ideale Voraussetzungen für die Realisierung von planaren Strahlteilern oder Resonatoren für Elektronen, die wiederum Perspektiven für neuartige Quantenoptikexperimente mit geführten Elektronen eröffnen.

Im Rahmen dieser Arbeit ist es zum ersten Mal gelungen, einen geführten Elektronenstrahl an der Oberfläche eines strukturierten Mikrowellensubstrats aufzuspalten und die Funktionsweise des Strahlteilers experimentell zu untersuchen. Die erfolgreiche Durchführung dieses Experiments basiert auf der Erzeugung eines mikrostrukturierten Strahlteilerpotentials und dem Einsatz von Treiberfrequenzen im Gigahertzbereich. Zu diesem Zweck haben wir ein Mikrowellensubstrat entwickelt, das ein einschließendes Potential erzeugt, in dem Elektronen entlang eines Pfades geführt werden, der sukzessive in zwei Pfade auffächert. In unserem Experiment beobachten wir hinter dem Strahlteilersubstrat zwei symmetrisch aufgespaltene Elektronenstrahlen. Außerdem stellen wir fest, dass ab einer Elektronenenergie von 3 eV erhebliche Verluste das Elektronensignal dominieren. Aus diesem Grund präsentieren wir Simulationen, die die Welleneigenschaften der Elektronen berücksichtigen und das Strahlteilerpotential in der Hinsicht verbessern, dass Anregungen der Elektronenbewegung während der Aufspaltung minimiert werden.

Ein weiterer Schwerpunkt liegt auf dem Entwurf und der experimentellen Vermessung einer Elektronenkanone, die auf eine scharfe Metallspitze als Elektronenquelle zurückgreift. Mit Hilfe dieser Elektronenkanone wollen wir einen gepulsten, beugungslimitierten Elektronenstrahl erzeugen und diesen in den Elektronenleiter einspeisen. Des Weiteren können wir im Rahmen dieses Experiments mittels Elektroneninterferenz nachweisen, dass ein von einer lasergetriebenen Metallspitze photoemittierter Elektronenstrahl hervorragende räumliche Kohärenzeigenschaften besitzt. Diese Beobachtung ist für alle zeitaufgelösten Anwendungen relevant, die eine lasergetriebene Metallspitze zur Erzeugung kohärenter Elektronenstrahlen einsetzen. In zukünftigen Experimenten wollen wir die hohe zeitliche Kontrolle der lasergetriebenen Elektronenquelle mit der räumlichen Kontrolle über geführte Elektronen vereinen.

Der transversale Einschluss geführter Elektronen führt naturgemäß dazu, dass die Dynamik im einschließenden Potential durch diskrete Quantenzustände beschrieben wird. Im Prinzip sollte es daher möglich sein, Elektronen in quantisierten Bewegungszuständen zu erzeugen, die tief im Potential des Elektronenleiters liegen. Grundvoraussetzung dafür ist eine beugungslimitierte Elektronenquelle, sowie ein Potential, das Elektronen einen sanften Übergang in den Elektronenleiter erlaubt. In dieser Arbeit zeigen wir, dass mit Hilfe einer optimierten Einkoppelstruktur und einer gepulsten Elektronenquelle Elektronen nahezu störungsfrei in das einschließende Potential überführt werden können. Dies ist eine wichtige Maßnahme, um Elektronen in weiterführenden Experimenten direkt in Quantenzustände des Elektronenleiters einzuspeisen.

Abstract

This work reports on the manipulation of slow electrons in free space using a microwave quadrupole guide. The generation of the electric fields by means of a planar microwave chip provides an entirely new electron toolkit that allows the guidance and steering of electrons with kinetic energies below 10 eV. As a key feature, this chip-based technology combines the flexibility to engineer microstructured guiding potentials in the near-field of the microwave excitation with tight transverse confinement of the guided electrons. This renders planar guiding structures ideally suited for the implementation of electron beam splitters or resonators with prospects for novel quantum optics experiments with guided electrons.

We present an experiment that demonstrates, for the first time, the realization of a chip-based beam splitter for low-energy electrons. Crucial for the success of the experiment is the generation of a finely structured beam splitter potential and the operation at drive frequencies in the gigahertz range. We report on the design of an optimized microwave chip that generates a beam splitter guiding potential by gradually transforming from a single-well harmonic confinement into a double well along the chip. In the experiment we observe an electron signal with two symmetrically split up output beams. Furthermore we find that with increasing electron kinetic energy, electron loss starts to dominate the electron signal for energies above 3 eV. To this end, we present results of wave-optical simulations that further optimize the guiding potential to reduce excitations in the electron motion as an adverse effect of the splitting process.

A second main result of this thesis is the construction and experimental characterization of an electron gun that is based on a nanotip electron emitter. It is specifically designed to provide a pulsed, diffraction-limited electron beam for injection into the guide. We prove that photoemitted electron beams from a laser-triggered nanotip are spatially highly coherent using an electron interference setup. This finding is of importance for all time-resolved applications that employ coherent electron beams from a laser-triggered nanotip. Unprecedented spatial and temporal control over guided electrons can be achieved when combining this coherent laser-triggered electron source with a microwave electron guide.

The transverse guiding potential naturally provides discretized motional quantum states that govern the dynamics of guided electrons. Ultimately, it should be possible to directly inject electrons into low-lying motional quantum states of the guiding potential. As prerequisites, this necessitates a diffraction-limited electron gun and a guiding potential that provides electrons a smooth passage into the guide. Therefore, we employ an optimized coupling electrode structure as well as a pulsed electron source to demonstrate experimentally that electron excitations at the guide entrance can be greatly reduced. This paves the way towards the direct injection of electrons into motional quantum states of the guide.

Contents

Zusammenfassung	vii
Abstract	ix
1 Introduction	3
2 Theoretical aspects of electron guiding	7
2.1 Dynamics of charged particles in a quadrupole guide	8
2.2 A surface-electrode electron guide	12
2.2.1 Conformal mapping	12
2.2.2 Five-wire electrode geometry	14
2.2.3 Microwave drive parameters for electron guiding	16
2.3 Quantum ground state electron guiding	17
2.3.1 Electron wave optics for mode-matching to the ground state	18
2.3.2 Quantum wave packet evolution in the guiding potential	24
3 Electron guiding and optimized injection into the guide	29
3.1 Experimental setup	29
3.1.1 Guiding substrates	30
3.1.2 Microwave equipment and power correction	33
3.1.3 Pulsed thermionic electron streaking gun	36
3.1.4 Vacuum chamber	41
3.2 Guiding of electrons along a curve	42
3.3 Microwave phase dependence of the guiding signal	44
3.3.1 Fringing electric fields at the substrate edge	44
3.3.2 Particle trajectory simulations	45
3.4 Optimized coupling structures for electron guiding	47
3.4.1 Numerical optimization of the electrode structure	48
3.4.2 Particle trajectory simulations	50
3.4.3 Electron guiding with optimized coupling structures	53
3.5 Phase-resolved electron guiding measurement	54
3.5.1 Synchronous electron injection setup	54
3.5.2 Microwave phase-resolved guiding signals	55
3.6 Next steps and future improvements	56
4 A microwave chip-based beam splitter for guided electrons	57
4.1 Beam splitter electrode design	57
4.1.1 Ideal hexapole intersection	58
4.1.2 Numerical optimization of electrode layout	60

4.2	Particle trajectory simulations	64
4.3	Microwave design of the beam splitter chip	67
4.4	Demonstration of electron beam splitting	70
4.4.1	Experimental beam splitter signal	70
4.4.2	Dependence of beam splitting on electron source position	72
4.4.3	Splitting with variable electron energy	74
4.5	Simulations towards adiabatic on-chip electron beam splitting	75
4.5.1	Optimized beam splitter potential	75
4.5.2	Drive parameter scaling	79
4.6	Next experimental steps and future perspectives	81
5	A highly coherent electron beam from a laser-triggered nanotip	83
5.1	Metal nanotip preparation and characterization	84
5.2	Single-atom tip electron emitters	88
5.3	Fiber coupled near UV laser light delivery for photoemission	91
5.4	Coherence measurement of laser-triggered electron emission	95
5.4.1	Spatial coherence in DC-field and photoemission	96
5.4.2	Electron interference at a carbon nanotube biprism	96
5.4.3	Demonstration of high spatial coherence in photoemission	98
6	A coherent field emission gun for electron guiding	101
6.1	UHV chamber and experimental setup	101
6.1.1	Experimental chamber	101
6.1.2	8D nanopositioning system	103
6.1.3	Electric and magnetic shielding	105
6.2	Electron optics	106
6.2.1	Design and trajectory simulations of the electron lens	107
6.2.2	Experimental performance of electron lens	111
6.3	Electron guiding using the field emission gun	114
7	Conclusion and outlook	117
	References	121
	Danksagung	131

1 Introduction

Electrons are elementary particles without inner structure and one might be tempted to say that, as isolated particles, they do not naturally embody many interesting properties of physics. On the contrary, the simple structure of electrons combined with their electric charge makes them handy specimens for studying fundamental quantum mechanics. As an example, the wave nature of massive particles is one of the most intriguing aspects of quantum physics. It is based on the direct correspondence between the concept of particles and waves established by de Broglie in 1924 [1]. The first direct observation of the wave nature of matter was accomplished by Davisson and Germer demonstrating the diffraction of free electrons from a single crystal of nickel [2]. Direct evidence for the particle-wave duality is provided by the interference pattern that is observable when detecting electrons after the passage through a sample with transmissive slits [3], the matter-wave analogon of Young's famous double-slit experiment. The collective build-up of an electron interference pattern from point-like particles that arrive one at a time was initially considered as an "impossible" thought experiment for physics students [4] and has been realized experimentally for the first time with electrons [5]. It was elected to be the most beautiful experiment in physics by the readers of *Physics World* [6].

Electron interferometers have a long and successful history in demonstrating matter-wave interference experiments investigating the particle-wave duality [5, 7, 8, 9] and other fundamental quantum effects like the Aharonov-Bohm effect [10], the Hanbury Brown-Twiss anticorrelations of free electrons [11] and decoherence effects close to semiconducting surfaces [12]. The superb performance of electron interferometers may be attributed mainly to the existence of coherent field emission electron sources, the paramount control over electron matter waves using sophisticated electron optics, and the existence of suitable coherent electron beam splitters, the key component of any interferometric measurement device [13].

This thesis is intended to advance a conceptually new approach to manipulate free electrons by creating a transverse guiding potential above the surface of a planar microwave chip. It offers prospects in reaching quantum control over the transverse electron motion in versatile potential landscapes in synchrony with excellent time resolution by employing short electron pulses from a laser-triggered nanotip. Ultimately, such a guided matter-wave system may allow new quantum optics experiments with electrons such as guided matter-wave interferometry or noninvasive electron microscopy [14, 15].

Precise control over the motion of charged particles rests upon their isolation in free space. However, any electrostatic potential has to satisfy the Poisson equation, which prevents the formation of a static potential minimum in free space. The Paul trap is a well established tool to circumvent this issue by employing time-dependent quadrupole electric fields to isolate and manipulate single atomic ions in vacuum [16]. Unprecedented quantum control over the internal and external states of trapped ions has been

reached [17]. The persistent progress in ion trapping provides ground-breaking experimental methods to manipulate individual quantum systems on the level of single motional quanta [18], an approach for which D. Wineland shared the Nobel Prize in Physics in 2012.

The manipulation of free electrons in a quadrupole guide employs the same principles as ion traps to transversely confine electrons with kinetic energies below 10 eV [19, 20]. The confinement of charged particles in time-dependent electric quadrupole fields is conceptually independent of the mass and the sign of the particle's charge, however, it has rarely been considered for electrons. This can mainly be attributed to the fact that for stable confinement the oscillation frequency of the quadrupole field has to be matched to the charge-to-mass ratio of the confined particle. Because of the high charge-to-mass ratio of electrons, the frequency of the quadrupole oscillation needs to lie in the gigahertz range. This imposes stringent requirements on the design of the trap electrodes that have to support the microwave signals. Generating the guiding potential by means of a planar electrode layout on a microwave substrate helps to keep electrode dimensions in a range that is compatible with microwave transmission line technology and allows for feeding of signals in the microwave range. Moreover, a planar electrode layout enables easy scalability of the guiding system and provides unprecedented flexibility to engineer versatile guiding potential landscapes by microstructuring the electrode layout.

In the experiments presented in this thesis, we demonstrate for the first time an on-chip beam splitter for guided electrons by making use of the unique possibility to achieve high field gradients in the near-field of a microstructured electrode design. We describe in detail the design, construction and operation of an experimental setup, in which beam splitting is achieved by gradually transforming the transverse guiding potential from a single-well harmonic confinement into a double-well potential. By virtue of this guiding potential we demonstrate the symmetric splitting of a guided electron beam with kinetic energies of up to 3 eV. Furthermore, excellent agreement with particle tracking simulations is found. Besides the first demonstration of beam splitting action, we present results of a further optimization of the beam splitter potential that will ultimately allow the adiabatic splitting of a guided electron wave packet in future experiments. The realization of such a beam splitter would represent a decisive step towards guided matter-wave interferometry experiments where the transverse motional quantum state of the guided electrons could be used as a carrier of quantum information.

As a prerequisite for these experiments, electrons have to be prepared in low-lying quantum states of the transverse guiding potential. In principle, this should be possible by matching the wavefunction of an electron wave packet impinging longitudinally on the guide entrance to the ground state wavefunction of the transverse guiding potential. The realization of this injection scheme poses, however, rigorous requirements on the electron source forming the beam as well as on the homogeneity of the guiding potential at the entrance of the guide. To this end, we numerically optimize the shape of the electrode layout to reduce lateral forces that deflect the electron during injection. We demonstrate experimentally that lateral excitations of the guided electrons after injection are significantly reduced allowing electrons a smooth passage into the guide. Concerning the electron source, a diffraction-limited electron beam is required to simultaneously match the ground state wavefunction both in position space and in momentum space.

To this end, the development and characterization of a field-emission electron source is a further main result of this thesis. It combines a nanometric tungsten tip field emitter with a compact electron lens to focus the electron beam. We present particle tracking simulations that suggest that, due to sufficiently low aberrations, focusing close to the diffraction limit should be possible with electron kinetic energies down to 1 eV. Furthermore, a compact fiber-based laser illumination setup has been developed to trigger the electron emission by near-ultraviolet laser light. This will allow for spatial and temporal control over the guided electrons when driving the electron source with ultrashort laser pulses, leading to the generation of short electron pulses.

Another focus of this thesis is the study of the spatial coherence properties of electron beams that are generated by laser-driven photoemission from nanometric tungsten tips. These tips have been shown to be coherent point sources of electrons in DC-field emission [21, 22]. They provide electron beams with flat wavefronts that can be focused to the fundamental physical limit given by matter-wave diffraction [23]. Although laser-driven metal nanotips promise to provide coherent electron pulses with high time resolution, a quantitative study of their spatial coherence has been elusive. We use the novel electron source to demonstrate that photoemitted electrons from a tungsten nanotip are highly coherent. These measurements reveal, for the first time, that nanotips, the most coherent DC electron sources used in microscopy, almost fully preserve their superior spatial coherence in laser-triggered emission. This has direct impact on all time-resolved electron-based imaging applications that need to combine high spatial resolution with ultimate time resolution. The implementation of this electron source in the electron guiding experiment promises to enable direct injection into low-lying quantum states of the transverse guiding potential, which might ultimately allow for quantum control over the motion of guided electrons in future experiments.

This thesis is organized as follows:

Chapter 1 gives a brief introduction.

Chapter 2 provides the basics of charged particle confinement in an oscillating quadrupole electric field and derives the experimental parameters for electron guiding. Fundamental aspects of matter-wave optics are acquired to elaborate the scheme for direct injection of electrons into the motional quantum ground state of the electron guide.

Chapter 3 presents the experimental apparatus used for electron guiding and gives a detailed study of the measured guiding signal. We report on the numerical optimization of the electrode layout, as well as the synchronized injection of short electron pulses to provide electrons a smooth passage into the guide.

Chapter 4 describes the design and the experimental demonstration of a new microwave chip-based beam splitter for low-energy guided electrons. We explore prospects to achieve the adiabatic splitting of a guided electron wave packet.

Chapter 5 provides a quantitative comparison of the spatial coherence of a metal nanotip electron source in DC-field and photoemission using a carbon nanotube as matter-wave beam splitter. The electron emission from a laser-triggered metal tip is found to be highly coherent.

Chapter 6 details the experimental setup of the nanotip electron gun as well as the electron optics that has been designed and constructed in the course of this thesis.

Chapter 7 concludes this thesis with an outlook on future developments.

Manuscripts published in peer-reviewed journals and books

- **Phase-resolved electron guiding in optimized chip-based microwave potentials**
J. Hammer, J. Hoffrogge, S. Heinrich, P. Hommelhoff, *Phys. Rev. Applied* **2**, 044015 (2014).
- **Tip-based source of femtosecond electron pulses at 30keV**
J. Hoffrogge, J.-P. Stein, M. Krüger, M. Förster, J. Hammer, D. Ehberger, P. Baum and P. Hommelhoff, *J. Appl. Phys.*, **115**, 094506 (2014).
- **From Above-Threshold Photoemission to Attosecond Physics at a Nanometric Tungsten Tip**
M. Krüger, M. Schenk, J. Breuer, M. Förster, J. Hammer, J. Hoffrogge, S. Thomas, and P. Hommelhoff, book chapter in *Progress in Ultrafast Intense Laser Science Vol. IX*, edited by K. Yamanouchi and K. Midorikawa (Springer 2013).
- **Interference between magnetic field and cavity modes in an extended Josephson junction**
V. Humbert, M. Aprili and J. Hammer, *Phys. Rev. B* **86**, 024520 (2012).
- **Microwave Cooling of Josephson Plasma Oscillations**
J. Hammer, I. Petkovic and M. Aprili, *Phys. Rev. Lett.* **107**, 017001 (2011).
(selected as Editor's Suggestion)
- **Precision angle sensor using an optical lever inside a Sagnac interferometer**
J. Hogan[†], J. Hammer[†], S.-W. Chiow, S. Dickerson, D.M.S. Johnson, T. Kovachy, A. Sugarbaker and M.A. Kasevich, *Optics Letters* **36**, 1698 (2011).

Manuscripts submitted to peer-reviewed journals

- **Microwave chip-based beam splitter for low-energy guided electrons**
J. Hammer, S. Thomas, Ph. Weber and P. Hommelhoff, manuscript submitted for publication, preprint at arXiv:1408.2658 (2014).
- **Highly coherent electron beam from a laser-triggered field emitter**
D. Ehberger[†], J. Hammer[†], M. Eisele, M. Krüger, J. Noe, A. Högele, and P. Hommelhoff, manuscript submitted for publication.

Patent applications

- **Ein Elektronenstrahlteiler basierend auf elektrischen Mikrowellenfeldern**
P. Hommelhoff, J. Hammer, European patent application no.,
PCT/EP2014/001784 (2014).

[†]These authors contributed equally.

2 Theoretical aspects of electron guiding

The ambitious goal to confine and isolate atomic particles in vacuum using purely electromagnetic fields emerged from molecular beam physics, mass spectrometry and particle accelerator physics. The intention to observe the structure of matter and to detect dynamic processes within it pushed W. Paul and co-workers to investigate the use of multipole electric and magnetic fields to confine charged particles [24, 25]. As a result of their pioneering work on the trapping of atomic ions in free space [16], W. Paul and H. Dehmelt shared the Nobel Prize in Physics in 1989 for developing two kinds of charged particle traps. One employs a combination of static electric and magnetic fields, the Penning trap [26], and the other uses time-dependent purely electric quadrupole fields, the Paul trap [27].

An essential technique that boosted the range of applications for particle trapping experiments was the development of laser cooling. It employs radiation pressure to cool freely suspended atoms [28]. This technique was soon adapted to freeze the motion of atomic ions that oscillate in a Paul trap [29] and resulted in the experimental demonstration of cooling atoms to their quantum zero-point energy, which is the ultimate limit to the trapped particle's energy [30]. The ability to cool and observe individual ions in their lowest quantum vibrational state in a trap and to manipulate their electronic states through resonant laser excitation paved the way for a plethora of modern quantum physics experiments. One application of the Paul trap is precision spectroscopy of free ions, which is also motivated by the need to establish an atomic clock frequency standard [31]. Using sophisticated cooling techniques also makes it possible to prepare and maintain trapped ions in a so-called entangled state [32], which opens up new perspectives in the field of quantum information processing [33, 34] and quantum simulation, like the investigation of quantum phase transitions in ion crystals [35, 36].

Here we discuss the manipulation of free electrons by purely electric fields above the surface of a planar microwave chip [19, 20, 37]. This technique allows to guide electrons using the tight transverse confinement provided by alternating quadrupole electric fields, which is based on a two-dimensional Paul trap. The confinement of electrons in time-dependent electric quadrupole fields employs the same principles as ion trapping, however, it requires higher oscillation frequencies of the quadrupole fields because of the larger charge-to-mass ratio of electrons. As a result, we need to operate the planar microwave structures with drive frequencies of about 1 GHz to achieve stable guiding of electrons with longitudinal kinetic energies below 10 eV. The first part of this chapter describes the working principle of the transverse electron confinement and derives the experimental parameters required for electron guiding based on a planar microwave chip.

Quantum control of the transverse motion of electrons in such a guide would enable

new quantum optics experiments with electrons such as guided matter-wave interferometry or noninvasive electron microscopy [14, 15]. A prerequisite for these experiments is the preparation of electrons in low-lying quantum states of the transverse guiding potential. With a collimated, diffraction-limited electron gun, it should be possible to directly inject electrons into the transverse ground state of the guide. This direct injection scheme requires mode-matching of the impinging electron wavefunction to the spatial and momentum profile of the transverse ground state, similar to the coupling of laser light into a defined transverse optical mode of a glass fiber. As a result, we necessitate electron optics that prepare electron wave packets for injection by adjusting their spatial and momentum wavefunction in a transformative way without imprinting electron-optical aberrations on it. The second part of this chapter establishes a wave-optical description for the investigation of the direct ground state injection. This allows us to illustrate the scheme and more importantly to provide a foundation for ongoing experimental progress.

2.1 Dynamics of charged particles in a quadrupole guide

The guiding of electrons in the electric field of a planar microwave chip combines existing technology from surface-electrode ion traps [38, 39] with electron matter-wave optics [13]. In contrast to conventional electron optics, where the transverse focusing is performed using static electromagnetic fields, the transverse confinement of guided electrons is provided by an oscillating, purely electric potential. The principle is based on the subsequent focusing of a charged particle beam in the transverse plane when passing through a sequence of alternately converging and diverging lenses. Such a sequence will exhibit a stable net confinement in the transverse plane if the proper conditions on the focal length and spacing of the lenses are fulfilled. The principles of quadrupole guides and traps has been reviewed in several publications, for example Refs. [16, 40, 41]. In this section we summarize the principles of trapping charged particles in two dimensions using an oscillating quadrupole field and discuss how electron guiding on a planar microwave substrate can be achieved.

A charged particle guide that provides a linear confining force when the guided particles depart from the origin of the lateral xz -plane requires an electric potential of the form

$$\phi = [V_{dc} + V_0 \cos(\Omega t)] (\alpha x^2 + \beta z^2) / 2, \quad (2.1)$$

where V_{dc} is a static voltage and V_0 the voltage amplitude of an oscillating electric potential with drive frequency Ω . The constants α and β can be derived from the Laplace condition $\Delta\phi = 0$, which yields $\alpha + \beta = 0$. This gives rise to a quadrupole potential in the transverse plane

$$\phi(x, z, t) = [V_{dc} + V_0 \cos(\Omega t)] \frac{x^2 - z^2}{2R_0^2}, \quad (2.2)$$

where R_0 is the distance from the guide's center to the metal electrodes that generate the potential. Figure 2.1(a) shows the original electrode geometry proposed by W. Paul to create the electric quadrupole potential for a charged particle guide. It illustrates how to establish an electric potential with vanishing monopole and dipole components using

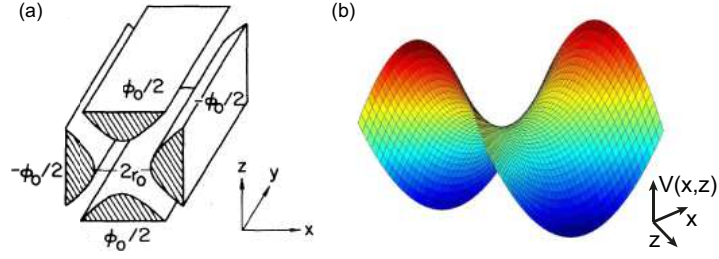


Figure 2.1: Quadrupole guide for charged particles. (a), Original electrode design proposed by W.Paul (taken from Ref [16]). The shape of the electrode geometry results in a quadrupole electric potential, which is shown in (b). Opposing electrodes lie on the same potential, whereas the polarity is opposite on the vertical and horizontal electrodes.

four metal electrodes and shaping the inside surfaces such that they approximate the equipotential surfaces of the quadrupole potential. Additionally, opposing electrodes must be held at the same electric potential, whereas the polarity is opposite on the vertical and horizontal electrodes. The electric quadrupole potential that is generated by such an electrode structure is depicted in Fig. 2.1(b). If one injects a charged particle at the saddle point of the static potential it is harmonically confined in one direction but repelled in the other (see Eq. 2.2). However, reversing the polarity of the applied voltages inverts the potential and likewise the directions along which confinement and repulsion is obtained. When switching the polarity of the voltages periodically, a time-averaged harmonic restoring force in both directions may emerge. This is the operation principle of a two-dimensional Paul trap.

Charged particle dynamics in oscillating quadrupole fields

The classical equation of motion of a charged particle in the time-dependent quadrupole potential, given by Eq. 2.2, is

$$\frac{d\mathbf{r}^2}{dt^2} = -\frac{Q}{M}\nabla\phi(\mathbf{r}, t). \quad (2.3)$$

Here Q and M denote the electron charge and mass and \mathbf{r} the position in the xz -plane. By means of appropriate substitutions the equation describing the particle dynamics can be cast into the form of a Mathieu equation

$$\frac{dr_i^2}{d\xi} \pm [a - 2q\cos(2\xi)]r_i = 0, \quad (2.4)$$

with the definitions

$$\xi = \frac{\Omega t}{2}, \quad a = \frac{4Q}{M} \frac{V_{dc}}{\Omega^2 R_0^2}, \quad \text{and} \quad q = \frac{2Q}{M} \frac{V_0}{\Omega^2 R_0^2}. \quad (2.5)$$

A general solution to the Mathieu equation features stable confined particle trajectories of the form

$$x(\xi) = A \sum_{+\infty}^{n=-\infty} C_{2n} \cos[(2n \pm \beta)\xi] + B \sum_{+\infty}^{n=-\infty} C_{2n} \sin[(2n \pm \beta)\xi], \quad (2.6)$$

where A and B are integration constants that are determined by the initial conditions. As can be seen from Eq. 2.6, the motional spectrum of the confined particle is composed of harmonic components with frequencies

$$\omega_n = (2n \pm \beta)\Omega/2 \quad (2.7)$$

The so-called characteristic exponent $\beta(a, q)$ and the amplitudes $C_{2n}(a, q)$ depend on a and q only and can take values according to continuous fraction expressions which can be found, e.g., in Ref [17]. From an analysis of the Mathieu equation one finds that stable solutions according to Eq. 2.6 correspond to diamond shaped stability areas in the a - q diagram. A detailed description of the stability regions is out of the scope of this work and is given in Ref. [40]. In the following we specifically consider the case without static potential component $V_{dc} = 0$ applied to the signal electrodes leading to $a = 0$. In this case the region of stable confinement lies within the range $0 < q < 0.908$. Accordingly, q is named the stability parameter.

Secular approximation

For typical conditions of stable confinement, i. e. $|a|, q \ll 1$, β is approximately given by

$$\beta^2 \approx a + \frac{q^2}{2}. \quad (2.8)$$

Furthermore, for small β , the expression of the charged particle's motion can be substantially simplified. The coefficients C_{2n} become rapidly small with increasing n and therefore the motion, according to Eq. 2.6, can be approximated to lowest order by

$$x(t) \approx C \left[1 - \frac{q}{2} \cos(\Omega t) \right] \cos\left(\frac{\beta}{2} \Omega t\right). \quad (2.9)$$

As can be seen, the dynamics of a stably confined electron is given by a slow *macro-motion*, often referred to as secular motion, oscillating with a frequency $\omega = \beta\Omega/2$. Additionally, there is a fast *micromotion* that oscillates at sidebands of the microwave drive frequency $\Omega \pm \omega$. Its oscillation amplitude is small compared to the secular motion and has a relative amplitude given by a factor of $q/4$.

Figure 2.2 shows typical particle trajectories in the transverse x -direction of a linear quadrupole guide for two different values of q and $V_{dc} = 0$, i.e. $a = 0$. The particle's secular motion is discernible as a slow harmonic oscillation with frequency ω . The fast micromotion is visible as superimposed oscillation at the drive frequency with a smaller amplitude. When comparing Fig. 2.2(a) with $q = 0.1$ and (b) with $q = 0.3$ one can clearly see that a smaller stability parameter is reflected in a smaller relative amplitude of the micromotion with respect to the macromotion.

As a result, if $V_{dc} = 0$, i.e. $a = 0$, and $q \ll 1$, the dynamics of a charged particle in the oscillating quadrupole potential are governed by the harmonic secular motion with the so-called transverse trap frequency

$$\omega = \frac{Q}{\sqrt{2}M} \frac{V_0}{\Omega R_0^2} = \frac{q}{\sqrt{8}} \Omega. \quad (2.10)$$

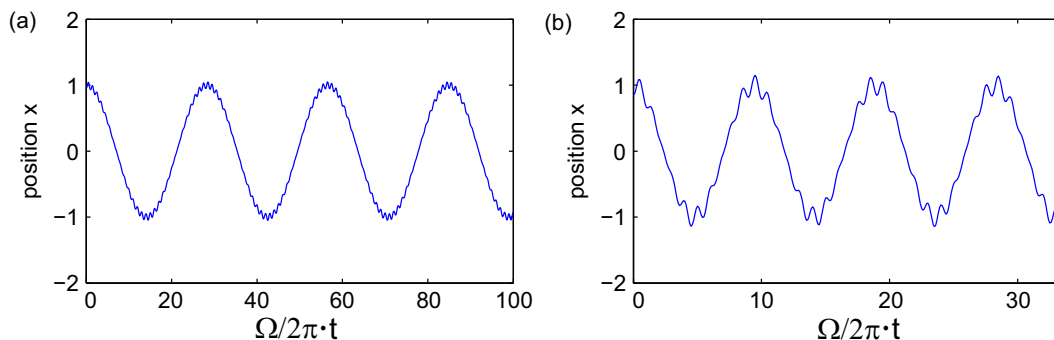


Figure 2.2: Particle trajectories in an ideal linear quadrupole guide. (a), shows a trajectory in the transverse x -direction for $q = 0.1$, whereas (b) results from $q = 0.3$. The particle's motion is dominated by the macromotion at the trap frequency ω , additionally the faster micromotion is superimposed with an oscillation amplitude at the drive frequency Ω . The relative amplitude of the micromotion with respect to the macromotion is observed when comparing (a) and (b) where a smaller q is reflected in a smaller amplitude of the micromotion.

Adiabatic approximation

An electron can be confined in any inhomogeneous high frequency electric potential $\phi(\vec{r}, t) = \phi_{RF} \cos(\Omega t)$ with amplitude ϕ_{RF} and angular frequency Ω , provided that the potential gradient that an electron experiences during its oscillation [41] is nearly constant. The motion of the electron is then effectively averaged over the high frequency oscillation of the potential and it experiences a time-averaged pseudopotential given by

$$\Psi = \frac{Q^2}{4M\Omega^2} |\nabla \phi_{RF}(\mathbf{r})|^2. \quad (2.11)$$

The adiabatic approximation, can be applied to the confinement of an electron in a quadrupole electric potential if $q \ll 1$. Inserting the quadrupole potential, given in Eq. 2.2, one obtains a harmonic pseudopotential with a characteristic frequency given by Eq. 2.10. Note that the micromotion observed in Fig. 2.2 is an indication for small deviations from the pseudopotential approximation for finite q .

The pseudopotential depth U , which corresponds to the value of the pseudopotential Ψ on the electrode surfaces is given by

$$U = \frac{Q^2}{4M} \frac{V_0^2}{\Omega^2 R_0^2} = \frac{q}{8} V_0. \quad (2.12)$$

The formulas for the trap frequency ω and the pseudopotential depth U can be applied provided that the microwave parameters Ω and V_0 are adjusted such that $q \ll 1$ with

$$q = \frac{2Q}{M} \frac{V_0}{\Omega^2 R_0^2}. \quad (2.13)$$

The electrode structure shown in Fig. 2.1(a) corresponds to the ideal configuration for the creation of a pure quadrupole potential. However, any electrode geometry which provides a saddle point in the electric potential creates a quadrupole component close

to the saddle point and is, hence, capable to provide dynamic confinement of charged particles. In the following we will focus on surface-electrode layouts that are implemented on a planar microwave substrate.

2.2 A surface-electrode electron guide

The implementation of the electron guide using surface-electrode structures on a planar microwave chip is beneficial in many respects. First of all, the large charge-to-mass ratio Q/M of electrons requires drive frequencies of about 1 GHz to realize stable confinement with small q , as can be seen from Eq. 2.13. As an essential feature, the dimensions of the planar electrode layout, which is used for electron guiding, are compatible with microwave transmission line technology and allow for feeding of signals in the microwave range. Besides this practical benefit, surface-electrode microwave chips provide unprecedented flexibility in the manipulation of the guided particles. By precise microfabrication of the chip electrodes high field gradients can be created in the near-field of the chip, which enables the generation of versatile pseudopotential landscapes for the guided particles. As an example, we will exploit this possibility in Ch. 4 where we employ higher order multipole fields to create a finely structured guiding potential that serves as a beam splitter for guided electrons. Furthermore, the planar design features easy scalability and will allow to interface the guided beam with other systems incorporated in the chip design in future experiments.

Planar surface-electrode ion traps are a prominent example for the flexibility provided by planar trap geometries [42, 39]. They have been employed to provide finely structured potential landscapes such as junctions for trapped ions [43], or double-well potentials where the small distances between the potential minima allow the direct coupling of separately trapped ions via the Coulomb force [44, 45]. Furthermore, this technology has been used to interface trapped ions to other systems integrated in the chip layout, like optical components [46, 47, 48, 49], microwave transmission lines [50, 51], or superconducting systems [52, 53]. Because of the ability to easily scale the planar ion trap system, surface-electrode traps are promising candidates in the field of quantum information processing [33, 34, 38].

2.2.1 Conformal mapping

We use a planar electrode structure on the surface of a microwave chip to generate an approximately quadrupole electric potential for the guiding of electrons. Suitable electrode layouts may be obtained by the conformal mapping of a circular electrode geometry onto a plane. The simplest electrode geometry that creates an electric potential with vanishing monopole and dipole components corresponds to a circular geometry that is segmented into four symmetric electrodes. Figure 2.3(a) depicts a cut through the electrode geometry in the xz -plane showing the four electrode segments, which are indicated in red and blue. The mapping of this structure on a planar chip can be done using the conformal Möbius map, as described in Ref. [54]. Figure 2.3(a) illustrates how the mapping is accomplished. A point P on the ring is projected onto the tangential plane, which is parallel to the x -axis but shifted by $-R_0$ along z , by constructing tangent lines

through the specific point. The intersection point of this tangent line with the tangential plane gives the coordinate of the projected point P' on the substrate. Arbitrary circular electrode geometries can be mapped by parameterizing the electrodes by an angular width θ_w and their position on the circle by a rotation angle θ_0 . The electric potential that is created by the surface-electrode layout can be analytically derived by calculating the potential of the respective circular configuration and then transforming it using the Möbius map [54]. As a special variant, Fig. 2.3(a) shows an electrode layout that will be used for electron guiding and is obtained for $\theta_0 = \theta_w = \pi/2$. It comprises five electrodes with a planar symmetry in the transverse x-direction. The central electrode has a width c' and is symmetrically surrounded by electrodes of width w' . Both outermost electrodes extend out to infinity. The microwave signal is applied to the red electrodes, whereas the blue electrodes are grounded. We refer to this configuration as the five-wire electrode geometry in the following.

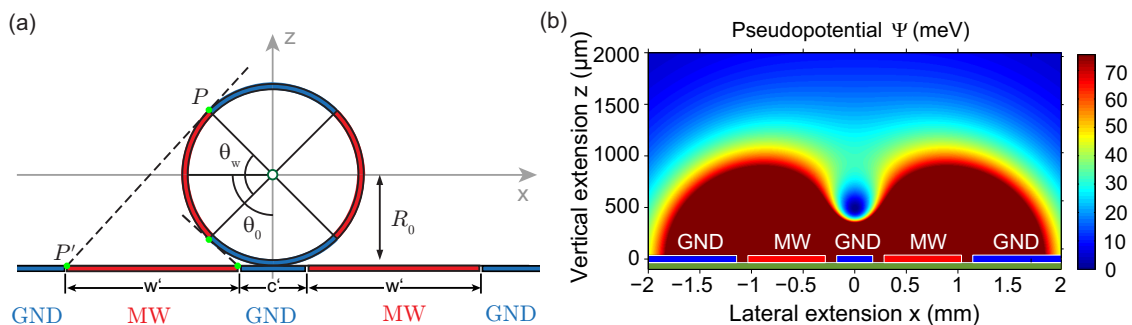


Figure 2.3: Mapping of a circular electrode layout on the tangential plane. The Möbius map used in Ref. [54] allows to derive the electrostatic potential created by a surface-electrode geometry. The guide center is located at the origin and the electrode plane is at $-R_0$. The microwave voltage is applied to the red electrodes, whereas the blue electrodes are grounded. A point P on the circle is mapped to a point P' that is constructed by the intersection of the electrode plane with the circle tangent through P . The circular electrodes have an angular width θ_w and their position on the circle is given by a rotation angle θ_0 . (a), shows a special variant of a five-wire design, which is symmetric with respect to the transverse axis and is characterized by $\theta_0 = \theta_w = \pi/2$. Structures with $\theta_0 = \theta_w/2$, would produce electrode patterns that consist of four wires. (b), Simulation of the pseudopotential formed above the planar five-wire electrode pattern with $\Omega = 2\pi \cdot 1\text{GHz}$, $V_0 = 30\text{V}$, $R_0 = 500\ \mu\text{m}$ and $c' = 460\ \mu\text{m}$, $w' = 860\ \mu\text{m}$ and $g = 110\ \mu\text{m}$, which is taken from Ref. [37].

In order to quantify the performance of the surface-electrode geometry, the strength of the quadrupole electric potential component that is generated by the planar electrodes can be compared to that of a pure quadrupole potential. The electric potential of the planar configuration can be expanded in a multipole series which yields a quadrupole coefficient $\alpha' = \eta \cdot \alpha$ with the quadrupole moment $\alpha = \frac{V_0}{2R_0^2}$ of the ideal quadrupole potential, according to Eq. 2.2. The effective quadrupole strength $\eta = \sin[\theta_w]/\pi$ that arises from the Möbius map results in a reduced quadrupole component of planar electrode structures. As one would expect, the maximum effective quadrupole strength $\eta_{max} = 0.318$ is obtained for $\theta_w = \pi/2$ corresponding to equal angular width of all four electrodes in the circular layout. However, the reduced quadrupole coefficient α' directly affects the

stability parameter and secular frequency of a surface-electrode (SE) guide,

$$q_{SE} = \eta \frac{2Q}{M} \frac{V_0}{\Omega^2 R_0^2} \quad (2.14)$$

and

$$\omega_{SE} = \eta \frac{Q}{\sqrt{2}M} \frac{V_0}{\Omega R_0^2} = \frac{q_{SE}}{\sqrt{8}} \Omega. \quad (2.15)$$

Compared to the ideal guiding electrode geometry, shown in Fig. 2.1(a), the implementation of planar surface-electrode geometry results in a reduction of the pseudopotential depth U . Figure 2.3(b) shows a simulation of the pseudopotential that is formed above the five-wire electrode geometry that was obtained from the conformal mapping and will be used for electron guiding (details are given below). Clearly a pseudopotential minimum forms above the central electrode at a height of $500 \mu\text{m}$ above the chip surface. Furthermore, because of the breaking of the circular symmetry, the potential depth U is weakest along the vertical z -direction perpendicular to the substrate. This effect is reflected in a geometric relative potential depth u , which results in a reduced potential depth for planar electrode geometries according to

$$U_{SE} = u \frac{Q^2}{4M} \frac{V_0^2}{\Omega^2 R_0^2} = \frac{u}{\eta} \frac{q_{SE}}{8} V_0 \quad (2.16)$$

By comparison of the potential depth of an ideal quadrupole field with that of the planar electrode pattern one finds to good approximation $u \propto \sin^2(\theta_w)$ with a maximum achievable geometric relative potential depth $u_{max} = 0.0091$.

The variations of the potential depth and transverse frequency with the angular electrode width θ_w are rather small around the optimum value $\theta_w = \pi/2$. Therefore, the choice of a particular geometry will be influenced rather by experimental constraints than by the optimum potential depth or transverse frequency achievable. In the remainder of this thesis we omit the index SE in the above equations for simplicity when referring to the trap parameters of a surface-electrode geometry.

2.2.2 Five-wire electrode geometry

The symmetric five-wire electrode layout obtained from the conformal mapping is employed for the microwave guiding of electrons. This design combines several practical advantages, which can be attributed to the planar symmetry of the electrode pattern. First of all, the location of the potential minimum above the center of the middle electrode leads to optimal geometric shielding of exposed dielectrics in the gaps between the conductors. Furthermore, it makes the guiding electrodes compatible with the implementation of a symmetric electrode intersection, which is essential for the realization of a planar beam splitter chip for guided electrons and will be discussed in detail in Ch. 4.

The principal guiding parameters of a symmetric five-wire electrode layout can be derived analytically as a function of the electrode dimensions [54, 55], which are defined in Fig. 2.3(a). The height of the potential minimum above the chip surface is

$$R_0 = \frac{1}{2} \sqrt{c'^2 + 2c'w'} \quad (2.17)$$

with c' the width of the central ground electrode and w' the width of the microwave electrodes. Furthermore, the maximum trap depth is realized for $c'/R_0 = 0.692$ and $w'/R_0 = 2.544$.

For the experimental realization of a planar microwave guiding substrate the electrodes of the guide have to be isolated by etching small gaps that define and isolate the metal electrodes. These gaps have a width g and effectively reduce the electrode widths $c' = c + g$ and $w' = w + g$. For the guiding of electrons typically a distance of $R_0 = 500 \mu\text{m}$ between the guiding minimum and the electrode surface is chosen. This results in electrode dimensions that can be fabricated by commercial printed circuit board (PCB) manufacturers. In most experiments presented in this thesis, the central ground electrode and the microwave electrodes have therefore a width of $c = 350 \mu\text{m}$ and $w = 750 \mu\text{m}$, respectively. Taking into account the typical gap width of $g = 110 \mu\text{m}$ this results in $c' = 460 \mu\text{m}$ and $w' = 860 \mu\text{m}$. The deviation from the optimum values ($c' = 350 \mu\text{m}$ and $w' = 1270 \mu\text{m}$) leads to $\eta = 0.314$ and $u = 0.008$ and does neither significantly reduce the transverse trap frequency nor the potential depth. In cases where a finely structured electrode layout is critical, more involved photolithographic processes may be employed. Microwave substrates with gap widths of $g = 50 \mu\text{m}$ and minimum electrode widths of $w = 20 \mu\text{m}$ have already been manufactured and successfully tested. However, the fabrication of these chip substrates is more time and cost consuming.

Gapless-plane approximation

Having obtained a suitable planar electrode layout, we use the gapless-plane approximation is very useful for the calculation of the electric fields above the planar electrode pattern [56]. It relies on the fact that the width of any gap g is very small compared to their distance R_0 to the guiding minimum. In the limit of $g \ll R_0$ the influence of the gaps in the electrode layout can be neglected and the electrodes are assumed to fully cover an infinite plane with no other conductors above the plane. Using the gapless-plane approximation the electric field of any planar electrode geometry can be analytically computed [54, 55].

Figure 2.3(b) shows a numerical simulation of the pseudopotential formed above the guiding substrate, including the effect of finite gaps between the electrodes. When simulating the pseudopotential with a gap width of $g = 110 \mu\text{m}$ we find that the distance of the pseudopotential minimum above the surface is slightly reduced to $R_0 = 496 \mu\text{m}$ compared to $R_0 = 500 \mu\text{m}$ in the gapless-plane approximation. To check the validity of the gapless-plane approximation further, we can similarly deduce the trap parameters ω and U from the numerical simulation with finite gap size $g = 110 \mu\text{m}$ and compare them to the values obtained from the gapless-plane approximation. For ω we find that the value obtained from numerical simulation agrees with the analytic one to better than 0.5% and the trap depth U to within 1.5%. The gapless-plane approximation is, hence, very well justified for the typical chip electrode layouts used for electron guiding and we will make use of it in Ch. 3 and Ch. 4, where we perform numerical optimizations of the shape of the chip electrodes.

2.2.3 Microwave drive parameters for electron guiding

The motion of electrons that are tightly confined in a microwave quadrupole guide is governed by the pseudopotential parameters, which have been derived in Sec. 2.2.1,

$$\omega = \frac{q}{\sqrt{8}}\Omega, \quad U = \frac{uq}{\eta 8}V_0, \quad q = \eta \frac{2Q}{M} \frac{V_0}{\Omega^2 R_0^2}. \quad (2.18)$$

Because of the high charge-to-mass ratio Q/M of electrons, the guiding structures have to be operated with frequencies in the microwave range in order to ensure stable confinement, i.e. $q \ll 1$. The guiding potential shown in Fig. 2.3(b) has been computed with an angular drive frequency of $\Omega = 2\pi \cdot 1$ GHz and a voltage amplitude of $V_0 = 30$ V, which are typical values used in the experiment. This leads to a guiding potential with a transverse frequency of $\omega = 2\pi \cdot 119$ MHz, a potential depth of $U = 32$ meV and a stability parameter of $q = 0.34$.

For comparison, the charge-to-mass ratio of atomic ions is typically a factor 10000 smaller than that of electrons [e.g. for ${}^9\text{Be}^+$ ions: $M({}^9\text{Be}^+)/M(e^-) \sim 16428$]. In order to perform a similar experiment with ions at the same q requires to scale the drive frequency, according to Eq. 2.14, by $\propto \sqrt{M(e^-)/M({}^{25}\text{Be}^+)}$ yielding $\Omega \sim 2\pi \cdot 8$ MHz and a trap frequency $\omega \sim 2\pi \cdot 1$ MHz.

Highest possible trap frequencies are desirable in electron guiding experiments as ω defines the characteristic timescale of the transverse electron motion in the guide. For example, high ω is of importance for the realization of a planar electron beam splitter chip for guided electrons. High trap frequencies allow the generation of strong gradients in the guiding potential, which are required for the division of the electron beam by means of a beam splitter pseudopotential. Also, electrons in tight potentials are less susceptible to heating by electric field noise [37], which has been shown to scale according to $\propto 1/\omega^2$ for trapped ions [57].

The microwave design of the guiding chip is simplified by the fact that the electrode dimensions are small compared to the on-chip microwave wavelength λ . The transverse extensions of the guiding electrodes are much smaller than λ , which ensures that the microwave excitation generates a quasi-TEM mode with an electric field that lies entirely in the transverse plane [58]. Furthermore, the electron guide is constrained to electrically short structures with longitudinal dimensions L that are smaller than a quarter of $\lambda \approx 200$ mm at a drive frequency $\Omega = 2\pi \cdot 1$ GHz. For electrically short structures a standing microwave voltage signal is established on the electrodes and propagation effects in the microwave excitation can be neglected. However, this restricts the guiding chip to $L < 50$ mm. For the same reason the drive frequency Ω cannot be significantly increased while operating the guiding chip in the electrically short limit, which finally limits the achievable ω for a constant q .

However, there are several possibilities to increase the trap frequency ω . A scaling of the chip electrodes along the transverse and longitudinal dimensions by a factor $k < 1$ results in a smaller length $L' = kL$, which allows to increase $\Omega' = k^{-1}\Omega$ while keeping the electrodes electrically short. The transverse scaling reduces the trap height $R'_0 = kR_0$. From the above equations we find that the scaling results in $q' = q$, however, the trap frequency is increased $\omega' = k^{-1}\omega$. Furthermore, electrically long structures can be realized by taking into account traveling microwave signals [19]. This would not only

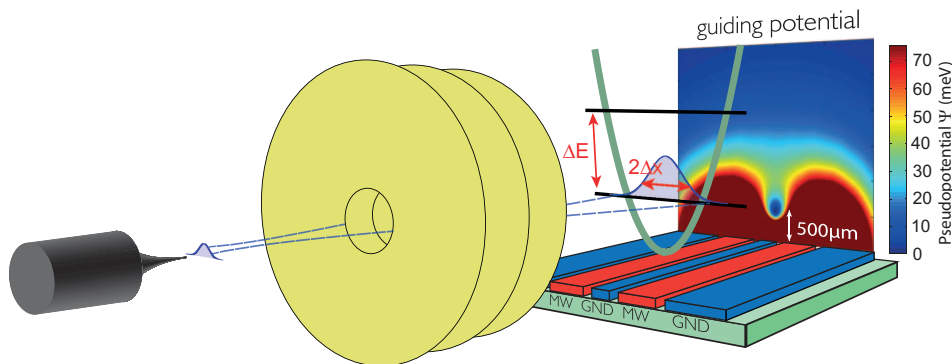


Figure 2.4: Envisioned scheme for direct quantum ground state injection. In a quantum mechanical description the transverse electron motion in the guide is governed by the quantum eigenstates that correspond to discretized energy levels of the harmonically approximated guiding potential. We employ a cold field emission tip, which is a perfect point source of electrons, to generate electron wave packets for the injection into the electron guide. By means of an (ideal) electrostatic lens, which provides the focusing of the beam, the electron wave packet can be matched to the spatial and momentum profile of the quantum ground state of the guiding potential.

allow to increase Ω and hence ω , but simultaneously higher stability could be achieved by decreasing q . We have performed first experiments in this direction and demonstrated electron guiding with electrically long structures up to $\Omega = 2\pi \cdot 1.7$ GHz [59].

The high trap frequencies that can be achieved in a microwave electron guide are particularly important aiming at the injection of electrons into low-lying motional quantum states of the transverse guiding potential, as described in the following section. The characteristic energy of the transverse quantum states in the harmonically approximated guiding potential increases linearly with ω . As a result, high trap frequency ω will help to resolve these quantum states individually.

2.3 Quantum ground state electron guiding

The experiments on electron guiding are motivated by the fundamental goal to reach quantum control over the transverse motion of the guided electrons. At present, quantum effects in the motion of guided electrons have not yet been demonstrated, however, the experiments described in this thesis provide important progress towards this goal. To this end, a quantum description of the electron motion is needed to provide a foundation for ongoing experimental progress. Once entering the realm of quantum mechanics, the transverse motion of the electron in the guide is governed by discretized eigenstates of the transverse guiding potential. Quantum effects in the motion of guided electrons may be revealed if the transverse energy of the electron in the guide approaches the characteristic energy of these quantized states. The respective motional ground state of the guide has a defined profile in position and momentum space. We rely on a direct injection scheme, where an electron is imaged into the ground state of the guide by matching the wavefunction of an impinging electron to the spatial and momentum profile of the guide's ground state. Figure 2.4 illustrates the envisioned injection scheme. We

use a metal nanotip electron emitter as a coherent point source of electron wave packets. However, the wave packets that are emitted from the tip are not inherently matched to the spatial and momentum profile of the ground state in the guiding potential. We, therefore, require electron optics that allow us to adjust the position and momentum wavefunction of the electron wave packet in a transformative way by using an electron lens. This imposes stringent requirements on the electron-optical properties of the electron gun. For a harmonically approximated guiding potential with a transverse frequency ω the spatial and momentum wavefunction of the ground state are given by a Gaussian distribution with position uncertainty $\Delta x = \sqrt{\hbar/(2M\omega)}$ and momentum uncertainty $\Delta p = \sqrt{\hbar M\omega/2}$ [60]. The product of Δx and Δp obeys the minimum possible measurement uncertainty imposed by the Heisenberg uncertainty relation, which represents the diffraction limit for matter waves. This raises the demand for a diffraction-limited electron source.

Using a diffraction-limited electron source it should be ultimately possible to directly inject all electrons into the transverse motional quantum ground state of the guide. This would set the grounds for chip-based guided matter-wave interferometry using the motional states as carrier of quantum information. As one potential application of such a guided matter-wave system a quantum enhanced electron microscopy scheme has been recently proposed, in Ref. [14], which could be used for the noninvasive investigation of biological samples.

In the following we establish a wave-optical description of the electron injection. We will show that a Gaussian beam of electrons can in principle be perfectly matched to the transverse quantum ground state of the guide. However, electron-optical aberrations may modify the properties of the electron beam and deteriorate the overlap with the spatial and momentum profile of the ground state. We study the effect of aberrations and present first wave-optical simulations that demonstrate the feasibility of direct ground state injection. Additionally, these simulations allow us to address effects like misalignment and aberrations on the dynamics of a guided electron wave packet after injection into the guide.

2.3.1 Electron wave optics for mode-matching to the ground state

The wave nature of massive particles is an intriguing aspect of modern physics experiments. Even though its understanding is unintuitive, the wave-optical properties of an electron beam are essentially similar to Gaussian wave optics, which is a well known description of light optics [61, 62]. The purpose of this section is to recapitulate the wave optics of an electron beam in purely electrostatic fields and to derive the resulting implications for the injection of electrons into quantized states of the guiding potential. A detailed discussion on electron wave optics, including a relativistic treatment, is given in Ref. [61].

The wave-optical properties of an electron wave packet in a static electric field are fully described by the single particle Schrödinger equation

$$\left\{ \frac{\hbar^2}{2M} \nabla^2 + Q\phi(\mathbf{r}) \right\} \psi(\mathbf{r}, t) = -i\hbar \frac{\partial}{\partial t} \psi(\mathbf{r}, t), \quad (2.19)$$

with the electrostatic potential $\phi(\mathbf{r}) = \phi(r, y)$ for rotationally symmetric systems and

y the optical axis. In the paraxial approximation, which is similarly known from light optics, the electric potential close to the optical axis can be approximated considering only terms up to quadratic order in r ,

$$\phi(r, y) = \varphi(y) - \frac{r^2}{4} \varphi''(y) + O(r^4) \approx \varphi(y) - \frac{r^2}{4} \varphi''(y). \quad (2.20)$$

An approximate solution of the electron wave function for the paraxial Schrödinger equation can be obtained using a solution of the form

$$\psi(\mathbf{r}, t) = \psi_0(y, t) \psi_p(\mathbf{r}). \quad (2.21)$$

If only the first term in Eq. 2.20 is considered, $\psi(\mathbf{r}, t)$ could be fully deconvoluted into a radial and longitudinal part. However, in order to account for the electron optical image formation we also include the next term, which is quadratic in r and couples the radial and longitudinal coordinates. Consequently the radial part $\psi_p(\mathbf{r})$ remains a (time-independent) function of all spatial dimensions.

Assuming a mono-energetic electron beam, the energy of the electron after the emission process is given by $E = Q\Delta\phi$, where $\Delta\phi$ accounts for a chromatic energy shift imprinted by the specific emission process. The time dependence of $\psi_0(y, t)$ is then expressed by an exponential factor $\exp(-iEt/\hbar)$.

Inserting Eq. 2.21 into Eq. 2.19, one obtains two differential equations, one for $\psi_0(y, t)$ and the other for the radial part $\psi_p(\mathbf{r})$. The first is given by

$$\frac{\partial^2}{\partial y^2} \psi_0 + \frac{p^2(y)}{\hbar^2} \psi_0 = 0 \quad (2.22)$$

with the longitudinal momentum $p(y) = \sqrt{2MQ\varphi(y) + 2MQ\Delta\phi}$. An approximate solution to Eq. 2.22 can be found using the semiclassical WKB method [63]

$$\psi_0 = \frac{C}{\sqrt{p(y)}} \exp\left(\frac{i}{\hbar} \int p dy - \frac{iQ\Delta\phi}{\hbar} t\right). \quad (2.23)$$

This is an accurate solution of Eq. 2.22 if higher order spatial derivatives of $p(y)$ ($p' = \frac{\partial p}{\partial y}$), which arise when inserting Eq. 2.23 in Eq. 2.22, can be neglected and the following assumption holds

$$\left| \frac{3p'^2}{4p^2} - \frac{p''}{2p} \right| \leq \left| \frac{p'^2}{p^2} \right| \ll \frac{p^2}{\hbar} = \frac{4\pi^2}{\lambda^2}. \quad (2.24)$$

This assumption essentially ensures that any variation in the electric potential is small compared to the longitudinal de Broglie wavelength of the electron. This inequality is fulfilled in almost any condition as $\lambda \sim 0.1 \dots 1 \text{ nm}$ for typical electron energies of 100 eV to 1 eV. Therefore, the right-hand side of the inequality is on the order of 10^{12} to 10^{14} mm^{-2} , whereas typical changes in the axial potential are on the order of 1 mm^{-2} .

The second differential equation, which is obtained when inserting Eq. 2.21 into the Eq. 2.19, governs the radial part of the wave function

$$-\frac{\hbar^2}{2M} \nabla^2 \psi_p + \frac{p^2 r^2}{2M} F(y) \psi_p = \frac{i\hbar p}{M} \partial_y \psi_p \quad (2.25)$$

with the so-called lens function

$$F(y) := \frac{1}{p^2(y)} \frac{QM}{2} \varphi''(y). \quad (2.26)$$

This equation describes the radial image formation in paraxial electron optics. Remarkably, it is the *longitudinal* curvature of the electric potential along the optical axis $\varphi''(y) \neq 0$ that leads to a focusing effect in the radial plane. In the paraxial approximation, this focusing is performed by a purely quadratic radial potential (see second term in Eq. 2.25) and therefore does not contribute to any aberrations. However, when taking into account the next higher order term in Eq. 2.20, the third order aberrations such as spherical aberration, coma and astigmatism are obtained, as will be discussed later.

Free electron wave packet without external electric potential

In the special case of no focusing, i.e. $F(y) = 0$, Eq. 2.25 takes the form of the paraxial approximation of the Helmholtz equation, which is well known from light optics. In direct analogy, Gaussian intensity profiles are obtained for the electron wave [60]

$$|\psi_p(x, y, z)|^2 = I_0 \left(\frac{\Delta x}{\Delta x(y)} \right)^2 \exp \left(\frac{-r^2}{2\Delta x(y)^2} \right), \quad (2.27)$$

with the normalization constant I_0 and the $1/\sqrt{e}$ -radius $\Delta x(y)$ given by

$$\Delta x(y) = \Delta x \sqrt{1 + \left(\frac{y\lambda}{4\pi\Delta x^2} \right)^2}. \quad (2.28)$$

Accordingly, the Gaussian beam has a minimum waist Δx at $y = 0$ and diverges along the optical axis with a half opening angle given by

$$\alpha = \frac{\Delta x(y)}{y} \simeq \frac{\lambda}{4\pi\Delta x}. \quad (2.29)$$

To avoid confusion about the definition of the opening angle, it should be pointed out that α is the opening angle of the electron wave function, which is defined by the $1/\sqrt{e}$ -position uncertainty. In light optics typically the divergence angle of the intensity θ is defined using the $1/e^2$ -radius w_0 of the beam intensity. This directly results in the intensity divergence $\theta = \lambda/(\pi w_0)$.

The wave function $\psi_p(x, y, z)$ can be interpreted as the amplitude of an electron wavepacket that propagates in free space with a momentum p along y . Because of dispersion, given by the transverse momentum uncertainty Δp , it diverges transversely giving rise to the opening angle $\alpha = \Delta p/p$. Using de Broglie's relation $p = 2\pi\hbar/\lambda$ one finds that Eq. 2.29 can be rewritten in the form

$$\Delta x \Delta p \simeq \hbar/2, \quad (2.30)$$

which is the well known limit of the Heisenberg relation. It can be interpreted in analogy to light optics as the diffraction limit for electron matter waves.

The quantum ground state of the harmonically approximated transverse guiding potential is, likewise, described by Gaussian profiles in position and momentum space, which obey the Heisenberg uncertainty relation. As a consequence of this ideal correspondence, it is possible to generate a Gaussian electron beam in free space that perfectly matches the ground state of the electron guide in its focus. Figure 2.5 shows a Gaussian electron beam according to Eq. 2.27 with a focusing angle of $\alpha = 0.35$ mrad and a longitudinal kinetic energy of 1 eV. In the focus, at $y=0$ mm, the beam reaches its minimum $1/\sqrt{e}$ -position uncertainty of $\Delta x = 278$ nm, which is perfectly matched to the spatial profile of the quantum ground state of the guide with a width $\Delta x = \sqrt{\hbar/(2M\omega)}$ for a trap frequency of $\omega = 2\pi \cdot 119$ MHz. As a result, a Gaussian beam can be perfectly mode-matched for direct injection into the guide.

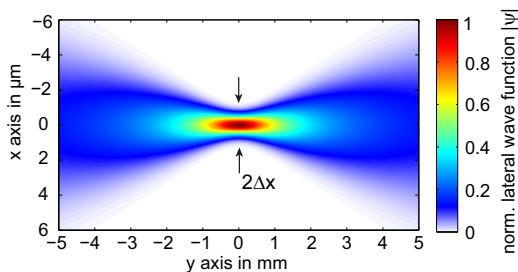


Figure 2.5: Gaussian electron beam with $E_{\text{kin}} = 1$ eV. Electron wave according to Eq. 2.27 with an opening angle of $\alpha = 0.35$ mrad resulting in $\Delta x = 278$ nm. In the focus, this Gaussian electron beam is perfectly matched to the harmonic ground state of a guiding potential with $\omega = 2\pi \cdot 119$ MHz.

Focusing of an electron wave packet in paraxial electric potentials

In the experiment, we are using metal nanotips, which are coherent point sources of electrons providing an electron beam that can be focused to the diffraction limit [23]. In order to match the wavefunction of the emitted electron beam to the guide's ground state, we require a suitable electron lens that allows to adjust the spatial and momentum profile of the beam by creating a magnified image. The action of an ideal lens can be described when accounting for a non-vanishing focusing action, i.e. $F(y) \neq 0$, in the solution to Eq. 2.25. One systematic procedure to find an approximate solution to Eq. 2.25 is the eikonal method, which is closely related to the Wentzel-Kramers-Brillouin (WKB) method [61]. Within the eikonal approximation, the calculation of the particle's wave function is reduced to the integration of a given set of classical trajectories that form the beam, the so called eikonals S . The surfaces $S = \text{const}$ of a beam of eikonals correspond to surfaces of constant wave phase. In that sense, wave optical properties can be deduced from essentially geometrical optics calculations.

A detailed description of the eikonal method is out of the scope of this work but can be found in Ref. [61]. Here only a general result shall be given that is obtained when applying the eikonal method to the image formation according to Eq. 2.25. One finds that the lens function $F(y)$ leads to the formation of a magnified image with a magnification M

$$|\Psi(x_i, y_i, z_i)|^2 = M^{-2} |\Psi(x_i/M, y_o, z_i/M)|^2, \quad (2.31)$$

where the index i and o refers to coordinates in the image and object plane. Here the assumption is made that the electric potential of the electron lens that produces $F(y)$ is confined to the lens such that the object and image plane are field free regions. Accordingly, a Gaussian beam with a waist Δx in the object plane becomes magnified in the image plane $\Delta x' = M\Delta x$ and we can use the lens to adjust the waist $\Delta x'$ in the image plane to match the quantum ground state of the guide.

Beyond the paraxial approximation: diffraction, spherical and chromatic aberrations

So far we have only considered Gaussian wave optics in the paraxial approximation and fully neglected electron-optical aberrations. The latter arise when taking into account diffraction of the electron wave packet at apertures, when including chromatic effects due to the finite longitudinal energy spread ΔE of the wave packet, or allowing higher order terms in the electric potential in Eq. 2.20, which results in spherical aberration. The effect of these aberrations can be investigated using the eikonal approach. Considering rotationally symmetric systems and provided that the object as well as the image plane are field free regions, the current density in the image plane can be obtained from a linear combination of eikonals $S(\theta)$ [61]

$$\Psi(r) \propto \int_0^{\theta_i} \exp\left[\frac{i}{\hbar}S(\theta)\right] J_0\left(\frac{p_i}{\hbar}r\theta\right) \theta d\theta. \quad (2.32)$$

This equation is very similar to a Fourier transformation over the angular components in the image plane using the zero-order Bessel function $J_0(x)$ as an orthonormal basis. Here, p_i is the electron momentum in the image plane and θ_i the image sided probe forming semi angle, which is defined by the ratio of the radius of the smallest aperture in the electron optics and the working distance of the lens.

For a constant eikonal, i.e. $S = \text{const}$, one obtains a spherical wave in the object plane and integration of Eq. 2.32 gives the intensity profile in the image plane. The finite integral of $J_0(x)$ gives an Airy pattern $I \propto |J_1(x)/x|^2$ in the image plane, which is the result of electron diffraction at the beam defining aperture. The Airy pattern leads to the formation of fringes in the focus of the diffracted beam with a diameter of the Airy disc d_d , which is the diameter of the first dark fringe,

$$d_d \approx 0.6 \frac{\lambda}{\theta_i}. \quad (2.33)$$

Taking into account the finite longitudinal energy spread ΔE as well as the next higher order term in Eq. 2.20 the eikonal including spherical and chromatic aberration takes the form [61]

$$S(\theta) = p_i \left(\frac{1}{2} \Delta_0 \theta^2 - C_c \frac{\Delta E}{E} \theta^2 - \frac{1}{4} C_s \theta^4 \right). \quad (2.34)$$

Here C_c and C_s are the aberration constants of spherical and chromatic aberration. These constants characterize the amount of aberration that a lens imprints on the electron beam in the focus. They depend on the geometry of the lens as well as its focal length. In Ch. 6 we will derive C_c and C_s from particle trajectory simulations for our particular

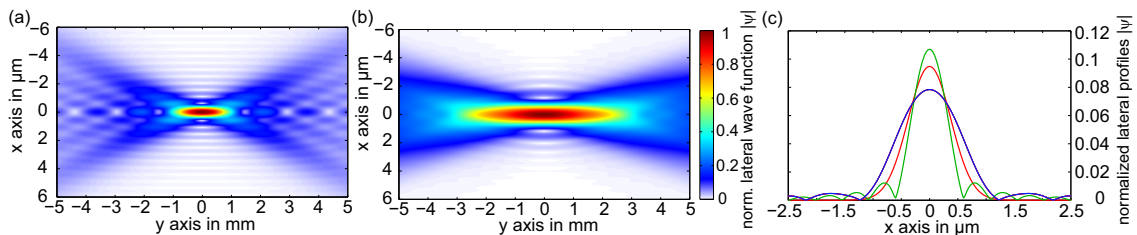


Figure 2.6: Wave-optical simulation of aberrated electron beam with $E_{kin} = 1$ eV. (a),(b), Aberrated electron wave distributions containing diffraction and chromatic aberrations with an opening angle of $\alpha = 0.35$ mrad. The electron distribution is obtained from the eikonal in Eq. 2.34 and numerically solving Eq. 2.32. Both simulations are performed for $\theta_i = 1.3$ mrad and $\Delta E = 0.3$ eV, whereas $C_c = 2$ mm in (a) and $C_c = 10$ mm (b). (c), Transverse beam profiles in the focus at $y = 0$ mm. The red line corresponds to the Gaussian beam in Fig. 2.5, the green line to the aberrated beam in (a) and the blue line to (b).

lens design. The constant $\Delta_0 = y - y_0$ accounts for the defocus when calculating the radial profile in the vicinity of the focal plane, which is at y_0 .

The effect of aberrations on a free electron wave-packet can be simulated close to the focus when inserting Eq. 2.34 into Eq. 2.32 and solving the integral numerically. The parameters assumed in this simulation correspond to realistic experimental parameters. The simulation accounts for a (longitudinal) Gaussian energy distribution with mean $E_{kin} = 1$ eV and a full-width at half-maximum of $\Delta E = 0.3$ eV. This value corresponds to that of a cold field emission electron source [23]. The probe forming semi angle is $\theta_i = 1.3$ mrad and the chromatic aberration constant was set to $C_c = 2$ mm, which corresponds to the value of our electron lens presented in Ch. 6. The spherical aberration was set to $C_s = 0$ as the beam profile is entirely dominated by chromatic effects and diffraction at these very low electron energies. Figure 2.6(a) shows the simulation result. For better visibility, the electron wave amplitude $|\Psi(x, y)|$ is plotted and not the intensity profile, as small features are more pronounced in the amplitude. The simulation shows that the electron wave reaches its focus at $y = 0$ mm. However, fringes form in the focal plane, which can be attributed to diffraction. These fringes effectively result in a larger position uncertainty of the electron wave in the focus. Compared to Fig. 2.5 showing a Gaussian beam, the fringes result in some fraction of wave amplitude to reach further out in the lateral direction. This can also be seen in Fig. 2.6(c), where the lateral profiles are shown in the focus. Here the red line corresponds to the Gaussian beam in Fig. 2.5, whereas the green profile corresponds to the aberrated profile, which has the form of an Airy pattern and was extracted from the simulation shown in Fig. 2.6(a). We can deduce the distance between the first minimum on the negative and positive x -axis of the aberrated profile yielding $d_{sim} = 597$ nm. For the parameters used in the simulation the diffraction disc with $\theta_i = 1.3$ mrad and $E_{kin} = 1$ eV can be calculated according to Eq. 2.33 yielding $d_d = 566$ nm, which is in good agreement with the simulated value. As a consequence, the aberrated beam with rather small chromatic aberration constant $C_c = 2$ mm is mainly dominated by diffraction.

In order to investigate the effect of larger chromatic aberrations, we simulate a diffracted beam for the exact same parameters but increase the aberration constant to $C_c = 10$ mm. The result of this simulation is shown in Fig. 2.6(b). The larger chromatic aberrations

clearly result in an elongated focus along y , which is a result of longitudinal dispersion. Furthermore, the beam is significantly broadened in the focus and the diffraction fringes are less pronounced. The corresponding lateral profile in the focus, shown as blue line in Fig. 2.6(c), confirms the chromatic broadening of the beam. We find a distance between the first minima of $d_c = 3.9 \mu\text{m}$, which is much larger than the expected Airy disc $d_d = 566 \text{ nm}$ and, hence, the beam profile is dominated by chromatic aberrations.

From classical ray optics one can derive approximate formulas to characterize the amount of aberration produced by an electron optical component [64]. The spot diameter obtained from ray optics contains a contribution of the spherical aberration

$$d_s = 0.5 C_s \theta_i^3 \quad (2.35)$$

and chromatic aberration

$$d_c = C_c \frac{\Delta E}{E} \theta_i. \quad (2.36)$$

However, the spatial profile of the different contributions can not be obtained from ray optics and are ignored in these formulas. More rigorous treatments that account for the spatial current density profile can be found in the literature [65].

The chromatic contribution according to Eq. 2.36 is $d_c = 663 \text{ nm}$ for $C_c = 2 \text{ mm}$ and $d_c = 3.9 \mu\text{m}$ for $C_c = 10 \text{ mm}$. Here the simulation shows different results. For $C_c = 2 \text{ mm}$ the contribution of chromatic aberrations seems negligible, whereas for $C_c = 10 \text{ mm}$ the distance between the first zeros is $d_c = 2.5 \mu\text{m}$, suggesting that Eq. 2.36 overestimates the chromatic aberrations for our specific simulation parameters. This should be kept in mind in Ch. 6, where we characterize the performance of the electron lens by classical raytracing simulations and use Eq. 2.36 to obtain C_c .

In order to directly inject electrons into the motional quantum ground state of the guide, the incoming focused electron beam has to be mode-matched to the ground state wavefunction of the transverse guiding potential. It is therefore of importance that the transverse beam profile has a large spatial overlap with the Gaussian ground state wavefunction. First of all this implies that the focal spot size of the electron beam has to be matched to the transverse extent of the quantum ground state Δx . In contrast to other applications that aim at highest possible currents in the smallest possible probe area, here a too small spot size also reduces the quality of the mode-matching. Furthermore, the specific spatial profile of the injected electron wave should match the Gaussian ground state distribution and hence the contributions of aberrations have to be minimized. In the next section we study the effect of aberrations and misalignment on the electron injection into the guide using the beam profiles that we have obtained from the above simulations.

2.3.2 Quantum wave packet evolution in the guiding potential

The requirements on the electron optics for the direct ground state injection have so far been derived from the Gaussian ground state wavefunction of the harmonically approximated guiding potential. For a trap frequency of $\omega = 2\pi \cdot 119 \text{ MHz}$ and an electron energy $E_{kin} = 1 \text{ eV}$ we obtain the a required spot radius of $\Delta x = \sqrt{\hbar/(2M\omega)} = 278 \text{ nm}$ and a half opening angle $\alpha = \Delta p/p = 1/2\sqrt{\hbar\omega/E_{kin}} = 0.35 \text{ mrad}$. Here the assumption

has been made that the quantum dynamics of the electron wave packet in the guide are fully described by the stationary eigenstates of the time-averaged pseudopotential. For a rigorous treatment of the electron's quantum evolution, one has to take into account that the electric potential varies in time and no stationary quantum mechanical states exist. However, it can be shown that by defining quasi-stationary states with wave functions that closely resemble the eigenstates of the harmonic pseudopotential the quantum evolution of an electron exhibits only an additional small periodic modulation at the drive frequency Ω [17]. This results in a temporal breathing of the guided wave packet and can be interpreted as quantum analogon to the micromotion of classical electron trajectories.

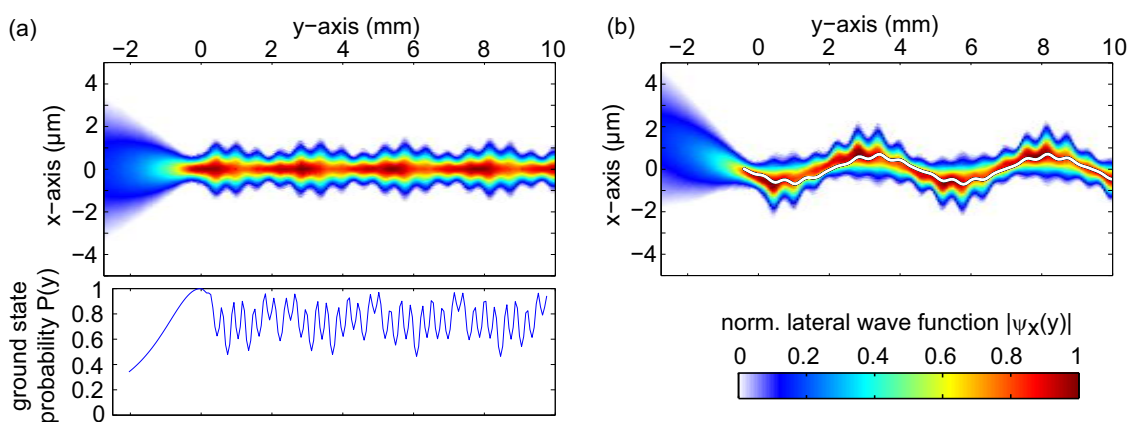


Figure 2.7: Guiding of a quantum electron wave packet. (a), Ideal injection of an electron wave packet into the quantum ground state of the guiding potential. In the simulation the Gaussian focus is perfectly matched to the ground state of the guiding potential. For the drive parameters $\Omega = 2\pi \cdot 1 \text{ GHz}$, $V_0 = 30 \text{ V}$ and $q = 0.34$ a small breathing of the guided wave packet at the drive frequency Ω is observed. Additionally, the probability $P(y)$ is shown which measures the overlap of the propagating electron wave with the Gaussian ground state wave function of the guide. (b), Injecting the wave packet under an angle increases the transverse energy of the electron wave packet and a coherent state is generated. The dynamics of the coherent state show remarkable correspondence with a classical trajectory (see white line).

We have carried out a two dimensional wave packet simulation using the split step method [66, 67] to investigate the quantum dynamics of an electron wave in the guide. In these simulations we numerically solve the time-dependent Schrödinger equation, i.e. Eq. 2.19, taking into account the time dependent electric potential of the five-wire electrode geometry in the transverse xz -plane with $\Omega = 2\pi \cdot 1 \text{ GHz}$ and $V_0 = 30 \text{ V}$. Along y a free particle is assumed with a kinetic energy of 1 eV .

Figure 2.7(a) shows the simulation result where we have propagated a Gaussian beam with a focusing angle of $\alpha = 0.35 \text{ mrad}$ and a longitudinal kinetic energy of 1 eV . The beam parameters are identical to the beam profile shown in Fig. 2.5 and are matched to the stationary pseudopotential ground state. First the wave packet propagates in free space and approaches its focus at $y = 0 \text{ mm}$ from the negative y -direction. As the wave packet reaches its focal point at $y = 0 \text{ mm}$ the guiding potential is instantaneously switched on and subsequently the electron wave is propagated in the oscillating mi-

crowave fields of the guide. The microwave parameters used in the simulation result in the trap parameters to $q = 0.34$, $\omega = 2\pi \cdot 119$ MHz and $U = 32$ meV, which corresponds to the Δx and α given above. As can be seen, the electron wave becomes confined by the guiding potential and the breathing described above is discernible. Specifically, in Fig. 2.7(a) we plot the absolute value of the electron wavefunction amplitude in a cut through the lateral xy -plane.

We can determine the probability for the wave packet to overlap with the stationary harmonic ground state of the guiding potential $P(y) = |c(y)|^2$ by calculating the overlap integral

$$c(y) = \int dx dz \Psi^*(x, y, z) \Psi_0(x, z). \quad (2.37)$$

Here Ψ_0 is the stationary ground state of the harmonic guiding potential, which is a Gaussian function with $\Delta x = 278$ nm, and Ψ the simulated electron wave amplitude obtained from the simulation. The ground state probability $P(y)$ is shown in Fig. 2.7(a), bottom, along the y -axis. As the wave packet reaches its focus, the matching to the ground state is discernible as $P(y)$ approaches 1. Subsequently the electron wave becomes confined in the guiding potential and about 80% of the electron wave overlap with the stationary ground state. The temporal breathing of the wave packet is discernible as fast oscillations in $P(y)$. When the microwave parameters are adjusted to yield a smaller q at the same ω the breathing amplitude can be further reduced yielding even better overlap. The result of this simulation demonstrates that it is in principle possible to confine a guided electron wave in the motional quantum ground state of the guiding potential by direct injection. The guiding potential used in the simulation is generated by the five-wire electrode geometry, which we employ in the experiments, and for realistic microwave drive parameters.

In the simulation result shown in Fig. 2.7(b), the incoming electron wave packet has a slight angle with respect to the guide axis. In this case, the electron wave oscillates in the guiding potential. The oscillation of the electron wave packet corresponds to a coherent state, which is a superposition of several eigenstates of the guiding potential [60]. The white line in Fig. 2.7(b) corresponds to a classical electron trajectory that is simulated at the same experimental parameters. It shows remarkable correspondence with the coherent state obtained in the quantum simulation.

Finally we can study the dynamics of a guided electron wave packet that results from an aberrated beam profile during injection. To this end, we use the diffracted beam with $C_c = 2$ mm, shown in Fig. 2.6(a), but switch on the guiding potential when the wave packet reaches its focus at $y = 0$ mm. Figure 2.8(a) shows the result of the wave packet propagation. Clearly, the aberrated electron density has a much more complex shape and shows some periodic behavior along the guide. For example, the beam profile in the focus, which is shown in Fig. 2.8(b), follows periodic revivals, as indicated by the arrows in Fig. 2.8(a). This profile reoccurs with a period of about 2.5 mm along the y -axis, which corresponds to a frequency of 237 MHz at $E_{kin} = 1$ eV. The profile of the guided wave packet between these revivals shows a varying, complicated structure, which is shown for two different locations along y in Fig. 2.8(c) and (d).

The aberrated beam profile leads to complicated transverse wave packet dynamics within the guide. In contrast to a slight angle of the injected wave packet, as shown in

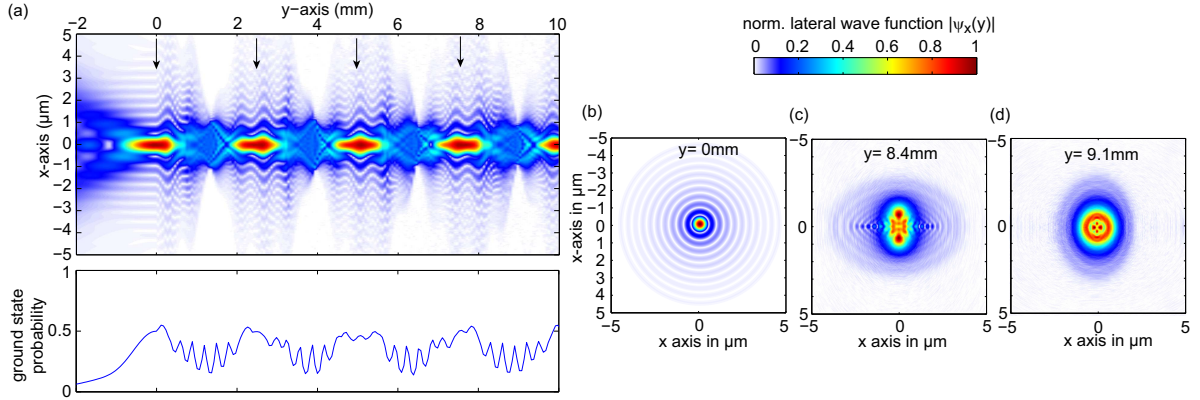


Figure 2.8: Guiding of an aberrated wave packet. (a), Injection of an aberrated electron wave packet into the guide. The electron density follows some complex and periodic dynamics. (b), The beam profile in the focus at $y = 0$ mm follows periodic revivals, which are indicated by the black arrows. The profile of the guided electron wave packet in between these revivals has a complicated structure as shown in (c) and (d) and contains contributions from higher energetic quantum eigenstates of the transverse guiding potential. The simulations are performed with $\Omega = 2\pi \cdot 1$ GHz, $V_0 = 30$ V at $E_{kin} = 1$ eV.

Fig. 2.7(b), the aberrations do not result in a quasi-classical coherent state that can be intuitively understood from classical particle tracking simulations. We can again calculate the spatial overlap of the guided wave packet with the stationary quantum ground state to obtain the probability $P(y)$ for the electron wave. As can be seen, $P(y)$ takes values up to 50%. This shows that despite from the rather complicated spatial profile, however, the electron wave is guided by the oscillating electric potential and exhibits an overlap of 50% with the quantum ground state, which similarly follows periodic revivals. This shows that for an aberrated beam profile, which has been obtained from a simulation using realistic parameters of our electron source to account for chromatic aberration and diffraction, large overlap with the quantum ground state can be achieved. Furthermore, these wave-optical simulations may allow us to investigate the possibility to develop a mode filter that selectively removes guided electrons as a function of their transverse motional state in the guide. Such a mode filter could function very similarly to the evaporative cooling of trapped atomic clouds by a controlled reduction of the transverse potential depth. In the ideal case a mode filter would allow to remove excitations in the quantum dynamics of the electron wave packet and in the simulation illustrated here, remove the 50% of the electrons such that only the part of the wavefunction that overlaps with the ground state remains.

In conclusion, the simulations confirm that by matching a diffraction-limited Gaussian electron beam to the wavefunction of the transverse ground state of the guiding potential a guided matter-wave mode can be generated that has a large overlap with the transverse motional ground state of the guide. Future experiments may employ the discretized transverse motional states as a carrier of quantum information. For example, guided electrons could be coupled to other quantum systems incorporated in the chip design, like e.g. quantum dots, or trapped atoms. Moreover, they could interact with another electron beam that closely passes by the guide. Any interaction of the electron wave,

which is guided in the ground state, with such a system could be detected by a change of the transverse motional state of the guided electron. Furthermore, the transverse motional states could be employed in a guided matter-wave interferometer [68, 69]. However, ground state injection requires a diffraction-limited electron source as well as a guiding potential that allows a smooth passage for the electron wave into the guide. In the course of this thesis we will address both these points experimentally. The above simulations were based on the simplifying assumption that the microwave potential of the guide is switched on instantaneously as the electron reaches its focus. In the experiments this assumption is not justified. In Ch. 3 we address how a smooth passage can be provided experimentally by studying the dynamics of electrons during injection into the guide. Furthermore, we have designed and constructed a coherent field emission electron source with the goal to provide a diffraction-limited electron beam for future experiments. A characterization of this novel source will be presented in Ch. 5 and Ch. 6.

3 Electron guiding and optimized injection into the guide

Slow electrons with kinetic energies below 10 eV can be guided in the oscillating electric fields of a linear quadrupole guide [19, 20], also known as linear Paul trap [16]. In order to achieve stable confinement of the electrons we need to drive the guide at frequencies in the gigahertz range. The resulting tight transverse confinement is described by a microwave pseudopotential and enables the precise control of the transverse motion of guided electrons. This chapter addresses the experimental implementation of electron guiding and discusses the characteristic dynamics of guided electrons in the linear quadrupole guide. First, the experimental apparatus is described and the guiding of electrons along a curved path is recapitulated [37]. The remaining part of this chapter, which has been published in Ref. [70], is concerned with the injection of electrons into the microwave guiding potential. Due to fringing electric fields at the edges of the guiding substrate, the electron beam experiences an initial deflection before it is injected into the guiding potential of the microwave chip. This leads to an excited motion of the electrons within the guiding potential or even loss of electrons from the guide. Here two possible strategies are discussed to provide an adiabatic injection of electrons from free space into the guiding potential, thereby increasing the guiding efficiency and paving the way towards quantum mechanical control over the transverse motion of the guided electrons.

3.1 Experimental setup

The setup employed for electron guiding is shown in Figure 3.1 from a top view. It comprises a thermionic electron source that provides a collimated electron beam with kinetic energies ranging from 1 to 10 eV, a planar guiding substrate and a microchannel plate (MCP) electron detector. Electrons that leave the exit aperture of the electron gun are injected into the guiding potential above one edge of the substrate. Successfully guided electrons propagate along the electrodes and are detected by the MCP detector. Due to the curved electrode design the guided electrons become deflected and are spatially separated from unguided electrons, which traverse the guiding chip along straight lines. Images are recorded by a CCD camera that captures the phosphorescent screen behind the MCP.

In the course of this thesis several modifications have been made to the experimental setup, which has been used for the first demonstration of electron guiding and is described in detail in Ref [37]. New guiding substrates with advanced coupling structures have been designed and tested. Furthermore, the microwave delivery setup has been improved by several components. They allow for the transmission of a higher microwave peak voltage V_0 to the guiding chip as well as an active stabilization of the microwave

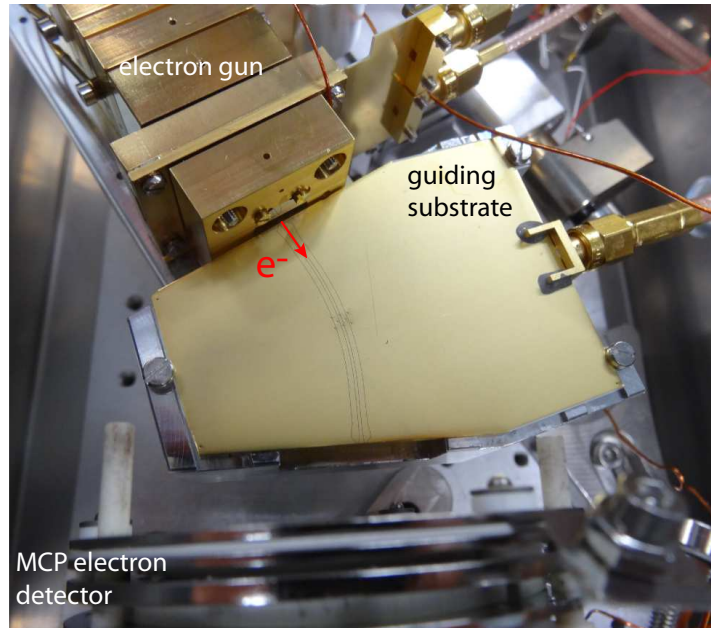


Figure 3.1: Photograph of the electron guiding experiment. It consists of a thermionic electron source (at the top left), a planar microwave guiding substrate (in the center) and a microchannel plate (MCP) electron detector (at the bottom). Electrons leave the electron gun above one edge of the substrate and are injected into the guiding potential. Guided electrons are deflected and spatially separated from unguided electrons due to the curved electrode design. Here the mu-metal shield and a gold-plated copper housing enclosing the experiment are removed in the image.

power. Finally, the electron gun has been modified by an additional streaking element that allows to operate the gun in pulsed mode. By these means we can temporally synchronize the injection of electron pulses to the microwave drive of the guide and perform a microwave phase-resolved measurement of the electron guiding efficiency.

3.1.1 Guiding substrates

A principle design requirement for the guiding substrates is that it supports microwave driving frequencies in the gigahertz range and that it needs to be compatible with ultra-high-vacuum (UHV) pressure. Additionally, the guiding electrodes on the chip surface have to be precisely patterned to fabricate the required guiding electrode layout with small isolating gaps and smooth electrode edges. To this end, printed-circuit-boards (PCB), which are commercially available, are ideally suited. They can be covered with thin metal films using electroplating and allow patterning of the electrodes using chemical etching of the metal layer. Furthermore, PCB substrates are compatible with coplanar waveguide structures for the microwave signal delivery to the guiding electrodes. The fabrication by a commercial supplier¹ enables fast turn-around times.

Figure 3.2 shows the top (a) and the backside (b) of a chip substrate employed for electron guiding along a curve. The guiding electrodes are discernible on the top side

¹Optiprint AG, Auerstrasse 37, CH-9442 Berneck, Switzerland, www.optiprint.ch

and follow a curved path with a zigzag-shaped tapering of the signal electrodes close to the substrate edge. The chip design is based on five wires across the electrode layout with a longitudinal electrode length of $L = 37$ mm. In order to avoid charging effects the entire chip is gold coated except for the small gaps defining the guiding electrodes. The microwave signal is delivered to the chip electrodes by a coplanar waveguide (cpw) structure on the backside of the chip, which is electrically connected to the guiding electrodes by plated through-holes [see Fig. 3.2(b)].

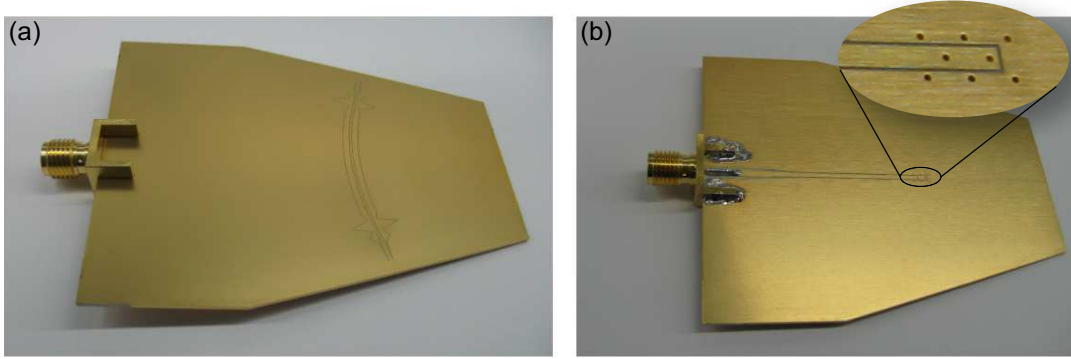


Figure 3.2: Images of a microwave chip used for electron guiding. (a), Top side of the chip design showing a curved electrode design for the guiding of electrons around a curve. (b), Back side of the guiding chip comprising the coplanar wave guide (cpw) structure for feeding of the signal electrodes. Plated via holes connect the backside cpw structure to the signal electrodes. The SMA end launch connector is soldered to the substrate edge and transmits the microwave power from a SMA cable to the planar transmission line.

The substrate is a 0.76 mm thick microwave compatible Rogers RO4350B laminate. This substrate is well suited for microwave applications up to several tens of gigahertz and features a high thermal conductivity of $0.69 \text{ W}/(\text{m K})$ and a low dielectric constant of $\epsilon_r = 3.66$. The high thermal conductivity is mandatory as we inject up to 100 W of microwave power to the guiding chip. The low dielectric constant is important regarding the on-chip microwave wavelength, which scales like $\lambda \propto 1/\sqrt{\epsilon_r}$. This is important, as we work in an electrically short configuration, where the longitudinal structure size L as well as the transverse extension of the guiding electrodes has to be small compared to the microwave wavelength λ . In the guiding experiment, $\lambda = 200$ mm at 1 GHz is much larger than the longitudinal structure length $L = 40$ mm. As a result, a standing voltage signal establishes on the guiding electrodes. A small dielectric constant results in large wavelength of the microwave signal, which allows for longer guiding electrodes. Figure 3.3 illustrates the result of a numerical microwave simulation showing the maximum electric field amplitude on the top and backside of the guiding chip at a microwave frequency of 1 GHz. Clearly, a standing wave forms with the electric field amplitude being at its maximum at the termination of the chip electrodes and decreasing towards the chip center. At the backside of the chip the first node of the electric field is visible.

The chip electrodes consist of $20 \mu\text{m}$ thick gold-plated copper. By means of a chemical etching process, $50 \mu\text{m}$ wide gaps are etched into the metal layer defining the electrodes. The microwave signal is delivered to the chip electrodes by a cpw structure on the backside of the chip, which is interconnected to the top side by laser machined, plated

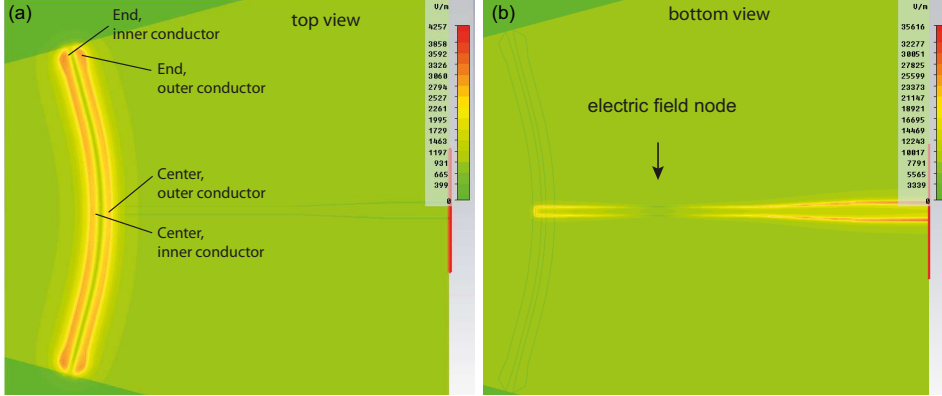


Figure 3.3: Simulation of microwave electric field amplitude at $\Omega = 2\pi \cdot 1$ GHz. (a), The length of the guiding electrodes $L = 37$ mm is much shorter than the microwave wavelength of $\lambda \sim 200$ mm leading to a standing wave electric field distribution. (a), The guiding electrodes represent an open termination for the microwave signal leading to the formation of a field node at the backside of the chip, shown in (b). Taken from Ref. [37].

through-holes with a diameter of $20 \mu\text{m}$. Of particular importance is the diameter of the through-holes and the minimum achievable gap size between the electrodes. Both set a limit to the smallest fabricable feature sizes of the guiding electrodes. The signal as well as the grounded electrodes of the guiding chip are electrically fed by the through-holes. Hence every electrode needs to be at least as wide as the diameter of the through-hole that connects it. At the edges of the substrate the guiding electrodes are tapered to reduce fringing electric fields at the substrate edge. Here the smallest producible width of the signal electrodes is comparable to the width of the gap forming the electrode. It is therefore important to achieve a small gap size to produce finely structured electrode designs, which is also crucial for the precise engineering of more versatile guiding potentials as required, for example, for the demonstration of an electron beam splitter chip, presented in Ch. 4.

We use high frequency end launch connectors, mounted to the substrate edge, to transmit the microwave signal from a coaxial SMA cable to the cpw line on the backside of the chip. The cpw then delivers the microwave signal via the plated through-holes to the guiding electrodes on the topside of the chip. The transverse dimensions of the guiding electrodes result from the conformal mapping described in Sec. 2.2.1. However, the transverse electrode dimensions also set the characteristic impedance of the chip electrodes. The electrode layout employed for electron guiding results in a characteristic impedance of $Z_0 = 20 \Omega$. The coplanar waveguide that transmits the microwave signal from standard SMA cables to the guiding chip has a characteristic impedance of $Z_0 = 50 \Omega$. As a result of the impedance mismatch, part of the microwave signal is reflected due to the impedance discontinuity before being transmitted to the guiding electrodes. In order to reduce these reflections a triangular impedance taper has been implemented on the latest microwave chips, as described in Ch. 4.

In order to estimate the actual voltage amplitude V_0 transmitted to the guiding electrodes the frequency response of the guiding chip has to be determined. The microwave setup as well as the power correction procedure are presented in the following.

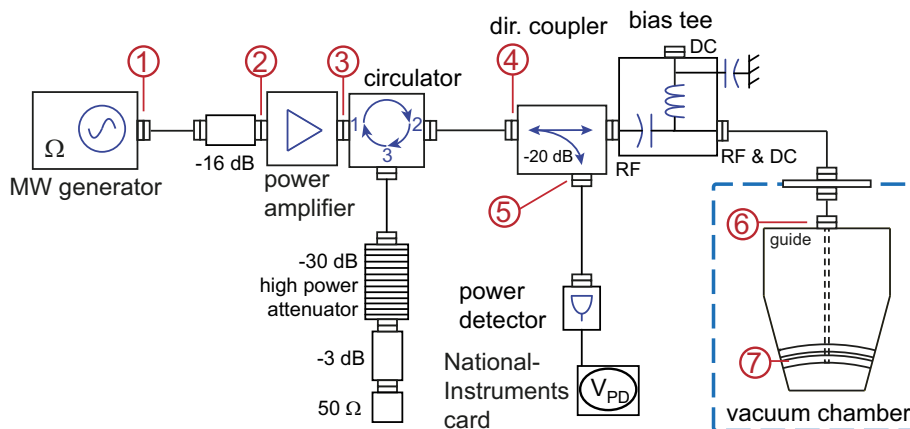


Figure 3.4: Schematic of microwave setup. The output of an analog signal generator is boosted by an amplifier with saturated gain of 47 dB. After a circulator and a directional coupler for microwave diagnostics the signal is fed to the guiding chip. The different positions for the scattering parameter measurements are indicated in red.

3.1.2 Microwave equipment and power correction

This section presents the microwave setup used for electron guiding and describes the power correction procedure, which allows to determine the voltage amplitude V_0 applied to the guiding electrodes. This is important as the characteristic electron motion in the guide is determined by V_0 and the drive frequency Ω (see Sec. 2.2.3). A detailed description of the microwave setup is already given in Ref. [37]. For this reason, the microwave setup is only briefly outlined here and focus is put on describing the modifications to the original setup.

We use an analog signal generator² as a microwave source. Its output is boosted by a microwave amplifier³ with an amplification bandwidth from 0.5 to 2.5 GHz and a saturated output power of 100 W. After passing several microwave components for diagnostics, e.g. a circulator⁴, a directional coupler⁵ and a bias tee, the amplified microwave power is directly fed to the vacuum chamber and transmitted to the guiding chip. As the guiding electrodes constitute an open termination for the microwave signal, large parts of microwave power are reflected back into the signal path. In order to circumvent that a substantial part of the microwave power is reflected back into the amplifier, we added a circulator with a bandwidth from 0.8 to 1 GHz to dump the reflected power into a high power attenuator⁶ and subsequently into a 50 Ω termination.

The gain curve of the microwave amplifier is shown in Fig. 3.5. It is measured between Pos. 2 and behind the directional coupler, at Pos. 5, as depicted in Fig. 3.4. The red line shows the measured gain with and the blue line without the circulator in the setup. Clearly, the circulator flattens the frequency response of the gain curve within the circulator bandwidth and removes step dips in the gain curve.

²Agilent E8257C, 100 kHz to 20 GHz.

³Microwave Amps, AM6-0.5-2.5-48-48

⁴MECA Electronics, CS-0.900

⁵MECA Electronics, 750-S-20-1500V

⁶Microlab AU-30N

Additionally, we inserted a power detector⁷ for an active stabilization of the guiding voltage V_0 behind Pos. 5. The power detector converts the incident microwave power into a DC voltage according to a linear characteristic, which can be read out by a National Instruments card⁸. Via remote control of the signal generator we can feed back the measured DC voltage and actively stabilize the microwave power level. A detailed characterization of the modified microwave setup obtained after the insertion of the circulator and the active power stabilization is presented in Ref [71].

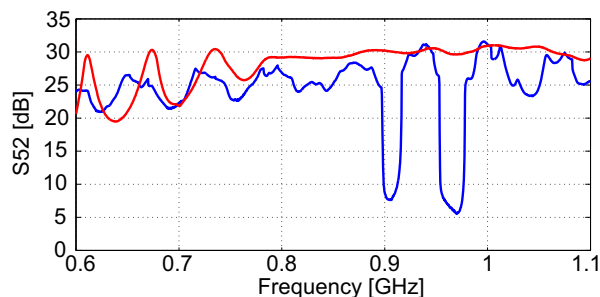


Figure 3.5: Frequency response of the microwave amplifier gain. The amplifier gain is measured at Pos. 5 where it is attenuated by -20 dB. The red line depicts the frequency response of the scattering parameter S_{52} with the circulator in the microwave signal path whereas the blue curve is measured with the circulator removed. The circulator reduces back reflections of the microwave power into the amplifier in a bandwidth from 0.8 to 1 GHz. As a result the amplifier gain curve becomes flattened and breakdown of the amplification around 900 MHz and 975 MHz is avoided.

The reliable estimation of V_0 requires a measurement of the frequency response of the microwave signal path from the analog signal generator, at Pos. 1, to the guiding electrodes, at Pos. 7. In order to perform the power correction we measure the scattering parameter S_{71} using a RF network analyzer⁹, according to the positions indicated in Fig. 3.4. We need to decompose the measurement of S_{71} into several measurements since the network analyzer cannot cope with the high microwave powers present at Pos. 7 when the network analyzer's excitation at Pos. 1 is fully amplified in between Pos. 2 and 3 by the amplifier. We therefore perform separate measurements of the scattering parameters. First, the amplifier gain is characterized by measuring S_{52} and correcting for the -20 dB attenuator at Pos. 5 by measuring S_{53} . Here the network analyzer is protected by the attenuator behind the directional coupler. Subsequently, we determine the scattering parameters S_{21} and S_{73} . From these measurements we obtain $S_{71} = S_{73} + S_{52} - S_{53} + S_{21}$ from the separate scattering parameters. Details about this measurement procedure are described in Ref [37]. As a result, the obtained scattering parameter S_{71} allows to directly convert the microwave power level set on the signal generator into the power level transmitted on the guiding electrode and hence determine the microwave voltage amplitude V_0 .

For the measurement of S_{73} we need to probe the microwave power transmitted to the guiding electrodes. This is done using a probe station and two separate microwave

⁷ *Mini-Circuits*, ZX47-40-S+

⁸ *National Instruments*, PCI-6229

⁹ *Agilent* E5071B ENA RF Network Analyzer

probes¹⁰, as shown in Fig. 3.6. From the joint measurement with both probes we can calibrate the frequency response of the microwave probes and obtain $S73$ simultaneously. Figure 3.7(a) shows the measured frequency response of the guiding substrate, which

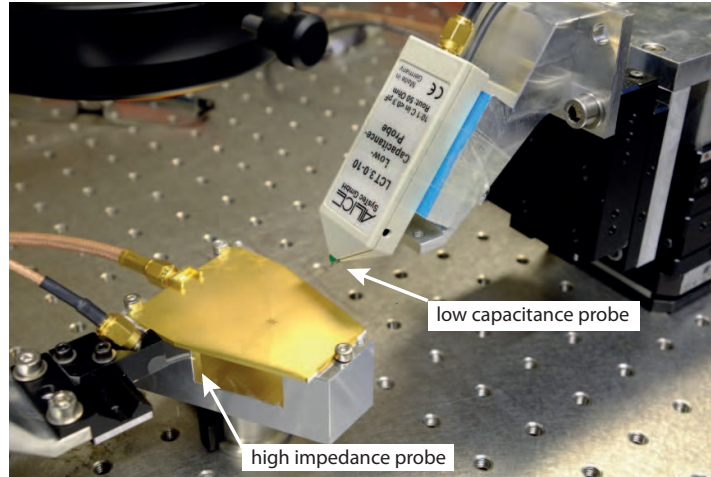


Figure 3.6: Photograph of probe station. Using a high impedance probe, which can be calibrated by the low capacitance probe, we can determine the microwave power transmitted to the signal electrodes.

can be obtained from the scattering parameter $S76$. Here the injected microwave power at Pos.6 was 1 W. The four different curves correspond to the voltage amplitudes measured at different points along the guiding electrodes, which are defined in Fig. 3.3. The black and green curve correspond to the voltages measured at the end of the inner and outer guiding electrodes, whereas blue and red are measured in the center of the inner and outer electrode. We attribute the drop in the voltage amplitude to the impedance mismatch of the guiding electrodes and the feeding cpw structure, which results in reflections and effectively reduces the microwave power transmitted to the guiding electrodes. Additionally, we observe that the voltages measured at the center of the electrodes (blue and red lines) are smaller than the voltages measured at the end of the electrodes (green and black line). This is because even though the microwave wavelength is much longer than the guiding electrodes, the voltage already drops along the electrodes, which can be attributed to the finite wavelength of the microwave signal. The resonance at about 2 GHz can be explained by the fact that here $\lambda/2 \sim 50$ mm becomes comparable to the electrode length $L = 37$ mm leading to a resonance effect.

The maximum achievable voltage amplitude, taking into account the entire signal path from the analog signal generator (Pos.1) to the guiding electrodes (Pos.7), with a saturated amplifier gain is shown in Fig. 3.7(b). The red curve shows the measured voltage amplitude of the modified microwave setup with the circulator installed behind the amplifier and the blue curve shows the same measurement without the circulator for comparison. The flattened gain curve shown in Fig. 3.5 is also reflected in a smoother frequency response of the measured scattering parameter $S71$, which underlies the voltage

¹⁰Hameg HZ553, low capacitance probe

GGB Industries Inc. Picoprobe model 40A-GSG-660/40A-GSG-660-D-1320

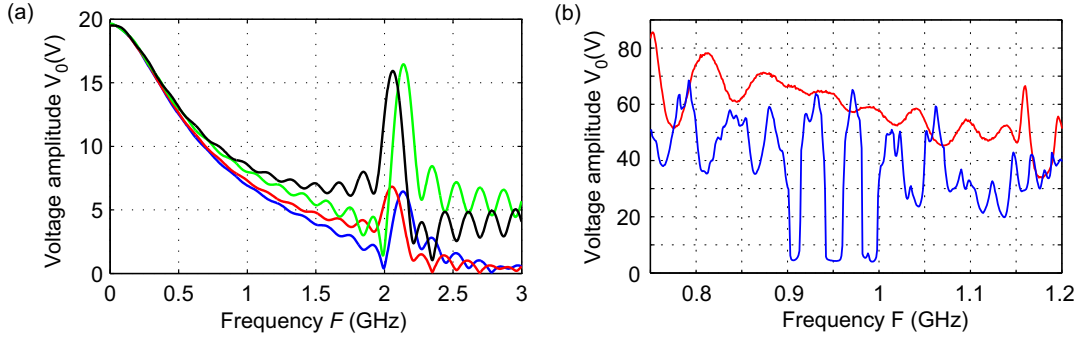


Figure 3.7: Measured voltage amplitude on the guiding electrodes. (a), Measured frequency response at the end of the inner (outer) electrode plotted as a black (green) line. The voltage amplitude at the center of the inner (outer) electrode are plotted in red (blue). The drop in the microwave voltage amplitude can be attributed to an impedance mismatch of the guiding electrode structure with the feeding cpw line. At a frequency of 2 GHz, a resonance is observed as the electrode length becomes comparable to $\lambda/2$ at 2 GHz. (b), Maximum achievable V_0 when the amplifier is operated in saturation with (red line) and without circulator (blue line).

amplitudes shown in Fig. 3.7(b). Typically electron guiding requires a voltage amplitude of $V_0 = 30$ V. Due to the insertion of the circulator and the resulting flattened gain curve, $V_0 > 50$ V is achieved in the full bandwidth from 800 MHz to 1.15 GHz.

3.1.3 Pulsed thermionic electron streaking gun

A reliable electron source that provides a low energy electron beam is indispensable for the injection of electrons into the guide. Besides a small spot size electron guiding also necessitates a high collimation of the electron beam at landing energies ranging from 1 to 10 eV. We use an electron gun that is based on the widely used Erdman-Zipf design [72]. However, we have modified the gun by additional elements that allow to operate the gun either in a continuous or a pulsed mode with electron pulse durations of several 100 ps. By these means, we can synchronize the injection of electron pulses to the microwave drive of the electron guide and perform a microwave phase-resolved measurement of the guiding efficiency. The electron gun described in the following is used in the experiments presented in this chapter and in Ch. 4.

Figure 3.8(a) shows an assembly drawing of the electron gun design. It consists of four different stages namely the electron source (1) providing a beam of slow electrons, a lens system for focusing the beam (2), a deflection element that generates electron pulses similar to a streak camera (3) and collimation apertures (4) that define the final spot size and the angular divergence of the electron beam. As can be seen from Fig. 3.8(b), all parts of the electron gun assembly are gold coated to avoid electrostatic charging, which may arise from oxidation of the metal parts. Furthermore, all gun elements have been manufactured from non-magnetic materials in order to avoid the deflection of the electron beam by unwanted magnetic fields.

We use a home-made filament consisting of a 0.1 mm diameter tungsten wire that is

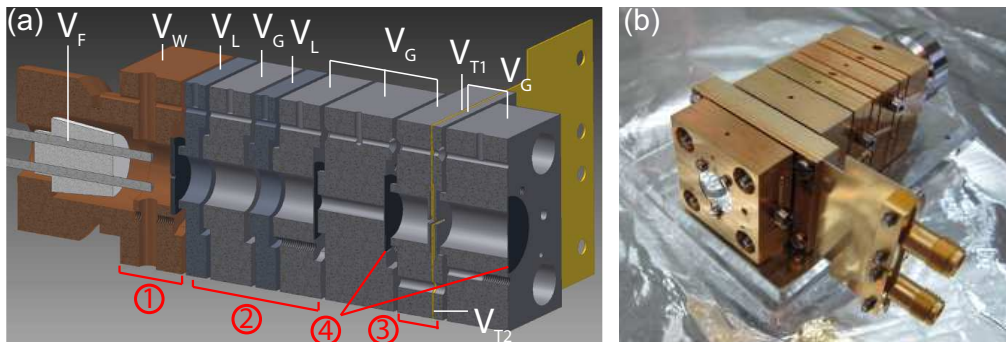


Figure 3.8: Thermionic electrons source design. (a), CAD drawing showing the elements of the electron source. The thermionic emission of the tungsten filament is confined on the optical axis by the Wehnelt electrode (1). The adjacent four elements focus the beam (2). A fast deflection element (3) allows to streak the beam over a small, beam-defining exit aperture. (b), Photograph of the electron source.

bent to hairpin shape and spot welded onto a Hitachi filament mount¹¹ as an electron source (1). Thermionic emission of electrons sets in when heating the filament to temperatures of about $T \sim 2500$ K by ohmic heating. The negative voltage V_F applied to the filament sets the final electron energy as the last gun element is electrically grounded. By means of a Wehnelt electrode surrounding the filament, the isotropic thermionic emission can be directed along the optical axis of the source by applying a negative voltage V_W to the Wehnelt with an aperture diameter of 0.6 mm. Typically, we apply $V_W = -5$ V to the Wehnelt. The electrostatic lens that focuses the electron beam (2) consists of four apertures with a central bore of 6 mm and is typically operated with a focusing voltage $V_L = 100$ V. The deflection element (3) comprises three rectangular apertures to deflect the beam. The center electrode is isolated such that we can apply a deflection voltage V_{T1} to the upper part and $-V_{T2}$ to the lower part of the electrode. The two surrounding rectangular apertures are grounded. Note that these electrodes are not rotationally symmetric but have a planar symmetry. A detailed description of the working principle of the deflection element is given below. Before leaving the gun the electron beam is collimated and clipped by two small apertures¹² (4) thereby defining the final opening angle as well as the spot size of the beam. We typically use a $100 \mu\text{m}$ pinhole as a first aperture and a $50 \mu\text{m}$ pinhole at the exit of the gun. By these means we obtain an electron beam with kinetic energies down to $E_{kin} = 1$ eV, a full opening angle below 15 mrad and spot size of about $100 \mu\text{m}$ at the entrance of the electron guide. The collimation of the electron beam using two small apertures is reflected in low electron currents on the order of several tens of femtoamperes.

In order to perform a microwave phase-resolved measurement of the electron guiding efficiency, we need a pulsed electron source with pulse durations that resolve a single cycle of the microwave drive. We have implemented a fast deflection element into the conventional electron gun design, similar to a streak camera. Using a fast deflection element, the electron beam is repeatedly swept over the exit aperture of the electron gun. Therefore, electron bunches are generated everytime the beam passes over the exit

¹¹Hitachi High-Technologies, part number 777-0179

¹²Plano GmbH, Pt apertures

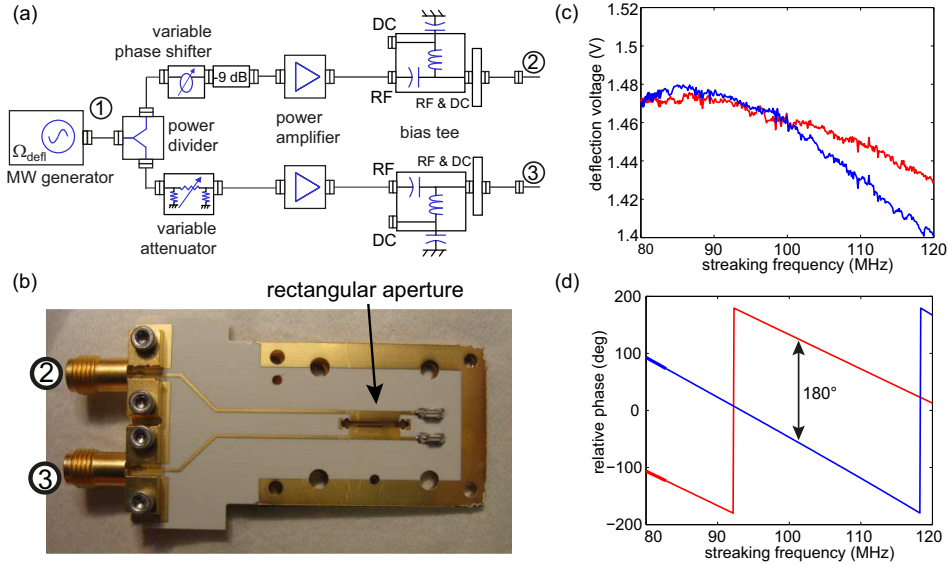


Figure 3.9: Microwave calibration of the fast electron streaking element. (a), Schematic of microwave feeding of the deflection element. The microwave signal is divided into two arms that incorporate a variable phase shifter and a variable attenuator allowing to match the microwave power at port 2 and 3 and to shift their relative phase to 180° . (b), Photograph of the central deflection aperture fabricated on a PCB substrate. (c), The deflection voltage at port 2 (blue) and 3 (red) can be adjusted by the variable attenuator to obtain identical deflection voltages in a range from 90 to 100 MHz. (d), The relative phase between port 2 (blue) and 3 (red) is tuned to 180° using the variable phase shifter.

pinhole. With increasing deflection amplitude the velocity at which the electron beam passes over the exit aperture rises, leading to shorter electron bunches behind the exit of the gun. The deflection element is manufactured from a printed circuit board substrate. Signals can be applied to the deflection electrodes by microwave compatible microstrip lines in order to deflect the electron beam at frequencies in the microwave range.

Figure 3.9(b) shows a photograph of the rectangular slit aperture for electron deflection. Two $50\text{-}\Omega$ microstrip lines connect the deflection electrodes. In order to achieve a symmetric deflection, the signals that are injected into the ports 2 and 3 need to have the same deflection voltage amplitudes V_{T1} and V_{T2} and, furthermore, should be 180° phase shifted with respect to each other. For this reason the microwave feeding of the deflection element, shown in Fig. 3.9(a), comprises a variable phase shifter¹³ in the signal arm of port 2 and a variable attenuator¹⁴ in the path feeding port 3 after dividing the microwave signal¹⁵ of an analog signal generator¹⁶. Both signals are then separately amplified¹⁷ and combined with DC voltages using bias tees¹⁸, which allows to apply a static offset to the beam deflection.

¹³ *Mini-Circuits* JSPHS-150

¹⁴ *Mini-Circuits* ZX-73-2500

¹⁵ *Mini-Circuits* ZFSCJ-2-1

¹⁶ *Agilent* E8257D, 100 kHz to 20 GHz.

¹⁷ *Mini-Circuits* ZHL-20W-13 (in signal arm of port2)

Mini-Circuits ZHL-5W-1 (in signal arm of port3)

¹⁸ *Mini-Circuits* ZFBT-4R26W

From a network analyzer measurement of the scattering parameters S21 and S31 we can adjust the amplitude as well as the phase offset of the microwave signal at port 2 and 3 using the variable attenuator and the variable phase shifter. Figure 3.9 shows the measured voltage amplitudes in (c) as well as the phases in (d) measured at both ports after adjusting the signals for an operation frequency of the deflection element of 100 MHz. We perform microwave simulations in order to obtain the frequency response of the streaking element printed circuit board. From these simulations we can estimate the voltage amplitudes that are applied to the deflection electrodes as a function of the injected microwave power.

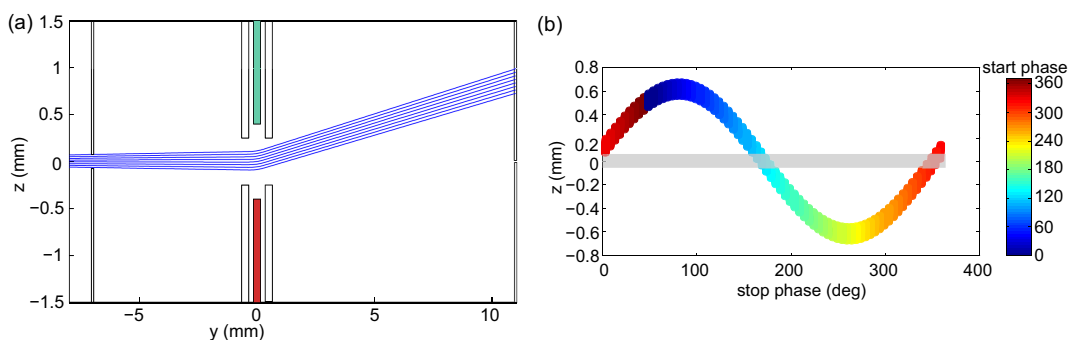


Figure 3.10: Trajectory simulations for the electron streaking element. (a), Electron particle trajectories (blue lines) are simulated with a static deflection voltage of 0.5 V applied to the upper (green) and -0.5 V to the lower (red) deflection electrode. The electron beam enters through an aperture at $y = -7\text{ mm}$ with a diameter of $150\text{ }\mu\text{m}$ and becomes deflected onto the exit aperture with a diameter of $50\text{ }\mu\text{m}$ at $y = 11\text{ mm}$. Only electrons that pass through the exit aperture, which is just visible at $z = 0\text{ mm}$, are later injected into the guide. (b), Applying a fast, alternating deflection voltage leads to a time dependent electron deflection. The trajectory release time as well as the time when a trajectory hits the exit aperture are given as a phase relative to the sinusoidal deflection voltage. Only electrons with a deflection smaller than the exit pinhole (gray area) can leave the electron gun.

Figure 3.10(a) shows a particle tracking simulation where a static deflection voltage of $V_{T1} = -V_{T2} = 0.5\text{ V}$ is applied to the deflection element. Obviously, in this setting no electrons will pass the last aperture with a diameter of $50\text{ }\mu\text{m}$. When an alternating microwave field with amplitude $V_{\text{defl}} = V_{T1} = -V_{T2}$ and angular frequency Ω_{defl} is applied to the deflection element, the electron beam is repeatedly swept over the exit aperture. Figure 3.10(b) shows the position of the electrons along the z -axis at the exit aperture. Here the release time and the time when the electron hits the exit aperture are measured with respect to the phase of the oscillating microwave signal that deflects the electron beam. Electrons can only leave the gun when their deflection is smaller than the exit aperture, which is indicated by the gray area. As a result, electron bunches are generated everytime the beam passes over the exit pinhole. With increasing deflection amplitude the velocity at which the electron beam passes over the exit aperture rises, leading to a steeper slope of the electron signal within the gray area of Fig. 3.10(b) and therefore shorter electron bunches behind the exit of the gun. At the same time we expect a decrease in the electron count rate.

The electron pulse duration of the gun is given by the time interval that the electron

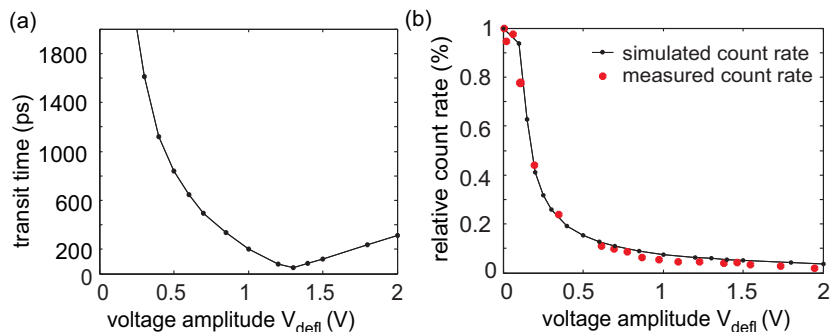


Figure 3.11: Characterization of the electron pulse duration using the fast deflection element. (a), Simulated transit time as a function of the deflection voltage V_{defl} . A minimum transit time of 51 ps can be reached by applying $V_{\text{defl}} = 1.3$ V. (b), Simulated (black) and measured (red) electron count rate after the exit pinhole as a function of V_{defl} .

beam spends over the exit aperture during one cycle of the deflection element. From the particle trajectory simulations we can extract the maximum time of flight difference between two electrons that leave the gun during one cycle. However, these simulations are performed for a monochromatic electron beam with a kinetic energy of 3 eV. The pulse duration obtained by these means does not account for the longitudinal energy spread of the electron source. It only depends on the geometry of the deflection element, the electron energy and the deflection amplitudes V_{defl} . We therefore refer to the pulse duration obtained by *monochromatic* particle tracking simulations as transit time interval. In order to determine the actual electron pulse duration, we also have to consider the longitudinal energy spread of the electron source and take into account dispersion within the deflection element. We call this time interval, which includes chromatic effects, the electron pulse duration. After presenting the particle tracking simulations and an experimental characterization of the deflection element, we discuss the longitudinal energy spread of the source, which turns out to currently limit the electron pulse duration.

We perform particle tracking simulations for a deflection frequency of $\Omega_{\text{defl}} = 2\pi \cdot 99.6$ MHz and varying deflection amplitudes $V_{\text{defl}} = V_{T1} = -V_{T2}$. We choose $\Omega_{\text{defl}} = 2\pi \cdot 99.6$ MHz, i.e., one tenth of the guide's drive frequency, in order to make sure that an electron experiences only one single cycle of the deflection amplitude while passing through the deflection element. From these simulations we can extract the duration that the mono-energetic electron beam spends over the exit aperture and determine the transit time interval. As depicted in Fig. 3.11(a) the simulations show a decrease in the transit time for increasing deflection amplitudes until a minimum is reached at $V_{\text{defl}} = 1.3$ V, corresponding to a time interval of 51 ps. The linear increase of the transit time for $V_{\text{defl}} > 1.3$ V is due to electric fields along the optical axis that are created by the deflection element. These fields lead to an acceleration of electrons passing close by the positive deflection electrode, whereas electrons close to the negative electrode are decelerated. As one would expect, this effect increases the transit time linearly with the electric field amplitude. Since we can not directly measure the transit time interval, we can only compare the measured and simulated drop in electron count rate as a function of the deflection amplitude after the last aperture. This is an indirect measurement of the transit time interval. As can be seen from Fig. 3.11(b), the measured count

rate agrees very well with the particle tracking simulation results. The phase-resolved measurements, described in Sec. 3.5, are performed with $V_{\text{def}} = 1.46 \text{ V}$, corresponding to a transit time of 105 ps, since this yields experimentally the best compromise between pulse duration and electron count rate.

So far, the particle tracking simulations were based on a perfectly monochromatic source. The electron gun, however, is based on a conventional thermionic tungsten filament emitter. The longitudinal full width at half maximum (FWHM) energy spread of such a source is $\Delta E = 2.446 k_B T = 0.53 \text{ eV}$ at a temperature $T = 2500 \text{ K}$ [73]. This results in a time of flight distribution with FWHM of $\Delta t \approx d\sqrt{M/2} [1/(E - \Delta E/2) - 1/(E + \Delta E/2)] = 693 \text{ ps}$. Here d is the distance between the deflection element and the exit aperture. In consequence the electron pulse duration is limited by the dispersive nature of the electron source rather than the deflection element itself.

We will use the pulsed electron source described in this section for the phase-resolved measurements presented in Sec. 3.5.

3.1.4 Vacuum chamber

A stable operation of the thermionic electron source as well as single electron detection using the MCP electron detector¹⁹ requires operation in vacuum. For this reason, the guiding experiments are performed in a UHV chamber typically reaching a background pressure of about $2 \cdot 10^{-7} \text{ mbar}$ using a turbo-molecular pump²⁰. This is low enough to avoid surface contaminations in the electron gun and to allow for single electron detection but does not require elaborate UHV treatments like vacuum bake-outs.

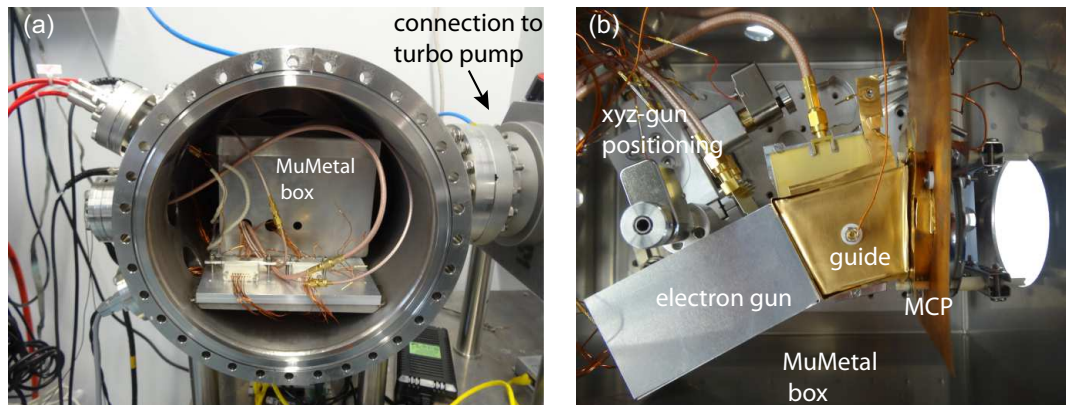


Figure 3.12: UHV chamber housing the electron guiding experiment. (a), View into the opened vacuum chamber showing the mu-metal box housing the guiding experiment and SMA microwave cables of the guide and the streaking element. (b), Interior of the mu-metal box showing the electron streaking gun, microwave guiding chip and the imaging electron microchannel-plate detector shielded by metallic housings.

Figure 3.12 shows images of the experimental apparatus. The guiding experiment is assembled inside a mu-metal box, which is comparable in size to a small shoebox and is placed inside the UHV chamber. The box can be closed with a lid and has several small

¹⁹PHOTONIS APD 2 PS 40/12/10/12 46:1 P20

²⁰Leybold Turbovac 340M

holes in order to feed through electrical connections and to provide optical access to the phosphor screen behind the MCP detector. The main purpose of the mu-metal box is to shield the experiment from static fields like the earth's magnetic field. In Ref. [37] the shielding has been measured to reduce the ambient static magnet field at the guide's position by a factor of over 200 to 2mG and magnetic field fluctuations to below 0.2 mG. The guiding setup inside the mu-metal box consists of the MCP detector, the guiding substrate and the electron gun, which is mounted on a xyz translational stage²¹ for precise positioning of the gun with respect to the microwave guide. As can be seen in Fig. 3.12(b), custom made metallic shields enclose the gun, the guiding chip and the MCP in order to screen any electric fields from the guided electron beam.

3.2 Guiding of electrons along a curve

The guiding of electrons has been demonstrated in a proof-of-principle experiment where a curved electrode design allowed to detect a collimated signal of guided electrons [19, 37]. Because of the curved path of the guiding electrodes the guided electrons are deflected by about 30° with respect to the unguided electrons. On the MCP detector, which is placed about 10 mm behind the guiding chip, this results in a separation of 20 mm between the guided and unguided components of the electron signal. Consequently, the guiding along a curve provides detailed information about the origin of electron loss from the guiding potential. Electrons that escape from the guiding potential on their way to the detector become less deflected the earlier they are lost on their curved path. The confinement of the quadrupole guide is weakest along the vertical z -direction. For this reasons unguided electrons are primarily lost along the vertical direction and are detected at larger z on the MCP detector.

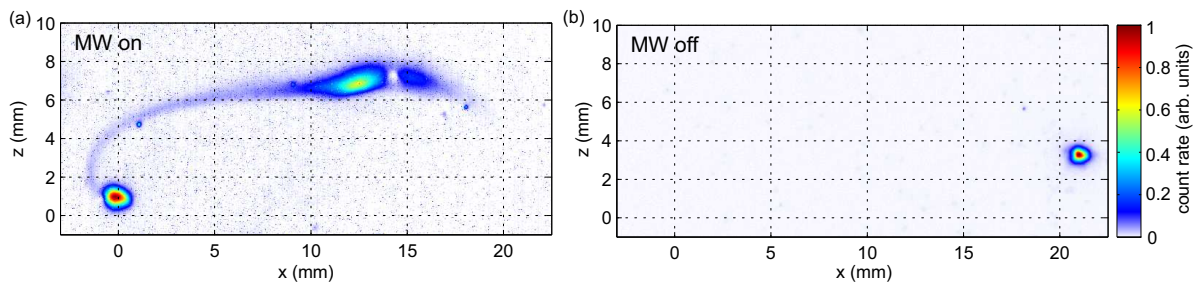


Figure 3.13: Experimental electron guiding signal. (a), Electron guiding signal with the guided electrons recorded at a position $x = 0$ mm and a faint signal of lost electrons that spirals around the guided spot. The guide is operated with a frequency $\Omega = 2\pi \cdot 996$ MHz and $V_0 = 29$ V. This results in the trap parameters $\omega = 2\pi \cdot 114$ MHz, $U = 30$ meV and $q = 0.32$. The electron kinetic energy is 3 eV and the color scale depicts the electron count rate. The artifact in the loss signal at $x \sim 15$ mm comes from MCP. (b), When the microwave drive is turned off the unguided electron spot is detected at $x = 21$ mm. The intensities in (a) and (b) are normalized separately.

Figure 3.13 shows electron signals with an electron energy $E_{kin} = 3$ eV, which are recorded with the microwave drive turned on (a) and off (b), respectively. In Fig. 3.13(a)

²¹New Focus 9066-XYZ-M-R-V stage with model 8353-V Picomotor actuators

the microwave drive frequency is $\Omega = 996$ MHz and the electrode voltage is $V_0 = 29$ V. This corresponds to the trap parameters $\omega = 2\pi \cdot 114$ MHz, $U = 30$ meV and $q = 0.32$. We observe a collimated spot of guided electrons detected at $x = 0$ mm. Additionally, there is a faint signal of lost electrons that spirals around the guided spot. This structure can be related to electrons that are lost from the guiding potential. In contrast, in Fig. 3.13(b), the microwave drive is turned off and we detect a collimated electron spot at $x = 21$ mm. Due to charging of the substrate, which is exposed to stray electrons between the insulating gaps of the guiding electrodes, the electron beam is deflected in the positive z -direction.

The dynamics of the electrons in the guiding potential is characterized by the trap parameters ω , U and q . In order to study the guiding efficiency as a function of these parameters, we sweep the microwave frequency Ω and voltage amplitude V_0 to scan the trap parameter range. Using the power correction described in Sec. 3.1.2, we can then convert the drive parameters into trap parameters. Figure 3.14(a) shows a stability diagram in the experimentally accessible microwave parameter range. Here the color scale displays the fraction of guided electrons as a function of Ω and V_0 . Clearly the microwave power correction is not perfect, as there is an artificial modulation of the guiding efficiency with the microwave frequency. However, we can distinguish a microwave parameter range of efficient guiding, which lies in between the two red lines indicating a constant trap depth of 30 meV and a constant stability parameter $q = 0.8$.

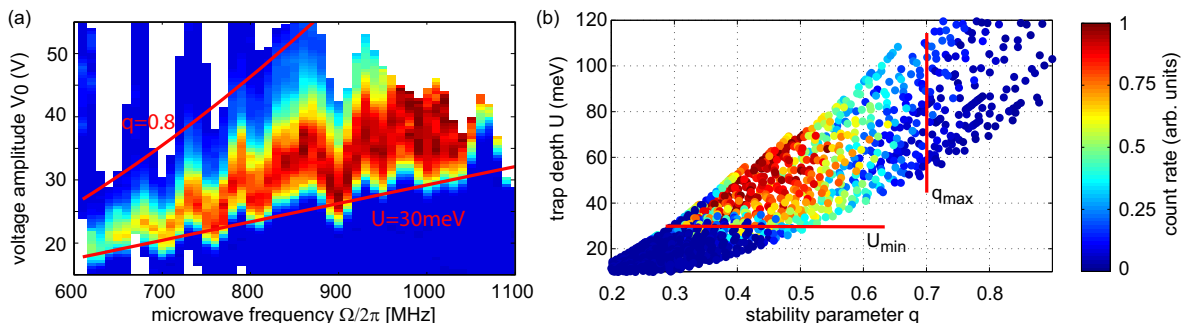


Figure 3.14: Experimental stability diagram of electron guiding with $E_{\text{kin}} = 3$ eV. (a), Drive parameter sweep showing the regions of stable electron guiding. The color scale corresponds to the fraction of guided electrons. (b), Same data with the plot axis converted to the trapping parameters U and q . As can be seen, stable guiding requires a minimum potential depth $U_{\min} = 28$ meV and $q < 0.7$. White areas in the plots are not accessible with the microwave setup currently available.

In Fig. 3.14(b) the same data is depicted but the plot axis have been converted to the trap parameters q and U using Eqs. 2.15, 2.16. We find that a minimum trap depth $U_{\min} = 28$ meV is required to compensate for the centrifugal force that acts on the electrons when following the curved path of the chip electrodes. Consequently, when the centrifugal force becomes sufficient to promote guided electrons over the potential barrier electron loss from the guide is observed. We also tested straight guiding chips and found guiding down to $U = 0$ confirming this interpretation [37]. Furthermore, electron guiding becomes unstable for stability parameters $q > 0.7$. Here the adiabatic approximation is reaching the limits of applicability rendering the confinement of the

electrons unstable. As outlined in Sec. 2.1, one would expect stable confinement up to stability parameters of $q = 0.9$. We attribute the experimentally observed maximum stability parameter of about $q = 0.7$ to experimental imperfections that additionally deteriorate the electron guiding efficiency.

3.3 Microwave phase dependence of the guiding signal

Progress towards the preparation of electrons in low-lying quantum states of the transverse guiding potential is one of the most important achievements of electron guiding. In addition to a diffraction-limited electron gun the direct injection into the transverse motional quantum states necessitates a guiding potential that minimizes excitations of the electrons during injection into the guide. Due to fringing electric fields at the edges of the guiding substrate, the electron beam experiences an initial deflection before it becomes injected into the guiding potential of the microwave chip. This leads to an excited motion of the electrons within the guiding potential or even loss of electrons from the guide. Here, the origin of the unwanted fringing electric fields is discussed and particle tracking simulations are performed in order to study the dynamics of electrons after injection into the guide. These simulations reproduce the measured guiding signal and allow to address the origin of an excited electron motion or loss of electrons from the guide.

3.3.1 Fringing electric fields at the substrate edge

The pseudopotential shown in Fig. 2.3(b) is simulated assuming infinitely long electrodes along the guide axis. As described in Sec. 2.1, the quadrupole symmetry of the electric field results in a stable harmonic confinement of the electrons in the microwave pseudopotential. In the case of finite electrode length, where the electrodes are terminated close to the substrate edge, we observe a significant deterioration of the guiding potential by fringing electric fields. These fringing fields lead to a deviation of the electric fields from the quadrupole symmetry and, therefore, diminish the electron confinement within the pseudopotential. Figure 3.15 shows a simulation of the absolute maximum electric field amplitude $|\mathbf{E}|$ close to the substrate edge. As can be seen, at a y -position larger than ~ 3 mm where the guiding potential is fully developed and not influenced by edge effects any more, the quadrupolar shape of the electric field results in an electric field null at a height of $R_0 = 500 \mu\text{m}$ above the substrate. Ideally, an electron traveling perfectly on-axis with the minimum of the guiding potential should propagate along the guide without experiencing any electric fields and should, therefore, not be subjected to any forces. However, due to the termination of the electrode design close to the substrate edge fringing electric fields are present on the guide axis between the electron gun and the microwave chip. As a consequence, an electron impinging at a height of $R_0 = 500 \mu\text{m}$ experiences an electric field in the vertical z -direction and becomes deflected prior to injection into the guiding potential. This will lead to an unwanted excited motion of the injected electron inside the guiding potential, no matter how good an electron beam the electron source is able to deliver. Hence, the impact of these fringing fields during electron injection has to be minimized on the first millimeters along the guide.

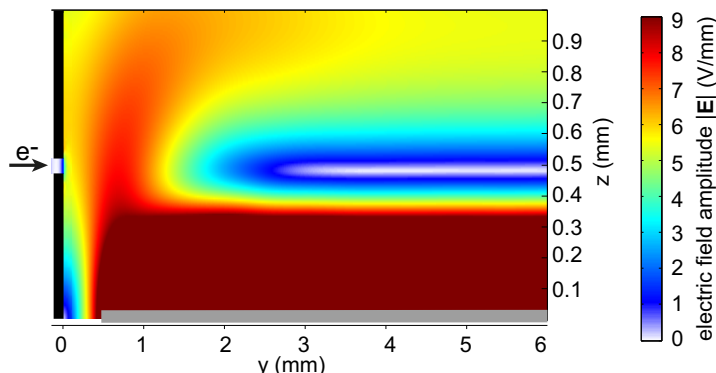


Figure 3.15: Simulation of electric fields close to the substrate edge where electrons are injected into the guiding potential. The color scale displays the absolute value of the electric field $|\mathbf{E}|$ at a snapshot in time where it is at its maximum. The last aperture of the electron gun is shown schematically at $y = 0$ mm (drawn in black). The microwave substrate at $z = 0$ mm is indicated in gray starting from $y = 0.5$ mm. Fringing fields near the substrate edge lead to significant local deviations of the electric field from the ideal quadrupolar shape. As a consequence, an electron impinging at a height $R_0 = 500 \mu\text{m}$ experiences an electric field amplitude E and becomes deflected during injection.

3.3.2 Particle trajectory simulations

We investigate the dynamics of electrons after injection into the guiding potential by performing particle tracking simulations and comparing these to the measured guiding signal. By these means we are able to study the impact of fringing electric fields on the electron motion, which may result in an excited oscillation within the guiding potential or even loss of electrons from the guide. The particle trajectories are simulated using the commercially available boundary element method solver CPO²². These simulations take into account the electric field, oscillating at the microwave driving frequency, and are performed according to the experimental parameters $\Omega = 2\pi \cdot 996$ MHz and $V_0 = 29$ V. This results in the trap parameters $\omega = 2\pi \cdot 114$ MHz, $U = 30$ meV and $q = 0.32$.

Figure 3.16(a) and (b) show a side view of the corresponding electron trajectories in the vertical yz -plane along the guiding electrodes. Electrons with a kinetic energy of 3 eV are injected into the guide at $y = 0$ mm, where the last aperture of the gun is shown schematically, and exit the guide at $y = 37$ mm. As can be seen, electrons perform the slow secular motion in the guiding potential given by the trap frequency ω and discernible as oscillations with a spatial period of ~ 9.5 mm at this particular electron velocity. On top of that harmonic motion, the fast micromotion of electrons can be identified as a high frequency component oscillating at the driving frequency Ω and leading to a spatial period of ~ 1 mm.

The unwanted fringing electric fields close to the substrate edge oscillate with the frequency Ω of the microwave drive. Furthermore, an electron experiences less than a single cycle of the driving electric field on the first millimeter between gun exit and the guiding chip where the amplitude of the fringing fields is largest. For this reason, the initial deflection and the resulting oscillation of the electron within the guiding

²²Charged particle optics, CPO

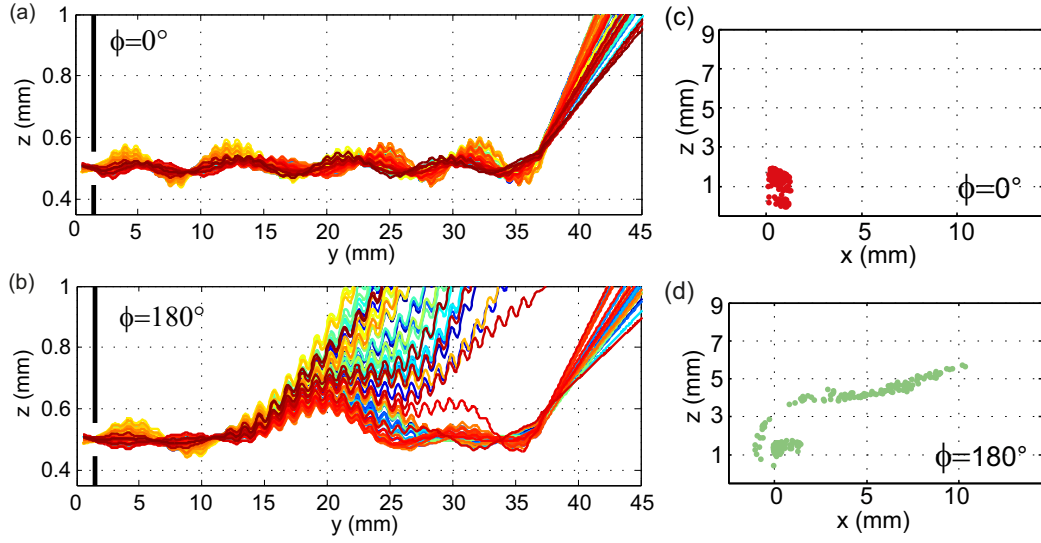


Figure 3.16: Electron trajectory simulations resolving the phase of the microwave drive. Electrons enter the guiding potential at $y = 0$ mm through the exit aperture of the electron gun (drawn in black) at a height of $z = 500 \mu\text{m}$ above the substrate. The initial electron spot size in the simulations is $60 \mu\text{m}$ in diameter. After propagation through the guiding potential electrons are released into free-space at $y = 37$ mm and detected in the detector plane at $y = 45$ mm (not shown). (a), (b), show a side view of particle tracking simulations in the yz -plane along the guiding electrodes. The color of the electron trajectories is chosen for better visibility and does not contain any further information here. (a), For a microwave phase of $\phi = 0^\circ$ all electrons are confined in the guiding potential and oscillate with the trap frequency ω corresponding to a spatial period of ~ 9.5 mm. In (b), a significant portion of electrons is lost for a microwave phase of $\phi = 180^\circ$. Here electrons are lost from the guiding potential in the vertical z -direction starting from $y = 15$ mm. The corresponding simulated guiding signals are shown for $\phi = 0^\circ$, in (c), where all trajectories are guided along the curve and hit the detector around $x = 0$, whereas, in (d), a large fraction of the trajectories is lost for $\phi = 180^\circ$. The trajectories are simulated with $\Omega = 2\pi \cdot 996$ MHz and $V_0 = 29$ V.

potential depends highly on the orientation and the amplitude of the fringing electric fields and, hence, the phase of the microwave driving signal. This becomes apparent in the particle tracking simulations when electron trajectories are released at different times with respect to the phase of the microwave driving signal. Depending on this phase electrons experience a different orientation of the electric field amplitude during injection, which governs the passage into the guiding potential. The simulations have been performed for a set of different release times covering a full evolution of 2π in the microwave phase.

Figure 3.16(a) shows trajectories for a microwave phase of $\phi = 0^\circ$ where all electrons are tightly confined by the guiding potential. In contrast, in Fig. 3.16(b) for $\phi = 180^\circ$, a large fraction of electrons is lost, starting from $y = 15$ mm, on their way to the detector in the vertical z -direction. The phase dependence of the electron guiding efficiency observed in these simulations can be attributed to electric fringing fields at the edges of the guiding substrate. For microwave phases around $\phi = 0^\circ$ a relatively small initial deflection results

in the characteristic oscillation of electrons in the guiding potential. In contrast, for microwave phases close to $\phi = 180^\circ$ electrons experience a stronger initial deflection giving rise to loss of electrons from the guide.

From the same particle tracking simulations we can infer the location of electrons impinging on the detector. In Fig. 3.16(c) and (d), the detector signals corresponding to the trajectory simulations are shown for two distinct microwave phases. For $\phi = 0^\circ$ all electrons are guided and reach the detector around $x = 0$ mm, whereas for $\phi = 180^\circ$ a significant portion of electrons is lost. This portion corresponds to the trajectories that are lost along the z -direction in Fig. 3.16(b). In Fig. 3.17(b) a simulated guiding signal

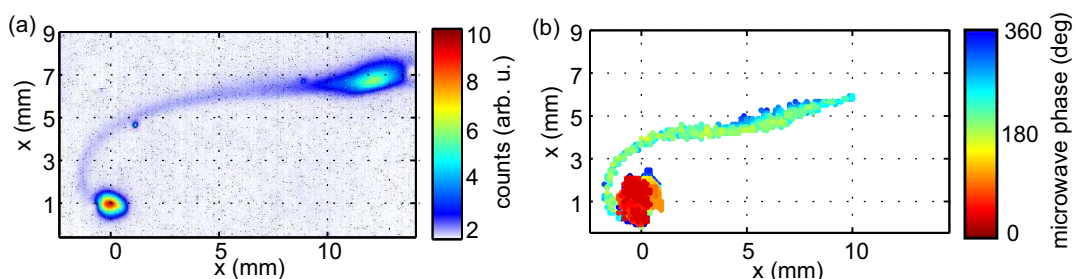


Figure 3.17: Comparison of experimental and simulated guiding signal with $E_{\text{kin}} = 3$ eV. (a), Electron guiding signal with the guided electrons recorded at a position $x = 0$ mm. The color scale depicts the electron count rate. (b), Simulated guiding signal. Here the color scale corresponds to the phase of the microwave driving signal at the instant in time when the electron is injected into the guide. The experiments as well as the simulation are performed with $\Omega = 2\pi \cdot 996$ MHz and $V_0 = 29$ V, which results in the trap parameters $\omega = 2\pi \cdot 114$ MHz, $U = 30$ meV and $q = 0.32$.

is shown taking into account all microwave phases. Here the color scale displays the relative phase ϕ of the microwave electric field. The simulations reproduce the general structure of the experimental guiding signal shown in Fig. 3.17(a) very well.

In the following sections we present a viable approach to reduce the amplitude of the vertically excited electron motion by minimizing forces that initially deflect the electron beam. First of all, we perform a numerical optimization of the shape of the chip electrodes in order to reduce the amplitude of unwanted fringing fields in Sec. 3.4. Then we experimentally employ the pulsed electron source to temporally synchronize the injection of electron pulses to a certain microwave phase in Sec. 3.5. By these means, we can control the specific orientation of the driving electric field during electron injection and, hence, increase the electron guiding efficiency. Both strategies allow to minimize the initial deflection of electrons during injection.

3.4 Optimized coupling structures for electron guiding

In this section we present an optimization of the shape of the electrode coupling structures close to the substrate edge in order to reduce the impact of fringing electric fields on the electron injection. We simulate particle trajectories to quantify the improved performance of the coupling structures and finally present first guiding measurements with the optimized design demonstrating an improved electron guiding efficiency.

3.4.1 Numerical optimization of the electrode structure

In order to reduce the unwanted fringing fields and to provide a smooth transition for electrons from the exit aperture of the electron gun into the guiding potential, we perform a numerical optimization of the chip electrode geometry. This is done by a parametrization of the shape of the guiding electrodes by a predetermined number of N points in the vicinity of the substrate edge. The optimization algorithm then systematically varies the position of these points in order to achieve a defined minimization goal that is given by a scalar merit function M .

Figure 3.18(a) shows the initial electrode layout that is used as a starting point for the design optimization. The signal electrodes [blue areas in (a)] are tapered by scaling the width of the signal electrodes linearly down to zero towards the substrate edge, which is located at $y = 0$ mm. At the same time the width of the grounded center electrode [white area in (a)] is increased according to Eq. 2.17, such that a constant trap height R_0 would be obtained for an adiabatic tapering. Figure 3.18(b) shows the pseudopotential obtained from this electrode taper. It significantly deviates from the ideal quadrupolar confinement on the first 15 mm along the guide. For example, the value of the pseudopotential minimum at a height $R_0 = 500 \mu\text{m}$ takes values up to 5 meV. As a result, an electron will experience forces in the vertical z -direction during injection and hence perform an excited, oscillatory motion within the guiding potential.

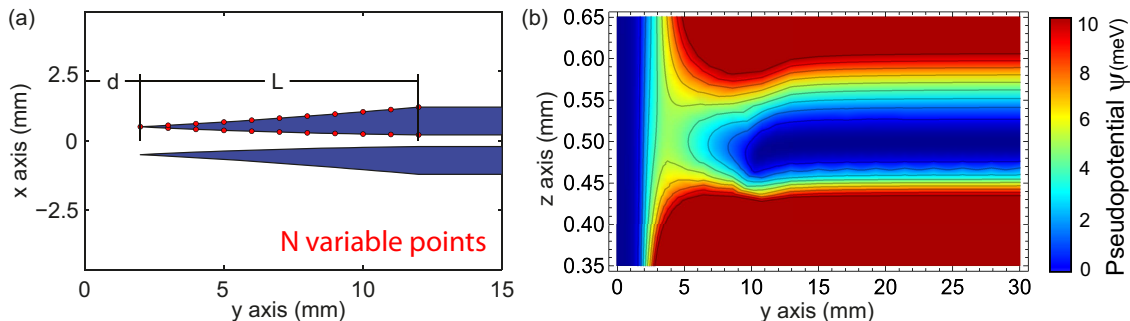


Figure 3.18: Parametrization of the electrode layout and a color plot of the corresponding pseudopotential. (a), The guiding electrodes close to the substrate edge are tapered in order to reduce the amplitude of vertical fringing fields. The electrode shape is parametrized by N points that are equally distributed over the length L of the taper. The distance of the electrodes to the exit aperture of the electron gun is given by the d . The pseudopotential for $L = 8$ mm, $d = 2$ mm and the drive parameters $\Omega = 2\pi \cdot 1\text{GHz}$, $V_0 = 30$ V is shown in (b). Clearly, there the pseudopotential is deteriorated on the first 15 mm along the guide axis, as the guiding potential minimum does not extend from within the guide to the electron gun at $y = 0$ mm.

We use the freely available *Surface Pattern* package [74, 56, 75], which is implemented in MATHEMATICA, to simulate the electric field of the guiding structure in the gapless plane approximation. This package is capable of yielding analytic results for any planar electrode structure, making optimizations fast. However, because the field simulation is constrained to planar electrode designs, the electron gun exit aperture is modeled as a closed conducting electrode located at $y = 0$ mm.

In order to quantify forces that act on the electrons during injection we define the normalized, dimensionless ponderomotive gradient force in the vertical z -direction

$$F_z = \frac{4M\Omega^2 R_0^3}{Q^2 V_0^2} \frac{\partial}{\partial z} \Psi. \quad (3.1)$$

This force deflects the incoming electron in the vertical z -direction, where the confinement of the guiding potential is weakest.

First we have checked whether the influence of an aperture can indeed be neglected by comparing the results obtained from Surface Pattern to a simulation in Comsol with a circular aperture with $500 \mu\text{m}$ in diameter. Figure 3.19(a) shows a comparison of the obtained F_z along the guide axis at a height R_0 , where the noisy blue line corresponds to the Comsol result. Clearly, both simulations agree very well and the modeling of the exit aperture by a closed planar electrode is hence well justified.

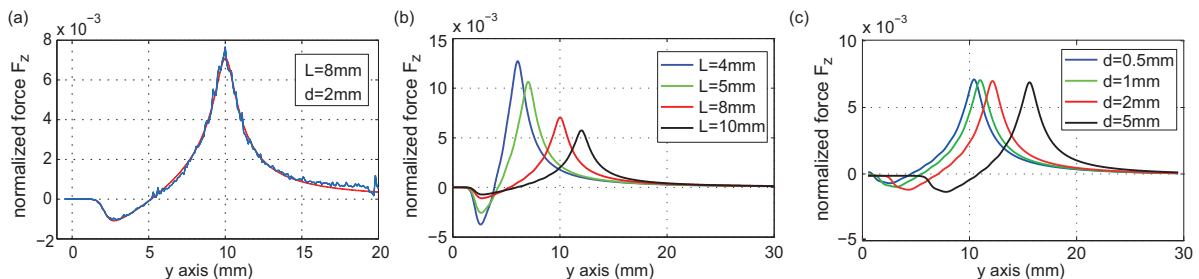


Figure 3.19: Ponderomotive gradient force along the guide axis. In (a), F_z is plotted along y using the Surface Pattern software (red line), which is compared to a Comsol simulation (blue line). In Surface Pattern the exit aperture of the gun is modeled as a closed flat electrode, whereas in Comsol the model includes a circular aperture with $500 \mu\text{m}$ diameter. The simulation results are nearly identical showing that the aperture can be neglected indeed. The dependence of F_z on the taper length L and the distance d are shown in (b), and (c), respectively.

The dependence of F_z on the taper length L is shown in Fig. 3.19(b). Clearly, increasing the length of the electrode taper reduces F_z as expected. However, as the guiding substrate is 40 mm long in current chip designs we do not consider tapers longer than $L = 10$ mm. In contrast, the amplitude of F_z can not be decreased when changing the distance d of the electron gun exit to the guiding electrodes, as depicted in Fig. 3.19(c), where a change in d only results in a shift of F_z along y . This indicates that the fringing fields that generate the vertical force F_z are merely produced by the electrode design itself and that they do not result from fields between the guiding electrodes and the exit aperture of the gun. These fields would critically depend on the distance d between electrodes and the gun aperture.

Figure 3.20(a) shows the electrode design close to the substrate edge that has been obtained by an initial optimization. A detailed discussion of the optimization of this geometry is given in [19, 37]. This electrode layout was obtained from minimizing directly the vertical fringing electric fields E_z using $N = 6$ adjustable points. To further optimize the electrode shape we use a Nelder-Mead simplex algorithm, to minimize a merit function M by a systematic variation of the N points parametrizing the electrodes. The

ponderomotive force F_z deflects the incoming electron in the vertical z -direction, where the confinement is weakest. There is no deflection in the x -direction due to the planar symmetry of the electrode layout. The minimization of the dimensionless, ponderomotive force will serve as a figure of merit in the optimization of the shape of the chip electrodes

$$M = \int_{0\text{mm}}^{15\text{mm}} |F_z| dy. \quad (3.2)$$

It is instructive to obtain an intuitive understanding of the resulting electrode geometries that arise from the numerical optimization. The optimization algorithm seeks to minimize pseudopotential gradients in the vertical z -direction at the guide's height. This gradient strongly depends on the electric field E_z in the vertical dimension. However, according to Maxwell's equations changing the electric field E_z in the vertical z -direction along the guide axis is directly reflected in a changing longitudinal field E_y along the y -direction (in x -direction no field is possible due to the planar electrode symmetry). As a result, the optimization algorithm seeks to create a longitudinal field gradient along y to increase E_y and similarly reduce E_z . A zigzag-shaped electrode layout produces such a longitudinal gradient and may therefore effectively reduce F_z .

The left column in Fig. 3.20 shows the result of the electrode design optimization with increasing number of points N along the electrode edges. From Fig. 3.20(a) with the initial design using $N = 6$ points to Fig. 3.20(c) with $N = 15$ there is a reduction in the maximum normalized gradient force F_z by a factor of 17. The improved properties of the electrode design in Fig. 3.20(c) can be mainly attributed to increased number of points and the increased length of the optimized electrode taper from 3 mm to 8 mm. The adjustable points in both designs are equally spaced along the guide axis by 1 mm distance. We have confirmed that further increasing the taper length does not yield a significantly improved merit function. The electrode design in Fig. 3.20(e), which features a decreased spacing of 0.5 mm between the optimization points and a total of $N = 39$ points, shows another reduction in the maximum normalized gradient force by a factor of 3 with respect to Fig. 3.20(c).

The Nelder-Mead simplex algorithm does not necessarily converge towards a global minimum. The optimum electrode shape depicted in Fig. 3.20(e) may therefore only correspond to a local minimum. Future optimizations of the electrode shape, employing other optimization algorithms might converge towards a global minimum and hence reduce fringing fields even further.

3.4.2 Particle trajectory simulations

The effect of the electrode optimization becomes clearly visible in particle trajectory simulations for the different geometries. The last column of Fig. 3.21 shows simulated trajectories for an electron with a kinetic energy of 1 eV, incident parallel to the guide axis, together with a color plot of the pseudopotential in the yz -plane. The trajectories are calculated taking into account the simulated electric fields and assuming a drive frequency of $\Omega = 2\pi \cdot 2.8$ GHz and a voltage amplitude of $V_0 = 72$ V. This results in a transverse frequency $\omega = 2\pi \cdot 100$ MHz, a potential depth $U = 23$ meV and a stability parameter $q = 0.1$ of the guiding potential. Compared to the microwave parameters used

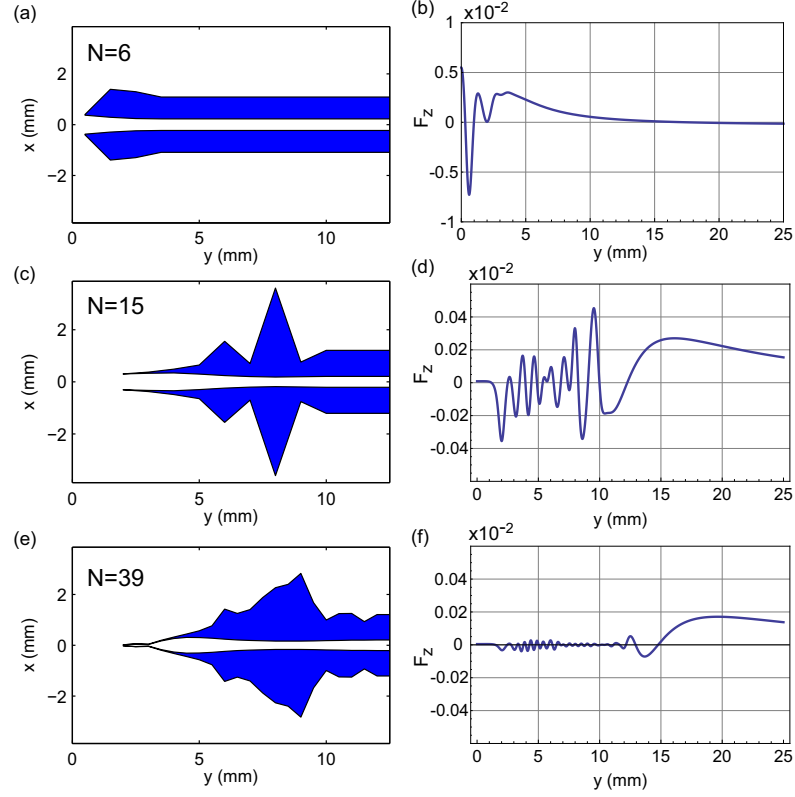


Figure 3.20: Conductor layout and vertical pseudopotential gradient along the guide axis for the optimized coupling structures. In (a), (c), and (e), the signal electrodes are drawn in blue whereas white corresponds to grounded areas (gapless plane approximation). In the numerical optimization of the electrode shape the width of each electrode is constraint to be larger than $20 \mu\text{m}$. In (b), (d), and (f), the corresponding dimensionless, vertical pseudopotential gradient F_z is shown.

in the experiments, the drive parameters of the particle tracking simulations are tuned to yield a smaller stability parameter q at a similar trap frequency ω and potential depth U . Effectively this leads to a more cycle-averaged motion of the electron due to the increased microwave driving frequency. This results in similar dynamics of the electron within the guiding potential (similar trap frequency). However, effects that are related to the phase of fringing fields are reduced during the electron injection, as is the micromotion inside the guiding potential. We show particle trajectories for two specific phases in Fig. 3.21 for which the effect of the fringing fields is maximum and minimum.

For the initial design, first row of Fig. 3.21, an electron incident on the guiding structure is exposed to relatively strong vertical fringing fields. This leads to an excitation of the electron within the guiding potential with an oscillation amplitude of $\delta z = 9.5 \mu\text{m}$ to $\delta z = 14 \mu\text{m}$, depending on the microwave phase. Going to $N = 15$ points in the second row of Fig. 3.21 yields a reduction of the on-axis gradient force that is directly reflected in a smaller oscillation amplitude of $\delta z = 1.4 \mu\text{m}$ to $\delta z = 2.88 \mu\text{m}$. For the best optimization result with $N = 39$ points in the last row of Fig. 3.21 the excitation of the

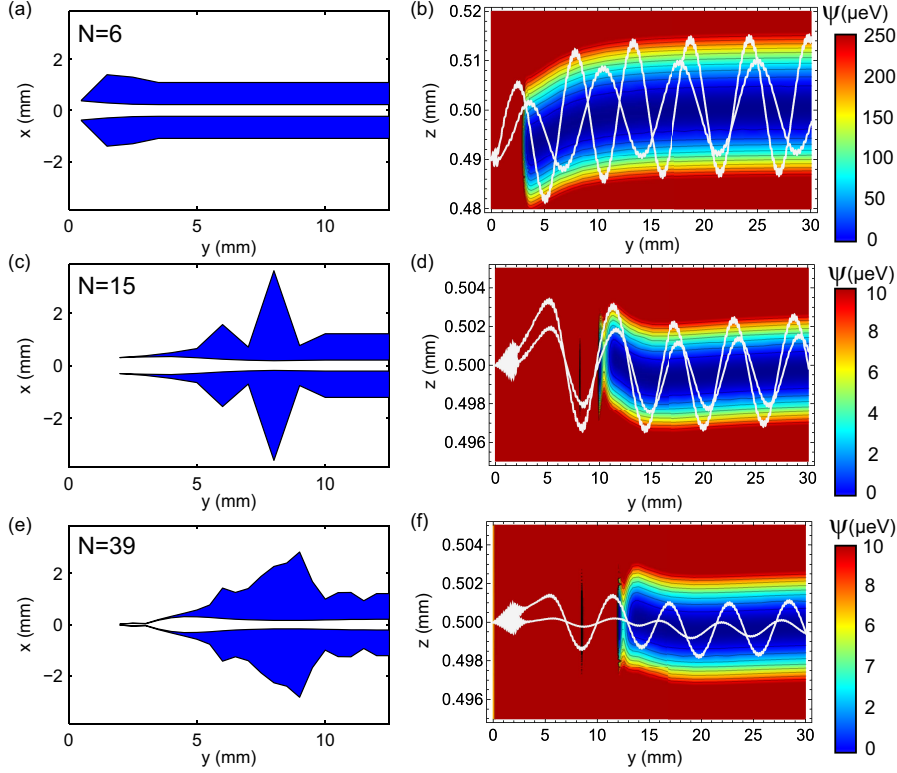


Figure 3.21: Conductor layout and electron trajectory simulations for optimized coupling structures. (b), (d), and (f), show simulated trajectories (white curves) together with a color plot of the pseudopotential for $\Omega = 2\pi \cdot 2.8$ GHz and $V_0 = 72$ V. For better visibility trajectories are shown for two selected microwave phases where the electron performs the most and the least excited oscillation within the guiding potential. Note the different scaling of the z -axis as well as the color scale going from (b) to (d) and (f). Clearly, the reduction in the vertical pseudopotential gradient is reflected in a smaller oscillation amplitude of the electron after injection.

electron oscillation is even further reduced and amounts to an amplitude of $\delta z = 400$ nm to $\delta z = 1.4 \mu\text{m}$. Taking into account trajectories for many different phases, we find that 25% of the trajectories oscillate with an amplitude smaller than 500 nm for the best optimization result with $N = 39$ points. More specifically, we can deduce from this phase dependence that within a time window of 40 ps all electrons can be injected with an oscillation amplitude below 500 nm by synchronized injection of electron pulses.

The transverse oscillation amplitude of $\delta z = 400$ nm is comparable to the width $\Delta z = \sqrt{\hbar/(2M\omega)} = 303$ nm of the quantum mechanical ground state of the harmonically approximated pseudopotential. This indicates that classical particle tracking simulations hit the limits of applicability and that the transverse motion of the electron has to be described by quantized eigenstates of the guiding potential. However, the particle tracking simulations suggest that by employing the optimized electrode structures and temporally synchronizing the injection of electron pulses to a specific phase of the driving electric field, the excited motion of an electron inside the guide can be minimized to a regime that allows the direct injection into low-lying quantum states of the transverse guiding potential.

3.4.3 Electron guiding with optimized coupling structures

We have experimentally investigated the improved properties of the optimized coupling structure, shown in Fig. 3.21(c), by measuring its electron guiding signal. A comparison of the respective guiding signals is shown in Fig. 3.22 for the zigzag-shaped, optimized design (a) and the initial design (b). Both images were taken at a drive frequency $\Omega = 2\pi \cdot 996$ MHz and the microwave power was adjusted to yield $V_0 = 29$ V in both measurements. This results in the trap parameters $\omega = 2\pi \cdot 114$ MHz, $U = 30$ meV and $q = 0.32$. Clearly, the amount of electron loss is reduced for the zigzag-shaped, optimized

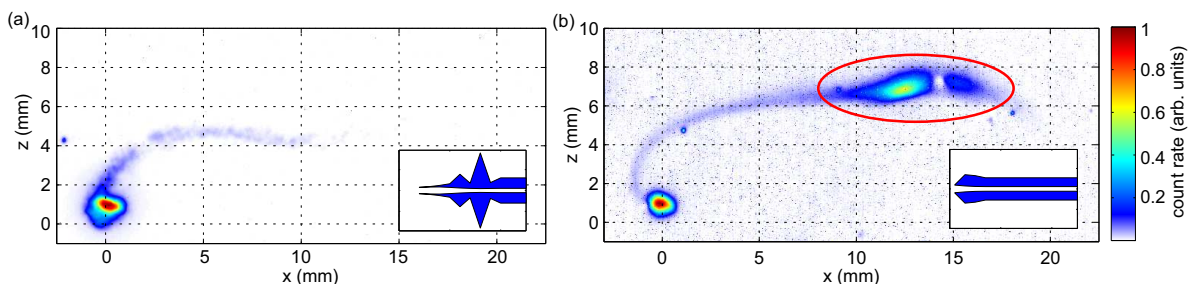


Figure 3.22: Guiding measurement with the optimized coupling structure. (a), Guiding signal with the zigzag-shaped coupling taper corresponding to the optimization result shown in Fig. 3.21(c). For comparison, (b), shows the guiding signal with old coupling taper shown in Fig. 3.21(a). Both measurements are performed at identical microwave parameters $\Omega = 2\pi \cdot 996$ MHz and $V_0 = 29$ V. Clearly, the optimized taper design features less electron loss.

coupler design in Fig. 3.22(a). Most noticeably the electron loss signal in the region $x = 10 \dots 15$ mm has fully vanished with the new coupler. This can be directly interpreted as a result of reduced fringing electric fields, which yields an improved electron injection. Electrons that are subject to large deflections during injection because of fringing electric fields become lost early after injection into the guide and are detected at larger x . We identify the signal of lost electrons highlighted by the red ellipse in Fig. 3.22(b) with electron losses that occur due to excitations during electron injection. Electrons that are lost further along their curved path on the way to the detector are detected at smaller x and spiral around the guided spot. This part of the electron loss signal is observed in the guiding signals of both coupler designs in Fig. 3.22. We attribute these losses to the large spot size and beam opening angle of the thermionic electron gun. Using the novel field emission electron gun with much better electron optical properties, we will show in Ch. 6 that guiding without any losses is possible using the optimized coupling structure, which support the interpretation that the remaining electron loss Fig. 3.22(a) is a result of the deficient beam quality of the thermionic source.

The comparison of the electron guiding signal, shown in Fig. 3.22, demonstrates that the electron injection efficiency can be significantly improved using the optimized coupling structure. Furthermore we conclude that using the zigzag-shaped, optimized coupler design, the beam quality of the thermionic source limits the electron guiding efficiency. In the following section we report on the synchronized injection of electron pulses into the guide, which also allows to reduce impact of fringing fields on the electron injection.

3.5 Phase-resolved electron guiding measurement

In this section we experimentally demonstrate synchronization of a pulsed electron source to the driving field of the microwave guide and present phase-resolved measurements of the electron guiding efficiency using the electrode design shown in Fig. 3.20(a). By these means all electrons experience the same orientation of the driving electric field and hence the impact of the microwave phase on the electron guiding efficiency can be studied. We find that for specific microwave phases the guiding efficiency is maximized allowing the electron beam a smoother passage from free space into the guiding potential.

3.5.1 Synchronous electron injection setup

In order to inject electrons at one specific phase of the microwave driving signal synchronicity between the pulsed streaking source and the microwave drive of the guide has to be established and maintained. In the following experiment this can be realized if the phase of the microwave drive $\Omega \cdot t + \Delta\phi$ and the phase of the deflection element $\Omega_{\text{defl}} \cdot t$ obey the condition $\Omega \cdot t = 2n \cdot \Omega_{\text{defl}} \cdot t$, where $\Delta\phi$ is a variable phase shift and n is an integer number.

We phase lock two analog signal generators and separately drive the microwave guide at a frequency Ω and the pulsed source at Ω_{defl} . In order to achieve synchronous electron injection, we set $\Omega = 2\pi \cdot 996 \text{ MHz}$ and $\Omega_{\text{defl}} = 2\pi \cdot 99.6 \text{ MHz}$, corresponding to $n = 5$. By inserting a variable phase shifter²³ in the microwave drive of the guide, we can shift the microwave phase of the guide relative to that of the pulsed source by a constant phase $\Delta\phi$. Figure 3.23 shows a simplified schematic of the experimental setup, which has been described in Sec. 3.1 in detail. We apply a deflection voltage $V_{\text{defl}} = 1.46 \text{ V}$

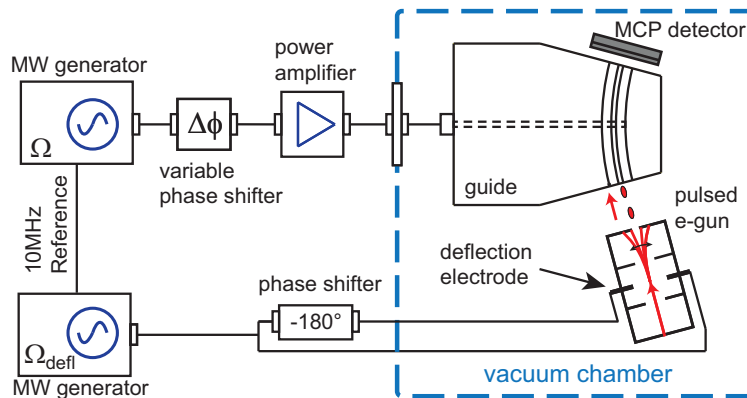


Figure 3.23: Schematic of the microwave phase-resolved measurement setup. A stable phase lock is established via the 10 MHz reference signal between two analog signal generators in order to separately drive the microwave guiding chip and the pulsed source. We insert a variable phase shifter in the signal path of the guiding chip to shift the microwave phase of the guide relative to the pulsed source. The -180° phase shifter in the signal path of the pulsed electron source yields an opposite sign of the deflection voltage V_{defl} on the upper and lower part of the deflection element.

²³ *Mini-Circuits* JSPHS-1000

to the streaking element corresponding to a transit time of 105 ps. As can be seen in Figure 3.11(b), the electron current of the pulsed streaking source reduces by about one order of magnitude when applying a deflection voltage of $V_{\text{defl}} = 1.46$ V. Here only at every fifth oscillation of the guide's microwave drive an electron pulse is injected. In future experiments it would be favorable to increase the repetition rate of the streaking source up to the driving frequency of the guide as this would allow a fivefold increase in the detected count rate. As a result of the small electron currents, acquisition times up to 4 minutes are required in the measurements described in the following. Furthermore, we made use of the active power stabilization described in Sec. 3.1.2 in order to account for a drifting microwave signal attenuation originating from the additional variable phase shifter in the microwave signal path of the guide.

3.5.2 Microwave phase-resolved guiding signals

Using the synchronized electron streaking gun we can measure guiding signals where the timing of electron pulses is controlled with respect to the driving field of the microwave guide. Figure 3.24(a) and (b) show two measured guiding signatures for $\Delta\phi = 3^\circ$ and $\Delta\phi = 185^\circ$. It can clearly be seen that the number of guided electrons as well as the number of lost electrons is strongly influenced by the phase $\Delta\phi$.

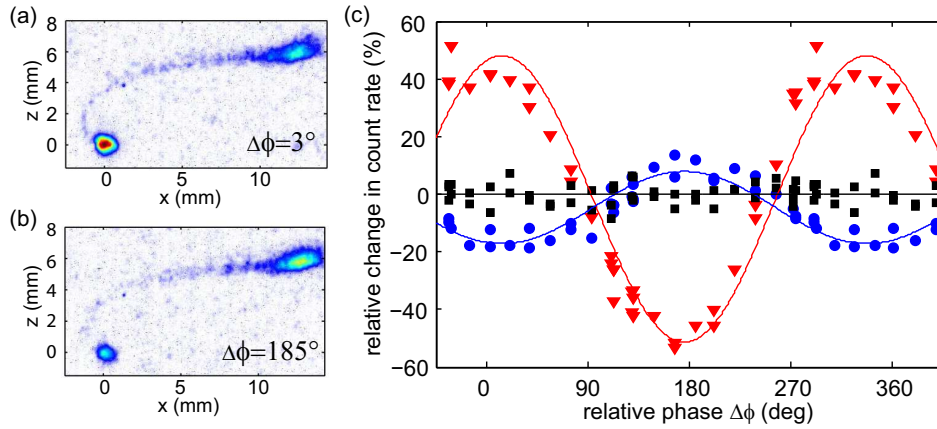


Figure 3.24: Microwave phase-resolved measurements. Electron signals are shown for $\Delta\phi = 3^\circ$, in (a), and for $\Delta\phi = 185^\circ$, in (b), where the number of guided electrons is at its maximum and minimum with respect to the microwave phase $\Delta\phi$. (c), Relative change in count rate of guided (red triangles) and lost (blue dots) electrons as a function of $\Delta\phi$ for synchronous operation of the electron gun. When the gun is operated in asynchronous mode, with $\Omega_{\text{defl}} = \Omega/(2n) + 2\pi \cdot 1$ mHz and image integration times $\gg \frac{1}{1\text{mHz}}$, we observe no change in the guided and unguided signal (black squares). Every data point is an average over 240 images with 1 s exposure time. The lines correspond to sinusoidal fits of the measured data.

In Fig. 3.24(c) a quantitative measurement of the phase dependent electron guiding efficiency is shown. The red triangles (blue dots) correspond to the relative change of the integrated count rate of guided (lost) electrons as a function of the relative phase $\Delta\phi$. This measurement shows that the injection of electrons is highly dependent on the microwave phase and hence the orientation of the electric field amplitude during injection. The two curves corresponding to the integrated guided and lost electron signals

are shifted in phase by 180° to each other. This confirms that we can increase (decrease) the electron guiding efficiency by controlling the relative phase $\Delta\phi$. Note that these observations can not be explained by a spurious loss mechanism that just occurs for certain settings. The red (blue) lines correspond to sinusoidal fits from which we infer the contrast of the modulated guided (lost) electron signal to be 50% (13%). The discrepancy in the contrast of the guided and unguided signal can be attributed to the fact that not all electrons that are lost from the guide are detected by the MCP detector. In order to verify that the above measurement relies on a phase-resolved, synchronous measurement we have carried out the exact same measurement with asynchronous phases. The result is shown as black squares in Fig. 3.24(c). No modulation is observed.

The phase-resolved measurement described above demonstrates a viable strategy to minimize the impact of unwanted fringing electric fields on the transverse electron motion after injection into the guide. However, the temporal resolution is still limited as the electron pulse duration only resolves half an oscillation of the microwave drive signal due to the large energy spread of the thermionic source. In the following we briefly discuss perspectives of important improvements of the electron guiding setup.

3.6 Next steps and future improvements

In order to combine the timing of 40 ps electron pulses with diffraction-limited electron optics, we assembled a new, home-built electron source that is based on a metal nanotip electron emitter. The appropriate electron optics comprising a focusing Einzel lens together with a quadrupole deflector and a deceleration stage is presented in Ch. 6. Particle tracking simulations at kinetic energies down to 1 eV suggest that, due to sufficiently low aberrations, focusing close to the diffraction limit should be possible with this source. As an important feature, the lens design allows optical access to the nanotip. Hence, temporal control over the electron pulses can be achieved by laser-triggered electron emission, which should allow the generation of electron pulses in the sub 100 fs range [76, 77, 78].

The guiding signal obtained for the zigzag-shaped, optimized coupling structure in Sec. 3.4.3 indicate that, due to the reduced fringing fields, the observed electron losses are mainly produced by the poor beam quality of the thermionic source. In Ch. 6 we present measurements using the field emission electron gun with highly collimated and focused electron beam with a diameter on the order of $\sim 1 \mu\text{m}$ and opening angle of $\theta \sim 1 \text{ mrad}$. As a result we observe a much more collimated guiding signal that barely contains any electron losses. This already indicates the superior properties of the field emission gun with respect to the thermionic source. However, so far the field emission gun is limited to electron energies above 5 eV and requires further improvements.

Apart from the electron gun, an important development for the adiabatic injection of electrons into the guide are electrically long microwave substrates. Taking into account traveling microwave signals for the guiding of electrons will allow to drive the guide with $\Omega = 2\pi \cdot 2.8 \text{ GHz}$ and $V_0 = 72 \text{ V}$. Currently electron guiding experiments are restricted to electrically short structures, which limits the drive frequencies to $\Omega < 2\pi \cdot 1.25 \text{ GHz}$. To this end impedance matched, electrically long guiding structures are required [20].

4 A microwave chip-based beam splitter for guided electrons

A beam splitter is the quintessential component in many modern physics experiments. The visualization of the quantum mechanical phase hinges on it. Its various realizations have enabled the observation of most fundamental physics phenomena like quantum optics experiments with photons [79], many-body interference experiments with cold atoms in optical lattices [80], neutron interferometry [81] and fundamental interference studies with heavy molecules [82], all resting on various realizations of beam splitters. Prominent among these studies are interference experiments with electrons, which have enabled groundbreaking insight into, for example, the wave-particle duality with massive particles [2, 7, 8, 5] and the Aharonov-Bohm effect [10].

A plethora of electron interferometry experiments [13] was triggered by the invention of the electrostatic biprism in 1955 [9]. It is a relatively rugged transverse beam splitting element and also serves as a workhorse in modern commercial electron microscopes that employ holographic techniques [83, 84].

In this chapter we show the concept and the experimental demonstration of a new beam splitter for slow electrons with energies in the electron-volt range, based on finely structured microwave fields. We demonstrate the splitting of a low-energy guided electron beam by means of a microwave pseudopotential formed above a planar chip substrate. Beam splitting arises from gradually transforming the transverse guiding potential for an electron beam from a single-well harmonic confinement into a double-well, thereby generating two separated output beams with 5 mm lateral spacing.

4.1 Beam splitter electrode design

As discussed in great detail in the previous chapters, the guiding of electrons above a planar microwave substrate is based on the generation of oscillating quadrupole electric fields with an oscillation frequency lying in the microwave range. Using higher orders in the multipole expansion of the electric field, more complex guiding potentials such as a double-well potential can be generated. In the following we will derive a suitable beam splitter chip electrode design to generate a pseudopotential junction, where electrons are initially injected into a quadrupole guiding potential that slowly emerges into a double-well potential along the guide. The guided electron beam is symmetrically divided by the separating minima of the double-well pseudopotential resulting in two guided output electron beams behind the beam splitter chip.

4.1.1 Ideal hexapole intersection

A detailed study on the construction of an ideal 2-dimensional pseudopotential intersection based on higher order electric fields can be found in Ref. [85]. Here we resume the analysis given in Ref. [85] to provide an intuitive understanding for the design criteria of the planar beam splitter chip.

To find the suitable electric field for the generation of a beam splitter pseudopotential, it can be expanded around the intersection point at the origin,

$$E_i = d_i + q_{i,j}r_j + \frac{1}{2}h_{i,j,k}r_jr_k + O(\mathbf{r}^3). \quad (4.1)$$

Here d_i denotes the dipole components, $q_{i,j} = \partial_j E_i$ the quadrupole terms and $h_{i,j,k} = \partial_j \partial_k E_i$ the hexapole components of the electric field. Summation over repeated indices is implied. As will be seen later, it is sufficient to consider only electric field components up to hexapole order. According to Maxwell's equations the electric field, which is related to the electric potential by $\mathbf{E}(\mathbf{r}) = -\nabla V(\mathbf{r})$, has to be irrotational, $\nabla \times \mathbf{E}(\mathbf{r}) = 0$, and divergence-free, $\nabla \cdot \mathbf{E}(\mathbf{r}) = 0$, as required by the Laplace equation $\partial_i \partial_i V(\mathbf{r}) = 0$. As a consequence, the quadrupole terms $q_{i,j}$ must be symmetric, $q_{i,j} = q_{j,i}$, and traceless, $q_{i,i} = 0$. For the hexapole terms this yields the following constraints: $h_{i,j,k} = h_{i,k,j} = h_{j,i,k}$ and $h_{i,i,j} = 0$ with $i \leq j \leq k$.

Furthermore, requiring that there are two paths $\gamma_i(\mathbf{r})$ of zero electric field, which intersect at the origin, constrains the dipole and quadrupole electric field components $d_i = q_{i,j} = 0$ and leaves a unique set of the hexapole components that give rise to a hexapole electric field of the form

$$\mathbf{E}(\mathbf{r}) = 3\alpha_X \begin{pmatrix} 2xz\cos^2(\theta) \\ -2yz\sin^2(\theta) \\ (z^2 - y^2)\sin^2(\theta) - (z^2 - x^2)\cos^2(\theta) \end{pmatrix}. \quad (4.2)$$

Here the only unknown constants remaining are the amplitude α_X and the opening angle θ , which is the angle between the zero-field paths $\gamma_i(\mathbf{r})$ close to their intersection point. In direct vicinity to the intersection point these paths lie on the curves given by

$$x = \pm \tan(\theta)y \quad \text{for } z = 0. \quad (4.3)$$

The electric field given in Eq. 4.2 describes an ideal 2-dimensional intersection based on purely hexapole electric fields. Fig. 4.1(a) shows an isopotential surface of the pseudopotential Ψ that is generated when inserting Eq. 4.2 in Eq. 2.11 with $\theta = \pi/20$. It is important to note that as a result of Maxwell's equations any hexapole intersection always consists of two incoming and two outgoing field minimum paths, often referred to as X-junction. It also implies that no ideal Y-junction can exist where a single incoming path symmetrically divides into two output paths at the intersection point. However, because of the longitudinal electron energy an X-junction electron beam splitter with equal beam splitting ratio is hard to realize as electrons would preferentially traverse the junction in a straight line, as indicated by the red arrows in Fig. 4.1(a).

A symmetric junction, very similar to a Y-junction, can be obtained from a hexapole intersection when adding a small electric field component $E_z = \alpha_H y$ in the vertical

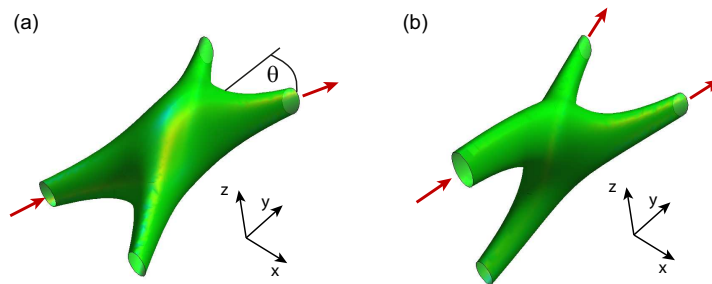


Figure 4.1: Isopotential surfaces of an ideal hexapole intersection. (a) Isopotential surface of the ideal hexapole intersection according to Eq. 4.2 with an opening angle $\theta = \pi/20$ and $\alpha_X = 1/3$. (b) When adding a vertical electric field $E_z = \alpha_H y$ the incoming zero field paths $\gamma_i(\mathbf{r})$ may be rotated into the yz -plane. Here the isopotential is plotted with $\theta = \pi/40$, $\alpha_X = 1/3$ and $\alpha_H = 0.15$.

direction. The vertical electric field effectively rotates the two incoming beam splitter paths into the yz -plane, which is shown in Fig. 4.1(b). As a result, when injecting the electron beam into one of the incoming paths the electron beam is symmetrically divided with respect to the lateral x -direction resulting in two outgoing paths. However, the presence of the additional fourth port may influence the electron trajectories in close vicinity of the beam splitter junction and in most cases this will lead to an excitation of the electron trajectories or even loss of electrons from the beam splitter pseudopotential. Because this additional port cannot be avoided, we will perform a numerical optimization of the precise shape of the beam splitter potential in the next section to minimize the influence of the additional port on the guided electrons.

In order to realize such a symmetric intersection a suitable electrode structure has to be derived that generates the required electric fields. Similar to the conformal mapping of a circular quadrupole geometry described in Sec. 2.2.1, a hexapole geometry may also be folded on a planar chip substrate. Here the six electrodes of the circular geometry give rise to seven electrodes in the planar surface-electrode design. In order to achieve a transition from a single-well harmonic confinement at the beginning of the chip to a hexapole intersection point that splits the guided electron beam, we introduce a tapered central electrode that continuously transforms the electrode pattern from five electrodes to seven electrodes. This central electrode also generates the vertical field component E_z that rotates the incoming paths into the xz -plane. Precise control over the electrode shape allows for a smooth transition of the electric field above the substrate from quadrupole to hexapole symmetry along the horizontal y -direction.

Figure 4.2 shows a top view on the beam splitter chip electrode design. The microwave signal is fed to the red electrodes, whereas the blue areas are grounded. The electric field line plots in Fig. 4.2 indicate the transition of the electric fields from quadrupole to hexapole symmetry in the vertical xz -plane. These electric field line plots are based on ideally symmetric quadrupole and hexapole fields as can be obtained from the quadrupole potential in Eq. 2.2 and the hexapole fields in Eq. 4.2. In order to obtain a suitable beam splitter potential and to reduce the influence of the unwanted beam splitter port on the guided electrons we perform a numerical optimization of the shape of chip electrodes.

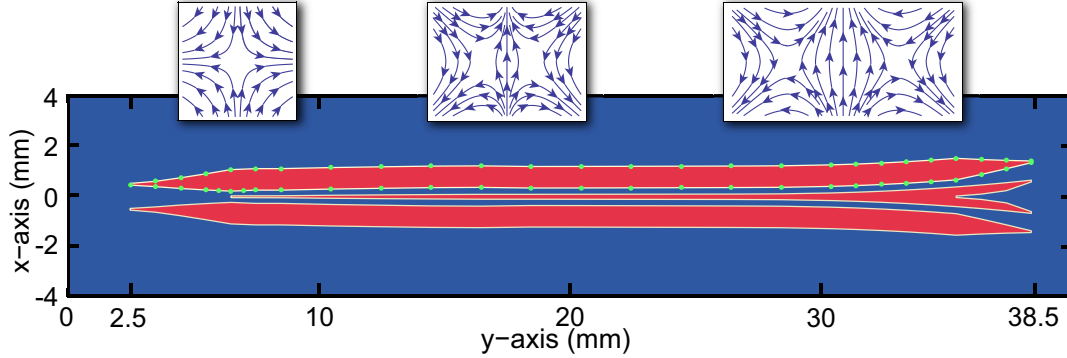


Figure 4.2: Conceptual electrode layout of the planar beam splitter chip and electric field line plots along the electrodes. The chip electrodes are shown from a top view with microwave signal applied to the red electrodes. The remaining blue area is grounded. By means of the tapered central electrode the transition of the electric fields from quadrupole to hexapole symmetry is achieved, as indicated by the electric field line plots. For clarity, the field lines of ideally symmetric quadrupole and hexapole fields are plotted here. The electrode design shown here is used as a starting point for the optimization described in Sec. 4.1.2.

4.1.2 Numerical optimization of electrode layout

In order to achieve a smooth transition from quadrupole to hexapole electric fields along the y -axis we have used the *Surface Pattern* package [74, 56, 75] to numerically optimize the shape of the chip electrodes. Electrons are injected into the guiding potential at the substrate edge and are then guided along the potential minimum path $\gamma(\mathbf{r})$ towards the beam splitter junction. Here the electron beam is symmetrically split-up and electrons follow the separating paths of the beam splitter pseudopotential.

This optimization routine uses a Nelder-Mead simplex algorithm, a built-in function in MATHEMATICA, to minimize a scalar merit function M by systematic variation of the position of a predetermined number of points (see green dots in Fig. 4.2), which parametrize the shape of the chip electrodes. Changes to the electrode shape are realized according to a planar symmetry around $x = 0$. The beam splitter electrode optimization is divided into three subsequent parts as different, competing merit functions are required at different locations along the beam splitter electrodes. The merit function M accordingly includes several terms that allow an optimization of the beam splitter potential

$$M = \int_{y_1}^{y_2} dy [a_1 \Psi(\gamma(\mathbf{r})) + a_2 |\partial_y \Psi(\gamma(\mathbf{r}))| + a_3 |\partial_z \Psi(\gamma(\mathbf{r}))| + a_4 [\omega_{z,0} - \partial_z^2 \Psi(\gamma(\mathbf{r}))] - a_5 \partial_x^2 \Psi(0, y, R_0)]. \quad (4.4)$$

The first term minimizes the value of the pseudopotential minimum along the beam splitter path $\gamma(\mathbf{r})$. The second term minimizes abrupt changes of the pseudopotential minimum along the longitudinal y -direction, whereas the vertical pseudopotential gradient is minimized by the third term. This way, unwanted excitations in the motion of guided electrons during the splitting process are reduced. The fourth component of the merit function results in a constant vertical trap frequency along the beam splitter

with an intended vertical trap frequency of $\omega_{z,0} = 2\pi \cdot 100$ MHz for a drive frequency $\Omega = 2\pi \cdot 1$ GHz, $V_0 = 30$ V and $R_0 = 450$ μm . Most importantly, the last term in Eq. 4.4 increases the lateral potential curvature along the x -direction. This term ensures efficient beam splitting by creating a lateral deflection force for electrons away from symmetry axis of the beam splitter potential. As will be shown later by means of particle tracking simulations, the lateral gradient of the beam splitter potential along the x -axis defines the strength of the beam splitting effect and limits the maximum possible longitudinal electron kinetic energy that is allowed for beam splitting. The minus sign in front of the fifth term in Eq. 4.4 results in a maximization of the beam splitter transverse curvature. The constants a_i allow to weight the different contributions to the merit function, as will be discussed in the following. The optimization of the beam splitter electrode shape is performed in three consecutive steps. For each step a set of suitable constants a_i has to be found. In fact, this was done by a brute force testing of weighting constants until a satisfactory result was obtained. Future optimizations of the electrode shape that find optimum constants a_i in a quantitative way may therefore obtained much better results.

The first step of the beam splitter electrode optimization is to provide a smooth injection from the electron source into the guiding potential. This part of the optimization is very similar to the one described in Sec. 3.4. Electrons are injected into the pseudopotential at the substrate edge at a height of 450 μm above the chip surface. In order to provide a smooth transition into the guiding potential, we optimize the coupling structure on the first 15 mm along the electrodes ($y_1 = 0$ mm and $y_2 = 15$ mm). This part of the optimization focuses on minimizing vertical gradients by choosing the coefficients a_i according to $a_1 = 10/\Psi(\gamma_0)$, $a_2 = 10/|\partial_y\Psi(\gamma_0)|$, $a_3 = 80/|\partial_z\Psi(\gamma_0)|$, $a_4 = 30/[\omega_{z,0} - \partial_z^2\Psi(\gamma_0)]$, $a_5 = 0$. Here $\gamma_0(\mathbf{r})$ is the original beam splitter path, which is obtained for the non-optimized electrode structure shown in Fig. 4.2.

In a subsequent optimization the region from $y_1 = 15$ mm to $y_2 = 30$ mm is addressed where the splitting of the electron beam arises. This part of the optimization is crucial as it includes the beam splitter intersection point. Because of the hexapole field symmetry an additional, unwanted potential minimum path converges towards the path of guided electrons at the junction and weakens the vertical confinement of the beam splitter potential. At the same time a potential gradient in the lateral x -direction forms as a result of the formation of the double-well potential. This gradient is essential in order to deflect the electron beam in the lateral direction into the separating beam splitter paths. The numerical optimization of the electrode layout in a region from $y_1 = 15$ mm to $y_2 = 30$ mm uses a merit function M according to the coefficients $a_1 = 100/\Psi(\gamma_0)$, $a_2 = 0$, $a_3 = 10/|\partial_z\Psi(\gamma_0)|$, $a_4 = 10/[\omega_{z,0} - \partial_z^2\Psi(\gamma_0)]$ and $a_5 = 10/\partial_x^2\Psi(0, y, R_0)$.

Finally, the remaining part of the beam splitter electrodes is optimized. This last segment separates the split-up electron beams and guides them towards the end of the beam splitter chip where the electrons are released into free space. The corresponding optimization of the electrode pattern minimizes the pseudopotential minimum and pseudopotential gradients along the y - and z -direction along the path of guided electrons. Here, $a_1 = 20/\Psi(\gamma_0)$, $a_2 = 20/|\partial_y\Psi(\gamma_0)|$, $a_3 = 80/|\partial_z\Psi(\gamma_0)|$, $a_4 = 0$ and $a_5 = 0$.

Fig. 4.3(a) shows the numerically optimized electrode design of the planar beam splitter chip [86] together with electric field line plots in the transverse xz -plane at three locations along the planar electrode structure. The electric field line plots have been

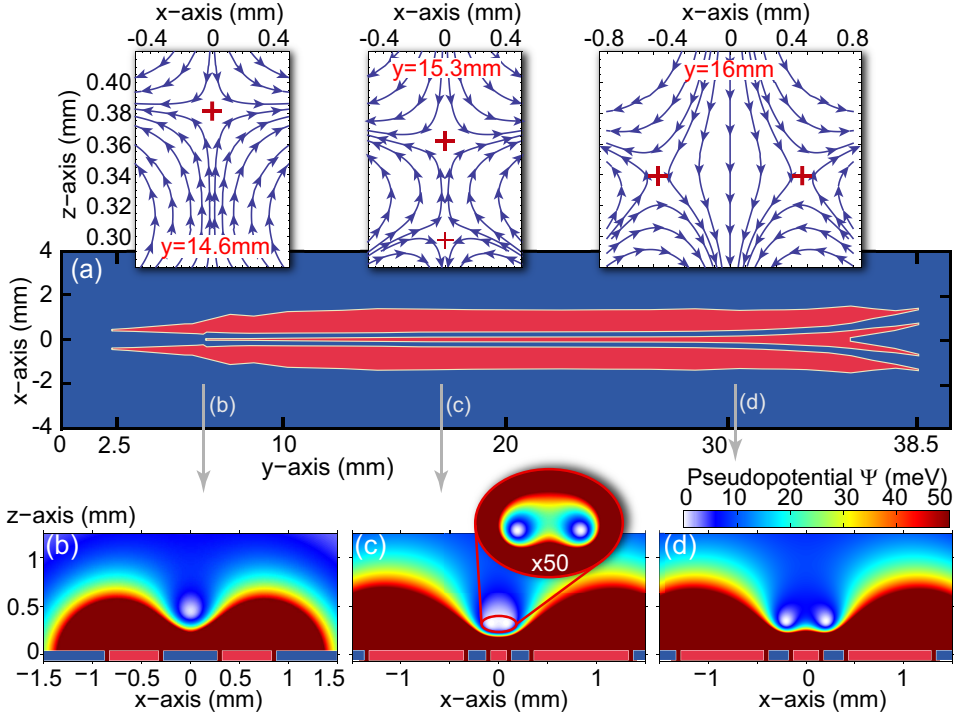


Figure 4.3: Numerically optimized electrode design of the planar beam splitter chip and pseudopotential simulations. (a), Optimized beam splitter electrode design obtained from the numerical optimization. (b), Cut through the electrode plane at $y = 6.5$ mm. The pseudopotential minimum forms at a height of $450 \mu\text{m}$ above the substrate providing harmonic confinement. (c), At $y = 17$ mm the additional central electrode, with a width of $160 \mu\text{m}$, leads to the creation of a double-well pseudopotential with a separation of $150 \mu\text{m}$ between the minima. A fourfold magnified zoom-in is shown in the inset with a 50 times amplified color code. By increasing the width of the center electrode the separation of the double-well minima is gradually increased. (d), At $y = 30$ mm the central electrode is $260 \mu\text{m}$ wide, leading to a separation of the minima of $400 \mu\text{m}$. The microwave parameters in the simulation are $\Omega = 2\pi \cdot 1 \text{ GHz}$ and $V_0 = 16 \text{ V}$. (e), (f), Electric field line plots that are created by the optimized electrode design in (a) at $y = 6.5$ mm and $y = 17.5$ mm.

obtained from simulating the electric field that is created by the planar electrode structure. At a position of $y = 14.6$ mm along the chip, the electric field is governed by a strong quadrupole component leading to the creation of a saddle point in the center, as indicated by the red cross. As a result, the transverse pseudopotential forms a minimum at the saddle point. A slight change in the electrode geometry allows us to increase the hexapole component of the electric field along the chip electrodes. The hexapole field gives rise to an additional saddle point that continuously approaches the saddle point, which forms the guiding potential minimum, from the chip surface. This is indicated in the field line plot at $y = 15.3$ mm. Further along the chip, both saddle points converge, intersect and subsequently depart in the transverse direction as shown in the field line plot beyond the intersection point at $y = 16$ mm. In Fig. 4.3(b) a simulation of the pseudopotential formed by the quadrupole electric fields above the planar five-wire electrode geometry at $y = 6.5$ mm is shown. The pseudopotential further along the chip electrodes

at $y = 17$ mm is shown in Fig. 4.3(c). As required, the additional central signal electrode leads to the creation of a double-well pseudopotential. By adjusting the width of the central electrode the separation of the double well can be designed. The separation of the double-well minima is $150 \mu\text{m}$ in Fig. 4.3(c) and $400 \mu\text{m}$ in Fig. 4.3(d), which shows the pseudopotential in a cut through the electrode plane at $y = 30$ mm. At $y = 17$ mm and $y = 30$ mm, the barrier height between the wells is 0.5 meV and 11.5 meV , respectively.

The optimized beam splitter pseudopotential with $\Omega = 2\pi \cdot 1 \text{ GHz}$ and $V_0 = 16 \text{ V}$ is shown in Fig. 4.4. In Fig. 4.4(a) the pseudopotential is plotted in the xy -plane. As the height of the pseudopotential minimum z_{min} varies along the chip electrodes, this plot is obtained by calculating z_{min} for every point along y and then plotting $\Psi(x, y, z_{min}(y))$. Similarly, the pseudopotential in the zy -plane is plotted in Fig. 4.4(b) by calculating $x_{min}(y)$ and plotting $\Psi(x_{min}(y), y, z)$. Because of fringing electric fields close to the substrate edge, the potential minimum is about 1.5 meV on the first 7 mm along the chip electrodes until quadrupolar fields are fully developed leading to a field null along the guide. Further along the electrodes, the intersection point of the beam splitter forms at about $y = 16 \text{ mm}$. Here, an additional potential minimum path converges towards the beam splitter path from the substrate surface, as can be seen in Fig. 4.4(b). As described in Sec. 4.1.1, the additional field minimum path is fundamentally related to hexapole symmetry of the electric field and can not be avoided. As a result, this path deteriorates the guiding potential in the vertical z -direction and weakens the confinement. As a consequence the pseudopotential minimum, which initially is at $z = 450 \mu\text{m}$, approaches the substrate down to $z = 350 \mu\text{m}$ at the beam splitter junction. Therefore, the trap frequency as well as the confinement are increased according to $\propto 1/R_0^2$, as can be seen from Eq. 2.15 and Eq. 2.16. However, it should be noted that as a result of the changing field symmetry along the guiding chip, from quadrupole to hexapole symmetry, the effective quadrupole strength η and the relative potential depth u vary along the y -direction. As described in Sec. 2.2, this results directly in a changing of the trap parameters ω , U and q along y . For example, right at the intersection point the electric field obeys a pure hexapole symmetry and therefore the effective quadrupole strength η goes to zero and similarly the trap frequency ω . In the remainder of this chapter we always specify the trap parameters ω , U and q at the position $y = 10 \text{ mm}$ where the quadrupolar fields are most developed. At $y = 10$ we find $\eta = 0.205$, $u = 0.007$ and $R_0 = 444 \mu\text{m}$. For the typical drive parameters that we use in the experiments later, $\Omega = 2\pi \cdot 1 \text{ GHz}$ and $V_0 = 16 \text{ V}$, this corresponds to a trap frequency $\omega = 2\pi \cdot 52 \text{ MHz}$, a pseudopotential depth $U = 10 \text{ meV}$ and $q = 0.15$.

From $y = 20 \text{ mm}$ to $y = 30 \text{ mm}$ the splitting region is established where the electron beam is smoothly separated into the linearly separating beam splitter paths. Further along the chip electrodes an increasing separation of the split-up electron beam is achieved by the rapidly increasing distance between the beam splitter paths.

The so optimized beam splitter electrode design is based on the minimization of the merit function M as described above. However, the merit function contains several competing terms, which makes it hard to obtain a quantitative understanding of the quality of the chip design that results from the optimization. A more direct and intuitive understanding can be obtained from particle tracking simulations. In order to confirm if the optimized beam splitter electrode design provides stable beam splitting and whether it

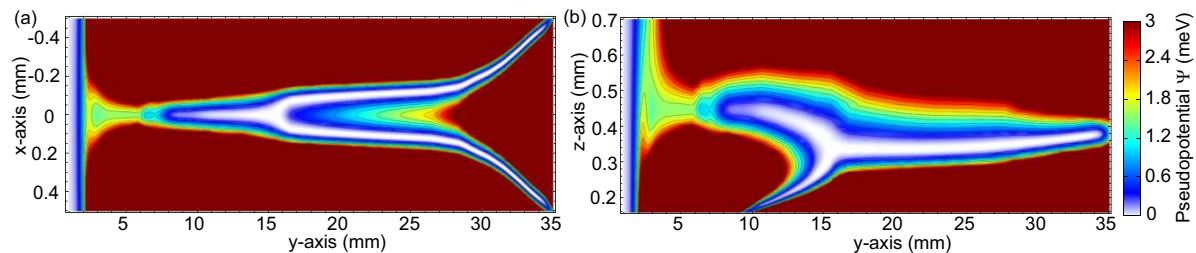


Figure 4.4: Pseudopotential of the optimized beam splitter design. (a), Color plot of the pseudopotential Ψ in the xy -plane parallel to the chip surface. As the height of the pseudopotential minimum z_{min} varies along the chip electrodes this plot is obtained by calculating z_{min} for every point along y and then plotting $\Psi(x, y, z_{min}(y))$. (b) Color plot of Ψ in the vertical zy -plane. Here $x_{min}(y)$ is inserted for every position along y . The drive parameters in the simulations are $\Omega = 2\pi \cdot 1 \text{ GHz}$ and $V_0 = 16 \text{ V}$.

is suited for the experimental realization, we simulate electron trajectories with experimentally achievable microwave parameters, realistic electron energies and also include the electron optical properties of the thermionic electron gun. This thermionic electron gun is also employed in the experiments and is described in Sec. 3.1.3.

4.2 Particle trajectory simulations

We perform classical particle tracking simulations taking into account the oscillating electric field of the optimized beam splitter chip. The simulations gather 1000 particle trajectories in total that are released at the substrate edge $y = 0 \text{ mm}$. More specifically, 100 rays are homogeneously distributed on a disk with a diameter of $100 \mu\text{m}$ and trajectories are released at ten different instants in time with respect to the phase of the microwave electric field. This allows us to study if the beam splitting depends on the phase of the microwave drive. The planar symmetry of the beam splitter potential is also reflected in the electron trajectories, which obey the same symmetry when being released at positions along the negative or positive x -axis.

We simulate electron trajectories with microwave drive parameters of $\Omega = 2\pi \cdot 1 \text{ GHz}$ and $V_0 = 16 \text{ V}$. Fig. 4.5(a) shows a top view on the simulated electron trajectories in the xy -plane. Clearly, the electrons perform oscillations after injection into the guiding potential with a spatial period of 14 mm corresponding to a trap frequency of $\omega = 2\pi \cdot 50 \text{ MHz}$ at an electron kinetic energy of 1.5 eV . In the splitting region from $y = 20 \text{ mm}$ to $y = 30 \text{ mm}$ the beam becomes symmetrically divided in the lateral x -direction. The color scale illustrates the initial lateral displacement of the electrons along the x -axis. The chip electrodes are indicated in light blue. In Fig. 4.5(b) the same trajectories are plotted in the vertical zy -plane. As can be seen, the electrons follow the beam splitter path $\gamma(\mathbf{r})$ that bends down towards the substrate when approaching the beam splitter junction at $x \sim 16 \text{ mm}$. Apparently, electrons released closest to the symmetry axis of the beam splitter potential [blue lines in Fig. 4.5(b)] are preferentially lost from the beam splitter potential in the vertical z -direction. This can be understood by considering the extreme case of an electron traveling perfectly along the symmetry axis of the beam splitter potential. Such a classical trajectory does not encounter any potential gradient in the

lateral x -direction and therefore no deflecting force. As a result, this trajectory cannot follow the pseudopotential minimum paths of the separating double wells and is only deflected away perpendicularly to the substrate. For this reason electrons that propagate closest to the symmetry axis may become lost from the beam splitter potential. Using quantum mechanical simulations we will show in Sec. 4.5 that *lossless*, adiabatic splitting of an electron beam can be achieved by means of an optimized beam splitter potential.

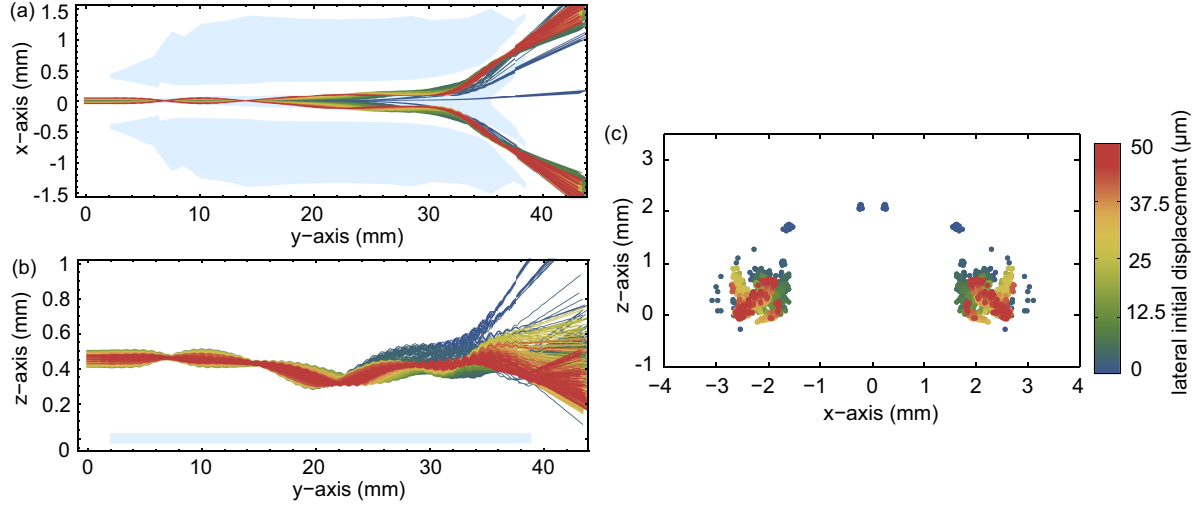


Figure 4.5: Electron trajectory simulations of the beam splitting with $E_{\text{kin}} = 1.5$ eV. (a), Electron trajectories in the xy -plane. The electrons perform a secular oscillation on the first 16 mm along the guide. At the beam splitter junction the beam becomes symmetrically divided and two split-up, guided beams are obtained. (b), Electron trajectories in the vertical zy -plane. Only trajectories that were released closest to the symmetry axis (blue lines) become lost in the vertical z -direction. (c), Simulated detector signal obtained from the trajectories in (a) and (b). The trajectories are simulated with $\Omega = 2\pi \cdot 1$ GHz and $V_0 = 16$ V corresponding to $\omega = 2\pi \cdot 52$ MHz, $U = 10$ meV and $q = 0.15$.

From the particle tracking simulations we can deduce the position of the electron trajectories when being detected at the MCP detector. Fig. 4.5(c) shows a simulated beam splitter signal. It comprises two guided components around $x = 2.5$ mm and $x = -2.5$ mm, which contains electrons that successfully followed the beam splitter paths. In between these components there are several trajectories that were lost from the guiding potential. Again the color scale shows that electrons that are released closest to the symmetry axis (blue dots) become primarily lost. For these specific microwave parameters and kinetic electron energy of 1.5 eV we find that all trajectories with an initial lateral displacement $x_0 > 650$ nm are successfully guided by the beam splitter potential. We also find that the microwave phase does not significantly influence the beam splitting process. Analyzing the phase dependence of trajectories that were released with different microwave phases but at the same initial position, we find that they all end up within a small area of the simulated signal, which is significantly smaller than the area of the guided components shown in Fig. 4.5(c). As a result, it is found that the initial position of the electrons within the beam almost fully determines the path taken by electrons within the beam splitter potential and the microwave phase has only a minor influence

on the trajectories. This is an important finding, as a strong microwave phase dependence of the trajectories would result in a phase dependent detector signal, similar to microwave phase effects described in Sec. 3.3. However, in an interference measurement, where the two output beams are overlapped on a detector behind the beam splitter, the signal would be integrated over all phases and, hence, lead to a reduced fringe contrast or even fully wash out the interference pattern.

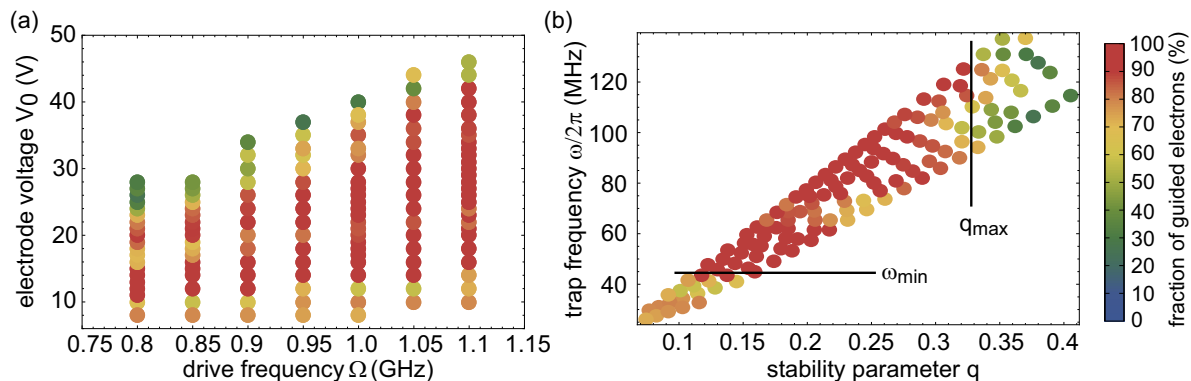


Figure 4.6: Simulated stability plots of the beam splitting with $E_{\text{kin}} = 1.5 \text{ eV}$.

(a), Stability diagram of electron beam splitting as a function of the drive parameters Ω and V_0 . The color scale depicts the fraction of guided electrons and indicates the region of stable splitting. (b), Stability diagram from the same simulations as a function of the trap parameters ω and q . The specific values of the trap parameters vary along the chip electrodes and are given at a position $y = 10 \text{ mm}$ here. The area stable splitting is restricted to trap frequencies larger than $\omega_{\text{min}} = 2\pi \cdot 45 \text{ MHz}$ and a stability parameter smaller than $q_{\text{max}} = 0.33$.

In order to investigate the efficiency of the beam splitting with respect to the microwave drive parameters we have simulated electron trajectories for varying Ω and V_0 . In Fig. 4.6(a) the color scale shows the ratio of the electrons ending up in the guided components and the number of lost electrons as a function of the microwave parameters at an electron energy of 1.5 eV . Accordingly, red dots correspond to a large fraction of electrons ending up in the split-up components, whereas green dots indicate large electron loss from the beam splitter potential. Clearly, the region of stable splitting increases for larger Ω . However, even at $\Omega = 2\pi \cdot 800 \text{ MHz}$ stable beam splitting is observed in the simulations.

The detailed structure of the stability plot can be more intuitively understood as a function of the trap parameters q and ω , as shown in Fig. 4.6(b). The area of stable beam splitting is mainly restricted to a region with $\omega > 2\pi \cdot 45 \text{ MHz}$ and $q < 0.33$. Generally, a large trap frequency ω is favorable for the splitting process as this results in a larger beam splitter curvature of the pseudopotential and hence stronger deflecting forces at the beam splitter junction. Moreover, small stability parameters are important to achieve smooth injection of the electron into the beam splitter potential (see detailed discussion in Sec. 3.3). For large q , electrons perform an excited oscillatory motion when reaching the beam splitter junction and are further excited by the approaching fourth port of the pseudopotential. As a result, for a stability $q > q_{\text{max}}$, electrons are lost from the beam splitter potential.

With regard to the experimental implementation we can deduce from Fig. 4.5(a) that the beam splitter microwave chip should support microwave frequencies in a range larger than 800 MHz and that simultaneously voltage amplitudes above 15 V are required for stable splitting. In the following subsection the realization of such a beam splitter microwave substrate is described.

4.3 Microwave design of the beam splitter chip

The electron beam splitter is implemented on a planar microwave chip design that was manufactured by a commercial supplier¹. It consists of a 0.76 mm thick microwave compatible Rogers RO4350B laminate coated with a 20 μm layer of gold-plated copper. The fabrication of the tapered central electrode that creates the transition from quadrupole to hexapole electric fields above the surface of the substrate requires a photo-lithographic process to achieve small isolating gaps with precise and smooth edges. Using the photo resist as mask, the electrodes are then defined by chemical etching of 50 μm wide gaps along the electrode contours into the metal layer. Furthermore, the diameter of the plated through-hole that feeds the microwave signal from the backside of the chip to the central electrode on the top side has to be significantly smaller than the width of the electrode, which is 100 μm wide. To this end, the through-holes are fabricated in two consecutive steps. First, holes with a diameter of 200 μm are drilled from the backside just 500 micron deep. The remaining 260 μm thick substrate is laser-drilled yielding a hole diameter of 20 μm at the top side of the microwave substrate.

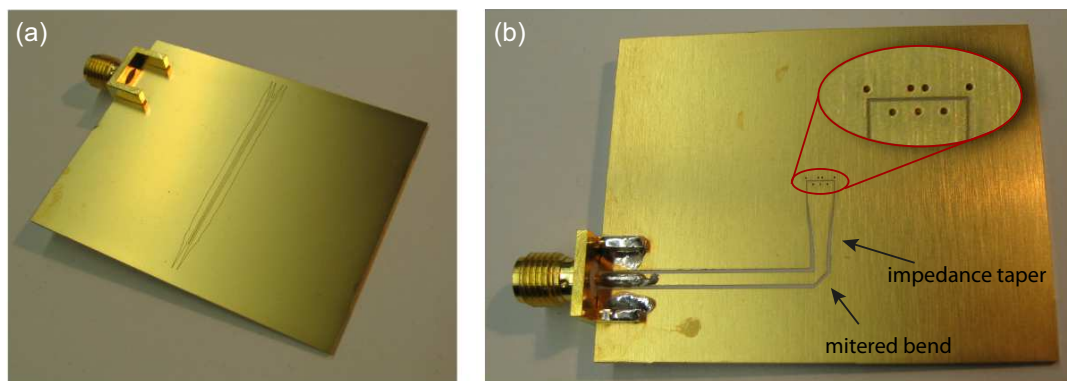


Figure 4.7: Electron beam splitter microwave substrate. (a), Top side of the microwave substrate comprising the numerically optimized beam splitter electrodes. (b) Back side of the chip showing the microwave feeding line with the mitered bend and impedance taper for improved frequency response. The inset shows a zoom on the plated through holes with a diameter of 200 μm on the backside. They transmit the signal from the feeding line to the beam splitter electrodes on the top side.

Compared to the guiding substrates presented in Sec. 3.1.1 two important improvements have been incorporated in the feeding coplanar waveguide (cpw) structure on the back side of the chip. In order to symmetrically feed all electrodes, the feeding cpw comprises a 90° mitered bend, as shown in Fig. 4.7(b). By these means the last

¹Optiprint AG, Auerstrasse 37, CH-9442 Berneck, Switzerland, www.optiprint.ch

third of the feeding cpw is aligned parallel to the beam splitter electrodes on the top side and all electrodes are fed symmetrically. As a second improvement, a triangular impedance taper was implemented in the cpw layout. This is required as the geometry of the guiding electrodes is optimized in order to generate the required electric fields for electron guiding and typically results in a characteristic impedance of the electrode structure of $Z_0 = 15\ \Omega$. On the other hand, we use a standard microwave generator with a $50\text{-}\Omega$ -matched output as well as $50\text{-}\Omega$ SMA connectors to transmit the microwave signal onto the guiding chip. In order to avoid reflections of the microwave signal at impedance discontinuities, the impedance taper has been implemented in the feeding cpw. Figure 4.7(b) shows the implementation of a triangular impedance taper from $50\ \Omega$ down to $25\ \Omega$ [58]. This taper is restricted to $25\ \Omega$ because of the limited space on the backside of the chip. A taper down to $15\ \Omega$ would exceed the length of the chip.

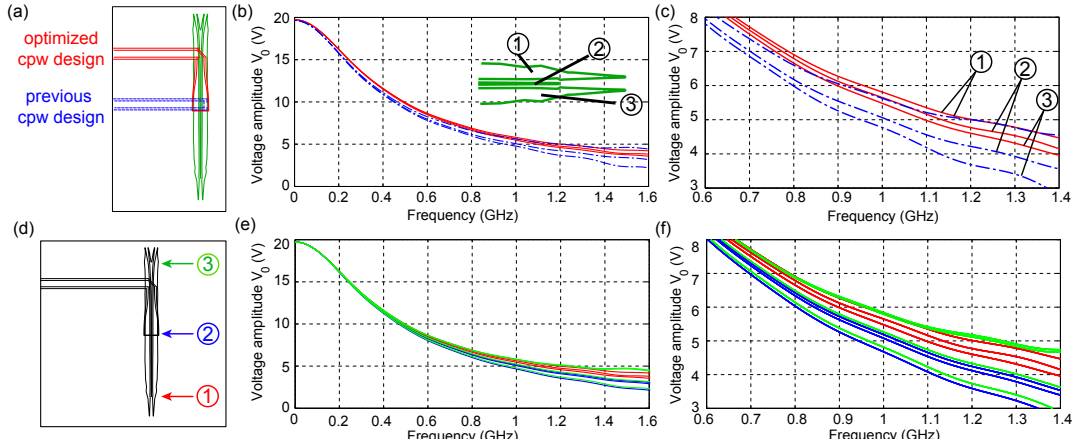


Figure 4.8: Microwave simulations of the beam splitter chip's frequency response.

The frequency response of the microwave chip is compared for two different feeding cpw designs. (a), Sketch indicating both cpw designs that are compared in the simulations. The optimized layout of the microwave feeding line comprising an impedance taper and a mitered bend is drawn in red. The cpw design used in previous experiments is indicated by the blue dashed lines. (b), Microwave voltage amplitudes V_0 on the three signal electrodes of the beam splitter chip at $y = 7\ \text{mm}$. The solid red lines corresponds to the simulation using the optimized cpw design, whereas the blue dashed lines correspond to the previous design. (c), shows a zoom of (b) in a frequency range from 0.6 to 1.4 GHz. The variation of V_0 across the signal electrodes is reduced to below 6% for the optimized feeding line. From the same simulations we obtain the microwave voltage amplitude on the signal electrodes (for the optimized cpw design) at three different locations along the chip. (d), Sketch indicating the positions where the microwave voltages, shown in (e), are deduced from the simulation. At every location the voltage on the three chip electrodes is measured. (e), The red lines correspond to V_0 taken at $y = 7\ \text{mm}$, the blue lines at $y = 20\ \text{mm}$ and the green lines at the end of the chip at $y = 36\ \text{mm}$. (f), shows a zoom of (e).

We have used a high frequency time domain simulation software² to simulate the frequency response of the beam splitter chip. First we want to investigate the performance of the feeding cpw design that we have implemented on the beam splitter microwave chip.

²CST Microwave Studio

The sketch in Fig. 4.8(a) shows the two different feeding cpws that have been compared in the simulation. The cpw design that is incorporated on the beam splitter chip is indicated in red. It comprises an impedance taper and a 90° mitered bend. As a result of the mitered bend, the last third of the cpw is oriented parallel to the chip electrodes leading to a symmetric feeding of the beam splitter electrodes. For comparison, the feeding line that was incorporated in previous chip designs is indicated by the dashed blue lines. It has $50\ \Omega$ impedance along its entire length and connects the electrodes at a right angle, which may result in an asymmetric feeding of the chip electrode that is on the far side of the cpw with respect to the electrode that is on the side from which the cpw approaches. Figure 4.8(b) shows the result of the microwave simulation in a frequency range up to 1.6 GHz with an injected microwave power of $P = 1\ \text{W}$. The resulting microwave voltage amplitude V_0 on the electrodes is plotted against the microwave frequency. The red lines correspond to a simulation with the optimized cpw design, whereas the blue dashed line corresponds to the previous design [as shown in Fig. 4.8(a)]. In both simulations the frequency response is measured at $y = 7\ \text{mm}$ and on all three microwave signal electrodes, which are labeled as electrodes (1), (2) and (3) in the inset to Fig. 4.8(b). Figure 4.8(c) shows a zoomed area of Fig. 4.8(b). The optimized feeding line (red lines in the figure) clearly results in a reduced voltage variation across the chip electrodes, which is observed when comparing the obtained voltages on electrode (1), (2) and (3). From Fig. 4.8(c) we deduce that for the cpw oriented vertically to the signal electrodes the variation of the electrode voltages on the three signal electrodes amounts to 17% at a frequency of 1 GHz. We obtain the highest voltage of 5.7 V for electrode (1), which is on the far side of the cpw, while the voltage on electrode (2), the center electrode, is 5.1 V and for the electrode (3) on the cpw side 4.8 V. The optimized feeding cpw design with the last third oriented parallel to the chip electrodes features a symmetric feeding of the beam splitter electrodes, which reduces this voltage asymmetry to below 6%. This reduction of the voltage asymmetry in the lateral dimension is important as different voltage amplitudes at a given y -position across the microwave electrodes will deteriorate the simulated beam splitter potential, described in Sec. 4.1.2, and might result in an asymmetric splitting of the electron beam.

Similarly, we can deduce the voltage amplitude at different positions in the longitudinal direction along the chip electrodes. The chip electrodes are $L = 37\ \text{mm}$ long and comparable in length to one quarter of the microwave wavelength of about $\lambda/4 = 50\ \text{mm}$ at 1 GHz. As a consequence, the microwave chip can be considered as electrically short and a standing voltage signal is established on the electrodes. However, as L is similar to $\lambda/4$ a voltage drop from the termination of the chip electrodes towards the center of the chip may be expected. Figure 4.8(d) indicates the three positions along the chip electrodes where the voltage amplitudes V_0 have been deduced from the simulation. The voltage amplitudes V_0 that are measured on the three electrodes at the different positions along the chip are shown in Fig. 4.8(e). The red lines correspond to the microwave voltage amplitudes at Pos. (1) for $y = 7\ \text{mm}$, the blue lines correspond to V_0 at Pos. (2) in the chip center at $y = 20\ \text{mm}$ and the green lines are measured at Pos. (3) towards the end of the electrodes at $y = 36\ \text{mm}$. Fig. 4.8(e) shows a zoom-in of (d) in the frequency range that is of interest for the beam splitting experiment. We find that the voltages measured at the center of the chip, which correspond to the blue lines, are smaller than

the measured voltages at the start [red lines, Pos. (1)] and the end [green lines, Pos. 3] of the chip. This effect can be attributed to the voltage drop arising from the comparable length of the chip electrodes to one quarter wavelength. Furthermore, we find that the variations of the voltages measured at different positions along the chip are comparable to the lateral variation of the voltages on the three electrodes. At this point, we can not give quantitative explanation of the specific voltage variations observed in the simulations. In order to obtain a better understanding, a measurement of the frequency response of the beam splitter microwave substrate (as described in Sec. 3.1.2) has to be performed in the future. So far, this was experimentally not possible as no suitable tip of the Picoprobe high impedance probe was available. For such a measurement one will need a custom high impedance probe that matches the geometry of the beam splitter electrodes.

The stability diagram, shown in Fig. 4.5(a), indicates the regions where stable electron beam splitting is expected from particle tracking simulations. Accordingly, voltage amplitudes V_0 in the range from 15 V to 35 V are required in a frequency range from $\Omega = 2\pi \cdot 800$ MHz to $\Omega = 2\pi \cdot 1100$ MHz to experimentally access this stable region. The microwave simulations are performed for an injected microwave power $P = 1$ W. In the experiment, we achieve an amplified microwave power of about 100 W. Taking into account the typical attenuation of the microwave equipment and cables of 2.2 dB, we can inject a microwave power of ~ 60 W to the beam splitter chip. The achievable voltage amplitude V_0 scales with $\propto \sqrt{P}$ resulting in a factor of $\sqrt{60} = 7.75$ in V_0 as compared to the microwave simulations. Scaling the V_0 obtained from the simulation accordingly, we can achieve voltages up to 35 V for microwave frequencies in a range up to 1.03 GHz, whereas 15 V can be obtained in the full range of the microwave simulation.

4.4 Demonstration of electron beam splitting

The previous sections described the essential steps in designing a suitable microwave chip for the demonstration of on-chip electron beam splitting. The experimental demonstration of the electron beam splitting described in the following represents a first and decisive step towards guided electron interferometry integrated on a planar microwave chip. Figure 4.9 shows a photograph of the experimental setup employed for the demonstration of electron beam splitting. A thermionic electron source generates a beam of slow electrons that is injected into the guiding potential above the surface of the planar microwave beam splitter chip. Electrons are guided in the beam splitter potential along the chip electrodes and are detected on the MCP electron detector that is placed behind a copper shield at the end of the substrate. Successful beam splitting is detected if two guided and spatially separated beams are observed on the detector screen.

4.4.1 Experimental beam splitter signal

We use the thermionic electron gun described in Ch. 3 for the beam splitter experiment. It reliably generates an electron beam with kinetic energies ranging from 1 to 10 eV and beam currents on the order of several ten femtoamperes. For the experiments described in the following, the streaking element has been removed to boost the electron count

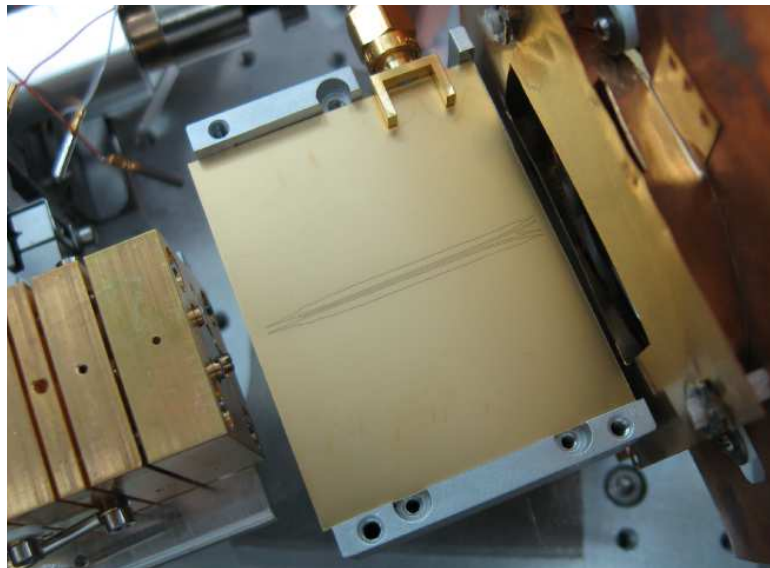


Figure 4.9: Photograph of the experimental setup employed for electron beam splitting. The thermionic electron source (left) generates a beam of slow electrons that is injected into the guiding potential above the surface of the beam splitter chip (center). Electrons travel along the chip electrodes and are detected on the MCP electron detector (right, hidden behind copper shield).

rate. The beam is collimated using two apertures resulting in a full opening angle of 14 mrad ($= 0.8^\circ$) and a spot diameter of about $100 \mu\text{m}$ at the guide entrance. Electrons are injected into the guiding potential and propagate along the beam splitter chip. They leave the guiding chip at $y = 40 \text{ mm}$ and are detected on a microchannel plate (MCP) electron detector after traveling 10 mm in free space. Images of the phosphor screen behind the MCP are recorded by a CCD camera.

The experiments are performed with a drive frequency of $\Omega = 2\pi \cdot 990 \text{ MHz}$ and an on-chip microwave power of 4.3 W . Taking into account the simulated frequency response of the beam splitter electrode layout this results in a microwave voltage amplitude of $V_0 \approx 16 \text{ V}$. It should be noted, however, that after testing various beam splitter microwave chips we observed that not all of the substrates showed a consistent frequency response. For this reason, the values given for V_0 are only a rough estimate. In future experiments a direct measurement of the frequency response of the beam splitter substrate will allow us to determine V_0 experimentally, which will also make the comparison between particle trajectory simulations and the measured signal more reliable.

Fig. 4.10(a) shows the detector signal recorded for $E_{kin} = 1.5 \text{ eV}$ and the microwave parameters given above. We clearly observe an electron signal with two symmetrically split up components, with a separation of 5 mm . These two components are detected as collimated spots on the detector screen illustrating that the electrons are guided until they reach the end of the beam splitter chip. In contrast, electrons that are lost from the beam splitting potential during the beam splitting process are detected as a more diffuse signal. This faint loss signal is detected in between the two guided components. The fraction of guided electrons comprises 80% of all the detected electron signal. Fig. 4.10(b) shows the simulated electron signal for comparison. It is in excellent agreement with the

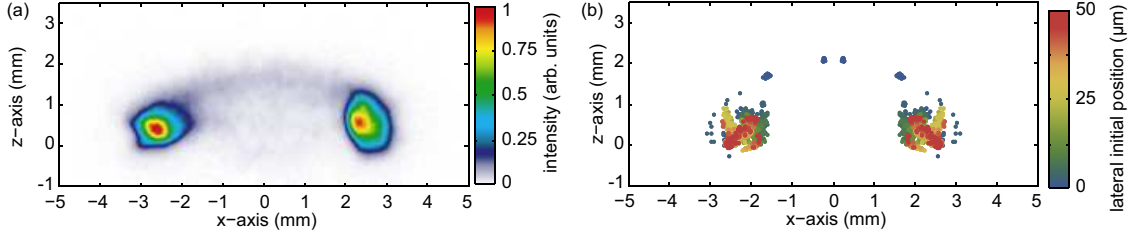


Figure 4.10: Experimental (a) and simulated (b) detector signal of the split electron beam. (a), Experimental electron signal. Clearly two beams are visible containing 80% of all detected electrons with $E_{kin} = 1.5$ eV. A faint signal of lost electrons is also detected between $x = -1.5 \dots 1.5$ mm. The color scale depicts the intensity of the raw CCD image. (b) Simulated beam splitter signal based on trajectory simulations. All signatures including the position and size of the output beams and the electron loss are reproduced. The color scale indicates the absolute value of the initial displacement of the electron trajectories from the x -axis. The experiment as well as the simulations have been performed with $\Omega = 2\pi \cdot 990$ MHz, $V_0 = 16$ V and $V_C = -0.17$ V.

experimentally observed beam splitter signal. The position and size of the output beams as well as the electron loss are reproduced.

For $V_0 = 16$ V we find a pseudopotential depth at $y = 10$ mm of $U = \Psi(0, 10, z_{max}) - \Psi(0, 10, z_{min}) = 10.33$ meV with $z_{min} = 0.445$ mm and $z_{max} = 0.96$ mm from the simulation. Here, z_{min} corresponds to the height above the chip surface where the minimum in Ψ forms, whereas z_{max} corresponds to the height of the maximum value of Ψ along the vertical direction of weakest confinement. Furthermore, in the experiment we apply a static negative voltage $V_C = -0.17$ V to a metal electrode, which is located at a height of 10 mm above the substrate and covers the entire microwave chip. The voltage V_C produces a static linear electric potential Ψ_{static} in the vertical z -direction that strengthens the electron confinement by $U_{dc} \approx \Psi_{static}(z_{max}) - \Psi_{static}(z_{min}) = 8.8$ meV. Effectively, the confinement in the z -direction is given by the sum of the static linear potential $\Psi_{static}(z)$ and the vertical pseudopotential $\Psi(x, y, z)$ with potential depth U . Hence, for $V_C = -0.17$ V, the total vertical confinement is given by $U + U_{dc} = 19.13$ meV.

The experiment is performed using the thermionic electron source with large electron beam diameter of about $100 \mu\text{m}$ and the full beam divergence angle of ~ 14 mrad, which is orders of magnitudes larger than required for the injection into low-lying motional quantum states of the guiding potential. Consequently, the dynamics of electrons in the guiding potential and during beam splitting is well captured by classical trajectory simulations. To investigate the classical dynamics of guided electrons within the beam splitter potential we study the dependence of the beam splitting process on the initial position of the electron source by comparing particle tracking simulations with experimental measurements.

4.4.2 Dependence of beam splitting on electron source position

We simulate electron trajectories for a centered and a displaced electron source to study the dependence of the beam splitting signal on misalignment of the electron source. Fig. 4.11(a) shows the result of the particle tracking simulations for three different

locations of the electron source along the x -direction. The simulation as well as the corresponding measurements are performed with $E_{kin} = 1.5$ eV and $V_0 = 16$ V. The drive frequency in the simulations was set to $\Omega = 2\pi \cdot 1$ GHz and the measurements were performed with $\Omega = 2\pi \cdot 1.082$ GHz. For a centered electron beam the trajectories (drawn in red) become symmetrically separated in the region from $y = 20$ mm to 25 mm. Electrons that are released at a positive (negative) x -position end up in the output beam at positive (negative) x -values. In contrast, for an electron source displaced about $125 \mu\text{m}$ along the positive or negative x -direction all trajectories of the beam (drawn in green and blue) end up in the same output port at negative or positive x -values, respectively. The initial lateral displacement of the trajectories sets the potential energy of the transverse electron oscillation. For the initially displaced beam the potential energy of the electron oscillation is larger and electrons may cross the potential barrier in the splitting region once more compared to the centered beam.

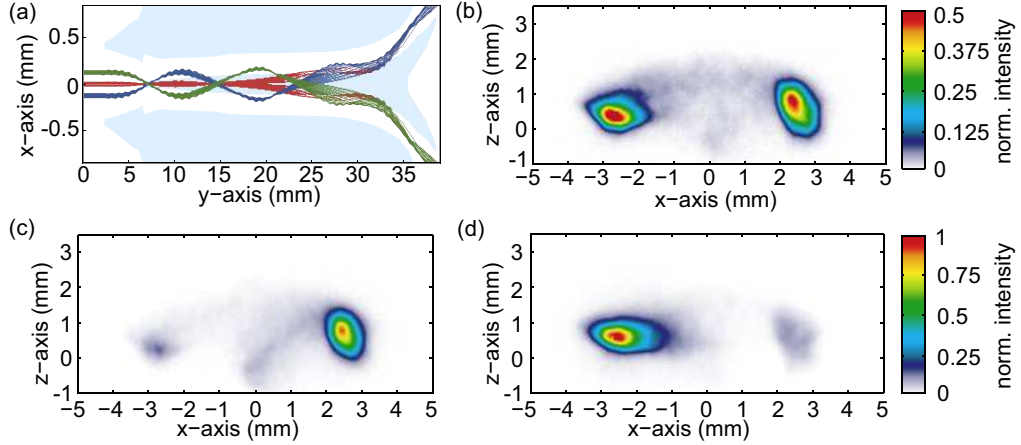


Figure 4.11: Dependence of beam splitting on the initial position of the electron source. (a), Simulated electron trajectories in the xy -plane for three different positions of the electron source along x with $E_{kin} = 1.5$ eV, $V_0 = 16$ V and $\Omega = 2\pi \cdot 1$ GHz. The underlying signal electrodes are indicated in light blue. (b) Symmetric beam splitting signal for a centered electron gun. (c), (d), Measured beam splitting signals for displacing the electron gun in the negative (c) and the positive (d) x -direction. For a displaced electron gun in (c) and (d) the measured count rate in one single output beam corresponds to the integrated count rate of both output beams for a centered electron gun in (b). The measurements are performed with $E_{kin} = 1$ eV, $V_0 = 16$ V and $\Omega = 2\pi \cdot 1.082$ GHz.

The same behavior is found experimentally when the electron source is displaced in the x -direction. In Fig. 4.11(c) the electron source is displaced in the negative x -direction, which results in the detection of a single guided spot at positive x . Displacing the source in the positive x -direction the signal in Fig. 4.11(d) is obtained. When the electron gun is centered we obtain a symmetric splitting, as shown in Fig. 4.11(b). It is thus possible to modify the ratio of the electron count rate in both output beams by simply displacing the electron source. Furthermore, we find experimentally that the displacement of the electron source does not increase the signal of lost electrons. Consequently, the measured count rate in one single output beam for the displaced source corresponds to the integrated count rate of both output beams for a centered electron gun. This is

reflected in the different color scale for Fig. 4.11(b) compared to Figs. 4.11(c),(d). For the centered beam in Fig. 4.11(b) the color scale used spans half the intensity of the color scale used for the displaced beam in Fig. 4.11(c) and (d). If we move the electron source even further away along the x -direction electron losses start to increase until no beam splitter signal is observed anymore.

4.4.3 Splitting with variable electron energy

We have studied beam splitting at electron kinetic energies ranging from 1 eV up to 4 eV. The corresponding detector signals of the measurement are shown in Fig. 4.12.

The beam splitter signal for $E_{\text{kin}} = 1$ eV in Fig. 4.12(a) is mainly the same as the one at $E_{\text{kin}} = 1.5$ eV shown in Fig. 4.10(a). The thermionic source is capable of yielding even lower electron energies, however, below 1 eV the electron current drops and the spatial profile of the beam becomes worse at the same time. An experimental comparison of the beam splitter signal at these very low electron energies is therefore not possible.

From $E_{\text{kin}} = 1$ eV to $E_{\text{kin}} = 3$ eV, we find that the signal of lost electrons becomes larger with energy. This is because with increasing electron energy the transverse deflecting force in the splitting region of the guiding potential becomes insufficient to significantly deflect the electrons in the lateral x -direction. Accordingly, the electron trajectories cannot follow the separating paths of the potential minimum and are lost from the potential. Additionally, for $E_{\text{kin}} = 3$ eV the two guided spots appear slightly tilted with respect to each other. This might result from slightly asymmetric microwave voltages along the lateral x -direction described in Sec. 4.3. Furthermore, an isolated and collimated signal of lost electrons around $x = 0$ mm is observed. This can be explained by a third guiding channel that forms at $x = 0$ mm towards the end of the beam splitter chip. The center electrode of the beam splitter electrode layout is divided laterally starting from $y = 35.5$ mm (see Fig. 4.3). This results not only in an increasing separation of the beam splitter paths but also in an additional field minimum that forms at $x = 0$ mm. Electrons that are lost from the guiding potential at the beam splitter junction may hence be recaptured into that additional minimum and guided along the symmetry axis. As a result, a third output beam is detected around $x = 0$ mm at smaller z -values than electrons that are fully lost from the guiding potential and form the arc between the two guided beams.

Increasing the electron energy to 4 eV, we observe no splitting anymore and all electrons are detected in a centered single spot, as can be seen in Fig. 4.12(c).

The observed dependence of the beam splitting on the kinetic energy indicates that for efficient beam splitting the longitudinal propagation along the beam splitter potential has to be slow compared to the transverse electron motion. More specifically, in order to achieve smooth and lossless splitting any variation in the pseudopotential landscape experienced by an electron has to be slow with respect to the time scale set by the transverse trap frequency. Consequently, to provide a smooth splitting of the electron beam without inducing an excited electron motion as detrimental effect of the splitting process it is essential to increase the transverse trap frequency and, furthermore, to find an optimum shape of the beam splitter potential.

In the following we perform a numerical optimization of the shape of the guiding potential aiming at smooth beam splitting. Additionally, we investigate the effect of

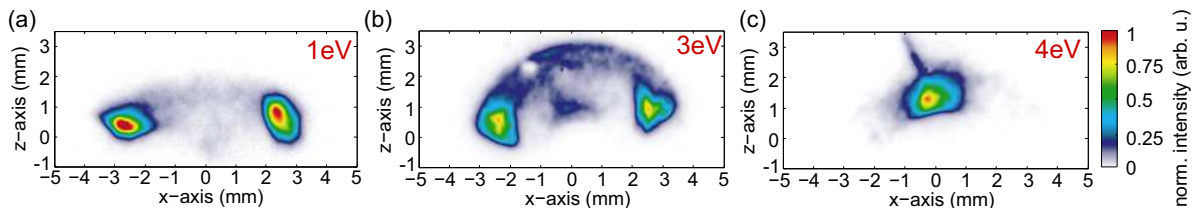


Figure 4.12: Dependence of the beam splitter signal on E_{kin} . (a), Detector signal for $E_{kin} = 1\text{ eV}$ with $V_0 = 16\text{ V}$ and $\Omega = 2\pi \cdot 1.082\text{ GHz}$ and $V_C = -0.17\text{ V}$. (b), (c) Detector signals for $E_{kin} = 3\text{ eV}$ and $E_{kin} = 4\text{ eV}$ with $\Omega = 2\pi \cdot 1.12\text{ GHz}$. These measurements were performed using a different beam splitter substrate than in (a). In (b), the microwave voltage is $V_0 \approx 34.7\text{ V}$ and $V_C = -0.88\text{ V}$ yielding an increased trap depth of $U \approx 38\text{ meV}$ and $U_{dc} = 45\text{ meV}$. In (c), $V_0 \approx 41.4\text{ V}$ and $V_C = -0.68\text{ V}$ yielding an increased trap depth of $U \approx 54\text{ meV}$ and $U_{dc} = 35\text{ meV}$. Although, the beam splitter chip used in (b), (c) provided similar detector signals compared to (a), the microwave frequency response of the substrate was highly irregular. For this reason the values given for V_0 are only rough estimates. Clearly, the electron loss increases with increasing electron energy. For $E_{kin} = 4\text{ eV}$ the beam splitting potential is too weak to achieve two split output beams.

increasing the transverse trap frequency on the beam splitting process.

4.5 Simulations towards adiabatic on-chip electron beam splitting

The ultimate goal of the electron beam splitter experiment is to split a guided electron wave packet that occupies a defined transverse motional quantum state in the guide and to maintain the quantum state during the splitting process. Quantum control over the transverse electron motion combined with the adiabatic splitting of an electron wave-packet would allow us to use the motional quantum states as a carrier of quantum information in an interference measurement. As a prerequisite of such an experiment, the transverse motional quantum state of the guided electron wave packet has to be controlled along the entire guiding potential. This requires not only the injection of electrons into a well defined quantum state of the guiding potential, as described in Sec. 2.3, but also necessitates that this state is maintained during the splitting process. Any transverse excitation of the electron within the confining potential that is comparable to the characteristic energy of the transverse quantum states prevents the operation of such a guided matter-wave interferometer. In order to examine the splitting process including wave-optical aspects, the temporal quantum evolution of an electron wave packet has to be investigated taking into account the discretized eigenstates of the microwave pseudopotential.

4.5.1 Optimized beam splitter potential

In a wave-optical description single electron wave packets have to be propagated in the potential landscape generated by the microwave beam splitter chip. More specifically, in order to achieve the transverse splitting of a guided wave packet this landscape needs

to provide a finely structured potential hill with dimensions on the order of the lateral extent of the wave packet to achieve the division of the latter into the adjacent wells of the guiding potential. The transverse motional quantum state of the electron can only be preserved during the splitting process if the propagation of the electron wave packet in the beam splitter potential is adiabatic. This means that the splitting is sufficiently slow that the electron is able to adapt its wave function continuously to the respective quantum state of the transverse guiding potential.

In the following we will employ wave-optical simulations to optimize the shape of the beam splitter potential. In order to avoid confusion in the notation we will refer to the pseudopotential that is generated by the numerically optimized microwave chip design, shown in Fig. 4.4(a) and was used in the experiments, as the Splitter1 potential and will refer to the potential that will be derived in the following as Splitter2 potential. The wave-optical simulations are one-dimensional and only consider the transverse x -direction, as this is the dimension where the splitting arises. Furthermore, only the time-averaged pseudopotential will be considered. We deduce the one-dimensional transverse potential from the Splitter1 potential at a given position y . Then we numerically solve for the quantum ground state in the potential landscape. From these simulations we find that the splitting of the quantum ground state arises at $y = 15.56$ mm as a result of the formation of the double-well potential. Fig. 4.13(a) shows the ground state probability density that we obtain from simulating the transverse ground state in a range of $L = 100$ μm around $y = 15.56$ mm where the splitting arises. At $y = 15.5$ mm the transverse potential is nearly harmonic, which results in a Gaussian probability density that is centered around $x = 0$ mm. Towards the end of the simulation range, at $y = 15.6$ mm the presence of a double-well potential results in a ground state probability density that is given by two Gaussians one in each well. In between, the potential transforms from a single well into a double well resulting in the splitting of the ground state wavefunction.

In the adiabatic limit an electron wave packet, initially prepared in the ground state of the transverse potential, propagates along the guiding potential and remains in the quantum ground state along the guide. If adiabaticity of the splitting process cannot be assured, non-adiabatic propagation of the electron wave packet within the splitting potential manifests itself by conversion of longitudinal energy into the transverse degree of freedom, thereby exciting the electron wave packet into a higher energy state of the transverse potential. In a frame moving with the electron in the longitudinal direction, an electron with constant E_{kin} experiences a time dependent potential $V(t)$, which is reflected in a time dependent Hamilton operator $H(t)$ that governs the dynamics of the wave packet within the beam splitter potential. As a result, the motional quantum state $|\varphi(t)\rangle$ as well as its energy expectation value $E(t) = \hbar\omega(t)$ are time dependent quantities.

The adiabaticity of the splitting process can be increased by following an optimization routine by Hänsel *et al* [68]. This approach was initially developed to achieve fast and adiabatic splitting of cold atomic clouds in an atom chip magnetic trap. The time scale on which the separation process can be achieved adiabatically may be obtained using a time-dependent interaction picture. The temporal evolution of the quantum state can

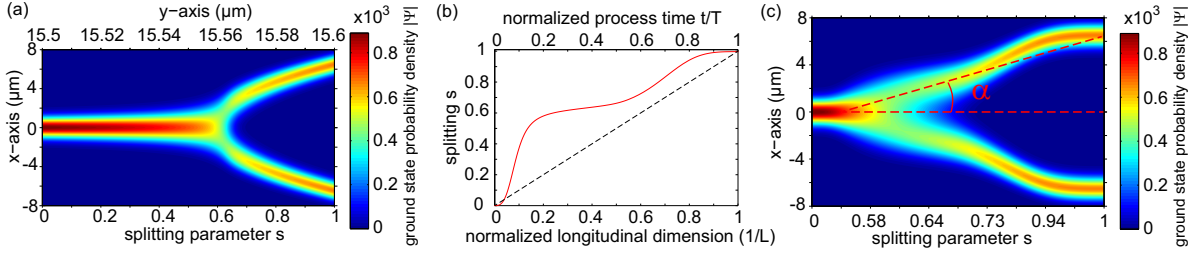


Figure 4.13: Adiabaticity optimization of the transverse beam splitter potential.

(a), Quantum ground state probability density over a length of $100 \mu\text{m}$ where the splitting evolves. The simulation is based on the beam splitter potential that was described in Sec. 4.1 and used for the experiments. (b), Splitting parameter s as a function of the longitudinal y dimension or time t , respectively. The splitting parameter parametrizes the separation of the beam splitter potential wells. The dashed black line shows the linear process speed ds/dy prior to the optimization, the red line corresponds to the optimized process speed. (c), Ground state probability density for the optimized beam splitter potential, according to the optimization of the splitting process speed ds/dy , shown in (b). A smooth splitting with reduced opening angle α is obtained from the optimization. The microwave parameters in (a) and (c) are $\Omega = 2\pi \cdot 5 \text{ GHz}$ and $V_0 = 75 \text{ V}$ corresponding to $\omega = 2\pi \cdot 264 \text{ MHz}$, $U = 48 \text{ meV}$ and $q = 0.15$.

be expressed by

$$|\psi(t)\rangle = \sum_k c_k(t) \exp \left[-i \int_0^t \omega_k(t') dt' \right] |\varphi_k(t)\rangle, \quad (4.5)$$

taking advantage of the natural evolution of the time dependent eigenstates $|\varphi_k(t)\rangle$ with the population coefficients $c_k(t)$. Here, $\hbar\omega_k(t)$ corresponds to the energy levels of the quantum eigenstates in the transverse potential $V(t)$. Inserting this Ansatz in the Schrödinger equation yields a set of coupled equations for the time-dependent state populations $c_k(t)$, given by

$$\frac{d}{dt} c_k(t) = - \sum_n c_n(t) \exp \left[-i \int_0^t [\omega_k(t') - \omega_n(t')] dt' \right] \langle \varphi_k(t) | \frac{d}{dt} | \varphi_n(t) \rangle \quad (4.6)$$

with the coupling terms $\langle \varphi_f(t) | \frac{d}{dt} | \varphi_i(t) \rangle$. Here $|\varphi_i\rangle$ and $|\varphi_f\rangle$ denote the initially occupied eigenstates and the eventually excited final states, respectively. Assuming that initially only one single eigenstate $|\varphi_i\rangle$ is populated and neglecting all transitions into other vibrational states except for one single final state $|\varphi_f\rangle$, the first-order transition probability $P_{if}(t) = |c_f(t)|^2$ is approximated by

$$c_f(t) = \int_0^t \exp \left[-i \int_0^t [\omega_f(t') - \omega_i(t')] dt' \right] \langle \varphi_f(t) | \frac{d}{dt} | \varphi_i(t) \rangle dt. \quad (4.7)$$

Here all quantities are expressed as time-dependent functions. Since in our case the potential is static but the electron is moving, the optimization will result in a deformation of the beam splitter potential along y yielding the optimized Splitter2 potential. Because

the electron travels at a constant velocity along the beam splitter potential the time dependence can also be substituted by a dependence along the longitudinal y -direction

$$\langle \varphi_f(t) | \frac{d}{dt} | \varphi_i(t) \rangle \iff \langle \varphi_f(y) | \frac{d}{dy} | \varphi_i(y) \rangle \quad \text{and} \quad \omega_k(t) \iff \omega_k(y), \quad (4.8)$$

allowing a somehow more intuitive description in the following discussion.

The goal of the adiabaticity optimization is to minimize the transition probability from the ground state into higher excited states. This is done by parameterizing the transverse potential $V(s)$ by the splitting parameter s . For a linear relation $s = y/L$ and, hence, a constant process speed ds/dy the transverse potential $V(s)$ corresponds to the Splitter1 potential. This is shown in Fig. 4.13(b), where the linear dependence of the splitting parameter (black, dashed line) directly results in a direct correspondence of the longitudinal y -direction (upper axis) and the splitting parameter (lower axis) on the x -axis in Fig. 4.13(a). As a result of the parametrization, the eigenstates as well as eigenfrequencies are functions of the splitting parameter s and the coupling terms become

$$\langle \varphi_f(y) | \frac{d}{dy} | \varphi_i(y) \rangle = \langle \varphi_f(s) | \frac{d}{ds} | \varphi_i(s) \rangle \frac{ds}{dy} \equiv a(s) \frac{ds}{dy}. \quad (4.9)$$

The adiabaticity of the splitting process can be increased by optimizing the process speed ds/dy along the beam splitter potential such that excitations of the ground state wave packet are minimized.

The splitting process (from $s = 0$ to $s = 1$) is performed over the length L of the splitting potential along y . A substitution of the longitudinal coordinate y to a new length scale τ is undertaken in order to linearize the exponent in Eq. 4.7

$$\int_0^y [\omega_f(y') - \omega_i(y')] dy' = \frac{L}{L_0} \tau(y). \quad (4.10)$$

Here L_0 sets the new length scale of the splitting process, chosen such that $\tau(y)$ runs from 0 to 1 during the splitting process. As a result, the first-order coupling coefficient in Eq. 4.7 takes the form of a Fourier transform

$$c_f(L) = \int_0^1 \exp \left[i \frac{L}{L_0} \tau \right] u(\tau) d\tau \quad (4.11)$$

$$\text{with } u(\tau) = a(s) \frac{ds_\tau}{d\tau}. \quad (4.12)$$

From this equation we can see that large transition coefficients c_f can be avoided if the shape of the redefined process speed $ds_\tau/d\tau$ is chosen such that it produces the least amount of side lobes possible in the Fourier transformation in Eq 4.11. An appropriate shape would, e.g., be a Blackman pulse [87]

$$u(\tau) = 1/L_0 \left[1 - \frac{25}{21} \cos(2\pi\tau) + \frac{4}{21} \cos(4\pi\tau) \right]. \quad (4.13)$$

An expression for an optimum process speed $s_\tau(\tau)$ and the process length scale L_0 can now be obtained explicitly by inserting $u(\tau)$ into Eq. 4.12 and solving for $s_\tau(\tau)$

requiring that the splitting parameter s matches the boundary conditions $s(\tau = 0) = 0$ and $s(\tau = 1) = 1$. Having determined L_0 and $s_\tau(\tau)$, Eq. 4.10 can be rewritten in the form

$$\frac{d\tau}{dy} = [\omega_f(s_\tau) - \omega_i(s_\tau)] \frac{L}{L_0} \quad (4.14)$$

and numerically evaluated when choosing $L = L_0$. The solution establishes the relation between the length scales and yields an expression for $\tau(y)$. Following the optimization routine we finally obtain an improved splitting parameter $s(y) = s_\tau[\tau(yL_0/L)]$.

The red line in Fig. 4.13(b) shows the improved splitting parameter obtained from the adiabaticity optimization of the transverse Splitter1 potential. Inserting the optimized s parameter into $V(s)$ we directly obtain an optimum shape of the beam splitter potential, the Splitter2 potential. Fig. 4.13(c) shows the quantum ground state probability density that results from the Splitter2 potential. As expected, a smooth transition into the split-up paths by means of a small splitting angle α is required and obtained from the optimization. Here α is defined as the angle between y -position where the wavefunction is split-up and the final position of the wavefunction's maximum on the x -axis at the end of the splitting process [see Fig. 4.13(c)].

The Splitter2 potential has been effectively obtained by stretching the Splitter1 potential along the y -direction. However, the electric fields produced by the chip electrodes do not simply scale when stretching the electrodes longitudinally. For this reason, a new electrode optimization has to be performed to find a suitable electrode structure that generates the Splitter2 potential. Furthermore, it should be stressed that we only considered the pseudopotential for the adiabaticity optimization. Hence, effects like the micromotion of electrons in the microwave electric fields are neglected here. In order to ensure the validity of this assumption, small stability parameters q have to be achieved experimentally. Furthermore, the quantum eigenstate evaluation was performed in a 1D potential where only the transverse x -dimension of the beam splitter potential has been taken into account. To this end, detrimental effects of the unwanted fourth port that approaches the beam splitter junction in the vertical z -direction are not accounted for. At this point we cannot determine whether the wave-packet dynamics in the vertical z -direction can be sufficiently decoupled from the lateral x -direction such that excitations in the z -direction do not influence the beam splitting process. This question will be addressed by a two-dimensional simulation in the future.

4.5.2 Drive parameter scaling

In the previous section the shape of the beam splitter potential was optimized in order to reduce the amount of transverse excitation during the splitting process. However, in order to achieve beam splitting without exciting the electron wave packet into higher energetic transverse quantum states the microwave drive parameters of the guide have to be adapted to the electron kinetic energy E_{kin} . As will be described below, we find for $E_{kin} = 1$ eV that splitting with less than 5% of the state population excited from the ground state into higher energetic states can be obtained with $\Omega = 2\pi \cdot 10$ GHz. This corresponds to a tenfold increased trap frequency ω with respect to the measurements presented in Sec. 4.4, according to Eq. 2.15. A constant stability parameter $q = 0.15$ is assured by increasing the voltage amplitude to $V_0 = 75$ V and scaling the section of the

beam splitter potential that underlies the probability density simulation in Fig. 4.13(c) in the longitudinal and transverse dimensions to a length $L = 40$ mm and a splitting angle $\alpha = 0.1$ mrad. The scaling of the beam splitter potential results in a relative reduction of the trap height $R'_0 = R_0/4.65 = 100 \mu\text{m}$ (at $y = 10$ mm) and a smaller beam separation of $\sim 10 \mu\text{m}$ at the end of the beam splitter chip as compared to a separation of 2 mm in the experiments described above.

We can calculate the state population $|c_i(t)|^2$ for the three lowest symmetric quantum states ($i=0, 2, 4$) in the beam splitter potential by solving a system of coupled differential equations for the population coefficients $c_i(t)$ according to Eq. 4.6. Only symmetric states are considered, as transitions only occur between states of the same parity due to the symmetry of the beam splitter potential. For the calculation of the transition probabilities we assume that initially only the ground state is populated. Fig. 4.14(a) shows the temporal evolution of the state populations during the splitting process for the Splitter2 potential and the microwave parameters given above. For $E_{kin} = 1$ eV we find that during splitting the state populations $|c_2(t)|^2$, $|c_4(t)|^2$ are transiently increasing, however, after the splitting process 95% of the state population ends up in the ground state. Strictly speaking, the splitting process does still not provide a fully adiabatic propagation as this would allow only negligible deviations of the ground state population from unity. As can be seen in Fig. 4.14(a), the state population $|c_2(t)|^2$ increases during the splitting process and takes values up to 20%. However, finally 95% of the state population ends up in the ground state after the splitting process and the intermediate excitation will only produce a global phase factor that is multiplied to both parts of the wave function that follow the separating paths of the beam splitter potential.

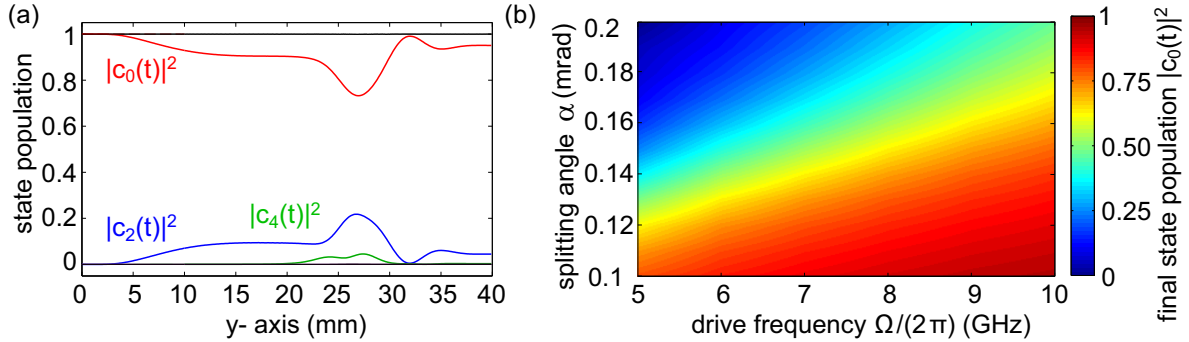


Figure 4.14: Transition probabilities during the splitting process. (a), Simulated transition probabilities for the optimized beam splitter potential with $\Omega = 2\pi \cdot 10$ GHz and $V_0 = 75$ V, which corresponds to $\omega = 2\pi \cdot 528$ MHz, $U = 48$ meV and $q = 0.15$. The optimized beam splitter potential allows splitting of the quantum ground state with more than 95% of the population remaining in the quantum ground state after the splitting process. (b), Simulation of the final ground state population after the splitting process as a function of Ω and the beam splitter angle α .

It is instructive to specify the scaling behavior of the transverse excitation probability with respect to the beam splitter opening angle α and the microwave drive frequency Ω . To increase the range of adiabatic splitting the transverse trap frequency ω can be raised by increasing the drive frequency Ω ($\omega \propto \Omega$, see Eq. 2.10). In order to obtain empirically how the transverse excitation probability scales with an increased drive frequency Ω we

simulate transition probabilities for $V_0 = 75$ V and varying drive frequencies in a range from 1 to 10 GHz. For every Ω we find that the transition probabilities highly depend on the splitting angle α . Figure 4.14(b) shows the result of these simulations, where the color indicates the fraction of the final ground state population $|c_0(t)|^2$ after the splitting process. Clearly, small splitting angles as well as a high drive frequency are favorable in order to achieve efficient splitting of the motional quantum ground state without vibrational excitations into higher transverse states.

The transition probabilities shown in Fig. 4.14(a) for $E_{kin} = 1$ eV were obtained for $\alpha = 0.1$ mrad by stretching the beam splitter potential by a factor of 400 in the y -direction. The requirement of achieving an opening angle on the order of $\alpha = 0.1$ mrad will impose stringent requirements on the fabrication tolerances of the chip electrodes and it remains to be seen whether such a structure can be realized with the fabrication technology currently available.

4.6 Next experimental steps and future perspectives

In Sec. 4.4 the splitting of a guided electron beam was demonstrated experimentally using a planar microwave chip. The action of the microwave beam splitter chip is to spatially divide the wavefront of the guided electron beam and to separate it into two output beams. As a result, in order to observe interference effects when overlapping these two split-up fragments a spatially coherent electron beam has to be injected into the beam splitter potential. Because of the poor coherence of the thermionic source used in the experiment, we do not expect interference effects when overlapping the two guided beams shown in Fig. 4.10(a). Future experiments aiming at the observation of matter-wave interference effects have to employ a coherent electron source, as the one described in Ch. 6.

The next essential step is to demonstrate electron interference based on a chip-based beam splitting device. This requires that the two guided and separated beams are overlapped at a distant detector. It is a delicate question in how far the formation of an interference pattern requires control over the transverse motional state of the guided electrons. In order to observe equidistant interference fringes both beams should provide flat wavefronts at the detector plane. To this end, a detailed study is required where a coherent electron beam, that has a flat wavefront before injection into the guide, is propagated through the beam splitter potential and subsequently to the electron detector. The wavefronts of the split-up beams behind the guide have to be extracted specifically for the case where the injected beam is not matched to the ground state of the guiding potential and therefore populates a large number of transverse motional states. However, even if these wavefronts reveal a complicated structure at the electron detector it should still be possible to observe correlations in the detected electron signal, similar to a speckle pattern, arising from interference of the distorted wavefronts.

Several improvements to the experimental setup have to be made. First of all, a collimated coherent electron beam should be used for the injection into the guiding potential. In Ch. 6 we will report on the construction of a coherent field emission electron gun, which will provide a coherent electron beam. Furthermore, deflection optics behind the beam splitter chip are required to overlap the electron beams on the electron detector.

This can simply be done by inserting a positively charged macroscopic biprism filament between the two split-up electron beams enclosed by two grounded metal electrodes. The expected fringe spacing dx depends on the angle θ between the two interfering beams and their wavelength λ according to $dx = \lambda/\theta$. Assuming a detector with a spatial resolution of several $10\ \mu\text{m}$ requires $\theta < 0.1\ \text{mrad}$. This can either be accomplished by placing the detector far away, by more sophisticated electron optics or by reducing the separation of the guided beams on the beam splitter chip. The last alternative combines several practical advantages. Most importantly, a reduced separation directly results in a smaller splitting angle α and, hence, smoother splitting. Additionally, it is favorable to only enclose a small area by the interferometer arms to reduce the vulnerability to disturbances like mechanical vibrations, electromagnetic noise or temperature drifts. Finally, chromatic effects will probably lead to a reduced visibility of the interference effects. The typical longitudinal energy width obtained in field emission from metal nanotips is $\Delta E \sim 0.3\ \text{eV}$.

The discretized transverse quantum states that govern the wave-optical propagation of a guided electron wave packet equip this novel beam splitter concept with an additional degree of freedom, which is not accessible for any other electron beam splitter device, like e.g., the electrostatic biprism. In the following, we will discuss important experimental steps towards the adiabatic on-chip splitting of guided electrons. With respect to the final goal to reach quantum control over the transverse electron motion in a chip-based electron interferometer several achievements have to be attained. Most importantly, a suitable electrode pattern that generates the optimized Splitter2 potential has to be found. Very likely the corresponding electrode layout will put stringent requirements on the fabrication tolerances of the microwave chip. Currently, the smallest feature sizes that were fabricated on the beam splitter chip are the tapered central electrode terminated by a round tip with an electrode thickness of $20\ \mu\text{m}$. Furthermore, the scaling of the microwave drive frequency to $5\ \text{GHz}$ requires that traveling microwave signals have to be taken into account. Here, the splitting of the central electrode that is divided into two parts will require impedance matching of the electrode structure. Apart from the microwave design of the beam splitter chip, any interferometric measurement requires the injection of electrons into a well defined transverse motional quantum state of the guiding potential. As discussed in Chapter 3, we investigate new electrode coupling structures in order to provide a smooth injection of electrons from the electron gun. The new beam splitter design should hence incorporate such a coupling structure. Furthermore, the injection into low-lying quantum states also necessitates a pulsed, diffraction-limited electron source.

5 A highly coherent electron beam from a laser-triggered nanotip

In this chapter we investigate the spatial coherence of metal nanotip electron sources, which temporarily shifts the focus from the manipulation of electrons in free space to the fundamental properties of electron emission. Even though the work presented in this chapter seems loosely associated with electron guiding at first sight, it is motivated by the goal to develop a coherent pulsed source for electron guiding and represents the first step towards the experimental realization of the latter.

We study the emission properties of metal nanotips, which are the most coherent sources of electrons used in commercial instruments when operated in DC-field emission. They provide electron beams with flat wavefronts that can be focused to the fundamental physical limit given by matter-wave diffraction [23]. Modern electron microscopes employ coherent electron beams to provide images of atomic structures reaching below 0.1 Å spatial resolution [88]. Currently, time-resolved electron based imaging is pursued with large efforts, both in real-space microscopy [89, 90] and in diffraction [91, 92]. Although laser-driven metal nanotips promise to provide coherent electron pulses with highest time resolution [93, 94], a quantitative study of their spatial coherence has been elusive. Here we demonstrate that photoemitted electrons from a laser-triggered tungsten nanotip are spatially almost as coherent as in DC-field emission. This is of importance for the field emission electron gun presented in Ch. 6 as we will laser-trigger the electron emission from the nanotip in future experiments. However, the findings presented here have much broader significance as they have direct impact on all time-resolved electron-based imaging applications that combine highest spatial resolution in synchrony with ultimate time resolution.

First we describe the fabrication and characterization of metal nanotips. They feature a spatially confined emission hot spot, which results in a bright and highly collimated electron beam. In order to investigate the spatial coherence of conventional tungsten nanotip emitters, we use a point projection microscope setup with a carbon nanotube as beam splitter for coherent electron matter waves. Recording interference fringes on the MCP, we measure an upper limit for the effective source radius of the nanotip, the figure of merit for the degree of spatial coherence. The ability to focus fiber-coupled laser light in the near ultraviolet (UV) onto the tip apex allows us to investigate the coherence properties of a laser-driven photoemitted electron beam and compare it to DC-field emission.

Using ultrathin film-induced faceting we can create an atomically sharp pyramid on top of the tungsten tip apex that ends in just one single atom. For these tips the electron emission is confined exclusively to the topmost atom of the atomically stacked pyramid. Such a single atom tip has been shown to provide an extremely bright and fully coherent

electron beam in DC-field emission [95]. Future experiments will employ these tips as perfect point sources of electrons, the prerequisite for diffraction-limited focusing.

5.1 Metal nanotip preparation and characterization

Sharp nanometric metal tips can be used as bright and coherent electron sources. These tips are routinely produced from a tungsten wire (chemical symbol W) and feature a hemispherical tip apex with radius of curvature in the range of several nanometers. A combination of in-situ characterization techniques allows us to obtain precise information about the field emission properties and to record an image of the tip apex with atomic resolution. The following paragraphs describe the usual work flow of the metal nanotip preparation starting from the tip etching to the characterization of the nanotip and then discuss eventually required cleaning procedures to obtain an atomically clean tip apex.

Chemical etching of tungsten nanotips

The fabrication method of tungsten tips is based on a chemical wet-etch technique using the so-called two-lamellae drop-off technique (see, e.g. Ref. [96]). A thin wire of tungsten, with a diameter of 0.1 mm, is mounted parallel to the gravitational force pointing through the center of two aligned gold rings, which are separated by several millimeters from each other along the wire. Both rings are dipped into an aqueous sodium hydroxide (NaOH) solution to create lamellae of the etchant solution in the rings and around the wire. By applying a positive electric potential of about 6 V to tip with respect to the upper gold ring the tungsten wire can be electrochemically etched. As the etching process at the interface of the lamella and the tungsten wire is isotropic the etch rate is highest at the center of the lamella and decreases towards the upper and lower boundary of the lamella. This results in a characteristic conical shape of the tip shank after the etching process. Ideally, etching currents from 1 to 5 mA are achieved during the etching. Once the tungsten wire is etched through at the very center of the lamella the lower part of the wire drops down due to gravity and induces a capacitive switch when falling through the lower lamella and the etching voltage is turned off quickly. By these means blunting of the wire by continued etching is avoided.

Figure 5.1 shows scanning electron microscope images of an etched tungsten nanotip. The inset in Fig. 5.1(a) is taken with an optical microscope, which is usually employed to inspect the general shape of the tip shank and to confirm whether the tip surface is smooth. Figure 5.1(b) shows a zoom on the tip's apex, where the tip is buried by a hazy oxide layer because of the fast oxidation of tungsten in ambient air. Typically tip radii of 5 to 20 nm are obtained using the described etching technique. The full opening angle of the tip shaft is usually between 6° and 10° .

Tips of different crystallographic orientation can be fabricated when using tungsten wires that are grown along a specific crystallographic direction. For example a W(310) orientation refers to a wire that is grown parallel to the crystallographic [310]-direction in the tungsten lattice, denoted by the Miller indices. Typically, experiments that require a bright and collimated electron beam employ a single-crystal W(310) wire for the etching of the tip. This is because the work function of tungsten varies for the different crystal

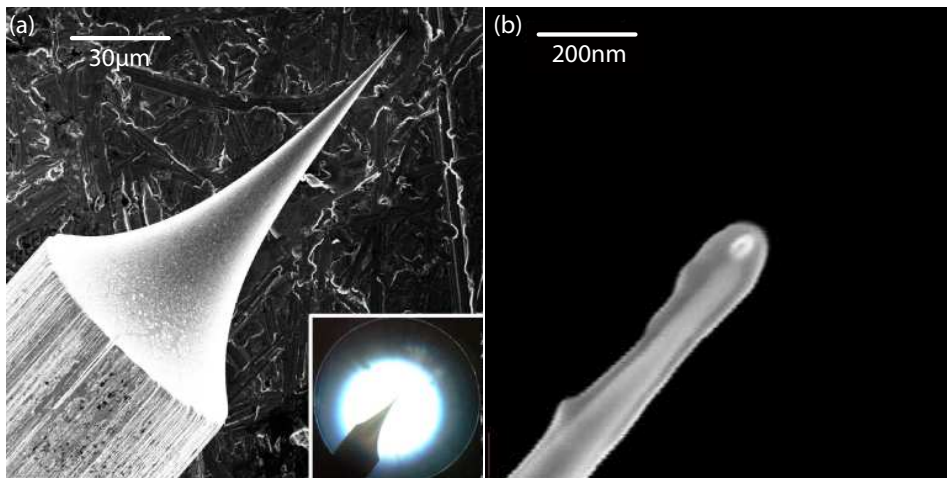


Figure 5.1: Electron microscopy images of a sharp metal nanotip. (a), A characteristic, conical shape of the tip's shank is obtained by the chemical etching process. The inset shows a shadow image of the tip in a light microscope. (b), Electron microscope image of the tip apex. The tip is covered by a thin layer of oxide blurring the image. Below the oxide layer the hemispherical tip apex can be distinguished. Images are taken from Ref [97].

directions and the W(310) surface has the lowest work function of $\Phi = 4.35$ eV of all possible orientations [98]. According to the Fowler-Nordheim theory [99], the field-emitted electron current $j(F) \propto F^2 \exp(-C\Phi^{2/3}/F)$ depends critically on the field strength F and the work function Φ with a constant C . As a result of their low work function in forward direction, the W(310) tips feature a bright and collimated beam of electrons along the tip axis. For this reason we use W(310) tips for the interference measurements in Sec. 5.4 and the characterization of the field emission electron gun in Ch. 6. However, for the fabrication process of single-atom tips, described in Sec. 5.2, a single-crystal W(111) tungsten wire is required.

To further characterize the metal nanotip we mount it on a tip holder, which is placed into a UHV chamber with pressure $p < 1 \cdot 10^{-9}$ mbar as described in Sec. 6.1. There we can perform field electron microscopy and field ion microscopy.

Field electron microscopy

Field electron microscopy (FEM) allows us to investigate the spatial pattern of the electrons emitted from the metal nanotip [100, 101]. When a negative electric potential of several hundreds of volts is applied to the nanotip with respect to the detector screen, the Schottky effect allows electrons close to the metal-vacuum interface to tunnel from the metal tip into the vacuum. This effect is called field emission and can be described by the Fowler-Nordheim theory [99]. A detailed description of the field emission process is out of the scope of this work but can be found, e.g., in Ref. [101]. Electrons that are field-emitted from the tip follow the electric field lines that point perpendicular to the hemispherical tip apex and are accelerated towards the MCP electron detector. The latter allows for spatial resolution and single electron detection at the same time as a result of the high MCP gain on the order of several millions. Due to the radial velocity

component of the propagating electron beam, a projection image is recorded at the MCP detector with a magnification that is given by the ratio of the tip-to-anode distance to the tip radius. Typically this yields magnifications of $M > 10^9$. Spatial variations in the pattern of the detected electron signal allow to map out emission hot spots on the tip apex. These hot spots can be related to local minima in the tungsten crystal's work function at the metal-vacuum interface, which governs the magnitude of the emitted current density.

Figure 5.2(a) shows the electron emission pattern of a tungsten single-crystal W(111) tip together with a ball model of the atomic structure of the hemispherical tip apex. This ball model allows to identify crystallographic orientations. It shows, a hemispherical cut in through a bcc lattice structure of tungsten. The color indicates the distance of each lattice site to the hemisphere surface leading to protrusions (red) and depressions (green). Since protrusion are subject to high local electric fields, they appear as bright spots in the FIM image, described below. Four localized electron spots are detected at the MCP, one in the center and three spots that are oriented along the corners of a triangle. This emission pattern originates from the preferential electron emission of two different crystallographic faces, which correspond to local minima in the work function map on the tip apex. As can be seen from the ball model, the centered electron spot comes from the W(111) face, which is aligned with the tip and has a work function of $\Phi = 4.47$ eV [102]. Furthermore, the triangular symmetry results from the crystallographic $\{211\}$ faces with a work function $\Phi = 4.5$ eV [98].

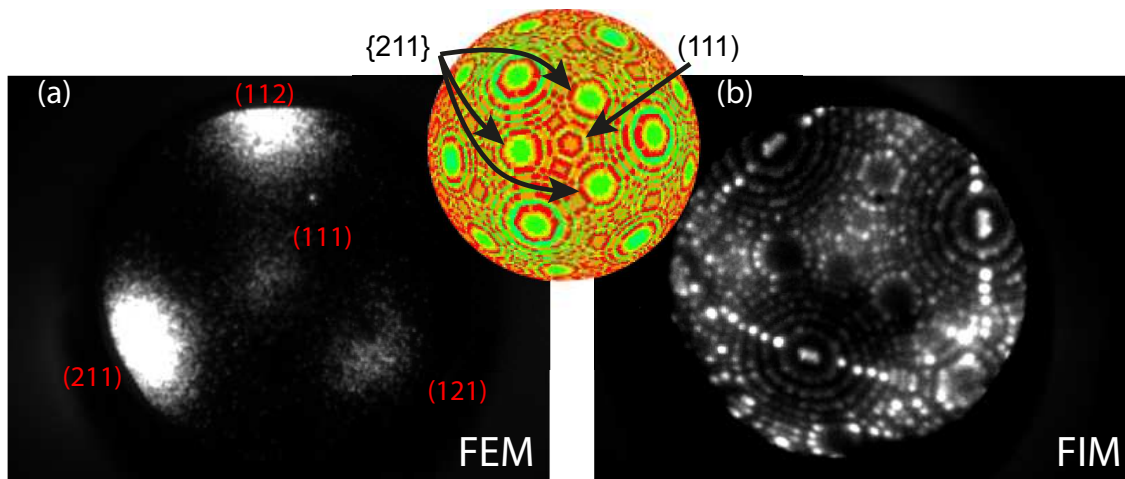


Figure 5.2: Characterization of a W(111) tip by FEM and FIM. (a), The field emission pattern originates from preferential emission of the tungsten $\{211\}$ and (111) facets. The crystal symmetry of tungsten is illustrated in the inset showing a ball model of a hemispherical bcc tungsten lattice. (b), Field ion microscopy image from the same tip. White dots correspond to single atoms on the tip's apex. Excellent agreement with the ball model confirms the crystallographic orientations.

Here we show images for the W(111) tip, as this specific crystallographic orientation is required for the creation of a single-atom tip, which is discussed in the next section. In all other experiments we use tungsten W(310) tips, which feature a single bright electron emission spot, because the (310)-direction corresponds to the global minimum

in the work function map.

Field ion microscopy

Field ion microscopy (FIM) provides an imaging method to investigate the nanotip's apex with atomic resolution. This method was invented by E. Müller in 1951 and allowed for the first time imaging of single atoms on a surface [103, 104]. Figure 5.2(b) shows a FIM image where the white dots correspond to single atoms on the apex of the metal tip. Again excellent agreement with the ball model is found indicating a hemispherical and atomically clean tip surface.

In order to record such an image we introduce an imaging gas with a partial pressure of $1 \cdot 10^{-5}$ mbar into the vacuum chamber. The imaging of the tip surface again relies on a conformal mapping of the hemispherical tip surface onto the MCP detector. As in the case of FEM the magnification is given by the ratio of the tip-to-anode distance to the tip radius. In contrast to FEM, in FIM mode the detected image is not generated by electrons impinging on the detector but is constituted by the more massive ionized atoms of the imaging gas. In order to obtain a projection image of the tip surface in FIM mode, a high *positive* voltage of several kV is applied to the tip leading to the ionization of imaging atoms close to the tip apex. As the ionization process of the imaging gas only occurs at very localized atomic protrusions on the tip apex where the electric field is the strongest, high spatial resolution is achieved. After ionization, the imaging gas atoms are accelerated towards the MCP detector, where they produce a spatially resolved image of the atomic structure of the tip surface.

We typically use He or Ne as an imaging gas. In order to achieve highest spatial resolution the ionization potential of the imaging gas has to be adequate. The best trade-off between high contrast at low electric fields and good spatial resolution at high fields is typically obtained using Helium with a so-called best imaging field of 47 GV/m. However, the field strength where the highest image quality is reached differs for the various imaging gases [105]. Figure 5.2(b) is recorded using Helium as image gas and a tip voltage of $V_{\text{tip}} = +8.52$ kV. The tip was cooled to a temperature of about 120 K using a liquid nitrogen feedthrough, which further increases the contrast of the FIM image.

Cleaning of the tip surface by resistive heating and field evaporation

After the etching process tungsten tips oxidize quickly at ambient air. In order to obtain a clean tip surface we can perform in-situ cleaning processes to remove adsorbates from the tip surface in the experiments. Tungsten has the highest melting point, at $T = 3683$ K, among all pure metals and can therefore withstand high temperatures. By means of resistive heating, adsorbates can be evaporated from the tip apex. Typically annealing temperatures of about 1000 K yield the best results as higher temperatures may lead to blunting of the metal nanotip. Usually, we use this annealing procedure when a new tip is assembled into the UHV chamber as this process cleans the entire emitter including the shaft of the tip. Eventually, the annealing of the tip also allows the tungsten crystal to heal crystal defects and deformations.

A very reliable and auxiliary process is the field evaporation of atoms from the tip apex. This process can be performed while imaging the tip in FIM mode and therefore

allows to monitor the cleaning of the tip apex with atomic resolution. When a large *positive* voltage is applied to the tip, protruding atoms on the tip apex are ionized and evaporated as a result of the high local electric field. Typically, field evaporation first removes adsorbates that are loosely attached to the tip apex. Increasing the tip voltage further the removal of atomic layers of tungsten can be observed one after another. The required electric field for field evaporation is usually slightly higher than the best image field in FIM mode. Due to this fact, we can record FIM images and when the applied voltage is increased above the best image field we can online monitor the progress of the cleaning process.

In the experiment we observe that after cleaning of the tip surface the field emission properties are stable over timescales of about one hour for pressures $p < 1 \cdot 10^{-9}$ mbar. After some hours we find a slight increase of the effective work function, which is most likely due to the adsorption of residual gas atoms.

5.2 Single-atom tip electron emitters

A single-atom tip (SAT) electron emitter consists of an atomically stacked pyramid on the apex of a sharp tungsten nanotip. Electron field emission from a SAT exclusively originates from the topmost atom of the pyramid [106]. These tips have been shown to emit a spatially fully coherent electron beam in a matter-wave interference experiment featuring very high contrast and a fringe pattern that spans over the entire beam width [95]. The origin of this high spatial coherence arises from the extreme localization of the electron emission. Because of the strong transverse confinement to the atomic scale, the electron wavefunction occupies discretized quantum states inside the metal tip before emission. Intuitively this can be understood by considering a particle confined inside an infinite potential well giving rise to discretized quantum states with a energy level separation being inversely proportional to the width of the potential well. In the case of a SAT, even at room temperature, the energetic spacing between these quantum states is comparable to the Fermi energy inside the metal due to the atomic scale spatial confinement. Thus, electrons primarily occupy the lowest transverse quantum state inside the metal giving raise to the excellent spatial coherence of the emitted electron beam [107, 108]. Interesting implications of this extreme spatial localization on the light matter interaction might be rendered observable if the electron emission is driven by few-cycle femtosecond laser pulses [76].

Fabrication recipe to create single-atom tips

Various techniques have been reported in the literature in order to create a SAT [109, 110, 111, 112], among the first was the controlled adsorption of a tungsten atom on a base tip [106]. Here, we exploit an ultrathin film-induced faceting of the tungsten crystal to reproducibly create SATs. As demonstrated by Fu *et al.* [113], an atomically sharp pyramid that ends in just one single atom can be obtained on the surface of the W(111) crystal facet. The formation of these atomically sharp tips is achieved by deposition of several physical mono-layers of Palladium (Pd) onto the clean tip surface followed by a thermal annealing procedure, which leads to the formation of an atomically ordered

pyramid of Pd atoms on top of the W(111) crystal facet.

The SAT fabrication recipe makes use of the fact that the W(111) facet is a morphologically unstable surface since the surface free energy of the tungsten crystal surface favors the ordering of atoms along the $\{211\}$ facets. As indicated in the sketch in Fig. 5.3(a), the tungsten $\{211\}$ facets grow towards the W(111)-direction when energy is provided by heating the tip to about 1500 K. By these means, the surface energy anisotropy of the tungsten crystal is reduced. When the growing $\{211\}$ facets start to merge they establish sharp edges between each other. As a result of the hemispherical shape of the tip apex, which ultimately leads to the formation of a three sided pyramid. If a pure tungsten crystal is used for the surface rearrangement a steady state is established before the completion of the pyramid formation as the accompanied increase in the total surface area counteracts the minimization of the surface energy anisotropy. However, when a physical mono-layer of Pd is evaporated onto the tungsten surface the surface energy anisotropy is further increased. Furthermore, the Pd atoms benefit from a higher mobility than the W atoms and they participate in the reordering of the crystal surface as Pd has approximately the same atomic dimensions and binding energy as W within the crystal lattice. As a result, faceting starts at lower temperatures of about 800 K and the completion of the atomically stacked pyramid that terminates in a single atom becomes more probable due to the increased surface anisotropy and the higher mobility of the Pd atoms.

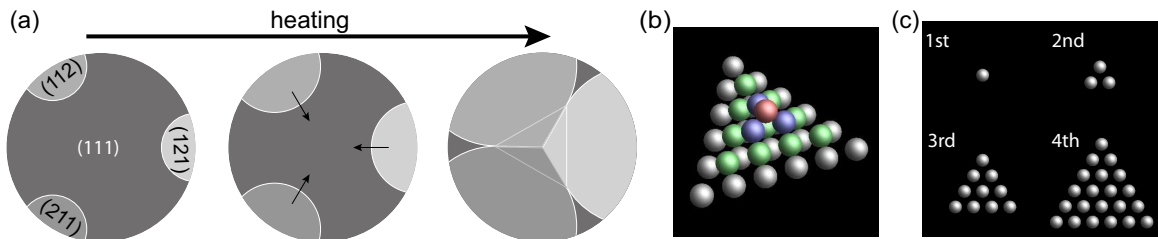


Figure 5.3: Formation of a single-atom tip induced by crystal faceting. (a), Due to the large surface energy anisotropy of tungsten the $\{211\}$ facets tend to grow when the crystal is heated. For a hemispherical crystal surface the faceting leads to the formation of a three sided pyramid. (b), Ball model an atomically stacked pyramid in the bcc lattice, as obtained during the SAT formation process. The color indicates the different layers of the pyramid. (c), The first four atomic layers of the pyramid shown in (b).

The recipe to obtain a SAT is as follows. First the tip surface is cleaned using field evaporation by applying a positive voltage of several kV to the tip. Then, roughly 1.6 physical mono-layers of Pd are deposited onto the tip. We use a linear translation stage, which allows to move a Pd filament at a distance of 15 mm in front of the tip for Pd evaporation. To calibrate the deposition rate of the Pd filament as a function of temperature, we have measured the evaporation rate using a vibrating quartz crystal and recorded the temperature of the Pd filament with a disappearing filament pyrometer. After the Pd evaporation we anneal the tip at 1000 K for 15 – 20 min, which leads to the formation of a pyramid on the tip apex that eventually terminates in a single atom.

An important property of the thermally induced faceting is that the formation of the atomic protrusion leads to a thermodynamically stable surface state. For this reason

SATs can be created several times using the same base tip simply by re-annealing the tip after deconstruction of the SAT. Figure 5.3(b) shows a ball model of the atomically stacked pyramid on top of the base tip. In Fig. 5.3(c) the four topmost single layers forming the pyramid are shown separately. In the case of a pyramidal protrusion quantum effects that arise from the extreme localization might be directly revealed in the electron emission, like e.g. the emission from localized states inside the metal. In order to confirm the successful formation of the pyramid we investigate the tip by FEM and FIM.

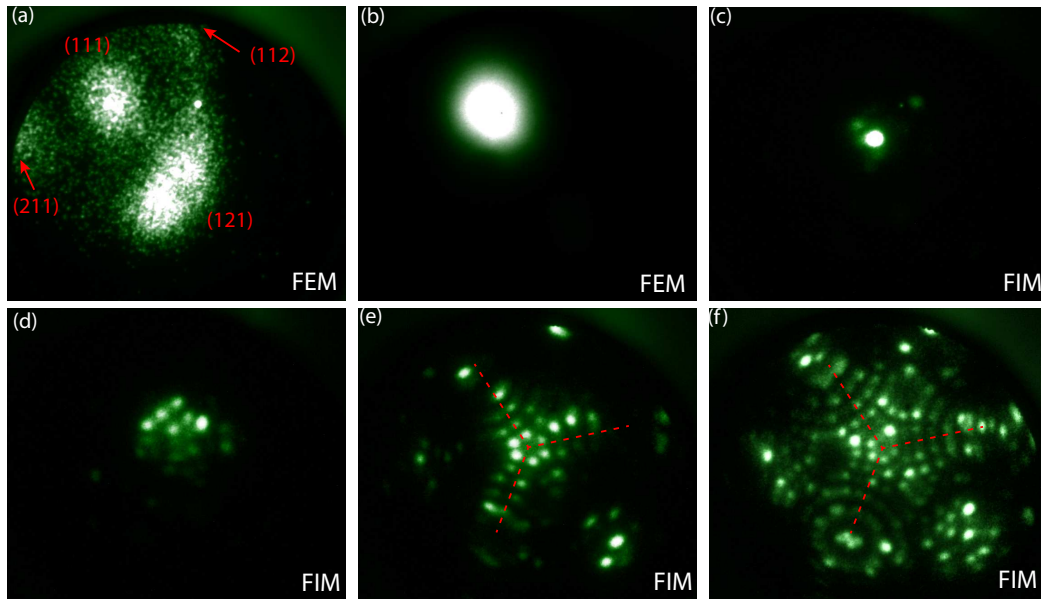


Figure 5.4: FEM and FIM images showing the generation of a SAT. (a), FEM pattern from the clean W(111) tip. (b), FEM after Pd evaporation and several annealings. (c), FIM image demonstrating the presence of a single atom on top of the atomic Pd pyramid. (d-f), FIM images illustrating the deconstruction of the Pd pyramid and the subsequent uncovering of the tungsten crystal of the base tip in (f). The color and contrast of the images has been treated to yield better visibility of small features.

FEM and FIM with a single-atom tip electron emitter

We can verify the successful formation of an atomically ordered pyramid performing FEM and FIM. A typical sequence of the investigation of a SAT is shown in Fig. 5.4. First a W(111) tip is cleaned by field evaporation, as described in Sec. 5.1, in order to start off with an atomically clean hemispherical base tip. The field emission pattern of the clean base tip is shown in Fig. 5.4(a) for a tip voltage $V_{\text{tip}} = -260$ V. Here, two of the emission spots from the $\{211\}$ facets miss the MCP and are only barely visible at the boundary of the active MCP area. Subsequently, the tip voltage is turned off and the fabrication recipe described above is conducted. After the successful SAT creation a FEM pattern as shown in Fig. 5.4(b) is observed. Now, there is only one bright and collimated emission spot at the position of the W(111)-direction for $V_{\text{tip}} = -409$ V. This already indicates the formation of the pyramid. In order to atomically resolve the SAT

pyramid we perform FIM using Neon as an imaging gas. Neon has a lower best-image field than Helium and therefore allows to record FIM images at lower voltages and to prevent any field evaporation that would deconstruct the atomically stacked pyramid. Figure 5.4(c) shows the FIM image recorded right after the SAT fabrication. Clearly, only a single atom is visible at a tip voltage of $V_{\text{tip}} = 3.85$ kV, which corresponds to the topmost atom of the pyramid. When the tip voltage is increased, field evaporation arises and evaporates the topmost atoms of the Pd pyramid leading to its deconstruction. From Fig. 5.4(c) to (f) successive snapshots of the SAT deconstruction are shown uncovering the underlying tungsten base tip step by step. The dashed red lines indicate the edges between the tungsten $\{211\}$ facets.

When applying a tip voltage of about -500 V to the successfully generated SAT we observe stable field emission with currents of $1 - 10$ nA in a single collimated spot along the W(111)-direction. The angular divergence of the field-emitted electrons can be determined from the FWHM of a Gaussian fit to the FEM spot. We typically obtain a full beam divergence angle of $6^\circ - 8^\circ$. Assuming an effective source size on the order of about 0.1 nm² the reduced brightness of the SAT at 10 nA emission current amounts to $B_r = 5.3 \cdot 10^9$ A/(m²srV) compared to typical values of $B_r \sim 10^7 \dots 10^8$ A/(m²srV) in field emission and $B_r \sim 3 \cdot 10^9$ A/(m²srV) for carbon nanotube electron emitters [114]. Repeating this recipe after destruction of the SAT we successfully reproduced up to five SATs on the same base tip before we had to assemble a new W(111) base tip.

Single-atom tips can be reliably obtained according to the above fabrication recipe. However, we removed the linear feed-through for the Pd evaporation, which introduced mechanical vibrations, in order to ensure maximum possible mechanical stability for the electron interference measurements described in the following section. To this end, all experiments described in the following are performed using conventional W(310) tips. In the near future a re-design of the Pd evaporation unit may be incorporated and single atom tips can be employed as perfect point source of electrons in the same experimental setup.

5.3 Fiber coupled near UV laser light delivery for photoemission

We have incorporated a flexible, fiber-optical setup in order to laser-trigger the electron emission from the metal nanotip. Illuminating the tip with laser light in the near ultraviolet (UV) allows to drive a one-photon emission process where the absorption of one photon results in the emission of one electron. As a result, this emission process is expected to yield high electron currents in laser-triggered emission. The implementation of a fiber-based setup benefits from several important features. First of all, the fiber coupling allows to circumvent obstacles in the vacuum chamber, like a mu-metal shield, in a very flexible manner. This might be of interest for any other application where laser light has to be delivered in narrow surroundings, for example, the electron optical column of an electron microscope. Furthermore, the fiber coupling allows to place the UHV chamber on standard air cushion supports for vibration damping without affecting the optical alignment. For these reasons, we regard our fiber-coupled laser pulse delivery

system as a prototype for laser-triggered microscopy columns, requiring high stability in the laser-tip alignment over typical acquisition times on the order of minutes [115].

Fiber coupled laser light setup

The setup described in this thesis is a refined version of a first design described in Ref. [116]. We investigated possibilities to generate near UV laser illumination. First, we generated light at a wavelength of 395 nm by using the second harmonic from 130 fs long pulses that were derived from a 2.7 MHz repetition rate long-cavity Ti:sapphire oscillator. However, an elliptical laser spot was obtained after the second harmonic generation and the maximum available laser power at the tip was limited to 5 mW. Details are described in Ref. [116]. In order to increase the available laser power we turned to a laser diode¹ providing continuous wave (cw) laser light at a wavelength of 405 nm with a saturated output power of 400 mW. By these means, we could increase the available laser power after the fiber, which reaches the tip, from 5 mW to 80 mW. Even more importantly, we incorporated new focusing optics in the UHV chamber, which allows to reduce the $1/e^2$ -beam radius of the focused light from approximately $4.7 \mu\text{m}$ down to 865 nm . This allows us to boost the laser-triggered electron yield as the laser intensity scales inversely quadratically with the beam radius. Combining the cw light source with the improved laser focus we expect an increased electron current in laser-triggered emission of about a factor of 450, which was the limiting factor in previous laser-triggered electron interference measurements described in Ref. [116].

As we will discuss in detail later, we drive a linear one-photon electron emission process at this particular wavelength where the absorption of one photon gives rise to the emission of an electron. This first order process depends on the time-averaged peak intensity of the laser beam and is completely independent on the temporal profile of the laser intensity. Hence, the emission process induced by the cw light source is the same as that for the pulsed laser. Figure 5.5(a) shows a schematic of the fiber-coupled setup. The cw laser light emitted by the diode is collimated and then coupled with a coupling lens to a polarization-maintaining (PM) fiber² with a cut-off wavelength of 350 nm and a core diameter of $2.5 \mu\text{m}$. We use four dielectric mirrors³ and an air-spaced achromatic doublet lens⁴ for alignment and tight focusing of the laser light into the PM fiber. By matching the focal spot size to the fiber's mode field diameter of $2.3 \mu\text{m}$ we achieve coupling efficiencies above 40%. We use a $\lambda/2$ -wave plate to rotate the polarization of the in-coupled light and to properly align it with either the *fast* or *slow* axis of the PM fiber leading to conservation of the polarization due to the birefringence of the PM fiber. Using a pulsed femtosecond laser source and dispersion compensation techniques, pulse durations on the order of 100 fs can in principle be achieved at the tip [117].

The fiber-coupled light is then fed into the UHV chamber using a custom made fiber feedthrough, which is designed similar to one in Ref. [118]. Inside the chamber the fiber is guided into the mu-metal box where Teflon sleeves are used to relieve any strain and to avoid breaking of the fiber. Tight focusing onto the metal nanotip is achieved

¹Wicked Lasers, Lunar S3

²Thorlabs, PM-S350-HP

³Thorlabs, BB1-E02

⁴Thorlabs, AC080-010-A-ML

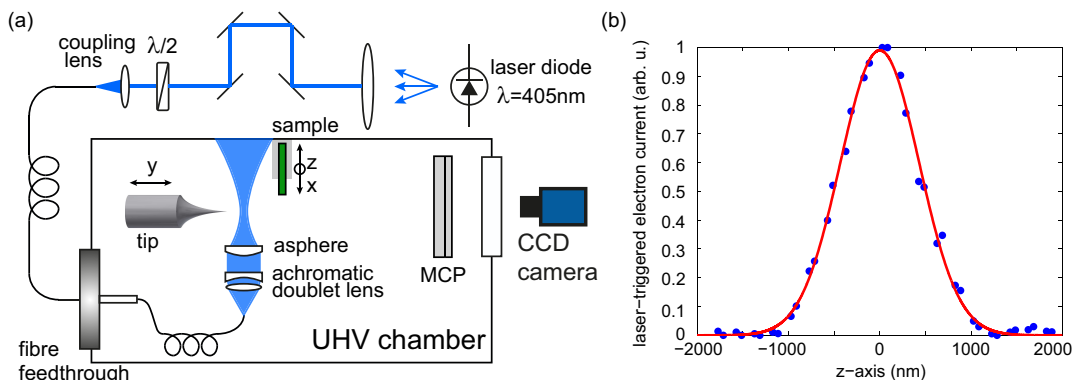


Figure 5.5: Fiber-coupled UHV laser delivery setup, focusing optics and measurement of the focal spot size. (a), Near UV light at 405 nm from a laser diode is coupled into a fiber and then transmitted into the UHV chamber. In the experimental chamber the light is focused onto the tip apex using an achromatic doublet and an asphere. (b), Spot size measurement of the focused laser light from the electron current obtained when moving the tip in z -direction through the focus. A $1/e^2$ -radius of $865 \pm 30 \text{ nm}$ is deduced.

using a combination of an air-space achromatic lens doublet⁵ for collimation of the beam and an aspheric lens⁶ with a numerical aperture of 0.5 that focuses the beam onto the tip. The assembly has been optimized using the freely available Winlens software⁷, which performs classical raytracing simulations for the estimation of aberrations. For the focusing optics optimization we fix the focal distance to a length of 15 mm in order to avoid charging of the glass surface of the focusing lens by the electron beam. The diffraction limited beam waist of the focus is 400 nm according to the simulation.

In the experiment both lenses are aligned using an aluminum tube with a diameter of 28 mm that houses both lenses (see Fig. 5.6). An inner thread allows to screw in spacer rings, which precisely set the distance between the lenses. The fiber end pointing towards the focusing optics is glued with a UHV compatible adhesive⁸ into a ferrule with a diameter of 1.8 mm, which is tightened in a v-groove on the same aluminum mount establishing a prealigned optical axis with the focusing lenses. We find a working distance of 15 mm as expected from the ray tracing simulations. Furthermore, we can deduce the beam waist of the focused laser beam by measuring the laser-triggered electron current as a function of the relative position of the tip in the focus. As will be described in the next paragraph, the photon energy at a wavelength $\lambda = 405 \text{ nm}$ leads to a linear dependence of the emitted electron current on the laser intensity [see Fig. 5.7(b)]. As a result of the linear dependence of current on the laser intensity, we can measure the beam profile of the focused laser light by moving the nanotip out of the focus and recording the emitted electron current as a function of the tip position. The finite radius of the tip of about 10 nm is much smaller than the focal spot and can be neglected. Figure 5.5(b) shows such a measurement, where a Gaussian beam profile with a $1/e^2$ -beam radius of $865 \pm 30 \text{ nm}$ is obtained from the fit (red line). We attribute the deviation of the measured spot size

⁵ Thorlabs, ACA254-050-A

⁶ Edmund Optics, Uncoated asphere, 0.5 numerical aperture, #66-310

⁷ QIOPTIC, Winlens

⁸ Epotek 301

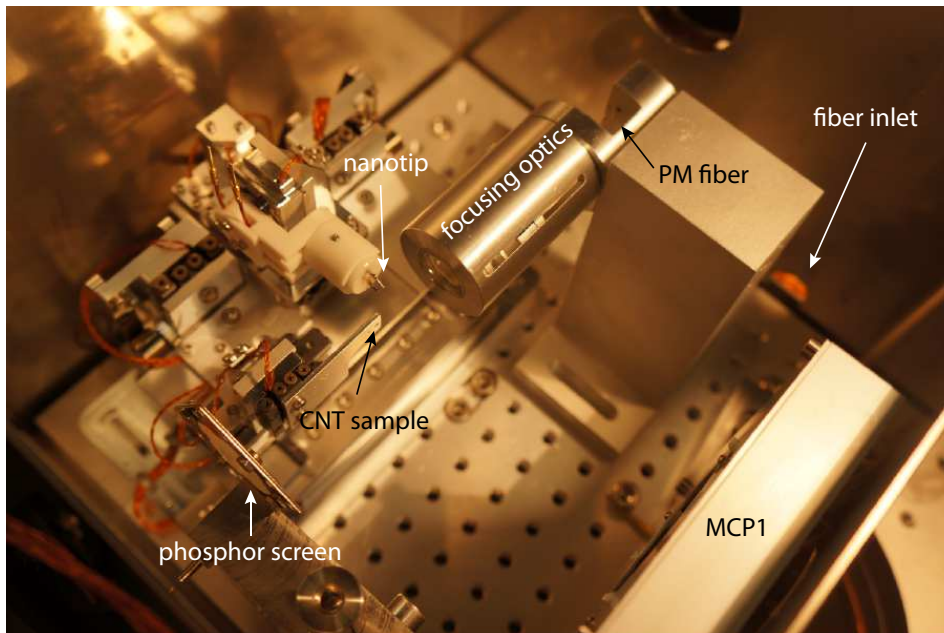


Figure 5.6: Experimental setup employed for laser-triggered electron interference measurements. Near UV laser light is focused onto the tip using a PM fiber that delivers laser light into the mu-metal box that houses the experiment. The achromatic lens doublet and the aspheric lens are mounted and aligned in an aluminum tube. The nanotip can be moved into the focus using a 8D manipulator, described in Sec. 6.1. Furthermore, a sample comprising a nitride membrane with freestanding CNTs can be brought into the electron beam path. The phosphor screen images the shadow of the tip created by the laser light and allows a coarse alignment of the tip and the laser focus.

from the simulated diffraction-limited spot size of 400 nm to aberrations arising from misalignment of the achromat and a slightly tilted aspheric lens.

Linear one-photon photoemission

Figure 5.7(a) illustrates the different mechanism of DC-field emission and one-photon photoemission in an energy level diagram close to the tip apex. The black dashed line corresponds to the potential barrier at the metal-vacuum interface for an unbiased tip. When a static negative voltage is applied to the tip DC-field emission sets in at electric fields ~ 2 GV/m and electrons are emitted from the tip by tunneling by through the effective barrier, which is reduced by the Schottky effect [indicated in green in Fig. 5.7(a)]. In order to obtain a large current in photoemission we illuminate the tip with the laser light and reduce the static voltage closely below the threshold of DC-field emission, as shown in blue in Fig. 5.7(a). In this case the DC tunneling current is still negligible, but the photoemitted current is maximized. At electric fields of 1.4 . . . 2 GV/m, the effective barrier height is reduced by the Schottky effect to 2.9 . . . 2.7 eV for the lowest work function plane in the $W(310)$ direction. At a wavelength of $\lambda = 405$ nm the photon energy is $E_{\text{ph}} = 3.06$ eV and hence the absorption of one photon provides enough energy for one electron to be emitted from the metal tip.

We have characterized the emission process experimentally and identify a one-photon

emission process, as expected. Figure 5.7(b) shows the measured dependence of the photocurrent J_{ph} with the laser power P . A linear dependence of J_{ph} with respect to the laser power is found, which verifies a one-photon process where the absorption of one photon results in the emission of one electron.

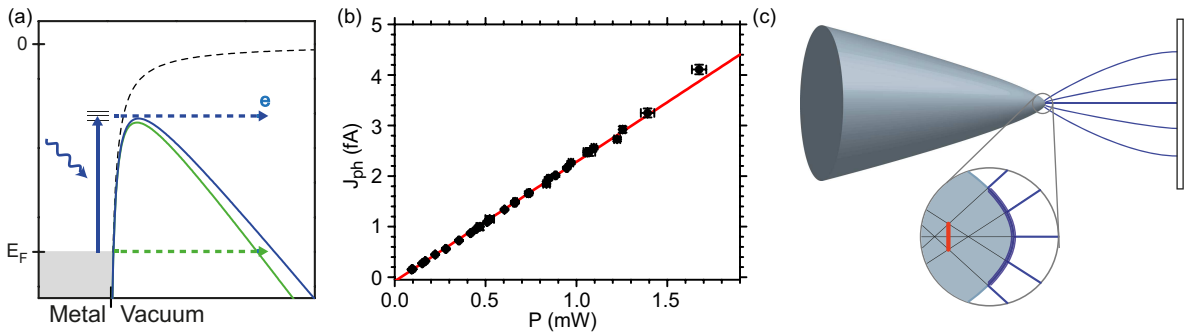


Figure 5.7: Illustration of electron emission processes and the virtual source together with experimental characterization of the photoemission process. (a), Schematic of one-photon photoemission (blue) and DC-field emission (green). Electrons from states below the Fermi-level E_F are excited by laser irradiation and emitted over the barrier, which is lowered due to the Schottky effect. At sufficiently high DC-fields the barrier becomes narrow enough to permit direct tunneling through it, giving rise to DC-field emission. **(b),** The linear dependence of the photocurrent on the applied laser power, clearly indicates a one-photon emission process. **(c),** A virtual (or effective) source (red) is formed behind the tip's apex by extrapolating electron trajectories back into the metal tip. This virtual source is substantially smaller than the geometrical source size (blue). Solid lines indicate electron trajectories.

The work function of tungsten depends upon the specific crystallographic direction of the tungsten crystal (see Sec. 5.1). In DC-field emission electrons are predominantly emitted from the [310] crystallographic plane, which has the lowest work function of tungsten $\Phi = 4.35$ eV. In photoemission, with $E_{ph} = 3.06$ eV and DC-fields closely below the field emission threshold the absorption of one photon provides enough energy for electrons from crystal planes with work functions up to 4.8 eV (without DC-field) to be photo-emitted over the Schottky-lowered barrier. In the experiment this manifests itself by the higher divergence of the photoemitted electron beam of 10° (half opening angle) compared to 6° in DC-field emission.

5.4 Coherence measurement of laser-triggered electron emission

Coherent electron sources are central to studying microscopic objects with the highest possible spatial resolution. Meanwhile, nanotips operated in DC-field emission are known for their paramount spatial coherence properties and employed in practical applications for almost half a century [119]. Hence, highest resolution microscopy as well as coherent imaging, such as holography and interferometry, have long been demonstrated using DC-field emission [13, 23, 120]. Here we investigate whether the high spatial coherence of

electron beams emitted from a metal nanotip is preserved in photoemission by comparing the spatial coherence of photoemitted electron beams to their DC counterparts.

5.4.1 Spatial coherence in DC-field and photoemission

The spatial coherence of electron sources is commonly quantified by means of their effective source radius r_{eff} . It equals the radius of a virtual incoherent emitter that resembles the coherence properties of the real emitter. A virtual source is formed in a finite area where electron trajectories intersect when extrapolating their paths back into the metal tip, like indicated in Fig. 5.7(c). Using the van Cittert-Zernicke theorem, it can be shown that r_{eff} scales inversely proportional with the transverse coherence length ξ_{\perp} of the emitted beam: the smaller the (effective) source, the more coherent the beam (see Eq. 5.1). For tungsten field emitters typical values for r_{eff} are on the order of 0.4...1 nm in DC-field emission, significantly smaller than the geometrical tip radius that is typically in the range of a few tens of nanometers [23, 22].

An upper bound for r_{eff} is obtained by measuring the full width of coherent illumination at the detector screen. Commonly this is done by identifying the distance between the outermost fringes in an interference pattern with ξ_{\perp} . This is based on the assumption that the interference pattern washes out because its width exceeds the transverse coherence length of the beam [121]. Under experimental conditions the interference pattern might also wash out because of mechanical vibrations or other imperfections and, hence, we can only give a lower bound for ξ_{\perp} . The van Cittert-Zernicke theorem relates ξ_{\perp} and the effective source radius r_{eff} for an incoherent emitter with Gaussian intensity profile [121, 122]

$$r_{\text{eff}} = \frac{\lambda_{\text{dB}} \cdot l_{\text{s-d}}}{\pi \cdot \xi_{\perp}}. \quad (5.1)$$

Here λ_{dB} is the electron de Broglie wavelength and $l_{\text{s-d}}$ the source-detector distance.

As illustrated in Fig. 5.7(a), DC-field and laser-driven emission occur due to fundamentally different emission processes [123]. The former is a tunneling process through a static potential barrier and covered within the Fowler-Nordheim-theory [99], whereas a variety of laser-driven emission processes exist. They are distinguishable into linear one-photon emission, nonlinear multi-photon and tunneling processes, with the respective prominent examples of Einstein's photoelectric effect and multi-photon photoemission [124]. The effective source radius is highly sensitive to the shape of the electron trajectories in close vicinity of the tip apex [125], and hence to the emission process. As a result, the coherence properties in photoemission might be drastically different from DC-field emission.

5.4.2 Electron interference at a carbon nanotube biprism

To compare the coherence properties of a W(310) tungsten tip electron emitter with a radius of ~ 10 nm in laser-triggered and DC-field emission we record electron matter-wave interference images in both emission modes. We use a freestanding carbon nanotube (CNT) as an electron beam splitter, which acts as a biprism filament with nanometer radius [13]. It splits the wavefront of the electron matter wave in two parts, which

are then overlapped at the electron detector, giving rise to interference fringes on the detector screen [22]. The electrically grounded CNT is brought into the electron beam path at a typical distance of less than one micrometer from the tip, resembling a point projection microscopy configuration [126]. The CNT and the gold coated holey silicon nitride membrane, which supports the CNT, act as a counter electrode for the biased tip. Electron interference can be observed in DC-field emission as well as in laser-triggered mode when a near-UV laser beam is focused on the tip's apex.

Electron interference patterns can be observed when approaching the tip to the CNT sample. Figure 5.8 shows a typical laser-triggered electron interference pattern for a tip-sample distance of $\sim 5 \mu\text{m}$ where several CNTs, freely suspended over a holey nitride membrane, can be observed. The substrate for supporting the CNTs is made of a 200 nm thin film of silicon nitride supported by a rigid silicon frame⁹. Arrays of holes with a diameter of $2 \mu\text{m}$ are arranged in a rectangular pattern with a pitch of $12 \mu\text{m}$. The CNTs are grown on the substrate and over its holes employing a chemical vapor deposition process. The CNT growth was performed by the group of Prof. A. Högele at the LMU and is described in detail in the supplement of Ref. [127]. After examination of the sample in a scanning electron microscope it is coated with a 5 nm layer of gold on both sides using a 5 nm layer of titanium as adhesion promoter for the sample to act as a (grounded) counter electrode in the experiment.

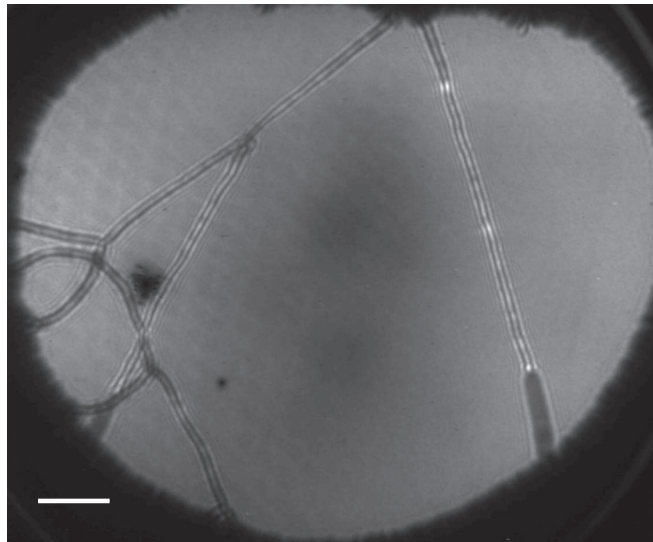


Figure 5.8: Laser-triggered point projection image of carbon nanotubes spanning a hole of the carrier substrate. At this magnification ($\sim 2 \times 10^4$), which corresponds to a tip-sample distance of $a \approx 5 \mu\text{m}$, the interference pattern is dominated by Fresnel diffraction and biprism contributions (see text) are less pronounced. The scale bar represents 4 mm on the MCP detector screen. The black spots in the image are artifacts of the MCP.

For this rather large tip-sample distance and hence low magnification, the interference pattern forms according to the so called holographic regime [128]. Here the projected image represents an in-line hologram of the CNT. The incident electron wave is scattered off the sample and interferes with the unscattered part of the wave, which gives

⁹DuraSiN, DTM-25231

rise to a Fresnel-like pattern with one broad fringe in its center (see Fig. 5.8). When approaching the CNT further, the magnification increases and the interference pattern forms according to the biprism regime, where the static electric fields around the CNT start to play a major role. Even though the CNT sample is electrically grounded the impinging electron beam creates secondary electron emission from the CNT, which results in a local positive charging of the suspended CNT because of its finite electrical conductivity [126]. As a consequence, electric fields are created that lead to the deflection and subsequent overlapping of the two parts of the electron beam, which are split by the CNT, in the detector plane. A cosinusoidal interference pattern is observed, equivalent to those obtained with an electrostatic biprism [129]. For intermediate magnifications the interference pattern is a convolution of both regimes with Fresnel and biprism contributions.

5.4.3 Demonstration of high spatial coherence in photoemission

Electron interference patterns in laser-triggered and DC-field emission are shown in Fig. 5.9(a) and (b), respectively, recorded at the identical CNT position with a tip-sample distance of less than $1\ \mu\text{m}$. Only very low static voltages are required to obtain DC-field emission because of the small geometrical tip radius of about 10 nm and the short tip-sample distance. Clearly, interference fringes that are aligned parallel to the CNT are observed in both modes. A tip voltage of $U_{\text{tip}} = -41\ \text{V}$ is chosen in laser-induced emission, such that the barrier is lowered for efficient photoemission. The measurement is performed with a focused laser power of $P = 5.7\ \text{mW}$, which results in a photocurrent of approximately 0.375 pA. For DC-field emission a voltage of $U_{\text{tip}} = -53\ \text{V}$ is applied, leading to a comparable field emission electron current as in photoemission. The slightly larger fringe spacing in Fig. 5.9(a) arises from the different electron deBroglie wavelengths, which are given below and result from the different tip bias voltage of $-41\ \text{V}$ compared to $-53\ \text{V}$ in DC-field emission.

The electron interference images shown in Fig. 5.9 represent an average of 200 individual images, each one recorded with an exposure time of 21 ms, with a standard 8-bit dynamic range CCD camera and a 35 mm objective from outside of the vacuum chamber. Individual images are superimposed but shifted against each other in order to cancel effects of slow linear drifts. These are most likely induced by heating of the sample with the cw-laser beam and slow cooling during image acquisition with the DC-field emission source (opposite signs of the drifts). The applied shift from image to image is found by fitting the central fringe of the pattern with a Gaussian function.

The panels in Fig. 5.9(c), (d) show line profiles obtained from integrating the count rate parallel to the fringes in the marked rectangular area in the inset to the figure. The spatial coherence width is obtained from these line profiles by counting the number of interference fringes (marked by arrows in the line profiles) and deducing the distance between the two outermost fringes. In laser-triggered mode we observe at least 21 fringes and we obtain $\xi_{\perp}^{\text{ph}} \geq 5.9\ \text{mm}$ for photoemission at a CNT-screen distance of 79.5 mm. With $\lambda_{\text{dB}} = 1.8\ \text{\AA}$, the effective source radius equals $r_{\text{eff}}^{\text{ph}} \leq 0.80 \pm 0.05\ \text{nm}$. In DC-field emission mode we count at least 35 fringes and a very comparable value of the coherence width is deduced from Fig. 5.9(d) with $\xi_{\perp} \geq 7.7\ \text{mm}$, albeit slightly larger.

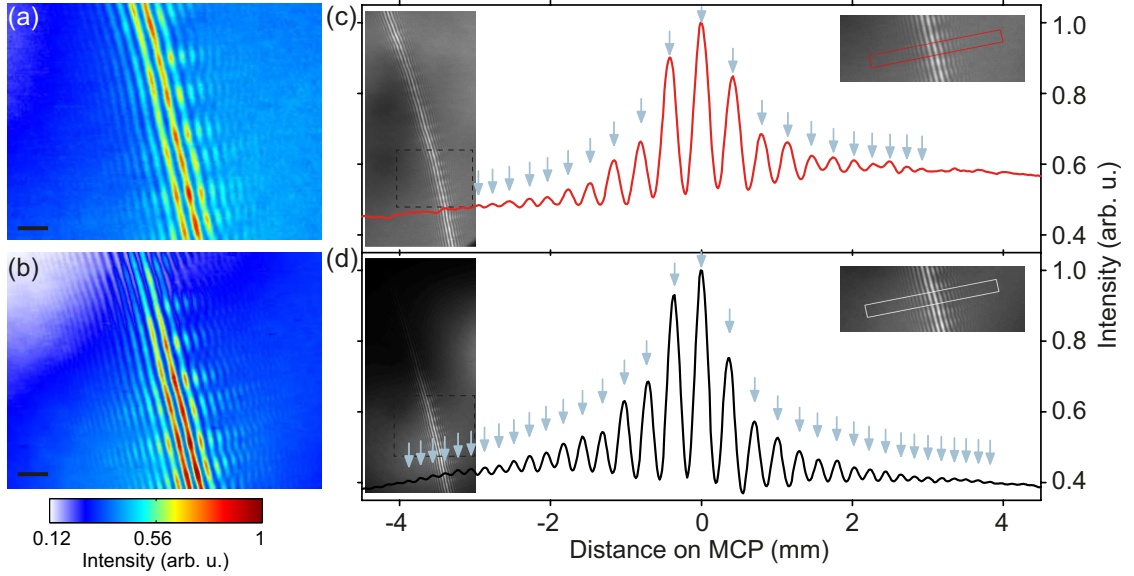


Figure 5.9: Electron interference measurement in DC-field and photoemission.

(a), Laser-triggered electron emission at a bias voltage of $U_{\text{tip}} = -41$ V. Without laser illumination no electrons are observed at this voltage. The scale bar corresponds to 1 mm on the detector screen. (b), DC-field emission with $U_{\text{tip}} = -53$ V. A modulation of the fringe pattern along the CNT direction is also clearly discernible, arising from local distortions of the CNT and locally enhanced DC-fields leading to de- and constructive interference effects. Line profiles of the interference fringes are integrated perpendicular to the orientation of the CNT in laser-triggered (c) and DC-field emission (d). The box in the right inset indicates the 9.3 mm^2 large integration area. The left inset shows a larger detector image. At least 21 fringes in the laser-triggered mode and 35 in DC-field emission mode are visible as indicated by the arrows. The slightly finer fringe spacing in laser-triggered emission is due to the smaller electron de Broglie wavelength.

With $\lambda_{\text{dB}} = 1.7 \text{ \AA}$ the effective source radius equals $r_{\text{eff}}^{\text{DC}} \leq 0.55 \pm 0.02 \text{ nm}$, in line with previously published values in Refs. [22, 121].

Clearly, the source radii in laser-triggered and DC-field emission mode differ only slightly, even though the emission process is qualitatively different. Furthermore, in both cases the effective source radius is more than an order of magnitude smaller than the geometrical source radius of 10 nm. For comparison, the record resolution laser-triggered electron microscope employs a fully illuminated flat LaB_6 cathode of a few tens of microns in diameter [130]. However, besides high spatial coherence, and hence a small effective source, a high photocurrent is required in most time-resolved imaging applications such as ultrafast electron diffraction. This requirement directly translates into the necessity of a high brightness of the electron beam. With increasing electron current it can be expected that the effective source size increases due to space charge and stochastic Coulomb electron-electron repulsion [125]. Strictly, these effects come into play for more than one electron per pulse emitted from the tip. Hence most conservatively, the maximum current attainable with highest spatial coherence is set by the repetition rate f_{rep} of the laser. For instance, laser pulses with $f_{\text{rep}} = 100 \text{ MHz}$ inducing emission of one electron per pulse yield a time averaged current of 16 pA. Even though this value is

low compared to the electron current emitted from standard field emission guns, electron imaging with a stably aligned laser beam, as demonstrated here, remains well possible as demonstrated in time-resolved scanning electron microscopy [115]. The restriction to one electron per pulse however, also prevents other unwanted detrimental effects such as temporal electron pulse broadening due to Coulomb repulsion [131].

Next to the transverse coherence, quantified by r_{eff} , the longitudinal energy spread of the electron beam ΔE is crucially important for most applications. The energy spread obtained from the one-photon electron emission has been measured in a previous work in our group [132] and here only the result is given. The energy spread ΔE of the photoemitted beam equals 0.51 ± 0.06 eV (FWHM), almost twice as much as in DC-field emission [23]. This implies that the longitudinal coherence length is smaller by a factor of about 2 in photoemission [120], likely causing the reduced visibility of the interference pattern in Fig. 5.9(c) compared to 5.9(d).

In conclusion, the coherence of the electron beam in one-photon photoemission close to the threshold is almost as high as that of a DC-field emitted beam. It has been previously shown that the initial electronic states inside the metal from which the electrons originate affect the coherence of the DC-field emitted electron beam [22]. Our measurements demonstrate that the coherence of the original electronic states inside the metal is maintained in photoemission as well. One may thus expect that a cooled tip also provides a fully coherent beam under laser irradiation, as demonstrated in DC-field emission [22]. Furthermore, the laser-triggered emission from a single-atom tip promises ultimate spatial coherence if photoemission originates from localized electron states inside the metal. The creation of an atomically ordered pyramid with a single atom termination might allow to study the light matter interaction of ultrashort laser pulses with extremely localized electrons in a single protruding atom.

The measurement of the effective source radius of a laser-triggered, tip-based electron source will be of great importance for an active research area investigating femtosecond point projection microscopy [133], ultrafast low-energy electron diffraction [134] and combinations of both [135] employing a laser-triggered nanotip as an electron source. With regard to the construction of a coherent pulsed electron source for the electron guiding experiment we conclude that we can employ the laser-triggered electron source without losing the superior spatial coherence of metal nanotip electron sources. In the following chapter we will report on the design and construction of a field emission electron gun specifically intended for the electron guiding experiment.

6 A coherent field emission gun for electron guiding

In this chapter we report on the construction of a field-emission electron gun specifically designed for the injection of electrons into a planar surface-electrode microwave guide. The injection of electrons into low-lying motional quantum states of the electron guide sets stringent requirements on the electron-optical properties of the electron source. Most importantly, the electron beam has to be focused to the diffraction limit and therefore excellent coherence properties of the electron emitter as well as electrostatic focusing optics with low aberrations are required. In Ch. 5 the excellent spatial coherence of metal nanotips has been demonstrated, revealing that the emitted electron beam is highly coherent in DC-field and photoemission. Furthermore, these tips feature a spatially confined emission hot spot and provide a bright and collimated beam. Here we describe the electron optics implemented in the electron gun and demonstrate first results from electron guiding experiments using this novel source. The ability to focus fiber-coupled laser light in the near-ultraviolet (UV) onto the tip apex will allow us to laser-trigger the electron source, which enables the injection of short electron pulses in future experiments.

6.1 UHV chamber and experimental setup

In the course of this thesis an ultra-high vacuum (UHV) chamber was assembled with the goal to study the spatial coherence of metal nanotip electron sources and to incorporate such a tip in a novel coherent electron gun design for the microwave guiding experiments. In order to obtain stable field emission from a metal nanotip UHV background pressures of below $1 \cdot 10^{-9}$ mbar are required. This implies the careful design of all components that are assembled in the UHV environment in addition to efficient pumping. In the following the experimental apparatus is introduced. It features a sophisticated nanopositioning system with eight degrees of freedom to position the nanotip with respect to the electron lens and the microwave guide. In order to focus near-UV laser light onto the nanotip, we use fiber-coupled focusing optics, which have been described in Ch. 5. This allows to avoid obstacles, as e.g. the mu-metal shield and to deliver laser light to the tip in a compact manner. All parts in the UHV chamber are placed inside a mu-metal box for the shielding of external magnetic fields.

6.1.1 Experimental chamber

The experimental chamber is pumped to UHV pressure, i.e. $p < 1 \cdot 10^{-9}$ mbar, in three stages. First the UHV chamber is evacuated to a pressure of $2 \cdot 10^{-2}$ mbar using a rotating

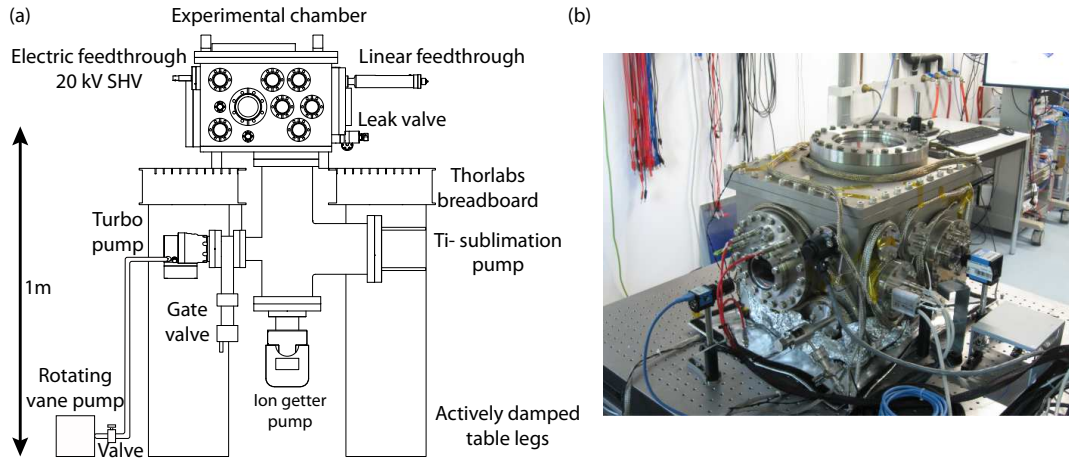


Figure 6.1: Experimental setup housing the field emission electron gun. (a), Close-up of the experimental apparatus comprising the vacuum system and the experimental chamber. (b), Photograph of the experimental chamber.

vane pump¹. Once a backing-pressure of $5 \cdot 10^{-1}$ mbar is reached the turbo pump² can be launched yielding a pressure of $1 \cdot 10^{-7}$ mbar. At this stage, usually, a bake-out of the vacuum chamber at temperatures of about 80°C is performed allowing to reach pressures in the low $1 \cdot 10^{-9}$ mbar range. This relatively low baking temperature is chosen due to the low glass transition temperature of the UHV compatible PEEK polymer, which is included in several parts that are assembled in the chamber, as e.g. the enclosure of the electrostatic lens. After the bake-out, the ion getter pump³ is switched on pumping the chamber down to $2 \cdot 10^{-10}$ mbar in combination with the titanium-sublimation pump⁴. Figure 6.1(a) shows a schematic of the experimental apparatus. The vacuum chamber is standing on a custom designed breadboard⁵, with a 30 cm centered hole, which allows to attach the pumping unit from below the table. The breadboard is mounted on actively damped table legs in order to reduce mechanical vibrations during the experiments. Furthermore, a UHV gate valve⁶ allows to turn off and disconnect the turbo pump from the vacuum side in order to avoid mechanical vibrations from the rotating blades. In order to reduce the outgassing rates of the assembled aluminum parts, the surfaces of all aluminum pieces are chemically treated according to the recipe given in Ref. [136].

Inside the UHV chamber a mu-metal box houses all the components of the electron guiding experiment in order to shield the low-energy electrons from ambient magnetic fields. A characterization of the magnetic shielding is given in Sec. 6.1.3. The field emission electron gun is depicted at the bottom of Fig. 6.2. A nanometric tungsten tip is spot-welded onto a support loop, which is fixed onto a standard SEM/TEM ceramic Kimball mount⁷. The tip is attached to a positioning unit, which will be described in

¹ Pfeiffer Vacuum, Duo 1.6/M

² Pfeiffer Vacuum, HiPace 60 P

³ Gamma Vacuum, TiTan 75S

⁴ Vacom, Titanium-sublimation pump

⁵ Thorlabs, Optical Breadboard 900x750x60mm

⁶ VAT, VATLOCK CF63 gate valve

⁷ Kimball Physics, Glass AEI Bases

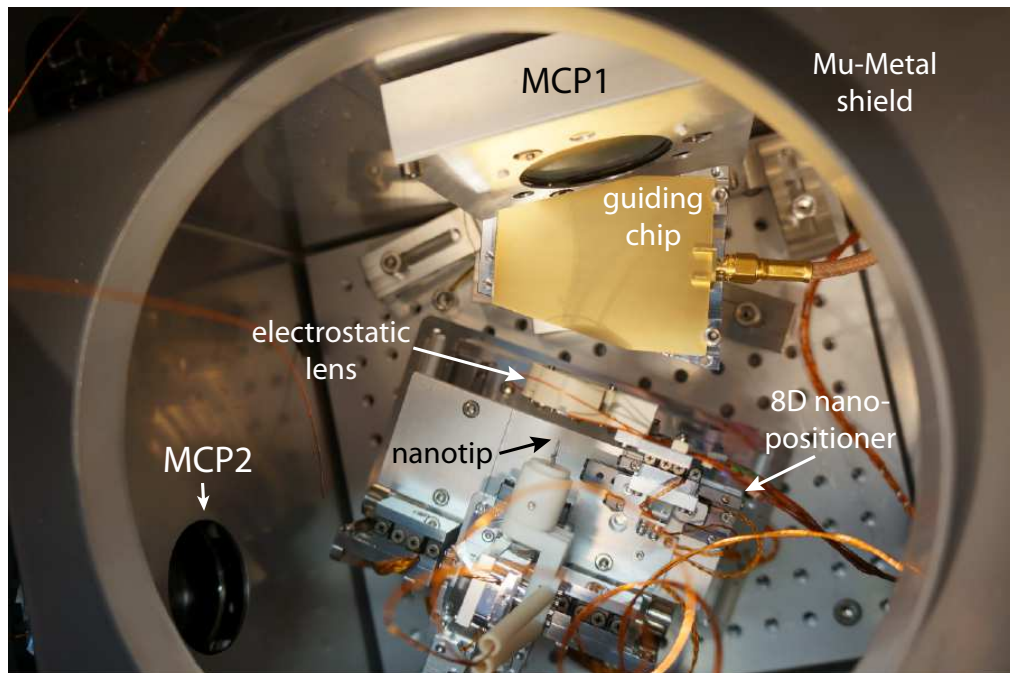


Figure 6.2: Experimental setup used for the microwave guiding of electrons. The metal nanotip can be positioned with the 8D nanopositioning stage with respect to the electron lens and the microwave guiding chip. Guided electrons are detected on a microchannel plate (MCP) electron detector, which is housed inside a metal box (MCP1) for screening of the supplied DC voltages. When the metal tip is rotated 90° counter-clockwise the second detector MCP2 can be used for a characterization of the metal tip without lens and guiding substrate. All the components are assembled inside a mu-metal box. Here the top cover was removed for better visibility.

detail in the next section. The positioner allows to precisely align the tip with respect to the electron lens, which is mounted upstream of the metal tip and itself sits on a positioning unit to move the lens in and out of the electron beam path. Furthermore, the tip and the electrostatic lens are mounted together on a separate manipulator, which can be positioned relative to the electron guiding substrate. Electrons that are injected into the microwave guide travel along the guiding electrodes and are detected by a microchannel plate detector⁸ behind the microwave chip (MCP1). Using a rotatable positioner, the metal tip can be rotated 90° counterclockwise and pointed towards a second detector (MCP2). Here the tip can be characterized in FEM and FIM without the electron lens and the guiding substrate in the electron beam path.

6.1.2 8D nanopositioning system

In the course of this thesis a dedicated, UHV compatible nanopositioning system comprising eight positioning degrees of freedom has been designed and constructed. The manipulator is based on stick-slip piezo driven positioners⁹ allowing to perform fine

⁸ *Photonis*, APD 2 PS 40/12/10/12 I 46:1 P20

⁹ *SmarAct GmbH*, <http://www.smaract.de>

steps down to 50 nm (step mode). Moreover, with a slow elongation of the piezo element the slide can be moved with sub-nanometer resolution within a range of about $1.4 \mu\text{m}$. The manipulator can be divided into two positioning units. One for the alignment of the nanotip with respect to the electrostatic lens, which defines the electron optical axis, and another that allows to position the aligned assembly of tip and lens together with respect to the electron guide. The alignment of the nanotip requires only small travel lengths of relatively light components. In contrast, the second manipulator unit for the positioning relative to the electron guide carries a total weight of about 500 g and requires travel ranges on the order of several centimeters.

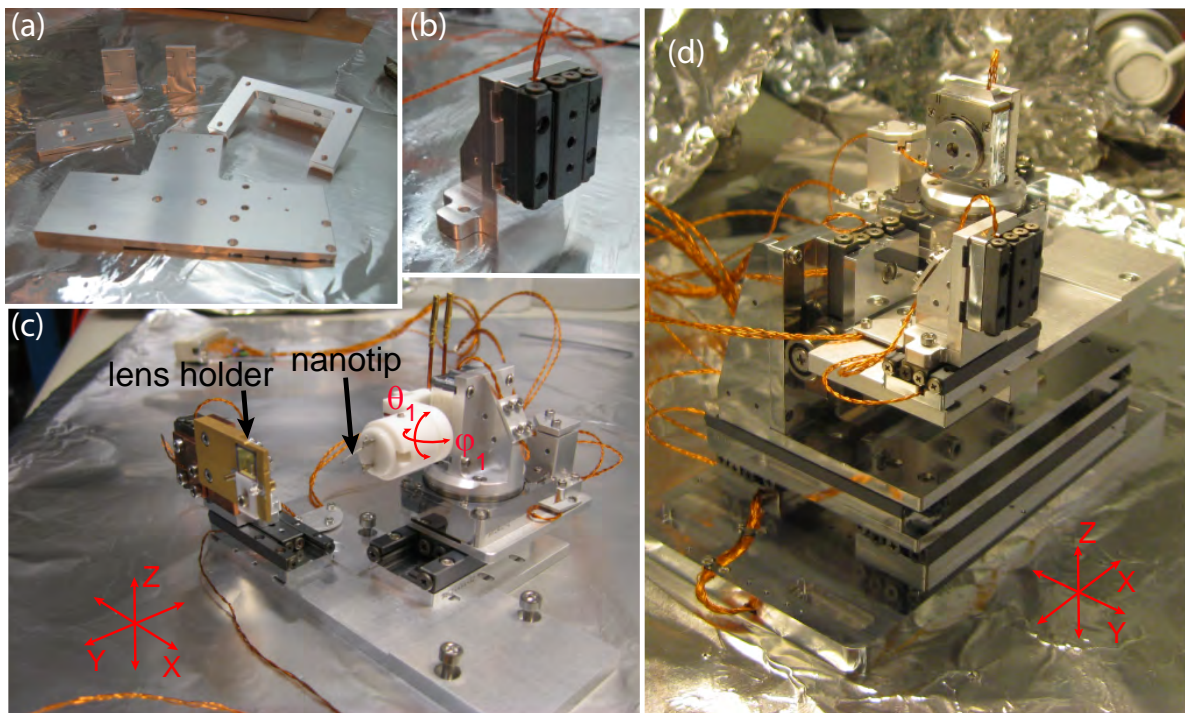


Figure 6.3: Photographs of the 8D nanopositioner. (a), Aluminum pieces connecting the different positioning stages. (b), Linear stick-slip positioner mounted on angle bracket. (c), Positioning unit for nanotip alignment with respect to the sample holder or electron lens respectively. (d), Entire 8D manipulator with both positioning units mounted together.

Figures 6.3(a) to (c) show the assembly of the tip-lens positioning unit with home built aluminum connecting pieces. The lens holder is movable in the xz -plane perpendicular to the nanotip's orientation, whereas the tip can be approached towards the lens along the y -axis. In the diffraction measurements described in Ch. 5, the lens holder was used to position the CNT sample. Additionally, the tip can be rotated left-right and up-down using two rotators. Altogether, this setup is fixed to a base plate, which can be screwed onto the second positioning unit. This second positioning unit comprises double railed positioning stages along the x -, y - and z -direction. Two calibrated support springs are attached to the z -positioner in order to compensate for the heavy load of the tip-lens unit. All positioners that require absolute positioning, as e.g. the y -axis that sets the tip-to-lens distance, are equipped with an optical sensor allowing for closed-loop operation with a position read-out accuracy of $\pm 5 \text{ nm}$. Furthermore, all positioners

can be controlled via Matlab allowing for automated movements like raster scans or an active signal feedback.

6.1.3 Electric and magnetic shielding

The guiding of electrons is performed at electron kinetic energies below 10 eV. For this reason, any perturbing electric or magnetic fields strongly deflect the slow electron beam and may easily prevent electron guiding. In order to eliminate any charging of dielectric surfaces, the electron beam is fully shielded along the electron optical axis. The electron lens design consists of a dielectric mount, which electrically isolates and aligns the lens elements from each other. Any dielectric surface is recessed into ditches from the electron optical axis with a minimum aspect ratio of 1 : 5. Furthermore, the guiding substrate is enclosed by gold plated copper covers, which have been removed in Fig. 6.2 for better visibility. The only dielectric surfaces that are exposed to the electron beam are the isolating gaps between the electrodes on the guiding chip. To this end, small isolating gaps are favorable, which currently have a width of 50 μm and a depth of 20 μm .

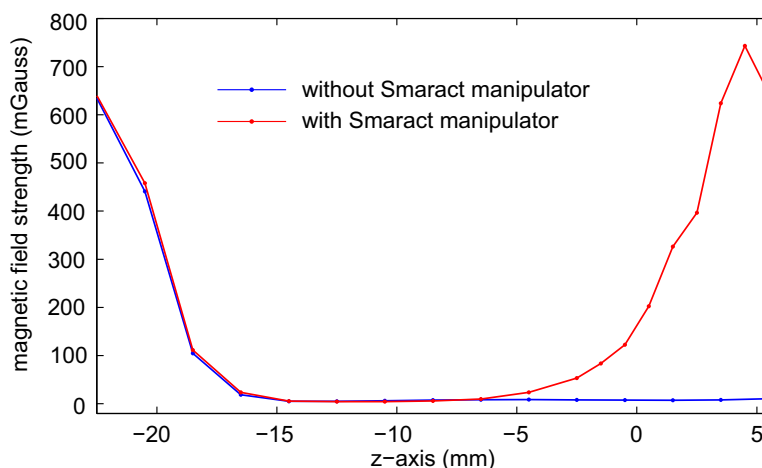


Figure 6.4: Measurement of residual magnetic fields in the guiding experiment.

The blue line shows the magnetic shielding of the mu-metal box when dipping the magnetic field sensor into the empty mu-metal box. Here $z = 0$ mm corresponds to the guide's height. The red line shows the same measurement when the Smaract positioner is inside the mu-metal box. The manipulator produces magnetic fields of about 200 mG at the guide's height.

The electron guiding setup is enclosed by a mu-metal box¹⁰ for shielding of external magnetic fields, like e.g. the earth's magnetic field. The mu-metal housing consists of four separate pieces that can be fitted into each other. However, there are several round openings with diameters from 5 to 50 mm in order to feed through electrical cables and to provide optical access to the fluorescent phosphor screens behind the MCP detectors. These holes reduce the magnetic shielding factor of the mu-metal housing. We have used a flux gate magnetic field sensor¹¹ to measure the magnetic shielding factor. Figure 6.4

¹⁰ *Magnetic Shields Ltd.*, <http://magneticshields.co.uk>

¹¹ *Stefan Mayer Instruments*, FLC3-70

shows the measured absolute magnetic field strength as a function of the height along the vertical z -axis. Here $z = 0$ mm corresponds to the height of the electron optical axis. The blue line shows a measurement with an empty mu-metal box in the UHV chamber. We find a shielding factor on the order of ~ 100 leading to a DC magnetic field strength $B < 10$ mG inside the mu-metal box. However, the Smaract manipulator turns out to produce large magnetic fields, as can be seen from the red line, which corresponds to the same measurement but with the manipulator placed in the mu-metal box. We find a DC magnetic field on the order of 200 mG at the height of the electron optical axis. In order to estimate the impact of magnetic fields on the guided electrons we equate the Lorentz force $F = evB$ with the harmonic restoring force $F = -m\omega^2\Delta x$ in the electron guide assuming a homogeneous magnetic field perpendicular to the electron motion. For an electron with $E_{kin} = 1$ eV and a trap frequency $\omega = 2\pi \cdot 100$ MHz this yields a displacement of $\Delta x = 5 \mu\text{m}$, which is much smaller than the transverse acceptance area of the electron guide and therefore the residual magnetic fields do not prevent electron guiding. However, without the guiding potential the deflection of an electron due to the Lorentz force is given by $dx = ez/(8mE_{kin}) \cdot B_y$ yielding a deflection of $\Delta x = 7.5$ mm when traveling a distance $z = 50$ mm. These large deflections make the alignment of the nanotip to the electron lens as well as the alignment of the electron gun with respect to the electron guide very difficult and currently limit the performance of the electron source. In future experiments either non-magnetic positioners have to be used, or a second mu-metal shield surrounding the manipulator has to be inserted as we observe a significant impact of the DC magnetic fields on the unguided electron beam, as will be described in Sec. 6.2.2.

6.2 Electron optics

We have simulated and tested several electron lens designs in the course of this thesis. The investigations have been restricted to electrostatic electron optics as magnetic components always result in a rotation of the electron beam around the optical axis, which is not wanted for electron guiding. Furthermore, electrostatic electron optics can be modified in a very flexible manner as the elements of the design basically consist of simple metallic apertures with a small pinhole in the center. The main difficulty for an electron lens operating at very low electron energies in the range from 1 to 10 eV, is to find a suitable geometry with moderate focusing action. In fact each radial electric field component that leads to focusing of the electron beam is directly connected by Maxwell's equations to the longitudinal component of the electric field, which results in the deceleration of the electron beam. In close vicinity to the electron optical axis one finds from Gauss's law that $E_r = -\frac{1}{2}r \frac{\partial E_y}{\partial y}$. Therefore, any decelerating field implicitly results in a focusing of the electron beam. Furthermore, the focusing of very low energy electrons suffers from strong chromatic aberrations, which scale inversely proportional to the electron landing energy, according to Eq. 2.36.

The following section describes the electron lens design that emerged from several iterations of particle tracking simulations and experimental tests. First, the working principle of the electron optics is described and then the focusing performance of the lens is characterized. Finally, some experimental measurements are presented demonstrating

the operation of the electron lens and technical difficulties are discussed regarding a quantitative measurement of the diameter of the focused electron beam.

6.2.1 Design and trajectory simulations of the electron lens

The design requirements that we impose on the field emission electron gun can be directly related to a minimum number of optical elements that have to be implemented. The need to set the final electron energy, to focus the electron beam, or to create a sufficiently high electric field at the tip to obtain field emission directly determine the voltages that have to be applied to specific elements in the electron optical column. Except for an deflection element, all elements of the electron optical system consist of circular metallic apertures, which may vary in the diameter of the pinhole and the outer diameter of the aperture disk.

Figure 6.5 shows a cut through the electrostatic lens design comprising the apertures. It is convenient to specify all electric potentials with respect to a ground potential, which is applied to the last aperture of the column and denoted with V_{B3} . The final electron energy is accordingly given by the negative potential applied to the field emission tip and will lie in the range $V_{tip} = -1 \dots -10$ V. In order to obtain electron field emission from the nanotip, which sets in at electric fields of ~ 2 GV/m at the tip apex, the first aperture facing the tip at a distance of about $200 \mu\text{m}$ has to be hold on a positive potential on the order of $V_{extr} = 100$ V. This aperture is called the extractor. After the electron beam has passed the extractor we use an aperture with a tiny pinhole, which we call beam forming aperture, to shapes the beam and cut out only paraxial rays. This way, the probe forming semi angle θ_i can be controlled to reduce spherical and chromatic aberrations (see Eqs. 2.35, 2.36).

The purpose of the electrostatic lens design is to focus and to decelerate the electron beam to the required electron energy. The deceleration to electron energies in the electron volt range intrinsically leads to a very strong focusing effect and therefore the task is rather to weaken the focusing of the electron lens sufficiently in order to assure that the focal spot of the lens lies behind the exit aperture of the gun and not already within the lens. From the particle tracking simulations presented below it is found that it is favorable to sequentially decelerate the electron beam. This is done by applying fixed electric potentials of $V_{B1} = 30$ V to the beam defining aperture, $V_{B2} = 10$ V to the last element of the focusing unit and $V_Q = 8$ V to all electrodes of the quadrupole deflector. The remaining voltage V_f , which is applied to the third electrode in the column, is used to perform the focusing of the electron beam and adjusted accordingly. Finally the beam passes a quadrupole aperture, which consists of four electrodes that where fabricated by milling a round aperture symmetrically into four quarters. An image of the quadrupole element is shown in Fig. 6.9. It can be used to deflect the beam and correct for misalignment from the optical axis until the electron beam approaches the last aperture and is decelerated to the final electron energy. In total this requires nine separate elements that can be biased with electric potentials.

The extractor as well as the two electrodes behind the small beam defining pinhole have an aperture diameter of $300 \mu\text{m}$. The quadrupole element has a large diameter of 4 mm in order to obtain as linear deflecting fields as possible close to the optical axis. The last aperture features a diameter of $500 \mu\text{m}$. The pinhole diameters as well as the

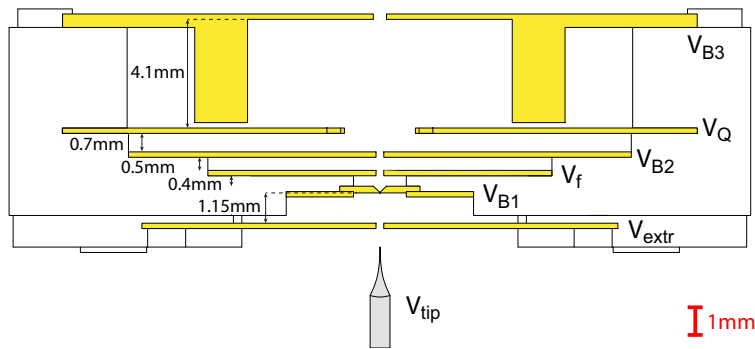


Figure 6.5: Cut through the electron lens design. The nanotip is placed in front of the extractor aperture with potential V_{extr} at a distance of about 0.15 mm. The electron beam is then confined by a $5\ \mu\text{m}$ pinhole V_{B1} and focused by the subsequent apertures. A quadrupole aperture allows to deflect the beam before it is decelerated to its final energy and leaves the exit aperture of the gun.

distance between the elements have been optimized using particle tracking simulations and minimizing the aberration coefficients of spherical and chromatic aberrations.

Figure 6.6(a) shows an exploded CAD drawing of the electrostatic lens design. In total six metallic elements can be mounted into precise fittings of a PEEK holder. This PEEK holder has a diameter of 30 mm and has been milled by a CNC machine in a single run in order to provide perfect alignment of the fitted aperture elements. Except from the beam defining aperture, which is manufactured from platinum and bought from a commercial supplier¹², all apertures comprising the lens design have been fabricated in the institutes machine shop. The apertures that are drawn in green in Fig. 6.6(a) are made out of a $200\ \mu\text{m}$ thick titanium sheet, whereas the elements indicated in red are made out of copper. Before assembling the lens all metallic pieces were polished, cleaned in an ultra-sonic cleaner using DMSO, annealed at 250°C and sputtered with a $\sim 1\ \mu\text{m}$ thick layer of gold. This method of preparing the apertures is crucial to avoid charging from any contaminations on surfaces that are exposed to the electron beam. Before mounting all elements into the PEEK holder, thin Kapton insulated copper wires are spot welded to the aperture electrodes. Figure 6.6(b) shows an image of the readily assembled electron lens.

Particle trajectory simulations

The particle trajectories have been simulated using the commercial boundary element method (BEM) software CPO¹³. They are performed for electron energies ranging from 1 to 5 eV in order to characterize the focusing performance of the electron lens. In the simulation, electron trajectories are released at the apex of the metal nanotip with a radius of curvature of 15 nm. The extractor voltage is adjusted such that an electric field of 2.1GV/m is generated at the tip apex, which is sufficient to obtain electron emission from the tip. For a tip-extractor distance of $200\ \mu\text{m}$ this results in a required potential

¹² *Plano GmbH*, Pt aperture, A0300P

¹³ *Charged particle optics*, CPO

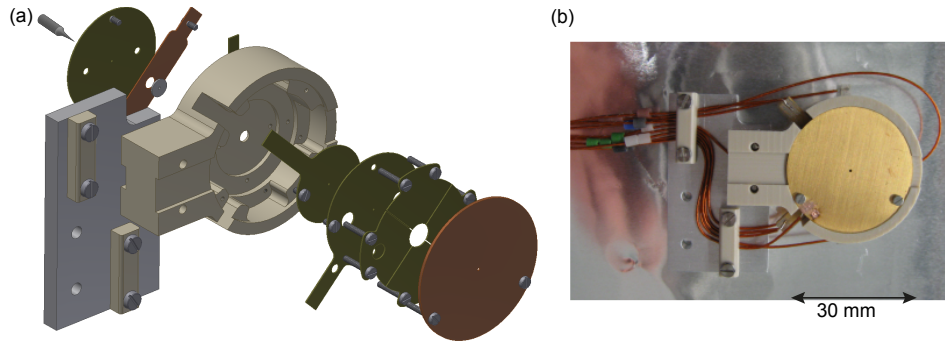


Figure 6.6: Electrostatic lens design comprising nine metallic electrodes. (a), Exploded assembly drawing showing the separate elements. The nanotip is shown in the upper left corner followed by the extractor aperture and a small Pt aperture fixed by a copper sheet. These apertures as well as all remaining elements are aligned by fitting them in precisely machined grooves of the peek holder. (b), Photograph of the readily assembled electron lens showing the last aperture and the wires connecting all elements of the lens.

difference of $V_{extr} - V_{tip} = 147.5 \text{ V}$ between tip and extractor. However, the extractor voltage can always be increased if higher electron currents are needed.

There are two possible modes to focus the electron beam when passing through the lens, called deceleration and acceleration mode. Choosing the focusing voltage V_f to be either much smaller or much higher than the potentials on the surrounding elements results in both cases in a radial focusing action. However in the one case the electron is decelerated inside the lens and in the other case it is accelerated. In both modes the electron beam ends up with the same kinetic energy behind the lens. However, it is a major advantage of the acceleration mode that the electron beam is at higher energy when passing through the lens, which generally results in less chromatic aberrations compared to the deceleration mode. For this reason we only consider the acceleration mode in the following.

From the particle trajectory simulations with varying energy and focusing voltage V_f we deduce the working distance behind the lens as well as the resulting diameter of the electron beam. Figure 6.7(a) shows the result of the simulations where the electron beam diameter is plotted as a function of the working distance for the different electron energies. As the beam diameter is extracted from classical particle tracking simulations, no diffraction effects are included here and the obtained finite beam diameter only arises from spherical and chromatic aberrations. The different colors indicate the final electron kinetic energy of the electrons behind the lens. Clearly, small working distances behind the lens are favorable as the beam diameter increases for all electron energies with the focal distance behind the lens. Furthermore, for a fixed working distance behind the lens the minimum achievable beam diameter decreases with increasing electron kinetic energy. This indicates that the beam diameter is dominated by chromatic aberrations.

In order to compare the different contributions of aberrations to the focused electron beam diameter it is helpful to study its dependence on the probe forming semi-angle θ_i . This angle θ_i is crucial to determine the effect of aberrations and diffraction. The diameter of the Airy disc, which results from diffraction, is inversely proportional to θ_i , whereas the contribution from chromatic aberration scales linearly and the spherical aberration

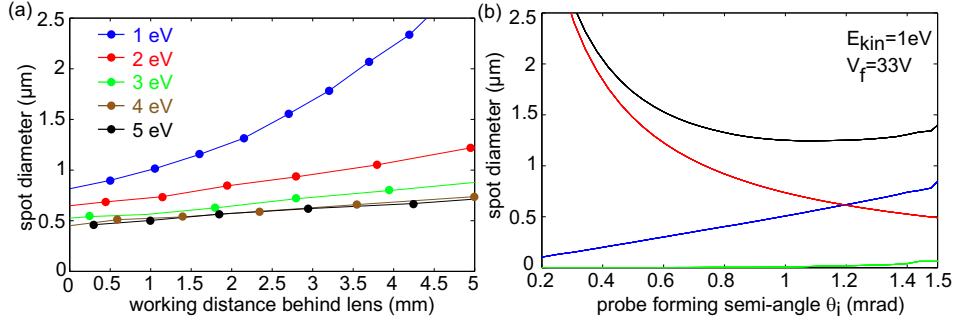


Figure 6.7: Simulation of the focusing performance of the electron lens. (a), Focused beam diameter from classical particle tracking simulations, without diffraction effects, as a function of the working distance. For every working distance and electron energy the focusing voltage V_f has been adjusted to yield a focus at the given working distance. For increasing energy a smaller beam can be achieved identifying chromatic aberrations as limiting effect. (b), Beam diameter including spherical and chromatic aberration as well as diffraction for $E_{kin} = 1 \text{ eV}$ and a working distance of 0.5 mm (black line). The contributions to the beam diameter from spherical (green line) and chromatic (blue line) aberrations and the Airy disc (red line) are shown. Here the focusing voltage is $V_f = 33 \text{ V}$.

according to the third power in θ_i , as can be seen from the Eqs. 2.33, 2.35 and 2.36. To this end, there is an optimum angle θ_i , which depends on the beam defining pinhole, with a diameter of $5 \mu\text{m}$, the distance to the nanotip and finally the magnification of the lens.

The spherical and chromatic aberrations can be deduced from the trajectory simulations. The chromatic aberration disc is obtained by simulating two extremal rays that form the envelope of the beam with $E_{kin} = 1 \text{ eV}$ and another with $E_{kin} = 1.3 \text{ eV}$. Here we assume $\Delta E = 0.3 \text{ eV}$, which is the reported value in field emission from metal nanotips [23]. As a result, two focal points are obtained and the contribution of chromatic aberration to the defocus can be determined. A similar procedure is performed to obtain the spherical aberration where a monochromatic beam with various starting angles is simulated. As the the diffraction disc is a mere wave-optical property of the electron beam and only depends on θ_i and the electron energy we can simply extract θ_i from the simulation and calculate the size of the diffraction disc d_d from Eq. 2.33. Figure 6.7(b) shows the separate contributions to the beam diameter resulting from the spherical d_s (green line) and chromatic d_c (blue line) aberrations as well as the diffraction disc d_d (red line) at $E_{kin} = 1 \text{ eV}$. Adding up all components according to $d_p = \sqrt{d_d^2 + d_s^2 + d_c^2}$, one obtains the total spot diameter including diffraction, which is plotted in black. The focusing voltage $V_f = 33 \text{ V}$ has been adjusted in the simulation to obtain a minimum focal spot size at the working distance of 0.5 mm .

As expected, one obtains the characteristic scaling of the different contributions to the spot size with θ_i . Furthermore, diffraction (red line) and chromatic aberrations (blue line) dominate the beam diameter at $E_{kin} = 1 \text{ eV}$, whereas spherical aberrations (green line) can be neglected. From these simulations we infer an optimum probe forming semi angle $\theta_i = 1.1 \text{ mrad}$. At this specific angle the total beam diameter reaches its minimum size with a spot diameter of $d_p = 1.24 \mu\text{m}$ for $E_{kin} = 1 \text{ eV}$. For smaller angles the beam diameter is limited by diffraction, whereas for larger θ_i chromatic aberration starts to

dominate. From the linear slope of the chromatic contribution we can determine the chromatic aberration constant $C_c = 2$ mm. The geometry shown in Fig. 6.5, which is also realized in the experiment, allows to reduce θ_i effectively by retracting the tip from the extractor aperture. However, the extractor voltage has to be simultaneously increased to keep the electric field at the tip high enough for field emission. Typically, we performed experiments at distances of about $200 \mu\text{m}$, which results in $\theta_i = 1.48$ mrad. As can be seen from Fig. 6.7(b), the corresponding spot diameter is still very close to its optimum.

As motivated in Sec. 2.3, the final goal is to image electron wave packets directly into the motional quantum ground state of the transverse harmonic guiding potential. As a result, we can directly estimate the required beam diameters for typical transverse trap frequencies ranging from $\omega = 2\pi \cdot 100 \dots 1000$ MHz. According to the spatial extent $\Delta x = \sqrt{\hbar/(2M\omega)}$ of the harmonic ground state in the electron guide we obtain a spatial width of the quantum ground intensity distribution ranging from $w_0 = 2\Delta x = 607 \dots 192$ nm and can estimate the required angles θ_i for an electron energy of 1 eV requesting a perfectly matched. According to Eq. 2.29 this yields $\theta_i \simeq \frac{\lambda}{\pi w_0} = 0.64 \dots 2$ mrad. If we additionally require that the beam diameter produced by chromatic aberrations should be smaller than the width of the Gaussian beam w_0 we can deduce an upper boundary for the chromatic aberration coefficient using Eq. 2.36. Accordingly, this yields $C_c \leq w_0 \frac{\Delta E}{E}^{-1} \theta_i^{-1} = 3.14 \dots 0.3$ mm. The chromatic aberration constant $C_c = 2$ mm obtained from the simulations lies within that range. This is in line with the wave-optical simulations presented in Sec. 2.3.1, where we found that with $C_c = 2$ mm and $E_{kin} = 1$ eV the beam is mainly limited by diffraction at the beam forming aperture. However, the above assessments have to be considered carefully and are supposed to give only a rough estimate on the electron lens performance. For a rigorous treatment of the injection efficiency into the quantized states of the electron guide one should consider the actual spatial current density distribution as well as radial phases, which accumulate due to diffraction effects and lens aberrations. Here only classical raytracing simulations are considered and the envelope of these rays is used as an estimate of the beam diameter.

In conclusion the electron lens design presented here provides focusing close to the diffraction limit in an energy range below 10 eV. With respect to the injection into the electron guide the chromatic aberrations of the lens are sufficiently low to obtain a large overlap between the focused electron beam and the ground state wavefunction of the guiding potential. In the following a first experimental characterization of the electron lens is presented.

6.2.2 Experimental performance of electron lens

We have set up the electrostatic lens, as shown in Fig. 6.2, in the UHV chamber to characterize the performance of the electrostatic lens. We use a National Instruments card¹⁴ to generate the required static voltages required for operating the lens. This allows to perform automatized voltage scans and measurements. After a coarse alignment of the tip to the extractor aperture typically a bright transmitted electron beam can be found

¹⁴National Instruments, PCI 6733

on the MCP detector, which is normally located at a distance of 70 mm behind the lens. Once a small electron current is transmitted through the electron lens, the fine alignment can be done by optimizing the circularity and the brightness of the transmitted electron beam.

The most important feature of the electron lens is to deliver an electron beam at energies below 10 eV for injection into the microwave guide. The lens design allows to decelerate the electron beam to the desired final energy without influencing the total electron current. This can be achieved by reducing the negative tip voltage V_{tip} to yield the desired final electron energy and simultaneously keeping the potential difference $V_{tip} - V_{extr}$ constant by increasing the extractor voltage V_{extr} and thus keeping the electric field at the tip apex constant.

Figure 6.8(a) shows the typical behavior of the detected electron beam when decreasing the final electron energy from 100 eV down to 5 eV as observed on the MCP. Most noticeable is the energy dependent drift of the electron beam. As can be seen the electron beam drifts about 7 mm on the phosphor screen, without deteriorating the beam profile (except for the 5 eV beam). We attribute these drifts to the residual magnetic fields of the 8D-manipulator (see Sec. 6.1.3), where we estimated an expected beam drift of ~ 7.5 mm for a 1 eV electron beam. Several attempts have been undertaken to compensate these magnetic fields using three pairs of coils in a Helmholtz configuration that were installed around the vacuum chamber. However, it turned out that the homogeneous magnetic field created by the Helmholtz coils did not allow to compensate the magnetic field drifts satisfactorily. Using a flux gate to measure the homogeneity of the residual magnetic fields, we found an inhomogeneous distribution of magnetic fields that were only present close to the manipulator and therefore a compensation by external homogeneous fields was not possible.

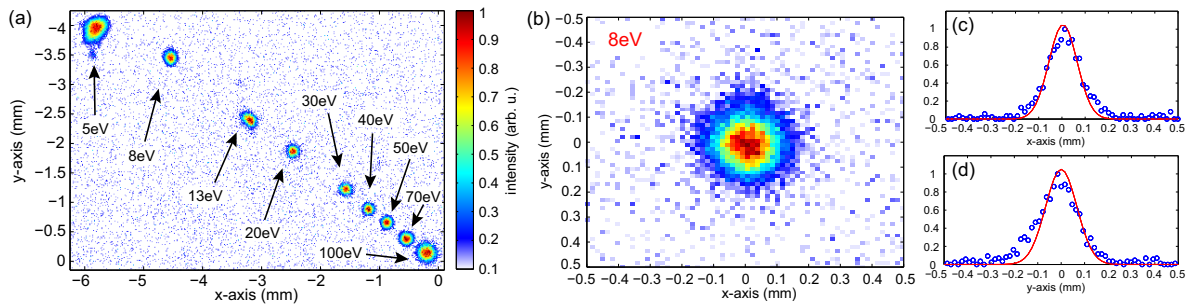


Figure 6.8: Experimental characterization of the electrostatic lens. (a), Drift of the electron beam with decreasing electron energy from 100 eV to 5 eV. Here individual images are added. (b), Electron beam profile at 8 eV detected 70 mm behind the lens. The focus of the beam is several millimeters behind the lens and hence the beam has diverged significantly when being detected. Profiles of the beam in the vertical (c) and horizontal (d) direction with a FWHM diameter of $\sim 150 \mu\text{m}$. We deduce a beam half opening angle of 1.07 mrad at 8 eV from the measurement.

We can use the quadrupole element to deflect the electron beam and to compensate for the magnetic field drift. Figure 6.9(a) shows an image of the quadrupole element. In the usual configuration all four electrodes are biased with a static voltage of $V_Q = 8$ V. Additionally, we can apply voltages to the individual elements to create electric fields

that deflect the beam. In order to create homogeneous electric fields on the optical axis, we always symmetrically shift voltages on the opposed electrodes. For example, a horizontal deflection voltage of $V_{defl}^H = 1\text{ V}$ is applied via a voltage of $V_Q - 0.5\text{ V}$ on the left electrode and $V_Q + 0.5\text{ V}$ on the right electrode of the quadrupole element. In Fig. 6.9(b) a summation of images is shown where we have applied a sequence of deflection voltages with an amplitude of $V_{defl} = 10\text{ V}$ and $V_Q = 5\text{ V}$ at an electron beam energy of 50 eV . We obtain a star-shaped image where the symmetry of all arms of the star confirms that the elements of the quadrupole are well aligned and symmetrically assembled in the holding frame of the lens. The quadrupole deflector is a useful element to compensate for the beam drifts during electron guiding experiments. At very low energies, where the beam drift inside the lens is so large that the beam cannot exit the last aperture anymore, the quadrupole deflector allows to deflect the beam back on the optical axis, however, under a considerable angle. Hence the magnetic field is a severe issue to reach final electron energies of about 1 eV and currently limits the performance of the field emission electron gun.

Despite the magnetic field drift we find a circular beam profile with reducing diameter for decreasing electron energy in Fig. 6.8. This is due to the fact that for low final electron energy the decelerating field in the lens has to be stronger, which automatically leads to a focusing effect. We find that below 10 eV any change to the focusing voltage V_f leads to an increasing beam diameter at the MCP. The reason for this is that at these very low energies the focusing effect of the deceleration already produces a beam focus between the electron gun and the detector. Every increase in the focusing strength reduces the distance of the focal plane to the electron source and, hence, a larger magnified beam profile is obtained at the MCP.

Figure 6.8(b) shows a beam profile at $E_{kin} = 8\text{ eV}$. As can be seen, the field emission electron gun delivers a nice circular electron beam even at electron energies below 10 eV . In addition, we do not observe any temporal drifts of the electron beam, which suggests that there are no unwanted charging effects that influence the performance of the electron optics. From the line profiles shown in Figs. 6.8(c) and (d) we deduce a FWHM spot diameter of $150\ \mu\text{m}$ at the position of the detector. The MCP detector has a spatial resolution on the order of tens of micrometers. Therefore, the measured beam profile shown in Figs. 6.8(b) was recorder for a large distance the lens and detector such that the diverged beam can be resolved by the MCP. However, this measurement does not provide about the focused spotsize in the focal plane of the lens, which is right behind the lens. The distance from the electron lens to the detector is 70 mm and we measure a half-opening angle of 1.07 mrad of the electron beam.

So far we did not find any means to measure the spot size of the focused electron beam that is produced by electron lens. Typically knife-edge measurements or a microscopy resolution measurement yield a reliable determination of the focal spot size of an electron gun. Here, as we are working with extremely low electron energies, any contact with a knife-edge or a surface for the determination of the spot size has a dramatic impact on the electron beam. We observe severe charging and scattering of the electron beam at metal surfaces. To this end, no reliable measurement has been performed so far and up to now we can only investigate the magnified beam profiles far behind the focal point at the MCP detector.

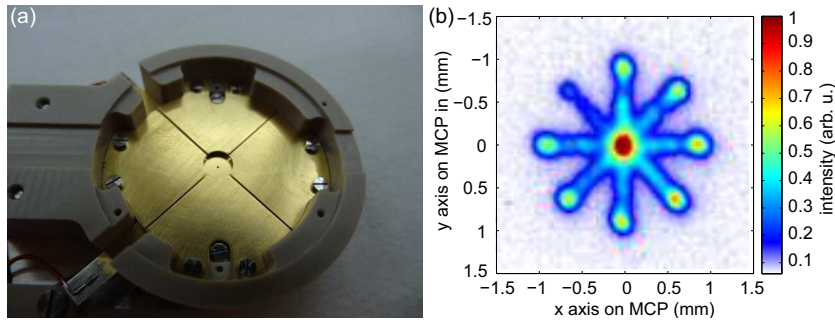


Figure 6.9: Characterization of the quadrupole deflector. (a), The quadrupole elements are mounted into the PEKK fitting of the electron lens. (b), Measured deflection of the electron beam when applying alternating deflection voltages to the horizontal and vertical deflection electrodes. Depending on the phase between the deflection voltages we can create star-shaped electron patterns when the image acquisition time is longer than the deflection sequence.

As a result of the residual magnetic fields of the positioning unit the electron gun is currently limited to electron energies larger than 5 eV. When reducing the energy below 5 eV the electron beam touches the last aperture of the electron lens which leads to a broadening of the electron beam. This can be seen for the beam profile with $E_{kin} = 5$ eV in Fig. 6.8(a). Accordingly, when reducing the electron energy further no electron beam is detected any more, as the electrons hit the last element of the lens.

In conclusion we can use the quadrupole element to compensate for magnetic field drifts and use the electron source down to energies of 5 eV. This is not a sufficient means to account for the magnetic field drifts in future experiments, as the required compensation differs, for example, when the source is moved to a different location inside the vacuum chamber because of the inhomogeneity of the residual magnetic fields. However, already now it allows us to employ the field emission electron gun for electron guiding experiments with much better beam quality as the thermionic electron gun described in Sec. 3.1.3. First electron guiding measurements employing the field emission electron source are described in the next section.

6.3 Electron guiding using the field emission gun

This thesis provides important progress towards the smooth injection of electrons into the guide. The final goal is to reduce the transverse energy of the guided electron beam to a regime where it becomes comparable to the energy quantization of the transverse guiding potential. In Ch. 3 we presented optimized electrode coupling structures that minimize disturbances during the passage from the electron gun into the guide. Experiments and simulations suggest that the transverse energy of the guided electron beam is now limited by the electron optical properties of the thermionic electron source with a spot size of $100 \mu\text{m}$ and an opening angle of 15 mrad. Here we report on the first electron guiding measurements using the field emission gun (FEG), described in the previous sections, for the injection of electrons in the guide.

We have performed electron guiding measurements with the FEG and the thermionic

source using the same microwave chip comprising the optimized zigzag-shaped coupler design shown in Fig. 3.20. A comparison of both guiding signals is shown in Fig. 6.10. We observe a collimated signal of guided electrons at the output of the guide at $x = 0$ mm using the FEG in Fig. 6.10(a). The signal is obtained for $E_{kin} = 7$ eV with $\Omega = 2\pi \cdot 1010$ MHz and $V_0 = 34.5$ V. Most remarkably, we do not observe any electron losses and a bright and collimated guided electron beam is detected with a FWHM width of $311 \mu\text{m}$. For comparison, Fig. 6.10(b) shows a guiding signal using the thermionic electron source with $E_{kin} = 3$ eV and similar microwave parameters $\Omega = 2\pi \cdot 1000$ MHz and $V_0 = 34$ V. A guided electron beam is obtained at $x = 0$ with a FWHM width of $650 \mu\text{m}$. Furthermore, there are several counts of lost electrons that spiral around the guided spot and extend to larger x values. This is an indication for a transverse energy of the guided beam that is comparable to the potential depth U of the guiding potential. When increasing the kinetic energy of the thermionic source the amount of electron loss increases and starting from 5 eV the electron loss signal starts to dominate the detected electron signal. This behavior can be explained by the centrifugal force acting on the guided electrons on their curved path to the detector increasing the transverse energy of the guided beam and leading to an increase of the loss signal for larger E_{kin} .

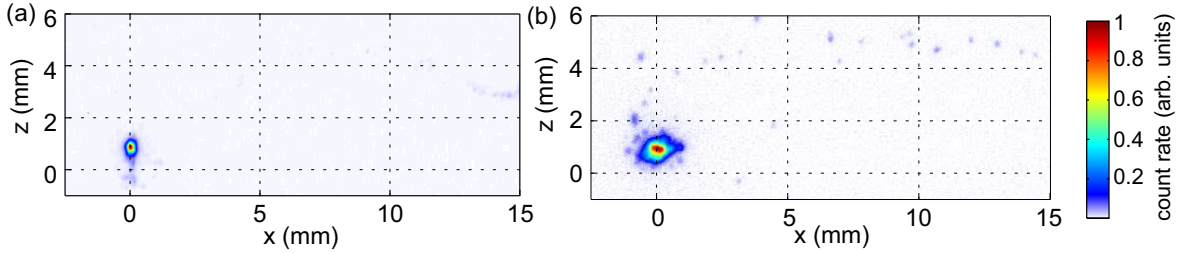


Figure 6.10: Guiding signals using the field emission source and the thermionic gun. (a), Electron guiding signal employing the FEG for electron injection with $E_{kin} = 7$ eV, $\Omega = 2\pi \cdot 1010$ MHz and $V_0 = 34.5$ V. No losses are detected. (b), Guiding signal using the thermionic source with $E_{kin} = 3$ eV, $\Omega = 2\pi \cdot 1000$ MHz and $V_0 = 34$ V for comparison. Both measurements have been performed using the optimized zigzag-shaped coupling structure shown in Fig. 3.21(c). The trap parameters are $\omega = 2\pi \cdot 133$ MHz, $U = 42$ meV and $q = 0.37$.

Both, the smaller spot size as well as the absence of electron losses provide a clear evidence of the superior electron optical properties of the FEG, which allows to significantly reduce the transverse energy of the guided electron beam. Using the FEG the transverse energy of the injected electron beam is low enough that the centrifugal force at $E_{kin} = 7$ eV, which additionally excites the electron beam, can be fully compensated by the guiding potential depth U . This also confirms that the electron losses observed when employing the thermionic source at the same energy originate from the deficient beam quality of the gun. No quantitative comparison of the electron guns is possible because we can not achieve sufficiently low electron energies with the FEG and increasing E_{kin} to 7 eV with the thermionic source, we do not observe a suitable guided signal anymore as needed for a comparison.

The FEG will allow to significantly improve the injection of electrons into the guide. However, modifications to the gun design are mandatory as we can currently not re-

duce the electron beam energy below 5 eV because of residual magnetic fields. We have designed a new mu-metal shield that will specifically house the guiding substrate and therefore screen the electron beam from the magnetic fields. This shield has already been ordered and only needs to be implemented in the setup. In future experiments, we will laser-trigger the electron emission from the nanotip electron source and synchronize the injection of electron pulses to the microwave drive of the guide. Using the fiber-coupled setup described in Ch. 5, we will be able to obtain electron pulse durations on the order of 10 ps. This corresponds to one hundredth of the the microwave drive frequency and therefore allows to fully resolve the microwave phase. Furthermore, the FEG provides a spatially coherent electron beam, which provides a starting point for on-chip electron interferometry using the novel electron beam splitter presented in Ch. 4.

7 Conclusion and outlook

This thesis presented two central experimental findings that will open new avenues in coherent control of electron matter waves. We conceived and performed an experiment that demonstrates, for the first time, the realization of a chip-based beam splitter for low-energy electrons. This represents a first and decisive step towards guided electron interferometry using this approach. Furthermore, we have provided experimental evidence that the spatial coherence of metal nanotips, which are employed as coherent electron sources in DC-field emission in commercial electron microscopes, is almost fully preserved in laser-triggered emission. A finding that has direct impact on all time-resolved applications that employ coherent electron beams.

The realization of the beam splitter for guided, low-energy electrons relies on the precise control over the electron motion that can be reached in the near-field of a planar microwave chip. The high field gradients that are achievable allow for the generation of versatile potential landscapes. By precise patterning of the planar chip electrodes, a finely structured beam splitter potential for guided electrons can be realized. We have conceived a suitable chip electrode layout that is compatible with planar transmission line technology for the feeding of microwave signals and allows the generation of a transverse beam splitter potential. This beam splitter potential is capable of splitting a guided electron beam symmetrically into two output arms. In the experiment we inject low-energy electrons into the beam splitter potential. The electrons are guided along the chip electrodes until they reach a junction where the potential gradually transforms from a single well into a double well, which results in the splitting of the guided beam. We observe efficient beam splitting for electron energies up to 3 eV. A comparison of the experimental electron signal with particle tracking simulations shows excellent qualitative agreement. The position and size of the output beams as well as the electron loss are reproduced. Furthermore, we performed wave-optical simulations to further optimize the shape of the beam splitter potential, which will ultimately allow to split a guided electron wave-packet while preserving its transverse motional quantum state during the beam splitting process.

In this thesis we additionally reported on important experimental progress for the direct injection of electrons into the motional quantum ground state of the transverse guiding potential. We have incorporated optimized coupling structures to provide electrons a smooth passage into the guide. Furthermore, we have performed a phase-resolved measurement demonstrating that the electron injection efficiency can be increased by synchronizing the injection of short electron pulses to a specific orientation of the driving microwave signal.

In addition, this thesis focused on the characterization of the spatial coherence of an electron beam that is emitted from a metal nanotip in laser-triggered photoemission. Although laser-driven nanotips are promising candidates for the generation of coherent

electron pulses with excellent time resolution, a quantitative study of their spatial coherence has been elusive. In the course of this thesis we have designed and constructed an experimental setup for electron interference measurements. We implemented a compact fiber-coupled laser light illumination setup to efficiently drive a one-photon electron emission process when focusing near-ultraviolet laser light on the nanotip. Furthermore, we used a freestanding carbon nanotube as electron matter-wave beam splitter in order to measure the effective source radius of the nanotip in DC-field and photoemission. Experimentally we observe electron interference patterns with at least 21 interference fringes in photoemission and 35 fringes in DC-field emission mode. Taking into account the slightly different deBroglie wavelength of the electrons in both emission modes, we find that the paramount spatial coherence of nanotip electron emitters in DC-field emission is almost fully preserved in photoemission.

Outlook

The experiments on electron guiding feature continuous progress in developing new tools to manipulate guided electrons. After the demonstration of electron guiding, which was achieved by the first doctoral research study on this project, the realization of a beam splitter for guided electrons represents the next important step towards on-chip electron interferometry. Future work will converge towards coherent electron matter-wave optics integrated on a planar microwave chip as will be described in the following.

Direct electron injection into transverse motional quantum states. One major motivation of the electron guiding experiment is the direct injection of electrons into the motional quantum ground state of the transverse guiding potential. In the course of this thesis we have built a field emission electron gun that will improve the mode matching of the injected electron wave packet to the quantum ground state wavefunction of the guide. Currently, this electron source is limited to electron energies above 5 eV because of residual magnetic fields in the setup. A new mu-metal shield that will resolve this issue has already been ordered and only needs to be implemented in the experiment. Furthermore, the gun design allows to laser-trigger the electron source, which enables a pulsed operation of the electron gun with electron pulse durations of several ten picoseconds. In order to inject electrons at a specific phase of the microwave drive, the laser source has to be synchronized with the microwave drive of the guide. A combination of the improved mode matching and the phase-resolved injection should allow the direct injection into low-lying quantum states of the electron guide. At the same time we are investigating the possibility to develop a mode filter that will allow us to selectively remove guided electrons as a function of their transverse energy in the guide. Such a mode filter could function very similarly to the evaporative cooling of trapped atomic clouds by a controlled reduction of the transverse potential depth and would complement the direct electron injection scheme.

Demonstration of electron interference using the microwave beam splitter chip.

It is one of our outstanding goals to realize an experiment that employs a microwave guiding chip to coherently control guided electron matter waves. The envisioned exper-

iment would demonstrate electron interference by overlapping both output beams that are released behind the beam splitter chip described in this thesis. This experiment relies on the coherent field emission electron source and requires electron energies in the single electronvolt range, which is in reach but not yet provided by the source. Additionally, we have to incorporate suitable deflection elements to overlap the two output beams of the beam splitter chip on a electron detector screen. The specific shape of the wavefronts released behind the chip should be studied by a wave-optical simulation to predict the interference pattern that eventually forms on the detector screen. In a more advanced experiment electrons could be injected into the transverse ground state of the beam splitter potential. As we have shown by wave-optical simulations in Ch. 4, we will employ an optimized beam splitter potential in future experiments that allows to preserve the transverse motional quantum state during the splitting process. As a result, the electron wave packet, initially prepared in the ground state, becomes coherently divided into both wells of the beam splitter potential where it populates the respective ground state of each well. Here an entirely new, fully integrated electron interferometer could arise when recombining the guided beam by mirroring the electrode structure and using the same beam splitter potential to recombine the beam. A relative phase shift in one of the interferometer arms would result in a change of the transverse vibrational state of the guided electron after recombination of both beam splitter paths. This kind of interferometer has already been discussed in the context of guided atom interferometry [68, 69].

A linear electron resonator. The surface-electrode design of the electron guide is ideally suited for the implementation of a linear electron resonator. By segmenting the microwave electrodes along the guide, the additional electrodes could be biased with DC voltages to generate a reflecting force in the longitudinal direction of the guide. Guided electrons can be reflected accordingly and hence a linear resonator would comprise two of these on-chip electron mirrors. The transverse guiding potential maintains the transverse confinement and stabilizes the operation of the resonator. A suitable segmentation of the guiding electrodes to realize such an on-chip electron mirror is currently being developed in our group [137]. In order to inject and extract electrons from the resonator, the DC voltages of the mirror have to be switched on and off in a time interval of about $(15 \text{ MHz})^{-1}$, which corresponds to half a round trip of an electron with $E_{kin} = 1 \text{ eV}$ in a 40 mm long resonator. Such a switchable mirror design can be implemented with the microwave technology already at hand for the electron guiding experiment.

Implementation of a quantum electron microscopy scheme. Recently, a new type of electron microscope has been proposed, which is based on the exploitation of quantum effects. The proposed scheme potentially allows imaging with orders of magnitude smaller radiation damage than a conventional electron microscope [14, 15]. A promising application of this quantum electron microscope is the imaging of biological samples, where radiation damage is particularly problematic. The proposal envisions an instrument where an electron wave packet coherently oscillates in either of two resonating structures, a reference and a sample resonator. These resonators are coupled by a coupling element that continuously transfers the amplitude of the quantum wave packet

from one resonator to the other. If an object is present in the sample resonator, it inhibits the coherent transfer between the two resonators due to the quantum Zeno effect [138]. Thus, the presence of an object in the sample resonator would be detected, without direct interaction, if the wave packet remains in the reference resonator. Crucial for the realization of such an instrument is the existence of a suitable coupling element. The microwave chip-based beam splitter could be used as a coupling element, provided that it preserves the transverse motional quantum state of the wave packet during the splitting process.

3D quadrupole guide based on a hollow core photonic crystal fiber (PCF). We have recently started a collaboration with the group of Prof. Ph. Russel to build a 3D quadrupole guide for electrons based on a hollow core fiber [139]. PCFs are fabricated by stacking glass capillaries with diameters of about $100\ \mu\text{m}$ in a defined geometry into a glass tube and fusing the stack to obtain a microstructured cane. Subsequently, these canes are drawn to a fiber and encased by a silica cladding. Because of their broad range in applications PCFs can already be fabricated with very complex geometries and, as an important feature, single capillaries of the cane can be filled with metals. We are currently investigating the use of these canes as a support structure for a 3D electrode geometry as a complementary approach for electron guiding. Here, a circular electrode geometry, like the one originally proposed by W. Paul (see Fig. 2.1), could be realized. It consists of four free-standing gold wires, which are held in place by two short cane segments with $5\ \text{mm}$ length at the start and the end of the wires with several cm distance between them. For such a 3D electron guide the electrodes creating the quadrupole potential have a rotational symmetry leading to an ideal electric field null every where on the guide axis. The electron injection therefore does not suffer from fringing fields on the guide axis. Furthermore, the 3D guide would allow the generation of about ten times larger trap depths U at similar q and ω . The flexibility in fabricable cane geometries also allows to create higher order multipole fields, like e.g. using a hexagonal geometry, which would allow to realize a 3D beam splitter structure based on this approach. We obtained first canes with a hollow core of $180\ \mu\text{m}$ and four holes on the circumference of a ring with a diameter of $130\ \mu\text{m}$, which will hold the metal electrodes. The microwave impedance of this electrode geometry can be matched to $50\ \Omega$, which makes it suitable for high frequency microwave signals. In a first experiment we are studying charging effects of the glassy canes when transmitting a low energy electron beam through its hollow core [140].

Controlled interactions with low-energy guided electrons. Another application of the microwave guide could be the delivery of transversely confined low-energy electrons for scattering experiments with charged or neutral atoms. For example, guided electrons have been considered recently for the controlled collisional excitation of Rydberg atoms [141]. For such an experiment the guide could be brought in close vicinity or overlapped with a (magneto-) optical trap for neutral atoms. Furthermore, the controlled interaction of slow electrons with ions could be studied by superimposing the microwave drive of the guide with a radio-frequency ion trap. This requires that both drive frequencies are sufficiently different from each other to achieve stable confinement.

Bibliography

- [1] de Broglie, L. *Recherches sur la théorie des quanta*. Ph.D. thesis, Université de Paris (1924).
- [2] Davisson, C. & Germer, L. H. Diffraction of electrons by a crystal of nickel. *Phys. Rev.* **30**, 705–740 (1927).
- [3] Jönsson, C. Elektroneninterferenzen an mehreren künstlich hergestellten feinspalten. *Zeitschrift für Physik* **161**, 454–474 (1961).
- [4] Feynman, R. P., Leighton, R. B. & Sands, M. *The Feynman Lectures on Physics, Vol. 3* (Addison-Wesley, 1965).
- [5] Tonomura, A., Endo, J., Matsuda, T., Kawasaki, T. & Ezawa, H. Demonstration of single-electron buildup of an interference pattern. *Am. J. Phys.* **57**, 117–120 (1989).
- [6] Crease, R. P. The most beautiful experiment in physics. *Phys. World* **15**, 15–17 (2002).
- [7] Boersch, H. Fresnelsche Beugung im Elektronenmikroskop. *Physik Z.* **44**, 202 (1943).
- [8] Marton, L., Simpson, J. A. & Suddeth, J. A. Electron beam interferometer. *Phys. Rev.* **90**, 490–491 (1953).
- [9] Möllenstedt, G. & Düker, H. Fresnelscher Interferenzversuch mit einem Biprisma für Elektronenwellen. *Naturwissenschaften* **42**, 41–41 (1955).
- [10] Tonomura, A., Osakabe, N., Matsuda, T., Kawasaki, T., Endo, J., Yano, S. & Yamada, H. Evidence for Aharonov-Bohm effect with magnetic field completely shielded from electron wave. *Phys. Rev. Lett.* **56**, 792–795 (1986).
- [11] Kiesel, H., Renz, A. & Hasselbach, F. Observation of Hanbury Brown-Twiss anticorrelations for free electrons. *Nature* **418**, 392–394 (2002).
- [12] Sonnentag, P. & Hasselbach, F. Measurement of decoherence of electron waves and visualization of the quantum-classical transition. *Phys. Rev. Lett.* **98**, 200402 (2007).
- [13] Hasselbach, F. Progress in electron- and ion-interferometry. *Rep. Progr. Phys.* **73**, 016101 (2010).

- [14] Putnam, W. P. & Yanik, M. F. Noninvasive electron microscopy with interaction-free quantum measurements. *Phys. Rev. A* **80**, 040902 (2009).
- [15] Thomas, S., Kohstall, C., Kruit, P. & Hommelhoff, P. Semitransparency in interaction-free measurements. *Phys. Rev. A* **90**, 053840 (2014).
- [16] Paul, W. Electromagnetic traps for charged and neutral particles. *Rev. Mod. Phys.* **62**, 531–540 (1990).
- [17] Leibfried, D., Blatt, R., Monroe, C. & Wineland, D. Quantum dynamics of single trapped ions. *Rev. Mod. Phys.* **75**, 281–324 (2003).
- [18] Wineland, D. J. Nobel lecture: Superposition, entanglement, and raising schrödinger's cat. *Rev. Mod. Phys.* **85**, 1103–1114 (2013).
- [19] Hoffrogge, J., Fröhlich, R., Kasevich, M. A. & Hommelhoff, P. Microwave guiding of electrons on a chip. *Phys. Rev. Lett.* **106**, 193001 (2011).
- [20] Hoffrogge, J. & Hommelhoff, P. Planar microwave structures for electron guiding. *New J. Phys.* **13**, 095012 (2011).
- [21] Fransen, M., Damen, E., Schiller, C., van Rooy, T., Groen, H. & Kruit, P. Characterization of ultrasharp field emitters by projection microscopy. *Appl. Surf. Sci.* **94/95**, 107 – 112 (1996).
- [22] Cho, B., Ichimura, T., Shimizu, R. & Oshima, C. Quantitative evaluation of spatial coherence of the electron beam from low temperature field emitters. *Phys. Rev. Lett.* **92**, 246103 (2004).
- [23] Spence, J. *High-Resolution Electron Microscopy* (Oxford University Press, 2013).
- [24] Paul, W. & Steinwedel, H. Ein neues Massenspektrometer ohne Magnetfeld. *Zeitschrift Naturforschung Teil A* **8**, 448 (1953).
- [25] Paul, W. & Raether, M. Das elektrische Massenfilter. *Zeitschrift für Physik* **140**, 262–273 (1955).
- [26] Penning, F. M. Die Glimmentladung bei niedrigem Druck zwischen koaxialen Zylindern in einem axialen Magnetfeld. *Physica* **3**, 873 – 894 (1936).
- [27] Paul, W., Osberghaus, O. & Fischer, E. Ein Ionenkäfig. *Forschungsberichte des Wirtschafts- und Verkehrsministers Nordrhein-Westfalen* **415** (1958).
- [28] Hänsch, T. W. & Schawlow, A. L. Cooling of gases by laser radiation. *Optics Comm.* **13**, 68 (1975).
- [29] Wineland, D. & Dehmelt, H. Proposed $10^{14}\delta\nu/\nu$ laser fluorescence spectroscopy on Ti^+ mono-ion oscillator III. *Bull. Am. Phys. Soc.* **20**, 637 (1975).
- [30] Diedrich, F., Bergquist, J. C., Itano, W. M. & Wineland, D. J. Laser cooling to the zero-point energy of motion. *Phys. Rev. Lett.* **62**, 403 (1989).

- [31] Oskay, W. H., Diddams, S. A., Donley, E. A., Fortier, T. M., Heavner, T. P., Hollberg, L., Itano, W. M., Jefferts, S. R., Delaney, M. J., Kim, K., Levi, F., Parker, T. E. & Bergquist, J. C. Single-atom optical clock with high accuracy. *Phys. Rev. Lett.* **97**, 020801 (2006).
- [32] Blatt, R. & Wineland, D. Entangled states of trapped atomic ions. *Nature* **453**, 1008–1015 (2008).
- [33] Wineland, D. J. & Leibfried, D. Quantum information processing and metrology with trapped ions. *Laser Physics Letters* **8**, 175–188 (2011).
- [34] Häffner, H., Roos, C. F. & Blatt, R. Quantum computing with trapped ions. *Phys. Rep.* **469**, 155–203 (2008).
- [35] Friedenauer, A., Schmitz, H., Glueckert, J. T., Porras, D. & Schaetz, T. Simulating a quantum magnet with trapped ions. *Nat. Phys.* **4**, 757–761 (2008).
- [36] Pyka, K., Keller, J., Partner, H. L., Nigmatullin, R., Burgermeister, T., Meier, D. M., Kuhlmann, K., Retzker, A., Plenio, M. B., Zurek, W. H., del Campo, A. & Mehlstäubler, T. E. Topological defect formation and spontaneous symmetry breaking in ion coulomb crystals. *Nat. Commun.* **4** (2013).
- [37] Hoffrogge, J. P. *A surface-electrode quadrupole guide for electrons*. Ph.D. thesis, Ludwig-Maximilians-Universität München (2012).
- [38] Chiaverini, J., Blakestad, R. B., Britton, J., Jost, J. D., Langer, C., Leibfried, D., Ozeri, R. & Wineland, D. J. Surface-electrode architecture for ion-trap quantum information processing. *Quant. Inf. Comp.* **5**, 419–439 (2005).
- [39] Hughes, M. D., Lekitsch, B., Broersma, J. A. & Hensinger, W. K. Microfabricated ion traps. *Contemporary Physics* **52**, 505–529 (2011). 1101.3207.
- [40] Ghosh, P. K. *Ion traps*. The international series of monographs on physics (Clarendon Press, Oxford, 1995).
- [41] Major, F. G., Gheorghe, V. N. & Werth, G. *Charged Particle Traps* (Springer, Berlin Heidelberg New York, 2005).
- [42] Seidelin, S., Chiaverini, J., Reichle, R., Bollinger, J. J., Leibfried, D., Britton, J., Wesenberg, J. H., Blakestad, R. B., Epstein, R. J., Hume, D. B., Itano, W. M., Jost, J. D., Langer, C., Ozeri, R., Shiga, N. & Wineland, D. J. Microfabricated surface-electrode ion trap for scalable quantum information processing. *Phys. Rev. Lett.* **96**, 253003 (2006).
- [43] Amini, J., Britton, J., Leibfried, D. & Wineland, D. J. Microfabricated chip traps for ions. In Reichel, J. & Vuletic, V. (eds.) *Atom Chips* (Wiley-VCH, Berlin, 2011).
- [44] Brown, K. R., Ospelkaus, C., Colombe, Y., Wilson, D., A. C. and Leibfried & Wineland, D. J. Coupled quantized mechanical oscillators. *Nature* **471**, 196 (2011).

-
- [45] Harlander, M., Lechner, R., Brownnutt, M., Blatt, R. & Hänsel, W. Trapped-ion antennae for the transmission of quantum information. *Nature* **471**, 200 (2011).
- [46] VanDevender, A. P., Colombe, Y., Amini, J., Leibfried, D. & Wineland, D. J. Efficient fiber optic detection of trapped ion fluorescence. *Phys. Rev. Lett.* **105**, 023001 (2010).
- [47] Kim, T. H., Herskind, P. F. & Chuang, I. L. Surface-electrode ion trap with integrated light source. *Applied Physics Letters* **98**, 214103 (2011).
- [48] Herskind, P. F., Wang, S. X., Shi, M., Ge, Y., Cetina, M. & Chuang, I. L. Microfabricated surface ion trap on a high-finesse optical mirror. *Optics Lett.* **36**, 3045–3047 (2011).
- [49] True Merrill, J., Volin, C., Landgren, D., Amini, J. M., Wright, K., Doret, S. C., Pai, C.-S., Hayden, H., Killian, T., Faircloth, D., Brown, K. R., Harter, A. W. & Slusher, R. E. Demonstration of integrated microscale optics in surface-electrode ion traps. *New Journal of Physics* **13**, 103005 (2011). 1105.4905.
- [50] Ospelkaus, C., Warring, U., Colombe, Y., Brown, K. R., Amini, J. M., Leibfried, D. & Wineland, D. J. Microwave quantum logic gates for trapped ions. *Nature* **476**, 181–184 (2011). 1104.3573.
- [51] Allcock, D. T. C., Harty, T. P., Ballance, C. J., Keitch, B. C., Linke, N. M., Stacey, D. N. & Lucas, D. M. A microfabricated ion trap with integrated microwave circuitry. *Appl. Phys. Lett.* **102**, 044103 (2013).
- [52] Wang, S. X., Labaziewicz, J., Ge, Y., Shewmon, R. & Chuang, I. L. Demonstration of a quantum logic gate in a cryogenic surface-electrode ion trap. *Phys. Rev. A* **81**, 062332 (2010).
- [53] Wang, S. X., Ge, Y., Labaziewicz, J., Dauler, E., Berggren, K. & Chuang, I. L. Superconducting microfabricated ion traps. *Appl. Phys. Lett.* **97**, 244102 (2010).
- [54] Wesenberg, J. H. Electrostatics of surface-electrode ion traps. *Phys. Rev. A* **78**, 063410 (2008).
- [55] House, M. G. Analytic model for electrostatic fields in surface-electrode ion traps. *Phys. Rev. A* **78**, 033402 (2008).
- [56] Schmied, R. Electrostatics of gapped and finite surface electrodes. *New J. Phys.* **12**, 023038 (2010).
- [57] Labaziewicz, J., Ge, Y., Leibbrandt, D. R., Wang, S. X., Shewmon, R. & Chuang, I. L. Temperature dependence of electric field noise above gold surfaces. *Phys. Rev. Lett.* **101**, 180602 (2008).
- [58] Pozar, D. M. *Microwave Engineering* (John Wiley and Sons, 2005), 3 edn.
- [59] Zech, T. *Planare elektrisch-lange Strukturen zur Führung von Elektronen in einem Quadrupol-Potential*. Bachelor's thesis, Universität Erlangen-Nürnberg (2014).

- [60] Cohen-Tannoudji, C., Diu, B. & Laloe, F. *Quantenmechanik*, vol. 1 (Walter de Gruyter, Berlin, New York, 1999), 2nd edn.
- [61] Hawkes, P. W. & Kasper, E. *Principles of Electron Optics, Vol. 3 Wave Optics* (Academic Press, London, 1994).
- [62] Born, M. & Wolf, E. *Principles of Optics* (Cambridge University Press, 1999), 7 edn.
- [63] Schiff, L. *Quantum Mechanics* (McGraw-Hill, 1968).
- [64] Reimer, L. *Scanning electron microscopy: physics of image formation and microanalysis* (Springer, 1985).
- [65] Barth, J. E. & Kruit, P. *Addition of different contributions to the charged particle probe size*. Optik (American Elsevier Publishing Company, Inc., Reutlingen, 1996).
- [66] Fleck, J., J.A., Morris, J. & Feit, M. Time-dependent propagation of high energy laser beams through the atmosphere. *Applied physics* **10**, 129–160 (1976).
- [67] Feit, M., Jr., J. F. & Steiger, A. Solution of the schrödinger equation by a spectral method. *Journal of Computational Physics* **47**, 412 – 433 (1982).
- [68] Hänsel, W., Reichel, J., Hommelhoff, P. & Hänsch, T. W. Trapped-atom interferometer in a magnetic microtrap. *Phys. Rev. A* **64**, 063607 (2001).
- [69] Andersson, E., Calarco, T., Folman, R., Andersson, M., Hessmo, B. & Schmiedmayer, J. Multimode interferometer for guided matter waves. *Phys. Rev. Lett.* **88**, 100401 (2002).
- [70] Hammer, J., Hoffrogge, J., Heinrich, S. & Hommelhoff, P. Phase-resolved electron guiding in optimized chip-based microwave potentials. *Phys. Rev. Applied* **2**, 044015 (2014).
- [71] Heinrich, S. *Charakterisierung und Herstellung von planaren Quadrupol-Elektronenleitern*. Master's thesis, Ludwig-Maximilians-Universität München (2014).
- [72] Erdman, P. W. & Zipf, E. C. Low-voltage, high-current electron gun. *Rev. Sci. Instr.* **53**(2), 225–227 (1982).
- [73] Hawkes, P. W. & Kasper, E. *Principles of Electron Optics, Vol.2 Applied Geometrical Optics* (Academic Press, London, 1989).
- [74] See <http://atom.physik.unibas.ch/people/romanschmied/code/SurfacePattern.php>.
- [75] Schmied, R., Wesenberg, J. H. & Leibfried, D. Optimal surface-electrode trap lattices for quantum simulation with trapped ions. *Phys. Rev. Lett.* **102**, 233002 (2009).

- [76] Hommelhoff, P., Kealhofer, C., Aghajani-Talesh, A., Sortais, Y. R., Foreman, S. M. & Kasevich, M. A. Extreme localization of electrons in space and time. *Ultramicroscopy* **109**, 423 – 429 (2009).
- [77] Paarmann, A., Gulde, M., Müller, M., Schäfer, S., Schweda, S., Maiti, M., Xu, C., Hohage, T., Schenk, F., Ropers, C. & Ernstorfer, R. Coherent femtosecond low-energy single-electron pulses for time-resolved diffraction and imaging: A numerical study. *J. Appl. Phys.* **112**, 113109 (2012).
- [78] Hoffrogge, J., Stein, J.-P., Krüger, M., Förster, M., Hammer, J., Ehberger, D., Baum, P. & Hommelhoff, P. Tip-based source of femtosecond electron pulses at 30 keV. *J. Appl. Phys.* **115** (2014).
- [79] Mandel, L. & Wolf, E. *Optical Coherence and Quantum Optics* (Cambridge University Press, 1995).
- [80] Bloch, I., Dalibard, J. & Zwierger, W. Many-body physics with ultracold gases. *Rev. Mod. Phys.* **80**, 885–964 (2008).
- [81] Rauch, H. & Werner, S. *Neutron Interferometry*. Oxford Series on Neutron Scattering in Condensed Matter (Oxford University Press, 2000).
- [82] Juffmann, T., Milic, A., Mullneritsch, M., Asenbaum, P., Tsukernik, A., Tuxen, J., Mayor, M., Cheshnovsky, O. & Arndt, M. Real-time single-molecule imaging of quantum interference. *Nature Nanotechnology* **7**, 297–300 (2012).
- [83] Gabor, D. A new microscopic principle. *Nature* **161**, 777–778 (1948).
- [84] Tonomura, A. *Electron Holography*. Springer Series in Optical Sciences (Springer, Heidelberg, 1999).
- [85] Wesenberg, J. H. Ideal intersections for radio-frequency trap networks. *Phys. Rev. A* **79**, 013416 (2009).
- [86] Hommelhoff, P. & Hammer, J. Patent pending (2014).
- [87] Blackman, R. B. & Tukey, J. W. *The measurement of power spectra from the point of view of communications engineering*, p 98 (Dover Publications, New York, 1958).
- [88] Erni, R., Rossell, M. D., Kisielowski, C. & Dahmen, U. Atomic-resolution imaging with a sub-50-pm electron probe. *Phys. Rev. Lett.* **102**, 096101 (2009).
- [89] Zewail, A. H. & Thomas, J. M. *4D Electron Microscopy Imaging in Space and Time* (Imperial College Press, 2010).
- [90] King, W. E., Campbell, G. H., Frank, A., Reed, B., Schmerge, J. F., Siwick, B. J., Stuart, B. C. & Weber, P. M. Ultrafast electron microscopy in materials science, biology and chemistry. *J. Appl. Phys.* **97**, 111101 (2005).

-
- [91] Sciaini, G. & Miller, R. J. D. Femtosecond electron diffraction: heralding the era of atomically resolved dynamics. *Rep. Progr. Phys.* **74**, 096101 (2011).
- [92] Baum, P., Yang, D.-S. & Zewail, A. H. 4d visualization of transitional structures in phase transformations by electron diffraction. *Science* **318**, 788–792 (2007).
- [93] Krüger, M., Schenk, M. & Hommelhoff, P. Attosecond control of electrons emitted from a nanoscale metal tip. *Nature* **475**, 78–81 (2011).
- [94] Herink, G., Solli, D. R., Gulde, M. & Ropers, C. Field-driven photoemission from nanostructures quenches the quiver motion. *Nature* **483**, 190–193 (2012).
- [95] Chang, C.-C., Kuo, H.-S., Hwang, I.-S. & Tsong, T. T. A fully coherent electron beam from a noble-metal covered W(111) single-atom emitter. *Nanotech.* **20**, 115401 (2009).
- [96] Klein, M. & Schwitzgebel, G. An improved lamellae drop-off technique for sharp tip preparation in scanning tunneling microscopy. *Rev. Sci. Instr.* **68**, 3099–3103 (1997).
- [97] Krüger, M. *Laser-Triggered Electron Emission From Tungsten Tips*. Master's thesis, Ludwig-Maximilians-Universität München (2009).
- [98] Mendenhall, C. E. & DeVoe, C. F. The photoelectric work functions of the 211 and 310 planes of tungsten. *Phys. Rev.* **51**, 346–349 (1937).
- [99] Fowler, R. H. & Nordheim, L. Electron emission in intense electric fields. *Proc. R. Soc. London A* **119**, 173–181 (1928).
- [100] Müller, E. W. Versuche zur Theorie der Elektronenemission unter der Einwirkung hoher Feldstärken. *Z. Tech. Phys.* **37**, 838–842 (1936).
- [101] Gomer, R. *Field Emission and Field Ionization* (Harvard University Press, Cambridge, Massachusetts, 1961).
- [102] Michaelson, H. B. The work function of the elements and its periodicity. *Journal of Applied Physics* **48**, 4729–4733 (1977).
- [103] Müller, E. W. & Bahadur, K. Field ionization of gases at a metal surface and the resolution of the field ion microscope. *Phys. Rev.* **102**, 624–631 (1956).
- [104] Tsong, T. T. *Atom-probe field ion microscopy* (Cambridge University Press, Cambridge, 1990).
- [105] Müller, E. W. & Tsong, T. T. *Field Ion Microscopy* (American Elsevier Publishing Company, Inc., New York, 1969).
- [106] Fink, H.-W. Point source for ions and electrons. *Phys. Scr.* **38**, 260–263 (1988).

- [107] Gohda, Y., Nakamura, Y., Watanabe, K. & Watanabe, S. Self-consistent density functional calculation of field emission currents from metals. *Phys. Rev. Lett.* **85**, 1750–1753 (2000).
- [108] Gohda, Y. & Watanabe, S. Total energy distribution of field-emitted electrons from al(100) surface with single-atom terminated protrusion. *Phys. Rev. Lett.* **87**, 177601 (2001).
- [109] Janssen, A. P. & Jones, J. P. The sharpening of field emitter tips by ion sputtering. *Journal of Physics D: Applied Physics* **4**, 118 (1971).
- [110] Binh, V. T., Purcell, S. T., Garcia, N. & Doglioni, J. Field-emission electron spectroscopy of single-atom tips. *Phys. Rev. Lett.* **69**, 2527–2530 (1992).
- [111] Nagaoka, K., Fujii, H., Matsuda, K., Komaki, M., Murata, Y., Oshima, C. & Sakurai, T. Field emission spectroscopy from field-enhanced diffusion-growth nano-tips. *Applied Surface Science* **182**, 12 – 19 (2001).
- [112] Kuo, H. S., Hwang, I. S., Fu, T. Y., Wu, J. Y., Chang, C. C. & Tsong, T. T. Preparation and characterization of single-atom tips. *Nano Letters* **4**, 2379–2382 (2004).
- [113] Fu, T.-Y., Cheng, L.-C., Nien, C.-H. & Tsong, T. T. Method of creating a Pd-covered single-atom sharp W pyramidal tip: Mechanism and energetics of its formation. *Phys. Rev. B* **64**, 113401 (2001).
- [114] de Jonge, N., Lamy, Y., Schoots, K. & Oosterkamp, T. H. High brightness electron beam from a multi-walled carbon nanotube. *Nature* **420**, 393–395 (2002).
- [115] Yang, D.-S., Mohammed, O. F. & Zewail, A. H. Scanning ultrafast electron microscopy. *Proc. Nat. Acad. Sci. USA* **107**, 14993–14998 (2010).
- [116] Ehberger, D. *Characterization of a tungsten tip based electron source triggered by fiber coupled laser pulses in the near-ultraviolet*. Master’s thesis, Ludwig-Maximilians-Universität München (2013).
- [117] Bao, H., Allen, J., Pattie, R., Vance, R. & Gu, M. Fast handheld two-photon fluorescence microendoscope with a $475\ \mu\text{m} \times 475\ \mu\text{m}$ field of view for in vivo imaging. *Opt. Lett.* **33**, 1333–1335 (2008).
- [118] Abraham, E. R. I. & Cornell, E. A. Teflon feedthrough for coupling optical fibers into ultrahigh vacuum systems. *Appl. Opt.* **37** (1998).
- [119] Crewe, A. V., Eggenberger, D. N., Wall, J. & Welter, L. M. Electron gun using a field emission source. *Rev. Sci. Instrum.* **39**, 576–583 (1968).
- [120] Lichte, H. & Lehmann, M. Electron holography: basics and applications. *Rep. Progr. Phys.* **71**, 016102 (2008).

- [121] Spence, J. C. H., Qian, W. & Silverman, M. P. Electron source brightness and degeneracy from Fresnel fringes in field emission point projection microscopy. *Journal of Vacuum Science Technology* **12**, 542–547 (1994).
- [122] Pozzi, G. Theoretical considerations on the spatial coherence in field emission electron microscopes. *Optik* **77**, 69–73 (1987).
- [123] Jensen, K. L., O’Shea, P. G., Feldman, D. W. & Shaw, J. L. Emittance of a field emission electron source. *J. Appl. Phys.* **107**, 014903 (2010).
- [124] Delone, N. B. & Krainov, V. P. *Multiphoton Processes in Atoms* (Springer, Berlin Heidelberg New York, 1994).
- [125] Cook, B., Verduin, T., Hagen, C. W. & Kruit, P. Brightness limitations of cold field emitters caused by coulomb interactions. *J. Vac. Sci. Tech. B* **28**, C6C74–C6C79 (2010).
- [126] Beyer, A. & Götzhäuser, A. Low energy electron point source microscopy: beyond imaging. *J. Phys.: Cond. Mat.* **22**, 343001 (2010).
- [127] Hofmann, M. S., Glückert, J. T., Noé, J., Bourjau, C., Dehmel, R. & Högele, A. Bright, long-lived and coherent excitons in carbon nanotube quantum dots. *Nature Nanotechnology* **8**, 502–505 (2013).
- [128] Hwang, I.-S., Chang, C.-C., Lu, C.-H., Liu, S.-C., Chang, Y.-C., Lee, T.-K., Jeng, H.-T., Kuo, H.-S., Lin, C.-Y., Chang, C.-S. & Tsong, T. T. Investigation of single-walled carbon nanotubes with a low-energy electron point projection microscope. *New J. Phys.* **15**, 043015 (2013).
- [129] Möllenstedt, G. & Düker, H. Beobachtungen und Messungen an Biprisma-Interferenzen mit Elektronenwellen. *Z. Phys.* **145**, 377–397 (1956).
- [130] Barwick, B., Park, H. S., Kwon, O.-H., Baskin, J. S. & Zewail, A. H. 4d imaging of transient structures and morphologies in ultrafast electron microscopy. *Science* **322**, 1227–1231 (2008).
- [131] Kirchner, F. O., Gliserin, A., Krausz, F. & Baum, P. Laser streaking of free electrons at 25 keV. *Nat. Phot.* **8**, 52–57 (2014).
- [132] Eisele, M. *Laser Triggered Electron Emission from Sharp Metal Tips with Femtosecond Laser Pulses in the near Ultraviolet*. Master’s thesis, Technische Universität München (2010).
- [133] Quinonez, E., Handali, J. & Barwick, B. Femtosecond photoelectron point projection microscope. *Rev. Sci. Instr.* **84** (2013).
- [134] Gulde, M., Schweda, S., Storeck, G., Maiti, M., Yu, H. K., Wodtke, A. M., Schäfer, S. & Ropers, C. Ultrafast low-energy electron diffraction in transmission resolves polymer/graphene superstructure dynamics. *Science* **345**, 200–204 (2014).

-
- [135] Müller, M., Paarmann, A. & Ernstorfer, R. Femtosecond electrons probing currents and atomic structure in nanomaterials. *Nat. Commun.* **5** (2014).
- [136] See <http://www.lnf.infn.it/acceleratori/dafne/NOTEDAFNE/V/V-2.pdf>.
- [137] Thomas, S. *To be published*. Ph.D. thesis, Ludwig-Maximilians-Universität München (exp. 2015).
- [138] Kwiat, P., Weinfurter, H., Herzog, T., Zeilinger, A. & Kasevich, M. A. Interaction-free measurement. *Phys. Rev. Lett.* **74**, 4763–4766 (1995).
- [139] Russell, P. Photonic crystal fibers. *Science* **299**, 358–362 (2003).
- [140] Weber, P. *To be published*. Ph.D. thesis, Friedrich-Alexander-Universität Erlangen-Nürnberg (exp. 2016).
- [141] Laycock, T., Olmos, B., Montgomery, T. W. A., Li, W., Fromhold, T. M. & Lesanovsky, I. Control of atomic Rydberg states using guided electrons. *Journal of Physics B: Atomic, Molecular and Optical Physics* **46**, 245502 (2013).

Danksagung

Mein Dank gebührt allen Freunden und Kollegen, die zum Gelingen dieser Arbeit beigetragen haben.

Zuallererst danke ich Professor Peter Hommelhoff für die Betreuung dieser Arbeit. Seine grenzenlose Begeisterung für die Physik und die besondere Gabe, diese in Diskussionen und Besprechungen auf ansteckende Weise zu teilen, waren mir stets ein großer Ansporn. Er hat mir von Beginn an großes Vertrauen entgegengebracht und es mir ermöglicht mit freier Hand die Experimente durchzuführen. Stets hat er mich mit zahllosen Ideen und Anregungen unterstützt. Durch sein unermüdliches Engagement hat er unserer Arbeitsgruppe ein ausgezeichnetes Forschungsumfeld geschaffen.

Mein großer Dank gilt allen gegenwärtigen und ehemaligen Mitgliedern der Hommelhoff-Gruppe. An erster Stelle sei hier Johannes Hoffrogge, der Elektronenfänger der ersten Stunde, genannt. Die gemeinsame Arbeit mit Jo am Guiding-Experiment war immer mit viel Spaß verbunden. Er hat zu großen Teilen zum Gelingen dieser Arbeit beigetragen. Zum einen durch das funktionierende Experiment, das er mir übergeben hat und zum anderen, weil er hervorragende Kommentare zu dieser Arbeit beigesteuert hat. Gleichmaßen möchte ich mich auch bei Dominik Ehberger und Stephan Heinrich bedanken. Ich habe mit Ihnen eine großartige Zeit im Labor verbracht. Beide haben als Masteranden maßgeblich zu den Ergebnissen dieser Arbeit beigetragen. Ich danke auch Sebastian Thomas und Philipp Weber, die mich am Guiding-Experiment unterstützt haben und bei denen das Experiment in Zukunft in den allerbesten Händen ist. An dieser Stelle sei auch Sebastian und Takuya Higuchi für ihre zahlreichen Kommentare zu dieser Arbeit gedankt.

Ich danke Takuya Higuchi, meinem Büronachbarn, für die schöne Zeit. Vielen Dank auch an John Breuer, Michael Förster, Michael Krüger, Lothar Maisenbacher, Markus Schenk und alle anderen Mitgliedern unserer Gruppe, die mir jederzeit unter die Arme gegriffen haben und zu einer guten Stimmung beigetragen haben. Außerdem danke ich Wolfgang Simon und Charly Linner, den hervorragenden Technikern am MPQ. Insbesondere Wolfgang hat mit seinem Ehrgeiz Lösungen zu finden, die Hand und Fuß haben, große (bzw. oft auch kleine) Stücke zu dieser Arbeit beigetragen. Ebenso danke ich Philipp Altpeter, der mich im Reinraum der Kotthausgruppe mit großem Engagement unterstützt hat.

Meinen Eltern und meinen beiden Brüdern danke ich von ganzem Herzen. Sie waren immer für mich da, haben mich jederzeit unterstützt und mir mit ihrem unermesslichen Vertrauen das Physikstudium ermöglicht und meine Auslandspläne gefördert.

Mein tiefer Dank gilt meiner Verlobten Bine. Sie hat mir uneingeschränkten Rückhalt gegeben und ich hoffe Ihr in der kommenden Zeit einen winzigen Teil davon zurückgeben zu können.